Università degli Studi di Torino
Doctoral School of the University of Torino
PhD Programme in Chemical and Materials Sciences XXXIII Cycle

Physico-chemical characterization of diopside in lapis lazuli: a study from luminescence activators and quenchers to material provenance investigations

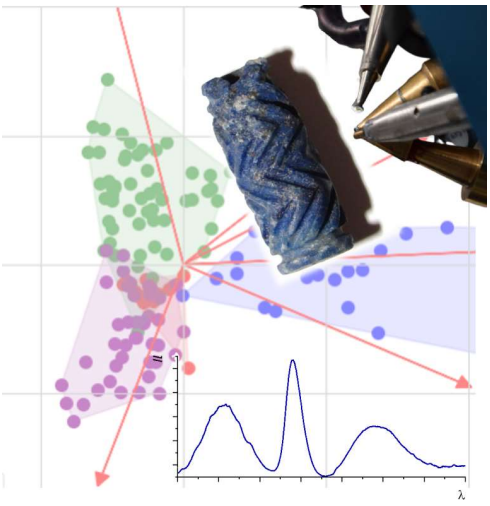

Laura Guidorzi

Supervisor:
Prof. Alessandro Lo Giudice
Co-supervisor:
Dr. Alessandro Re

Università degli Studi di Torino

Doctoral School of the University of Torino

PhD Programme in Chemical and Materials Sciences XXXIII cycle

Physico-chemical characterization of diopside in lapis lazuli: a study from luminescence activators and quenchers to material provenance investigations

Candidate: **Laura Guidorzi**

Supervisor: Prof. **Alessandro Lo Giudice**

Co-supervisor: Dr. **Alessandro Re**

Jury Members: Prof. **Lorenzo Giuntini**
Università degli Studi di Firenze
Department of Physics and Astronomy

Prof. **Lara Maritan**
Università degli Studi di Padova
Department of Geosciences

Prof. **Ettore Vittone**
Università degli Studi di Torino
Department of Physics

Head of the Doctoral School: Prof. Alberto Rizzuti
PhD Programme Coordinator: Prof. Bartolomeo Civalleri

Torino, March 30th, 2021

Table of contents

List of Abbreviations and Acronyms

AAS – Atomic Absorption Spectroscopy
AGLAE – Accélerateur Grand Louvre d'Analyse Elémentaire
C2RMF – Centre de Recherche et de Restauration des Musées de France
CAT – Chemometric Agile Tool
CB – Conduction Band
CL – CathodoLuminescence
CV – Cross Validation
CW – Continuous Wavelength
EDA – Exploratory Data Analysis
EDX – Energy Dispersive X-ray (Spectrometry)
EXAFS – Extended X-ray Absorption Fine Structure (Spectroscopy)
FEG – Field Emission Gun
FTIR – Fourier Transform InfraRed (Spectroscopy)
IBA – Ion Beam Analysis
(μ-)IBIL – (micro) Ion Beam Induced Luminescence
aka (μ-)IL – (micro) IonoLuminescence
ICP-MS – Inductively Coupled Plasma Mass Spectrometry
INFN-LNL – Legnaro National Laboratories of the Italian National Institute of Nuclear Physics
IVC – Indus Valley Civilisation
LDA – Linear Discriminant Analysis
LOD – Limit of Detection
MD – Mahalanobis Distance
MVA – Multivariate Analysis
NIPALS - Nonlinear Iterative Partial Least Squares
OM – Optical Microscopy
PCA – Principal Component Analysis
PIGE – Particle Induced Gamma-ray Emission
(μ-)PIXE – (micro) Particle Induced X-ray Emission
PGAA – Prompt Gamma-Ray Activation Analysis
PLSR – Partial Least Squared Regression
RBS – Rutherford Backscattering Spectrometry
REE – Rare Earth Element
RMSEC - Root Mean Squared Error in Calibration
RMSECV – Root Mean Squared Error in Cross Validation
RMSEP – Root Mean Squared Error in Prediction
SD – Standard Deviation
SEM – Scanning Electron Microscopy
SIBILLA – Simultaneous Ion Beam Investigations for Lapis Lazuli provenance Analysis
SIMCA – Soft Independent Modelling of Class Analogy
SNV – Standard Normal Variate
VB – Valence Band
WDX – Wavelength Dispersive X-ray (Spectrometry)
XANES – X-ray Absorption Near Edge Structure (Spectroscopy)
XRD – X-Ray Diffraction
XRF – X-Ray Fluorescence

1. Thesis overview

Lapis lazuli is a semi-precious blue stone widely used for different purposes since the antiquity but, at present, information about both its ancient trades and the quarries exploited from different civilisations is still lacking. The restraining geological conditions in which it can form limit its sources to only a few places around the world. This represents a possibility for tracing back the original quarry exploited for the manufacturing of an ancient object on the basis of the physico-chemical characteristics of the material.

The present work is part of the wide provenance study on lapis lazuli that was started almost fifteen years ago by the group at the Physics Department of the University of Torino, in collaboration with the Italian National Institute of Nuclear Physics (INFN). The study is based on a multi-technique approach, including both invasive (optical microscopy, cold-cathodoluminescence and SEM-EDX on thick and cross sections) and non-invasive (X-ray fluorescence or Ion Beam Analyses (IBA), such as Particle Induced X-ray Emission and Ionoluminescence) techniques and involving a multidisciplinary team of physicists, geologists, chemists, but also archaeologists, conservation scientists and museum curators.

As lapis lazuli can present a wide variety of mineral phases, the provenance study focuses on the most widespread ones, as lazurite, pyrite, wollastonite and diopside, a mineral of the pyroxene group. The investigation of single mineral phases requires the use of techniques that can go down to the microscale. Some provenance markers have been defined so far for four different provenances (Afghanistan, Tajikistan, Siberia and Chile) and used in the compilation of a provenance protocol, that has already been applied to archaeological samples with interesting results, but still need to be integrated with other provenances. Ionoluminescence features in diopside crystals within lapis lazuli seems to have a role in the discrimination of quarries, but their occurrence is not the same in all samples and, as consequence, they could not have been considered so far strong markers for provenance. One of the aims of this work is then to focus on the diopside mineral phase to better understand the synchronous mechanisms that link luminescence emission and trace element composition, looking for correlations among them.

After an introduction on the archaeological issue of lapis lazuli provenance, diopside structure and its known luminescent mechanisms are described. All geological and archaeological samples available for this study are subsequently presented, comprehending a total of 60 reference geological samples and 24 fragments and artefacts of archaeological interest.

Then, results obtained by means of the aforementioned techniques are discussed, with a view on both aspects of this research. The first goal, following the provenance quest, was to deepen the knowledge of raw lapis lazuli characterisation, and possibly to extend the protocol, with new samples from Myanmar quarries and from the hypothetical source in Chagai Hills (Pakistan). Also, the provenance protocol was

applied to archaeological samples such as lapis lazuli fragments from the working site of Shahr-i Sokhta (Iran, III millennium BCE), a seal found on the same site and several shards from settlements of the Indus Valley Civilization (IV-II millennium BCE). For this purpose, markers in diopside and pyrite crystals have been analysed with μ-IBA techniques. Additionally, a test in using SEM-WDX technique as an alternative to μ-PIXE for trace element quantification was performed on diopside crystals from lapis lazuli of different origin.

The second goal, using as a starting point the data collected for provenance purposes, was a further deepening of the knowledge on Ionoluminescence activation and quenching phenomena in diopside. A specific project was created with this purpose during the PhD, granting access to international IBA facilities thanks to the European IPERION CH/IPERION HS programmes. The analyses were carried out in particular at the recently improved Accélerateur Grand Louvre d'Analyse Elémentaire (NewAGLAE) of the C2RMF (Centre de Recherche et de Restauration des Musées de France) in Paris.

Moreover, on both research topics the application of multivariate analysis was introduced, in order to simplify the visualisation and interpretation of the results with unsupervised methods such as Principal Component Analysis, as well as to develop models for provenance classification and for the regression of the μ-IL spectra with supervised methods.

2. Lapis lazuli and its provenance

Lapis lazuli, the blue semi-precious stone, has been in times awe-inspiring for the artistic traditions of ancient civilisations. As it requires peculiar conditions to be formed, this rock occurs only in few places in the world: this uniqueness has enhanced its prestige in the past and, at the same time, has stimulated the archaeological and archaeometrical research on its provenance and ancient trade routes. In the following sections, a concise but comprehensive introduction to lapis lazuli and its characteristics is given, from the historical point of view to the geological aspects, all linked in the wide provenance issue.

2.1. History of lapis lazuli

The ancient tradition of crafting jewellery and carving objects from stones and soft material (bone, ivory, horns, shells and calcareous stones) began in the Upper Palaeolithic and continued onwards through Mesolithic and Neolithic [Casanova 2013]. Such items represented symbols of social prestige, but served also veneration purposes, as they acted as a connection between people and divinity [Bulgarelli and Tosi 1977]. This perception was exalted by the rarity of some of the stones used, findable only in few places of the world and hence transported for thousands kilometres away from their origin via complex networks of exchanges and trades routes.

Lapis lazuli is one of the first and rarest semi-precious stones to be employed in this production and trade, due also to its appealing characteristic blue colour (figure 2.1). Archaeological objects, like beads, gems, seals and small decorative items made of lapis lazuli are widely distributed in particular in the Ancient East. The most ancient archaeological evidence of the use of lapis lazuli consists in a cylindrical bead found at Mehrgarh (Pakistan), one of the most important Neolithic settlements, considered as the precursor of the Indus Valley Civilization [Jarrige 1991].

Several archaeological studies [Herrmann 1968; Tosi and Vidale 1990; Casanova 2013] allow to reconstruct trade and diffusion of the use of this rocks in a temporal frame between 7000 and 2000 BCE, from the Neolithic to the Bronze age, which corresponds to the height of the diffusion of lapis lazuli [Casanova 1992; Casanova 2001; Casanova 2013]. After the second millennium BCE, a gradual replacement of this material by other synthetic ones, such as faïence or glass paste, began [Moorey 1994].

The narrow range of geological conditions in which lapis lazuli can form is the reason for the rarity of its sources [von Rosen 1988]. The Badakhshan region in Afghanistan is historically considered to be the lapis

lazuli supplier for the whole Middle East and the Mediterranean region, including the Egyptian civilization. Many different mines are present in this region, such as Sar-e-sang in particular, but also Chilmak, Shaga-Darra-i-Robat-i-Paskaran, and Stromby [Herrmann 1968]. Nevertheless, in recent times other quarries have started to be taken into consideration as possible providers: Liadjuar Dara, Pamir Mountains (Tajikistan), Chagai Hills (Pakistan), the Lake Baikal area (Siberia) [Delmas and Casanova 1990] (see section 2.2 for further details).

All of these sources were in very inaccessible places and had to be reached through impervious routes, knowledge of which is still largely incomplete, especially for ancient contexts where there is scarceness of written evidences [Tosi 1974]; it follows that the possibility to associate the raw material to man-made objects could be extremely helpful to reconstruct trade routes and improve knowledge about specific historical periods.

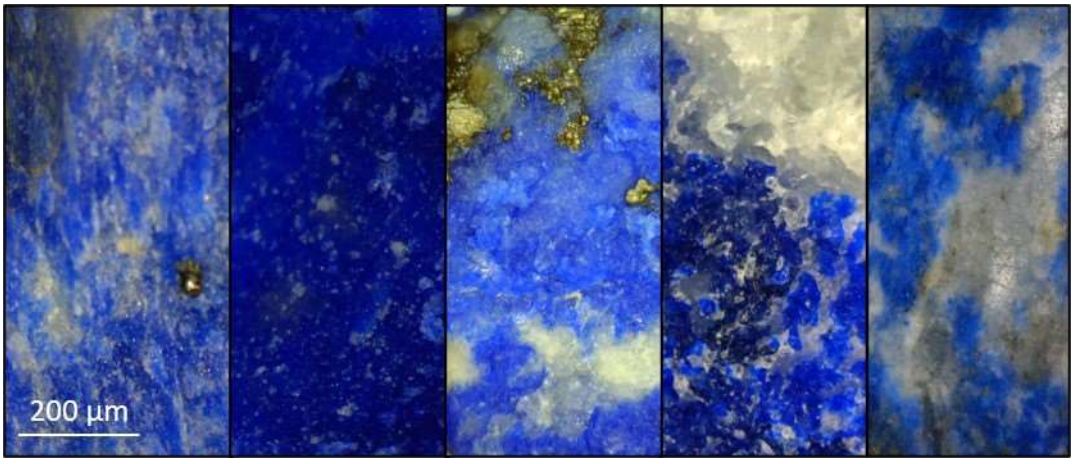

Figure 2.1. Photomicrographs of lapis lazuli rocks, that can present different shades of blue colour and different mineralogical textures.

Testimonies of the spread of lapis lazuli in the Middle East from the second half of the IV millennium BCE can be found in different areas, from Central Asia, Turkmenistan, Iran, Indus Valley, Balochistan to Egypt and Mesopotamia [Sarianidi and Kowalski 1971]. It is reasonable to believe that in time alternative routes have been followed, depending on the economic and political conditions [Moorey 1994]. Among the authors making inferences on trade itineraries, Tosi suggested the existence of three main trade routes to import lapis lazuli in Mesopotamia (figure 2.2) [Tosi 1974]. The “northern route” led along the northern parts of Iran, passed through the site of Tepe Hissar and travelled further alongside to the heart of Mesopotamia; the “southern route” ran towards Shahr-i Sokhta, then moved over Kerman to the area of Suse and from there to Mesopotamia itself; the “sea route” played instead a notable role in lapis lazuli

sea trade between the political and economic centres during the first half of the third millennium BCE, running along the Indus River and sites located in southern Mesopotamia.

Regarding instead trading to the Egypt area, an extended study is present in the work carried out by D'Amato [D'Amato 2000]. The author identified two main different routes: northern and southern routes (figure 2.3). The northern route was followed during the first phases of lapis lazuli trade in Egypt (Naqada IIA –IID2) [Mark 1997] and it was suggested that three variants for different commercial phases might have been exploited. The routes initially passed through Tepe Gawra, source of gold, later shifted towards Tell Brak and crossed Tigris and Euphrates rivers up to the Nile delta.

The southern routes instead allowed to reach Egypt through maritime paths; in this case as well, the existence of two sea routes is hypothesized [D'Amato 2000; Derakhshani 1999]. The first one, "the Amu via" [Derakhshani 1999] ran through centre Asia and travelled to Samarkand, reaching Bukhara, Merv, Sarakhs, Mashhad, Gonabad, Shahr-i Sokhta, Tepe Yahya until Hormuz and from there the routes went

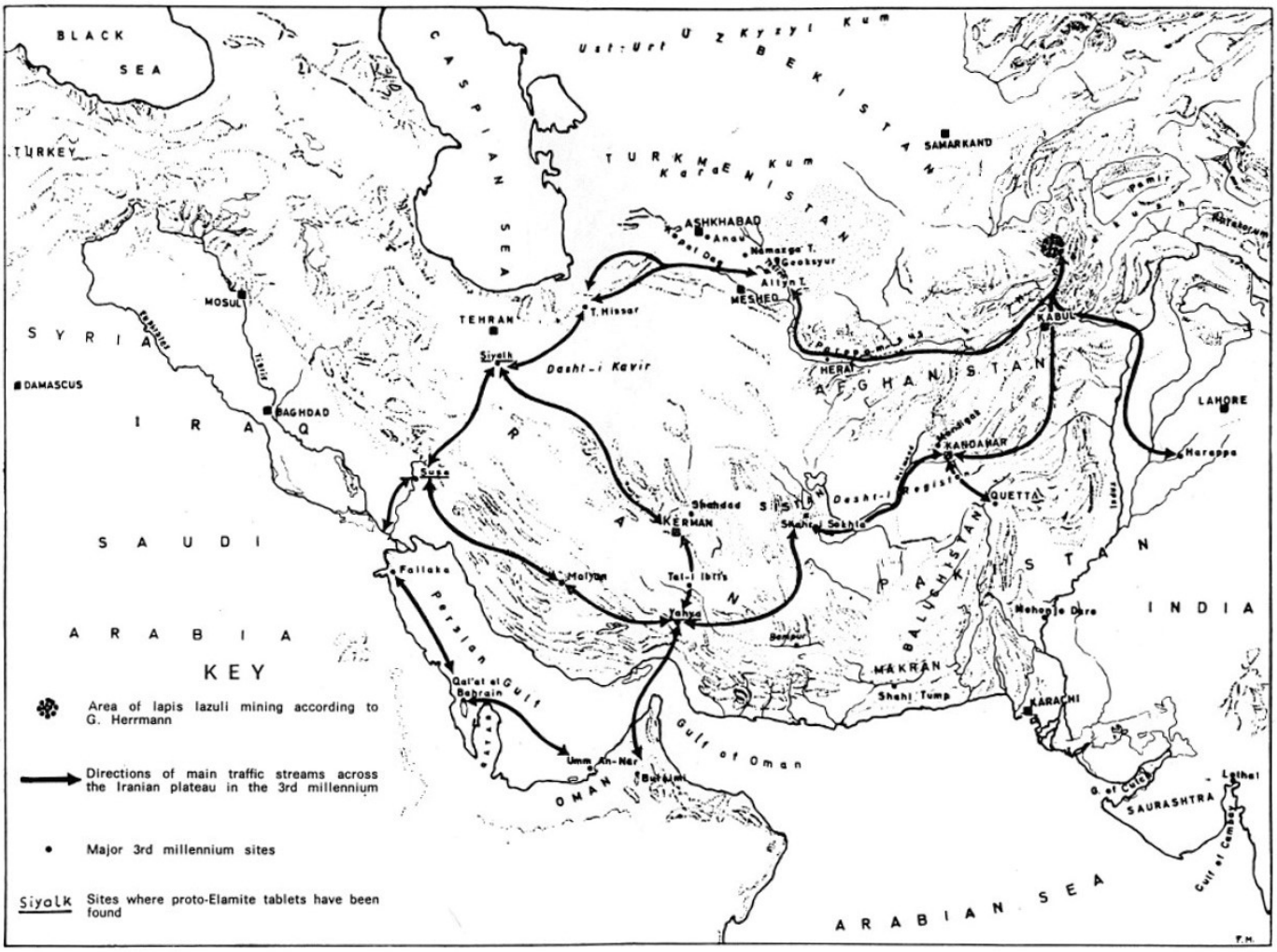

Figure 2.2. The main trade routes of lapis lazuli during the 3rd millennium BCE [Tosi 1974].

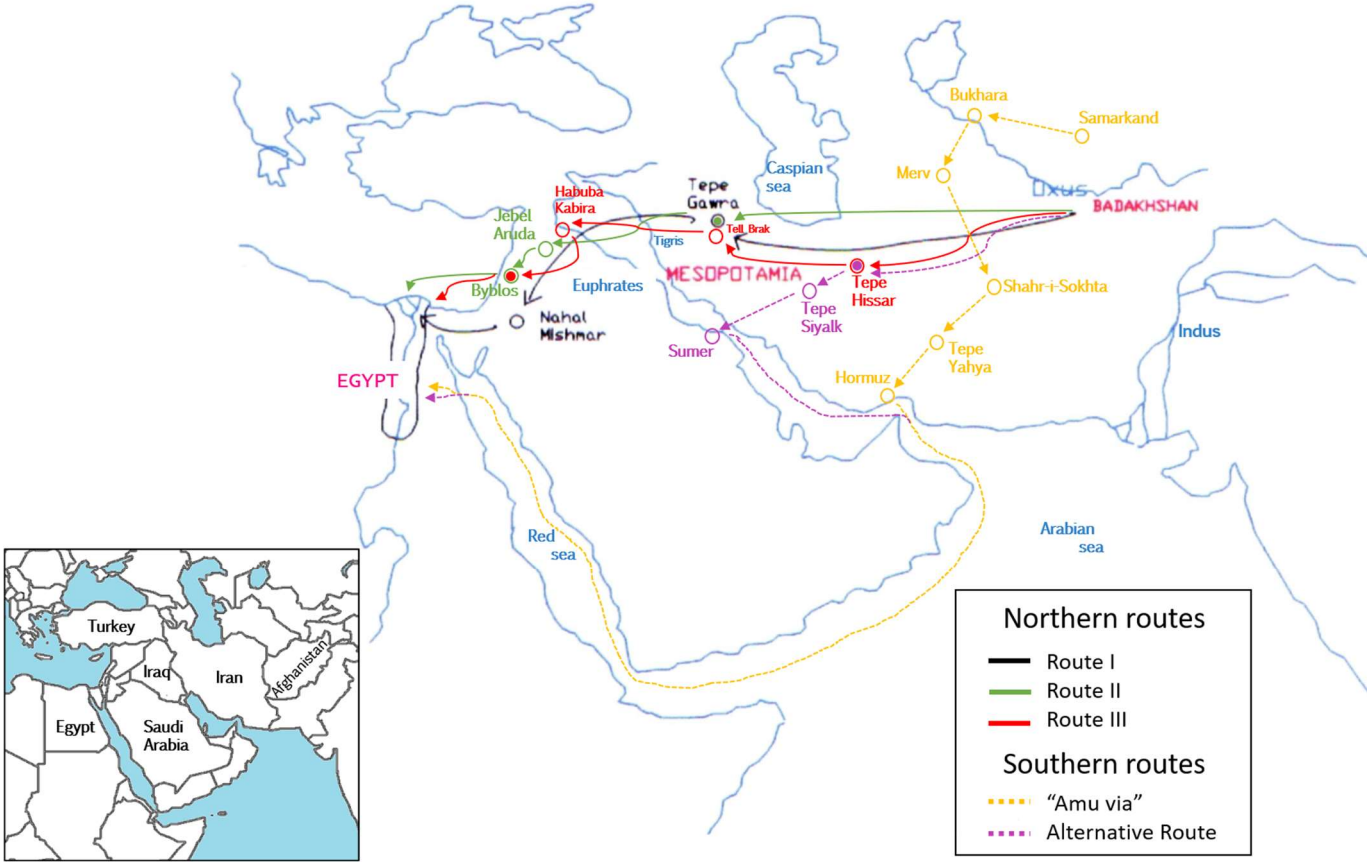

Figure 2.3. The trade routes of lapis lazuli to Egypt through the Ancient Near East (modified after [D'Amato 2000]). A geopolitical map is also reported for reference on modern nations boundaries.

through sea ways. The main exchange centres of the second route, which grew further north, were Tepe Hissar and Tepe Siyalk, from where it was easy and convenient to reach Sumer and then embark on a sea voyage to Egypt. Both these two trade routes followed the pathway from the Persian Gulf to Egypt via the Red Sea and the Wadi Hammamat, but they were not used at the same time, being exploited instead according to market needs.

In general, it seems that extraction and transportation of the very precious lapis lazuli in antiquity should not be considered as part of the normal trade-mechanism, but rather to be the task of royal expeditions with a clearly specified target. The role of this semi-precious stone as a very important and highly valued mercantile commodity is very well supported by the numerous discoveries of lapis lazuli throughout the Ancient Near East [Winter 1999].

For its peculiarity and colour, during all the Bronze Age, lapis lazuli was used in association with other precious materials: carnelian, turquoise, steatite, agate, gold or silver. It was employed mainly as beads in necklaces, secondly in pendants, amulets and inlays for various objects; some examples can be found

in figure 2.4. Through the archaeological data it is possible to understand all the different operating steps involved in the production of these beads [Tosi and Piperno 1973]. The manufacturing process, according to what has been shown by observations and experimental simulations, appears to have a common operating system both in Ur, Iran (Suse, Shahr-i Sokhta) and in Central Asia (Mundigak, Mehrgarh, Sarazm), with some differences in the style of the products and in the tools used [Casanova 2013; Tosi and Vidale 1990].

Despite not reaching a diffusion comparable with the one achieved in the Mesopotamian area, lapis lazuli was nonetheless greatly employed also in the glyptic art of Ancient Egypt, where it was used to recreate scarabs, pendants, amulets and inlaid jewels (figure 2.4) since the IV millennium BCE [Sofianides and Harlow 1990]. The oldest written reference to lapis lazuli in this area seems to be about a group of vessels included in a funerary items list from the tomb of Rahotpe, that dates back to the IV dynasty (III millennium BCE) [Crowfoot Payne 1968].

Lapis lazuli was used in more recent times also for the manufacture of cups, bowls and urns, and was inlaid into clock faces and tables. In Florence, the passion of the Medici family for importing precious stones led to the foundation in 1588 of the Gran-ducal workshops: a court manufactory, located in a wing of the Uffizi, which fabricated precious works with polychrome stones. The so-called “Galleria dei Lavori” quickly won international acclaim for its magnificent products, and it still exists today as the “Opificio delle Pietre Dure”, one of the main Italian restoration centres. Also, the Museum of Natural History of the University of Florence currently hosts the “Collezione Medicea di pietre lavorate”, a collection of great historical value composed by precious stones, both polished and carved, collected since the XV century CE [Re et al. 2015]. Among the 700 specimens belonging to the collection there are carved ornaments, panels and *tesserae* used for the *pietra dura* decorative technique, together with some precious stone objects carved and decorated with high quality craftsmanship (figure 2.5).

Since the XVI century CE, all the most important European courts imported and collected precious stones, remarkable pieces that are nowadays collected in some of the most important museums such as the Louvre Museum in Paris, the Fersman Museum in Moscow or the Hermitage Museum in St. Petersburg.

More recently, at the run of XX century CE, Russian jeweller and artist Peter Carl Fabergè (1846-1920) used lapis lazuli in many of his major works. Among these was one of his 58 Imperial Easter Eggs, a gift from Czar Nicholas II of Russia to Czarina Alexandra in 1912 (figure 2.5) [Coenraads and Canut de Bon 2000]. In Russia, lapis lazuli was mainly employed as a decorative stone: remarkable examples are nowadays visible at the Winter Palace in St. Petersburg and the Palace of Catherine the Great in Pushkin city [Bauer 1904].

Figure 2.4. Examples of the use of lapis lazuli in manufacturing from Ancient Egypt. *Top left*: carved amulet (wdjat eye) from the 3rd Intermediate–Late Period [Lo Giudice et al. 2017]. *Bottom left*: pierced beads, partially altered, from the Treasure of Tôd [Calligaro et al. 2014]. *Right*: Pendant with the Name of King Osorkon II portraying the God Osiris's Family (XX dynasty).

Figure 2.5. Examples of the use of lapis lazuli in the II millennium CE. *Left*: *commesso in pietra dura* by unknown Florentine Master, Opificio delle Pietre Dure (c. 1615 CE). *Right*: the Tsarevich jewelled egg by Peter Carl Fabergè (1912 CE) *(public domain for both images).*

Finally, it should not be forgotten that grinded lapis lazuli is the basis for the production of ultramarine blue pigment, in use in the European art scene since the XI century CE [Herrmann and Moorey 1983] until late XIX century CE, when was largely replaced by its synthetic counterpart [Roy 1986; Harley 1970]. From the Renaissance onwards this was actually the primary employment for lapis lazuli and therefore subject of numerous artistic and archaeometrical studies [Gambardella et al. 2020; Ganio et al. 2018; van Loon et al. 2020].

2.2. Genesis and mineralogical composition

As previously mentioned, the mechanism that leads to lapis lazuli formation is quite complex and up to now not completely understood. Lapis lazuli is generally classified as a metamorphic rock, despite it might have either a metamorphic or magmatic origin, presenting a peculiar and sometimes unusual paragenesis. Generally, the mineral assemblage is characterised by the extensive or localised occurrence of a blue feldspathoid: in the majority of cases this is lazurite, a sulphur-bearing member of the sodalite group with formula $(Na, Ca)_{7.5\text{-}8}\,(Si, Al)_{12}\,(O, S)_{24}\,(SO_4, Cl)_{1.3\text{-}2}$ [Hogarth and Griffin 1976].

The main occurrences of lapis lazuli are found in limestone or dolostone, typically in areas interested by contact metamorphism, where S, Cl and Na essential to the formation of lazurite are provided by hydrotermal fluxes [Angelici 2015]. This kind of genesis, firstly proposed by Brögger and Backstrom [Brögger and Backstrom 1891], is proper of the deposits in the Italian Mountains, in Colorado [Hogarth and Griffin 1980] and of the ones in Coquimbo, Chile [Coenraads and Canut de Bon 2000; Cuitino 1986; Esquivela and Benavides Muñoz 2005]. A different origin is instead proposed for the deposits on Baffin Island, Canada [Hogarth and Griffin 1978] and for the famous quarries of the Badakhshan area (Afghanistan), that is due to a regional metamorphism, involving high temperatures and pressures. Anyway, the processes leading to feldspathoid mineralization are still uncertain [Moore and Woodside 2014].

For the Siberian district of the Baikal area another process can occur in the lazurite mineralization, genetically related to the metasomatic alterations of sedimentary dolomites and magnesites in contact with magmatic intrusions or other aluminosilicate rocks [Aleksandrov and Senin 2006].

The need of coexistence of restricted ranges of igneous or evaporite rocks and carbonates and specific metasomatic and metamorphic conditions accounts for the rare occurrence of lapis lazuli in a worldwide scale. All geological occurrences are reported in figure 2.6, with a distinction between main quarry districts, reported as the historical providers of high-quality lapis lazuli traded in ancient times, and secondary or recent ones, suppliers of lower-quality material with limited or no exploitation in the past.

Besides the world-famous Badakhshan mines - for a long time considered as the only possible historical source of the ancient near East - two other districts are in geographical range with Mesopotamia and could have been exploited as well: Pamir Mountains in Tajikistan [von Rosen 1988] and Chagai Hills in the Balochistan region (Pakistan) [Casanova 2001]. It should be stressed out, however, that Chagai Hills deposits have been reported to be located at Bi-Bi-Dick (between Quetta and the Iranian border) [Jarrige 1988], but there is no geological evidence of their actual existence [Law 2008; Law 2014]. One possible explanation for this inconsistency is the depletion of the deposits directly in ancient times, so that no lapis lazuli traces can be found nowadays in that area. Additional information about this disputed source can be found in section 4.4.

On the other hand, the lake Baikal deposit in Siberia cannot be excluded as historical source only on the basis of its long distance from Mesopotamia. In fact, other alternative sources should be considered since the early trade route system is still largely unknown. It should also be taken into account the important role played by Siberian sources starting from the XVIII century CE, period in which the production of remarkable pieces of art confirms a dynamic background in the hard stones manufacturing, that could nonetheless lead to attribution issues and questions of historical importance. Lastly, Chilean deposit has

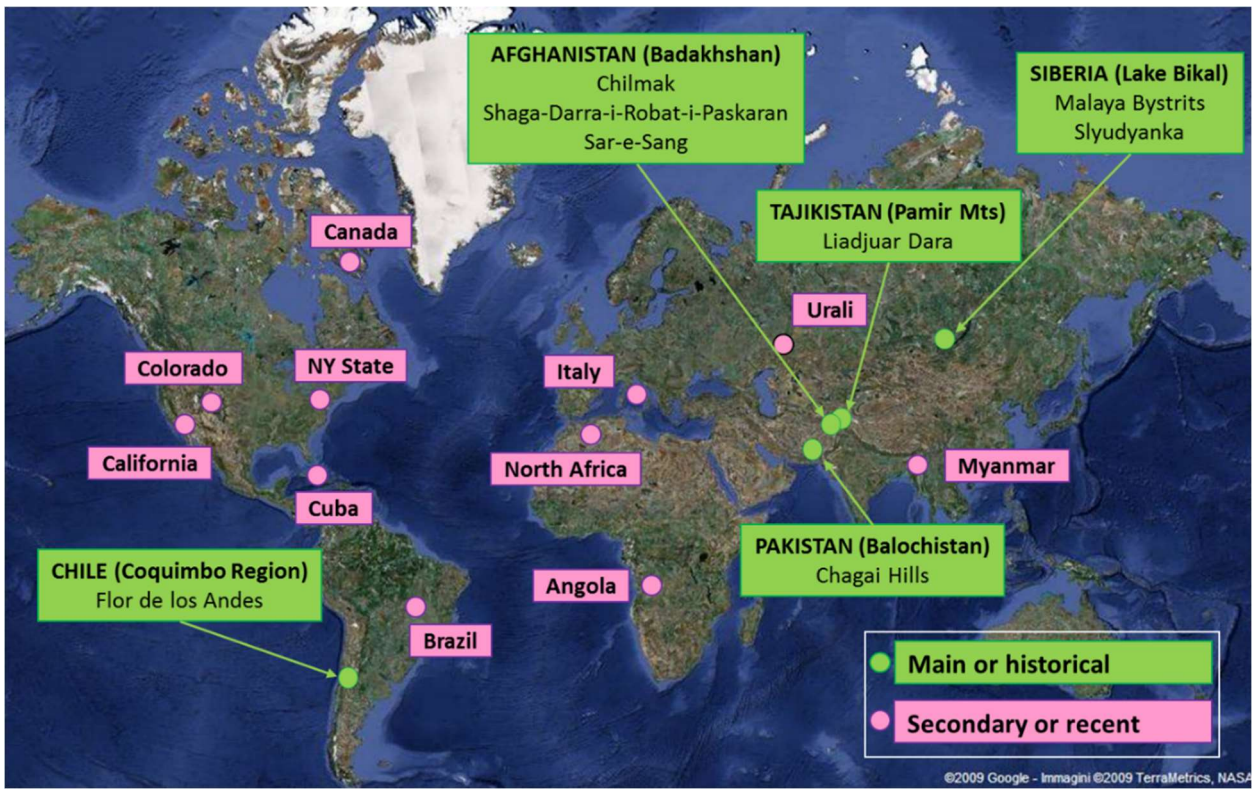

Figure 2.6. Map of the geological occurrences of lapis lazuli in the world. The main or historical quarry districts are marked in green, whereas the secondary or recent ones are marked in pink [Angelici 2015].

been taken into account as an historical source, because of its (still questioned) possible exploitation by ancient civilizations of the American continent [Rivano 1975; Sofianides and Harlow 1990].
Among secondary districts it is worth mentioning Myanmar, where lapis lazuli is listed as one of the gemstones occurring in the Mandalay District, Shan State and Kachin State [Kammerling et al. 1994; Mitchell 2018] together with the more famous Myanmar ruby. However, the knowledge of geological sources of this material in that area is still largely incomplete.

As regards in specific the paragenesis of the rock, lazurite is typically present as aggregates of quite small crystals crossed by grey-white or yellowish veins, that are due to the presence of numerous and different mineralogical phases such as diopside, wollastonite, phlogopite, K-feldspar or calcite, to cite the most common [Hogarth and Griffin 1978]. Pyrite is also frequently present, providing to the rock the poetic epithet “a starry night sky” for the metallic golden aspect of its small crystals. Moreover, other feldspathoids, like haüyne, sodalite, nosean, as well as others minerals belonging to the cancrinite group, like afghanite, can be present. Finally, other mineralogical phases such as biotite, apatite, titanite, garnet, epidote, nepheline, olivine, ilmenite, etc. may also occur, but in minor quantities or less frequently [Angelici 2015]. In Table 2.1 a comprehensive list of the different mineral phases occurring in lapis lazuli is reported, gathering data from literature related to the several studies focused on lapis lazuli coming from the abovementioned historical sources (Afghanistan, Tajikistan, Siberia and Chile) with the addition of a recent study [Vaggelli et al. 2019] on Myanmar samples, that are as well under investigation in this work. Furthermore, a focus on diopside, main target of the research conducted here, is given in chapter 3.

2.3. Lapis lazuli provenance: the state of the art

Provenance studies are particularly in demand and a source of interest in the archaeometry field, as not only they provide information on the raw materials *per se*, but they also help archaeologists to reconstruct their ancient and less known trade routes. This latter point results in a better understanding of the economic and social structure in ancient societies, revealing significant insights for the historical knowledge.
A lot of different archaeological and historical materials have been investigated with the aim to identify their origin: a fascinating example is obsidian [Freund 2013], but a wide range from lithics to ceramics was object of study in the last decades [Tykot 2004]. It is common to find studies that apply a multi-technique approach, depending on the materials available: in the case of artistic or archaeological artefacts non-invasive techniques are always preferable, if not mandatory.

Table 2.1. Mineralogical phases identified in lapis lazuli rocks that shares the same provenances of samples analysed in this work. Legend encloses all parameters from the different studies. (modified from [Angelici 2015] adding data from [Vaggelli et al. 2019]; separation into the three group identified in the latter work is maintained)

LEGEND:
(•) principal minerals (more than 0.3%)

(×) minor minerals (less than 0.3%)

(·) secondary minerals

(*) minerals associated to lazurite-bearing rocks

(XXX) very abundant (main)

(XX) abundant

(X) rare (accessory)

	Minerals	Afghanistan							Siberia					Chile			Tajikistan	Myanmar		
	Quarries / Provenances	Badakhshan (Sar-e-sang)	Badakhshan	-	Badakhshan (Sar-e-Sang)	Badakhshan	Badakhshan	Badakhshan (Sar-e-Sang)	Malaya Bystraya (Staryi)	Malo Bystrinsk, Slyudyansk, Tultuysk	-	Lake Baikal	Baikal area	Flor de Los Andes	-	Flor de Los Andes	Lyadzhvardara	Mogok, Mandalay region		
	Year / Authors	1981 Wyart et al	1985 Yurgenson and Sukharev	1986 Borelli et al	2001 Anthony et al	2003 Zöldföldi and Kasztovszky	2004 Kostov	2006 Aleksandrov and Senin	1970 Hogarth	1976 Ivanov	1986 Borelli et al	2003 Zöldföldi and Kasztovszky	2006 Aleksandrov and Senin	1986 Cuiñño	1986 Borelli et al	2005 Corona Esquivel and Benavides Muñoz	2006 Aleksandrov and Senin	2019 Vaggelli et al		
Feldsphatoids	Lazurite	•	•	•	•	•	•	•	•	•	•	•	•	•	•	•	*	XXX	XX	XXX
	Haüyne		•		•			•	•					•		•			XX	
	Nepheline		•			•		•				•	•						XX	
	Sodalite		•	·			•	*			·			•					X	X
	Feldspathoids												•			•				
	Afghanite		•			•		•		•			*	x			*			
	Cancrinite												•							
	Vishnevite																			
Pyrox-Amph	Diopside	•	•	•	•	•	•	•	•	•	•	•	•	•		*	*	XXX	XX	XXX
	Wollastonite									•				•	•	•				
	Amphibole						•	*									*			XX
	Tremolite		•				•	*						•						
Opaque minerals	Pyrite	•	•	x	•	•	•	•	•		·	•	•	•	·	•		X	X	X
	Pyrrhotite		•					•	•							*				
	Chalcopyrite													•		*				
	Arsenopyrite													x		*				
Feldspars	Feldspars	•		•		•	•	*	•		•	•		•			*			
	Plagioclase	•					•							•					XX	
	Feldspar (generic)					•			•			•								
	Albite							*								*	*		XX	
	K-Feldspars			•							•									
	Oligoclase																			
Others	Calcite	•	•	·	•	•		*	•	•	x	•	*	•	•	•	*	XXX	XX	XXX
	Dolomite					•						•	*				*			
	Scapolite	•	•			•	•		•	•		•	*	•		*				
	Phlogopite		•	x		•	•		•	•	•	•	•			*	*			
	Apatite					•			•			•	*					X	X	X
	Epidote					•						•		•						
	Garnet					•						•								
	Quartz						•	*	•											
	Native Sulphur								•				•							
	Titanite					•						•								
	Olivine					•						•								
	Forsterite	•	•		•	•	•					•	•				*			
	Biotite					•						•					*			
	Ilmenite					•						•								
	Muscovite				•															

The issue related to the use of lapis lazuli in the past arose the interest of both archaeologists and scientists and in the past decades attempts at provenance studies have been done with various purposes and methods. Nevertheless, its scientific characterization in the literature is incomplete and limited in terms of number of samples, especially if compared to provenance studies on materials such as ceramic, metal and glass. One possible explanation is the rareness and imperviousness of the geological sources and related difficulty of retrieving geo-referenced rock samples. At the same time, artefacts coming from museums or private collections in most cases lack of reliable and precise provenance information, making them untrustworthy to be used as reference in a rigorous study, but still very interesting cases for provenance assignation.

The study published by the archaeologist Georgina Hermann in 1968 [Herrmann 1968] is the first one related to the lapis lazuli provenance issue. The author presented an archaeological overview of the exploitation, trade routes and occurrence of this material, focusing the attention on the Afghan mines. Her conclusion from an archaeometrical point of view was that it is not possible to discriminate between Afghan and Siberian rocks through the sole use of Optical Microscopy, Optical Spectroscopy and X-Ray Fluorescence.

Some years later, in 1972, Isotope Mass Spectroscopy - a destructive analytical technique - was applied to lapis lazuli and artificial ultramarine pigments. In this case a distinction between the Afghan lapis lazuli and both artificial ultramarine and rocks from Chile and Siberia was achieved [Keisch 1972]. Unfortunately, in neither of these works the authors reported detailed information about the experimental procedure adopted and the obtained results. A similar study was attempted by Favaro *et al.* [Favaro et al. 2012], who successfully achieved the same discrimination, but with the employment of multivariate analysis on Scanning Electron Microscopy with Energy Dispersive X-ray Spectrometry (SEM-EDX) data. They had actually moved to a non-destructive technique, but the number of samples was still very limited, as they admit themselves.

A first marker for provenance discrimination was identified in the 1980's [Borelli et al. 1986; Cipriani et al. 1988], by means of Optical Microscopy, SEM-EDX and X-Ray Diffraction (XRD) applied to rocks belonging to the collection of the Museum of Mineralogy of Florence and to objects of the Medici Family (XV century CE). The results showed the presence of a wollastonite-lazurite association in Chilean samples, absent in both Afghan and Siberian samples. Moreover, a higher content of Cl in lazurite was found in Siberian samples, compared to the Afghan ones. Another more recent provenance study has focused on lazurite, investigating more than 30 samples from different origins with sulphur K-Edge X-ray Absorption Near Edge Structure (XANES) spectroscopy [Gambardella et al. 2016]. This kind of analysis demonstrated as well the possibility to discriminate between Chilean and Afghan provenance, underlining at the same time the difficulties in distinguishing Tajikistan from Afghanistan.

The first studies attempting at a provenance attribution for archaeological lapis lazuli evidences of unknown geographical origin were performed in the next decade by Casanova and Delmas [Casanova 1992; Delmas and Casanova 1990]. Cut wastes excavated from the site of Shahr-i Sokhta (III millennium BCE, Iran, see section 4.2) and 21 rocks from 4 historical sources (Badakhshan, Pamir Mountains, Chagai Hills and Ural Mountains) were analysed by Atomic Absorption Spectroscopy (AAS), then the results were processed by Principal Component Analysis (PCA). With this work, the authors found out that taking into account only six variables (Si, Al, Ca, Mg, Ba and Sr[1] contents) it was possible to discriminate between the deposits. The results showed that the Shahr-i Sokhta samples are more comparable to Pamir Mountains (Tajikistan) and Chagai Hills provenance than to Afghanistan, proving the possible exploitation of other mines in antiquity besides Badakhshan.

In the 2000s a greater attention to the non-invasiveness of the techniques used was growing, such as in the first experiment by Zöldföldi and Kasztovszky [Zöldföldi and Kasztovszky 2003; Zöldföldi et al. 2006] that employed Prompt Gamma Activation Analysis (PGAA) together with PCA again. A total of 37 rocks from Badakhshan, Lake Baikal, Chile and Ural Mountains were tested, isolating the results in three main clusters based in particular on S and Cl content: one with the Chilean samples, another with the Afghan samples and a third one containing samples both from Siberia and Ural Mountains. It is worth stressing that this analytical approach provides information on the chemical composition of the whole sample, so these results are not directly comparable to the ones obtained in Borelli's work [Borelli et al. 1986], performed specifically on lazurite. Moreover, about archaeological samples the authors show only some qualitative or unpublished data presented elsewhere [Zöldföldi 2011].

The French group of the C2RMF (Centre de Recherche et de Restauration des Musées de France) in Paris also started employing non-invasive physical techniques on lapis lazuli rocks [Calligaro et al. 2011]. Ion Beam Analysis measurements were performed at AGLAE external micro-beam (see section 5.5.2), demonstrating the potentialities of this facility in the analysis of precious objects. Their applications on Cultural Heritage materials stimulated a prolific collaboration with researchers from the University of Torino and they are also one of the main partners for this PhD work. A very interesting analysis carried out at the C2RMF involved some lapis lazuli findings belonging to the Egyptian treasure of Tôd (XX century BCE), studied with combined μ-PIXE and μ-IL measurements[2] [Calligaro et al. 2014]. The main goal of the study was the identification of alteration and decay processes of the artworks (mainly beads), but the authors also inferred some hypotheses about the provenance of the raw material employed, suggesting an Afghan origin.

[1] The content of Sr and Ba as characteristic for Siberian provenance was previously suggested in the work of Ivanov [Ivanov 1976].

[2] For details about Particle Induced X-ray Emission (PIXE) and Ionoluminescence (IL) techniques, see Chapter 5.

Many other works focus on lapis lazuli as pigment and on the distinction between natural and artificial ultramarine, but some of them also try to find in the pigment some markers useful for a provenance determination. It should be noted that pigments are less suitable for this purpose, because of the possible effects induced by the fabrication process, that can introduce contaminants or remove minerals. Fourier-Transform Infrared Spectroscopy (FTIR) is a very popular technique for this kind of material, frequently associated with Raman Spectroscopy: results indicated an infrared band (at about 2340 cm^{-1}) that seems to be peculiar of the Afghan provenance [Bacci et al. 2009; Derrick 1990], or rather, of all the Asian provenances [Ajò et al. 2004; Smith and Klinshaw 2009]. Other techniques used for ultramarine pigments are Inductively Coupled Plasma Mass Spectrometry (ICP-MS) or FEG-SEM-EDX and XRD [Schmidt et al. 2009; Favaro et al. 2012]. A very interesting work [Ballirano and Maras 2006] is focused on the provenance identification of the ultramarine pigment used by Michelangelo in his "The Last Judgment". The authors performed a comparison between the pigment and 10 rocks from 4 provenances (Badakhshan, Chagai Hills, Pakistan and Iran), concluding that the most similar source is the one in Chagai Hills. This unprecedented result is actually questioned by Law, who presented himself [Law 2014] a study focused on the comparison of 18 rocks (Afghanistan, Chagai Hills, Myanmar and Lake Baikal) with 7 artefacts from six different archaeological sites of the Indo-Iranian area and rose doubts about the "Chagai Hills" origin for samples employed in these works (his included).

Despite the existence of all these studies, a systematic characterization of lapis lazuli for provenance purposes is still lacking. Indeed, the total number of all the artefacts and rock samples analysed in each work is limited and not representative, and the analytical approaches adopted are often invasive or destructive, therefore non applicable in the field of Cultural Heritage. To overcome these issues, in 2008 a long-term research, involving an interdisciplinary team, was started at the University of Torino; 56 lapis lazuli rocks of known provenance from 5 quarry districts have been analysed so far, creating a large database for the compilation of a final non-invasive provenance protocol to be applied to archaeological and artistic manufacts.

2.3.1. The provenance protocol

The protocol for the provenance determination of lapis lazuli developed by the University of Torino is the starting point of this work, that aims at its expansion and further provenance coverage with the collection of additional data and the application of innovative methods for data analysis.
The 56 rocks composing the current geographical reference database are reported in detail in section 4.1.

In order to achieve a complete characterization of the rock, a multi-technique approach was adopted for their investigation, including both invasive and non-invasive techniques and using bench-top instruments and large scale facilities.

The first step of the systematic study is the observation of all the samples by means of an optical microscope, in order to acquire optical maps that can be used as reference during the subsequent analyses. The second step is the cold-cathodoluminescence (cold-CL) microscopy mapping, to obtain the spatial distribution and signal intensities of luminescent mineral phases. After this preliminary mapping, geological samples are carbon-coated for SEM imaging and EDX analyses to perform minerals identification. Being lapis lazuli a very heterogeneous material, the analyses were focused on the single mineral phases to identify specific minero-chemical markers: the crystals selected for the analysis are chosen for dimension among the biggest for each cold-CL colour emission. The quantitative EDX analysis allows to associate a chemical composition to each phase, obtaining in many cases a univocal correspondence with a specific colour of luminescence. The different identified phases have been compared to the ones already found in lapis lazuli by other authors and further confirmation was obtained with Raman spectroscopy. After this step, for the most important and diffused phases in lapis lazuli (lazurite, diopside [Re et al. 2011] and pyrite [Re et al. 2013]), the trace elements composition has also been investigated by means of micro-Particle Induced X-ray Emission (μ-PIXE). In parallel, micro-Ionoluminescence (μ-IL) measurements have been performed, always confirming the qualitative results obtained by means of CL [Lo Giudice et al. 2009]. The Ion Beam Analysis measurements have been carried out so far both at the external microbeam line at AGLAE (Paris) and in-vacuum at INFN-LNL (Padua), facilities extensively described in section 5.5.

Focusing on diopside and pyrite, up to now we have analysed 138 and 90 crystals respectively. This led to the compilation of a primary provenance protocol, that was successfully applied to some carved artefacts from the Egyptian Museum of Florence [Lo Giudice et al. 2017]. A schematic representation of the steps in the protocol can be found in figure 2.7. Both elemental content and luminescence features candidate as markers useful to distinguish among four lapis lazuli provenances. The fifth provenance, Myanmar, is not yet included in the published protocol; some preliminary results can be found in [Vaggelli et al. 2019], whereas the complete characterisation of the samples performed within this work allowed to modify the protocol accordingly (section 8.1.1.1). The markers have been identified using an ion microbeam (via μ-PIXE and μ-IL); with the same techniques it is possible to look for them both on lapis lazuli stones and artworks, and when working in air with the extracted beam a completely non-invasive analysis is achieved. Moreover, the comparability of the results obtained by using μ-XRF and μ-PIXE was demonstrated [Angelici et al. 2015].

Further information or specifics on the techniques and instrumentation can be found in chapter 5.

Physico-chemical features present or absent in all the analysed samples of historical sources (the “strong markers”) are shown in the main block diagram of figure 2.7. For Chilean and Afghan samples “weaker markers” are also reported, which are features very frequent but not observed in all the samples.

Chilean lapis lazuli is of easy identification, due to the widespread presence of wollastonite ($CaSiO_3$), observed in all the analysed rock samples. This mineral phase can be recognized with the simple acquisition of the ionoluminescence spectrum [Calusi et al. 2008; Czelusniak et al. 2016; Lo Giudice et al. 2009; Re et al. 2015]. In addition, Se was detected in several pyrite crystals from Chilean samples, with contents above 40 ppm [Re et al. 2013].

Siberian samples, instead, are the only ones characterised by iron oxide-hydroxide minerals pseudomorphosed after pyrite, only sometimes occurring as relict: these mineral phases show an intensive compositional zoning, with the predominance of sulphur-free zones in the crystals [Angelici et al. 2015]. Samples from Siberia also present a Sr content higher than about 180 ppm in diopside crystals [Re et al. 2013; Re et al. 2015].

As regards to Tajikistan and Afghanistan samples, the presence of well preserved and idiomorphic pyrite crystals was generally detected. These two provenances can be discriminated on the basis of the trace element content in pyrite crystals [Re et al. 2013]. In particular, for Afghan rock samples the Ni content is higher than 330 ppm, whereas Cu content is below 240 ppm; Tajikistan rocks have instead Ni below 270 ppm and Cu above 150 ppm. Finally, regarding weaker markers, diopside crystals show a Ti content above 710 ppm, V content above 210 ppm and Cr content above 220 ppm, together with a strong ionoluminescence band centred at about 770 nm [Re et al. 2015].

It is worth stressing that the discrimination among the quarry districts presented in the protocol is based on the results obtained so far and that the number of information can be increased. Implementing the protocol is one of the aims of this study, together with a further application to archaeological samples of unknown origin.

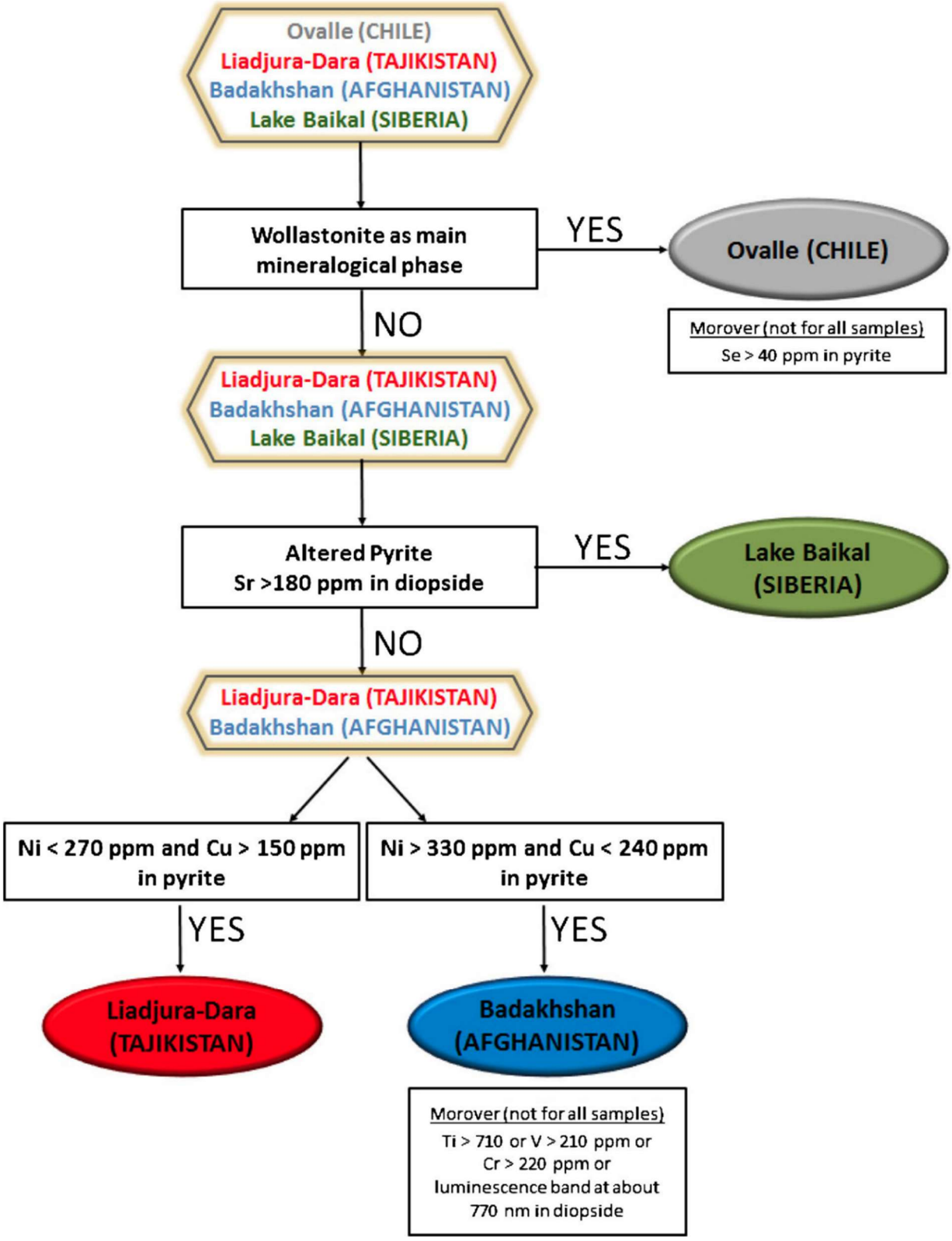

Figure 2.7. Schematic diagram of the proposed protocol for lapis lazuli provenance determination by means of non-invasive techniques [Lo Giudice et al. 2017].

3. Luminescence in diopside

Luminescence is a feature extensively exploited for the investigation of materials. With a simple spectroscopic analysis, usually non-invasive, a lot of information on the structure and composition can be retrieved. This is one of the main reasons for its employment in the study of lapis lazuli, whose constitutive minerals may present luminescence. The focus of this work is on diopside, mineral that shows a very intense yellow luminescence and whose luminescent features are already at the centre of the provenance protocol (see section 2.3.1). The step forward is the attempt at identifying the trace elements present in its composition as activators or quenchers of the luminescence. To better understand the results obtained in this work, a brief review of the luminescence mechanisms is provided, with a specific attention to minerals. Also, the characteristics of diopside structure have to be reported, together with a state of the art of the knowledge on its activators and quenchers.

3.1. Luminescence mechanisms in solids and minerals

A luminescent mineral is a solid able to convert certain types of energy into electromagnetic radiation over and above thermal radiation. The electromagnetic radiation emitted is usually in the visible range, thus from 380 nm (3.3 eV) to 680 nm (1.8 eV), but can also occur in the UV or infrared range. It is possible to excite the luminescence of minerals by UV and visible radiation (Photoluminescence), by X-rays (X-ray luminescence), by a beam of energetic electrons (Cathodoluminescence) or ions (Ionoluminescence) and so on. A special case is so-called Thermoluminescence, which is the stimulation by heating of luminescence in a material previously excited in a different way [McKeever 1985].
The two components needed to have a luminescent mineral are a host lattice and a luminescence centre or *activator*. Correlating the mere observation of the luminescence with a particular impurity concentration in the overall mineral may give an indication of the source of the characteristic emission, but it does not give details about the precise nature of the centre and can sometimes be misleading. Spectroscopic studies may provide a number of important parameters which aid identification of the luminescence centre.

Luminescence emission occurs as a result of a radiative electronic transition in which an electron, previously excited, jumps from a higher energy state to a lower one, the difference in energy being released as a photon

$$E_{ph} = E_i - E_f = h\nu = \frac{hc}{\lambda} \quad \text{(eV)} \tag{3.1}$$

where E_i and E_f are the energies of the higher and lower energy levels respectively, h is Planck constant, c is the speed of light in vacuum, v the frequency and λ its wavelength. Another characteristic parameter is the *luminescence lifetime*, defined as the time required to luminescence intensity to drop to 1/e of its original value. Measurements of luminescence lifetime requires excitation by a pulsed source, whose duration is negligible as compared to the lifetime of the emission process. The luminescence intensity of the luminescence centres is a function of their concentration, of their absorbing power at the excitation wavelength, and of their quantum yield[3] at the emission wavelength [Gaft et al. 2015].
Two radiative processes are possible: spontaneous emission, such as radioactivity, and stimulated (or induced) emission. However, not every mineral shows luminescence, due to the possible process of non-radiative return to the ground state. In that process, the energy of the excited state is used to excite in turn the vibrations of the host lattice (i.e. heating the host lattice).

Many luminescence properties and peculiarities of different minerals have been related to the crystal-chemical and structural state of mineral species, varieties and individuals, searching at the same time for possibilities to associate the luminescent behaviour with the different conditions of mineral formation and alteration. Moreover, as the knowledge of luminescent mechanisms expanded, the possibility to tailor the luminescence properties of synthetic crystals arose. All of this has induced countless applications of the luminescence properties of minerals in several fields: geosciences, remote sensing, natural dosimetry, archaeological dating, synthesis of phosphors and quantum electronic materials, etc. [Gaft et al. 2015; Aitken 1985; Smith 1949; Guidorzi et al. 2020; Re et al. 2018; Ditalia Tchernij et al. 2017; DeAcha et al. 2017; Garnier et al. 2002]. A short list of minerals that show luminescence under UV excitation is reported in table 3.1.

To fully understand the luminescent process and its origin, one should give thought to how the atoms forming a mineral influence each other. When individual atoms are combined forming minerals, and so are located within a periodic and anisotropic crystal lattice, all the involved energy levels change, resulting in a different system of energy levels which is typical of the considered mineral [Marfunin 1979]. The processes of developing new energy level systems can be described using different theories of solid state physics which can explain absorption and luminescence properties. For insulators, to which many minerals belong, Crystal Field Theory can be used to explain luminescence, whereas Band Theory is often employed when considering semiconductor crystals [Yacobi and Holt 1990].

[3] The quantum yield is the ratio of the number of photons emitted to the number of photons absorbed.

Table 3.1. Minerals luminescent under UV lamp excitation, from [Gaft 2015].

Native	Diamond
Oxides	Brucite $Mg(OH)_2$, corundum Al_2O_3, ruby Al_2O_3, sapphire Al_2O_3
Halogenides	Fluorite CaF_2, halite NaCl, calomel HgCl
Silica	Agate SiO_2, opal SiO_2, quartz SiO_2
Phyllosilicates	Pyrophyllite $AlSi_2O_5OH$, talc $Mg_3Si_4O_{10}(OH)_2$, serpentine $(Mg, Fe)_3Si_2O_5(OH)_4$
Feldspar	Albite $NaAlSi_3O_8$, microcline $KAlSi_3O_8$
Pyroxenes	Diopside $CaMgSi_2O_6$, spodumene $LiAlSi_2O_6$
Amphiboles	Anthophyllite $(Mg, Fe)_7Si_8O_{22}(OH)_2$, tremolite $Ca_2Mg_5Si_8O_{22}(OH)_2$
Zeolites	Natrolite $Na_2Al_2Si_3O_{10} \times 2H_2O$, laumontite $CaAl_2Si_4O_{12} \times 4H_2O$, analcite $NaAlSi_2O_6 \times H_2O$
Feldspathoids	Sodalite $Na_4Al_3(SiO_4)_3Cl$
Other silicates	Zircon $ZrSiO_4$, datolite $CaBSiO_4(OH)$, danburite $CaB_2Si_2O_8$, eucryptite $LiAlSiO_4$, willemite Zn_2SiO_4, wollastonite $CaSiO_3$, sphene $CaTiSiO_5$, scapolite $Na_4(Al, Si)_{12}O_{24}Cl$, manganaxinite $Ca_2(Mn, Fe, Mg)Al_2(BO_3OH)(SiO_3)_4$, benitoite $BaTiSi_3O_9$, thorite $(Th, U)SiO_4$
Carbonates	Aragonite $CaCO_3$, calcite $CaCO_3$, cerussite $PbCO_3$, magnesite $MgCO_3$, strontianite $SrCO_3$, witherite $BaCO_3$
Sulfides	Sphalerite (Zn, Fe)S, wurtzite (Zn, Fe)S
Sulphates	Barite $BaSO_4$, celestine $SrSO_4$, gypsum $CaSO_4 \times 2H_2O$, anhydrite $CaSO_4$, alunite $KAl_3(SO_4)_2(OH)_6$, zippeite $K_4(UO_2)_6(SO_4)_3OH_{10} \times 4H_2O$, ettringite $Ca_6Al_2(SO_4)_3(OH)_{12} \times 26H_2O$, hanksite $Na_{22}K(SO_4)_9(CO_3)_2Cl$
Phosphates	Apatite $Ca_5(PO_4)_3(OH,F,Cl)$, wavellite $Al_3(PO_4)_2(OH)_3 \times 5(H_2O)$, amblygonite (Li, Na)$AlPO_4$(F, OH), pyromorphite $Pb_5(PO_4)_3Cl$, monazite $(Ce, La, Th, Nd, Y)PO_4$, autunite $Ca(UO_2)_2(PO_4)_2 \times 10H_2O$, xenotime$YPO_4$
Tungstates	Scheelite $CaWO_4$
Molybdates	Powellite $CaMoO_4$, wulfenite $PbMoO_4$
Borates	Colemanite $CaB_3O_4(OH)_3$-H_2O
Organics	Amber $C_{10}H_{16}O$

3.1.1. Band Theory

In minerals, atoms are very close and they tend to strongly influence one another, with a resulting overlap of their atomic orbitals. As consequence, in certain minerals the energy levels are combined in a very large number of closely packed discrete levels, which form energy zones – or *bands* – that can be filled by electrons.

The last filled zone is called *valence band* (VB), as valence electrons take part in its occupation, and it is formed by the outer atom orbitals. All the higher energy zones are empty because they are formed by empty electron orbitals; the lowest of these empty zones is called the *conduction band* (CB) (figure 3.1). The interval between the valence and the conduction band is called the *energy* (or band) *gap* E_g. The energy value of this band gap allows to distinguish among insulators, where the band gap is higher than

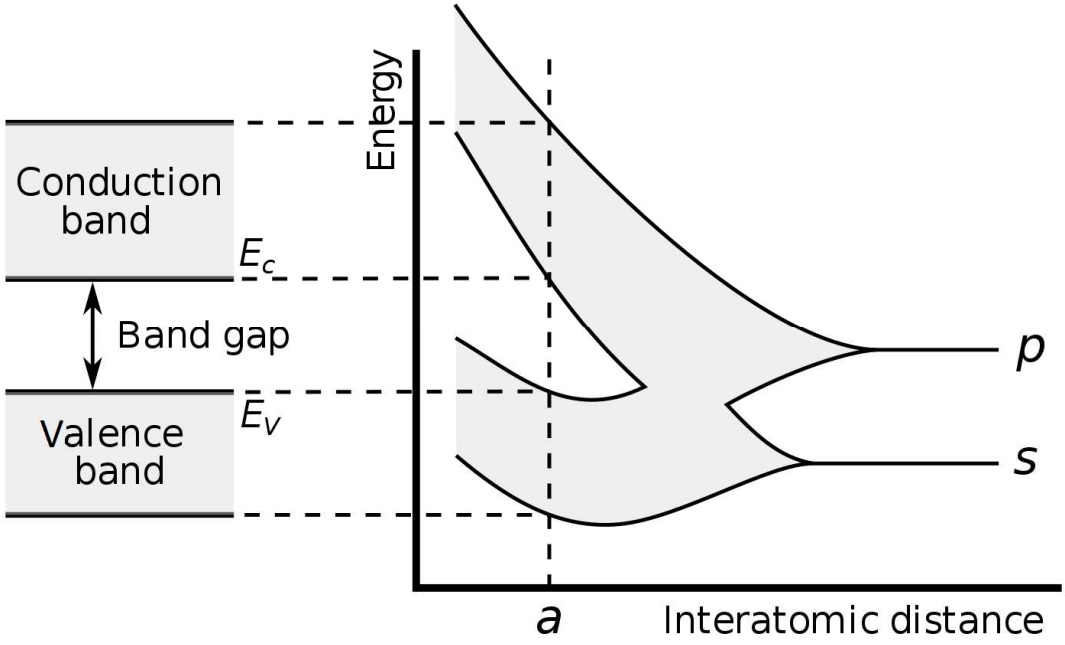

Figure 3.1. Electronic band structure from a large number of carbon atoms that form a diamond crystal. The graph shows the energy levels as a function of the spacing between atoms. When the atoms are considered separately (right side of graph) each one has degenerate valence atomic orbitals *p* and *s*. However, when the atoms come closer together in a crystal, their orbitals begin to overlap and splits into N molecular orbitals each with a different energy. In an actual crystal of diamond at atomic spacing *a*, the orbitals form two energy bands, the valence and conduction bands, with a 5.5 eV band gap between them.

3 eV, semiconductors (E_g 1.5-3 eV) and conductors (E_g lower than 1.5 eV and with the bands overlapping). In the energy gap additional discrete energy levels can reside, which are due to the presence of luminescence centres in the crystal lattice. The nature of these centres or *activators* can be related to pure lattice defects (i.e. vacancies or electron-hole centres), or impurities of foreign ions or atoms [Henderson and Imbusch 1989].

If the forbidden gap has small enough dimensions, the electron transfer from the defective levels or from the VB to the CB may take place. For example, with an interband spacing of about 3 eV, a UV irradiation with a wavelength of less than 300 nm has enough energy to detach electrons and transfer them from the filled valence band into an empty conduction band [Gaft et al. 2015]. After this electron promotion, the situation involves a free electron in CB and a free hole in VB. These free elements can be entrapped in defective levels and become centres.

Various kinds of processes may occur in the band configuration (see figure 3.2 for visual reference):

a) Intrinsic luminescence, where an electron is excited from VB to CB; this is the so called interband transition. Recombination of this electron with a hole in the VB generates a photon with an energy

corresponding to the energy gap value. This process is related to crystal lattice properties such as lattice intrinsic defects (anion vacancies). Before recombining, the lattice may adjust nuclei positions to the new excited situation; in this mechanism, called *relaxation*, part of the excited electron energy is transferred to the crystal lattice by increasing atomic vibrations. The emission occurs in this case at a lower energy than the absorption, and the energy difference between the Eg and the actual emission energy is called *Stokes shift*.

b) Recombination of the promoted electron with an activator (1) or a *trap* (2) (caused by defects in the crystal lattice) within the forbidden gap. In the first case we have luminescence emission with photon energy $<E_g$, in the second case the entrapment of the free electron. This is quite common in minerals for the presence of impurity ions. In this case the energy of the emission depends on the type of luminescence centre involved.

c) Stimulated release of an electron from the trap to the CB by heat (thermoluminescence) or by light (optically stimulated luminescence), followed by emissive recombination with an activator.

d) Luminescence generation through direct recombination of electron from a trap with an activator *or*

e) with a hole in the VB.

f) Extrinsic luminescence, where after being excited, electrons of defect ions recombine with their own ground state with luminescence emission. The energy (or wavelength) of the emitted luminescence can be related to the type of the impurity defect.

Additional complex mechanisms can also take place in many luminescent materials. For example, instead of returning to the ground state, the electrons may transfer the excitation energy from the excited centre S* to another centre A, followed by the emission of a photon from A*. The transfer, though, can only occur if the energy differences between the ground and excited state of both centres are equal (*resonance condition*) and if a suitable interaction exists, such as an exchange interaction when their wave functions overlap [Gaft et al. 2015].

The centre that absorbs the radiation (S*) is called *sensitizer* or *co-activator* and the centre that emits the photon (A) is the activator or luminescence centre. The energy can be transferred directly from the excited sensitizer to the activator, or the sensitizer may go through emission itself and the emitted radiation is then absorbed by the activator. In addition, if the centre A decays non-radiatively it is called a *quencher* of the sensitizer emission.

The section 3.1.3 will discuss more thoroughly the presence of activators, sensitizers and quenchers within minerals.

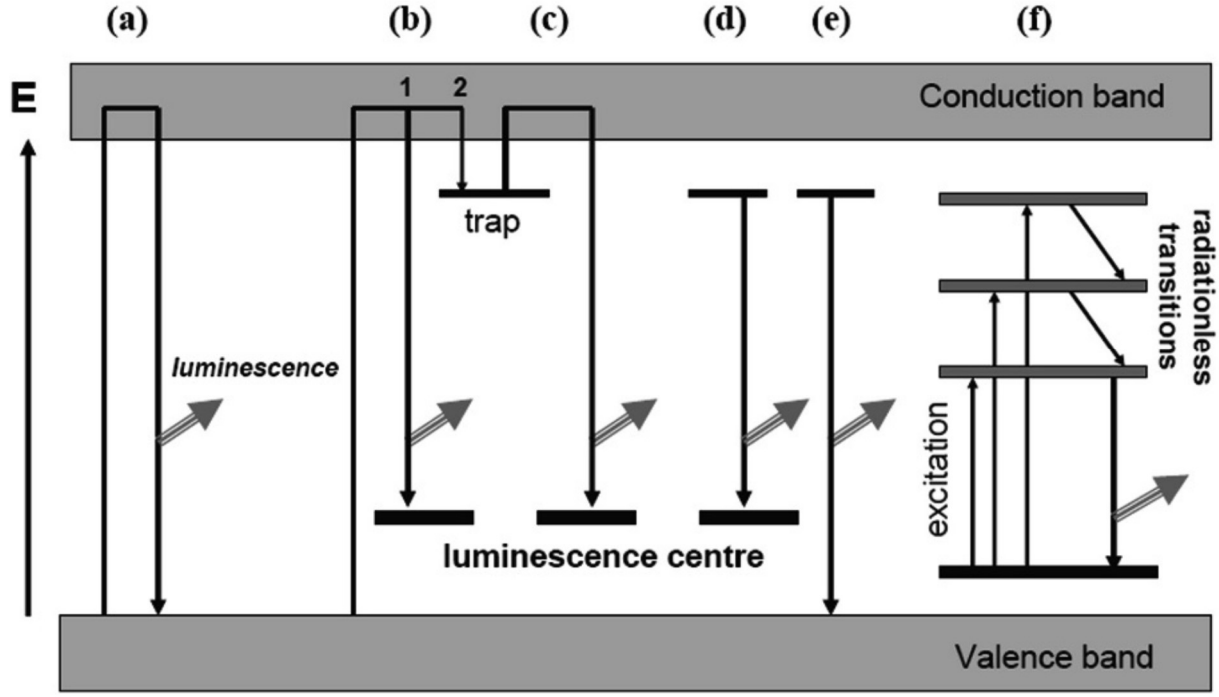

Figure 3.2. Processes of charge transfer and luminescence production in insulator crystals. (a) intrinsic luminescence; (b) excitation of electrons followed by recombination with an activator and resulting luminescence emission of a photon (1) or trapping of the electron (2); (c) thermal or optical stimulation of a trapped electron to the conduction band with subsequent recombination with an activator; direct transition of the electron to the recombination centre (d) or to the valence band (e); (f) extrinsic luminescence. From [Gucsik 2009].

3.1.2. Crystal Field Theory

In the interpretation of luminescence spectra, beside the three basic processes (excitation, emission and non-radiative transitions) it has to be considered as well the interaction of the activator ion with the surroundings. Luminescence centres in minerals are mainly transition and rare-earth elements (the latter also indicated as REE). The ground and excited levels in these cases are those of *d* and *f* orbitals, while *d-d* and *d-f* emission transitions are subjected to a strong influence from the nearest neighbours, the so called *ligands*. The splitting of *d* orbital energies and its consequences are at the heart of the crystal field theory. When the metal ion is surrounded by a coordinating system not of spherical symmetry, such as what happens in a crystal lattice, its *d* orbitals will interact with the new charges in different ways depending on their lying axes. Basically, in this situation the *d* orbitals of the activator become non-degenerate and separate in two sets with two different energy values: (*xy*, *xz*, *yz*) and (z^2, x^2-y^2); the parameter Δ_0 (or 10Dq) represents the extent to which these two sets of orbitals are split. Actually, the

results of the theory are seldom strictly linked to the presence of a lattice, but it is possible to extend most of them to the general model of the *coordination cluster*. With this term it is meant a central metal ion associated with a number of attached ligands, the whole forming a distinguishable entity and possibly bearing a net electric charge [Gaft et al. 2015]. Hence, the electrons of the central ion are subjected from the ligand atoms to a potential not necessarily of simple electronic origin. From this approach is was introduced the more recent term *ligand field theory*.

As seen in the band theory, excitation of the ion and subsequent emission are separated by a time interval in which the surrounding ligands shift to a new equilibrium position with a new distance to the excited luminescent ion. During this process, some of the excitation energy is transferred to the crystal lattice, resulting in a shift (the Stokes shift) of the emission band in relation to the corresponding absorption band towards longer wavelengths (i.e. to lower energies).

The process of excitation and emission of an individual luminescence centre can thus be described using a configurational coordinate diagram, as shown in Figure 3.3. This scheme shows the potential energy curves of the absorbing centre as a function of the relative distance R of the nucleus to the equilibrium position (i.e. electron in the ground state with vibrational level $n = 0$). Due to the excitation energy E_a, the electron is promoted from the ground state to a higher vibrational state of the excited state. Since the electron transitions are faster ($\Delta t \sim 10^{-16}$ s) than lattice relaxation ($\Delta t \sim 10^{-13}$ s), the transition occurs as a nearly "vertical" transition (Franck-Condon principle) [Lindon et al. 2017]. After the absorption, the system relaxes at first into the lowest level of the excited state $m = 0$ accompanied by emission of phonons, and then the electron returns into the ground level (luminescent emission with energy E_e). The wavelength and width of the emission band are dependent on the potential curve of the excited state. In particular, the horizontal displacement ΔR is the cause of line broadening: the larger the value of ΔR, the broader are the absorption and the emission bands. The displacement is temperature-dependent, hence the radiation-less return to the ground state via the point of intersection of the potential curves becomes more important at higher temperatures (i.e. leads to the effect of "thermal quenching" of luminescence, see section 3.1.3).

The activator-ligand distances in the different states and the slopes of the energy levels depend on the extent of the crystal field interaction (expressed as crystal field splitting parameter Δ_0). The stronger is the interaction of the activator ion with the lattice, the greater are the Stokes shift and the width of the emission line. Δ_0 is influenced by many factors including the type of cations, the type and number of ligands, the symmetry of the ligand environment, the oxidation state of the element and of the ligands, and ultimately the inter-atomic distances [Gaft et al. 2015]. It follows that the luminescence of a given ion may strongly depend upon its position in the crystal and on the crystal field.

In conclusion, two possible cases of interaction with the crystal field are possible:

1) if the electronic energy levels mainly responsible for the absorption and emission are not involved in the bonding to nearby atoms, the influence of the crystal field is weak, with a small splitting of the energy levels and, consequently, narrow emission lines without significant Stokes shift. This is the case of most of the trivalent ions of the rare earth elements (Eu^{3+}, Sm^{3+}, Dy^{3+}, Nd^{3+},…) whose emission spectra are relatively independent on the crystal structure of the host crystal, as transitions within the *4f* orbitals are shielded from the influence of the crystal field by the electron shells of the *5s* and *6p* orbitals;

2) if the electronic transitions happen between energy levels affected by the local crystal field, there is an enlargement of the splitting and luminescence emission spectra show relatively broad bands. Examples of this behaviour include *3d* transition elements such as Ti^{4+}, V^{4+}, Mn^{2+} and iron ions. Moreover, due to the variable entity of field parameter Dq, the wavelength of the luminescence emission of each activator element differs from mineral to mineral and is specific for the crystal structure of the host crystal. Hence, one type of ions can produce a great variety of luminescence spectra.

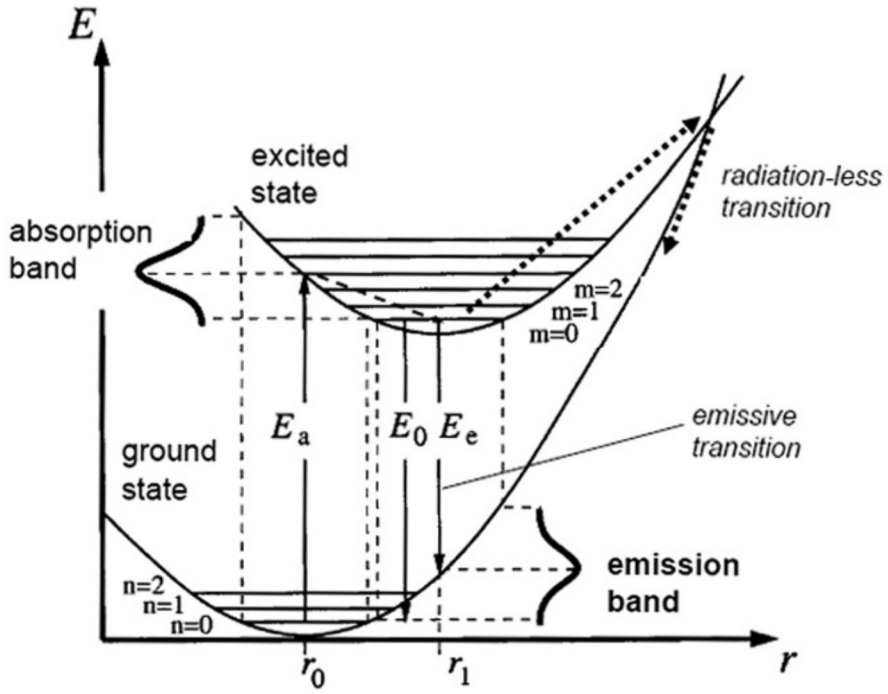

Figure 3.3. Configurational coordinate diagram for transitions according to the Franck-Condon principle, with related absorption and emission spectra. Radiation-less transitions are possible via the point of intersection of the potential curves (e.g. at higher temperatures). From [Gucsik 2009].

3.1.3. Activators, sensitizers and quenchers

The periodic crystal lattice of the minerals is in reality less than perfect and its regular patterns can be often interrupted by crystallographic defects. Among them can be cited the point defects (such as vacancies, interstitials, Frenkel defects, impurity ions and inorganic radicals, both intrinsic or extrinsic), the line defects (e.g. dislocations) or the planar defects (such as grain boundaries or stacking faults) [Gersten and Smith 2001]. As seen in the previous sections, such defects create accessible levels in the forbidden energy gap or modify the interaction with the crystal field, introducing a whole new set of possible electronic transitions.
The elements that can be found responsible of the luminescent phenomena in minerals are commonly metals, and in particular:

- transition metal ions (Mn^{2+}, Cr^{3+}, Fe^{3+}, etc.)
- rare earth elements cations ($REE^{2+/3+}$)
- actinides (particularly uranyl ions $[UO_2]^{2+}$)
- heavy metals (such as Pb^{2+})

The impurities accountable of the luminescence are defined *activators*. In fact, the term activator is given to all the trace impurities with an electron configuration of $3d^{(1-9)}$, that can interact strongly with the crystal field. As seen in the previous section, usually the luminescence activated by transition metal ions is characterised by a broad band width and a band position strongly dependent upon the host matrix. The centre and width of the peak are sensitive to the chemical surroundings in the crystal and may also be used to distinguish the host matrices involved.

In natural materials the complexity of luminescence spectra is enhanced, as they usually contain a great variety of different luminescent and non-luminescent centres, with the possibility to have interactions between them and the result of a change in their luminescent spectra and intensities due to transfer of excitation energy from one centre to another. A distinction in two group of activators can then be done:

- Native activators: transition elements or rare earth elements such as Cr^{3+}, Eu^{3+}, Mn^{2+}, Pb^{2+}, Fe^{3+};
- Intensifier activators: elements such as Ti^{4+} which amplify the luminescent signal.

To better explain the role of the impurities as activators, the case of the manganese ion, the most common activator [Rakovan and Waychunas 1996], can be taken in consideration. Mn^{2+} has the most important oxidation state within the minerals in terms of their luminescence. This ion can substitute for example

Ca^{2+} or Mg^{2+} in many carbonates, as well as in other minerals such as phosphates or silicates. Unlike Na^{+} and Ca^{2+}, which have full outer shells, Mn^{2+} has in the *d* orbitals only 5 electrons out of 10. These electrons are easily excitable because they require a lesser energy than the inner ones.

A specific activator can also be present in different minerals providing a variable luminescence colour; for example, tetrahedrally coordinated Mn^{2+} gives a yellow-green emission, whereas the emission from octahedrally coordinated Mn^{2+} is in the orange-red range. This effect can be observed for the Mn^{2+} activated luminescence in carbonates, which show shifting emission maxima (and with that change in visible luminescence colours) in dependence on the crystal type [Gucsik 2009]. Other activators can be Cr^{3+}, responsible for the fluorescence of rubies, spinels, and several silicate minerals, or Fe^{3+} , which gives a deep red emission in many scapolites and different silicates. Trivalent REE and most bivalent REE ions, such as Ce^{3+}, Eu^{2+}, Eu^{3+}, Sm^{3+} or Dy^{3+}, can also act simultaneously, with the resulting luminescence colour being a combination of them all; these activators are of particular interest in phosphates like apatite (Table 3.2) [Marfunin 1979].

Furthermore, the luminescent signal is affected by the presence of certain *sensitizer-activator* pairs; sensitizer are ions that work in combination with an activator by absorbing the energy and subsequently transferring it (or part of it) to the activator. Typical sensitizers are ions with intense absorption bands in the UV region of the spectrum (Tl^{+}, Cu^{+}, Pb^{2+}, Ge^{4+}) for sensitization of Mn^{2+}, ions of transition metals (Cr^{3+}, Mn^{2+}) for sensitization of REE^{3+}, and $REE^{2+/3+}$ or uranyl ions for sensitization of REE^{3+} [Gucsik 2009]. An example of an activator-sensitizer pair can be found in the case of the calcite: the ion Ca^{2+} in the calcite lattice can be replaced by Mn^{2+}, which would have a very small probability of absorption of UV light without the presence of the sensitizer Pb^{2+}; this ion transfers the absorbed energy to Mn^{2+}, whose electrons boost into an excited state and then generate the typical orange-reddish luminescent signal [Rakovan and Waychunas 1996].

Alongside activators and sensitizer-activator pairs, *quenchers* also take part in the luminescence phenomena. These are elements which inhibit the luminescence signal, and even the actual activators or sensitizers can start to act as quencher, depending in particular on their concentration. An example is the previously mentioned Fe^{3+}, that may quench the luminescent activity from other activator ions such as Mn^{2+}, Mn^{4+}, Sn^{2+}, Pb^{2+} [Götze 2002].

There are various types of quenching:

- *concentration quenching* or *self-quenching,* that occurs at high activator concentration levels (Figure 3.4). When the activator is present to the extent of 0.1% to perhaps a few percent, it will produce the maximum luminescence brightness. At higher activator concentrations, the intensity may actually decrease. That is because at increased concentration, activator atoms begin to cluster. This often allows

the energy that was absorbed earlier to be passed rapidly from activator atom to activator atom before luminescence can take place. In this process, the energy may be intercepted by a non-luminescent atom and completely converted to heat rather than visible light [Robbins 1990].

- quenching by ions with intense charge transfer bands, that influences especially the visible and near UV region, whereas luminescence emissions in the IR region are more or less unaffected. Because of this effect, the luminescence intensity is often not only a result of the activator content but of the ratio of activator and quencher ions.
- quenching due to lattice defects or impurities that causes the creation of new levels between the conduction band and the valence band. This results in absorption of the excitation energy, radiation-less energy transfer or emission at lower frequencies.
- *thermal quenching* which may occur at elevated temperatures; during excitation part of the energy given by irradiation on the sample can be transformed into heat [Marshall 1988] and the electrons will return to the ground state not by emissive transition, but via the point of intersect of the potential energy curves (see Figure 3.3) resulting in radiation-less transition.

Table 3.2 gives an overview of different types of activators identified as responsible of certain luminescence bands for the most common mineral phases present in lapis lazuli rocks.

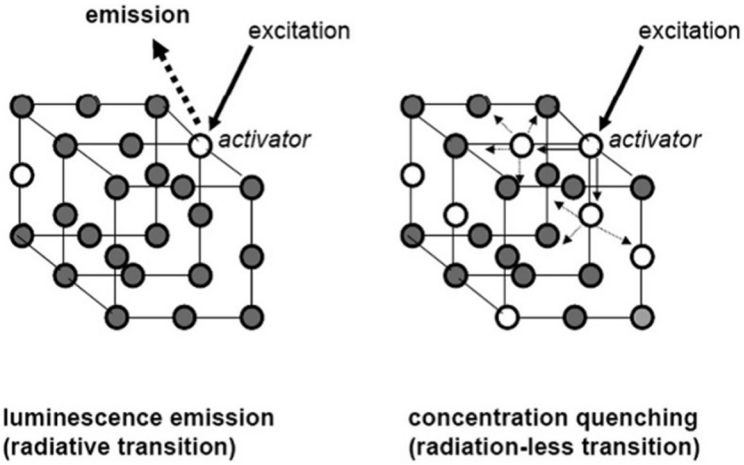

Figure 3.4. Concentration quenching: if there is a high activator concentration, some of the excitation energy is quantitatively transferred to other activator ions with resulting suppression of the luminescence emission of the ion [Gucsik 2009].

Mineral	Formula	Activator	Emission bands (nm)
Lazurite	$Na_6Ca_2(Al_6Si_6O_{24})(SO_4,S_3,S_2,Cl,OH)_2$	Mn^{2+}	575
		S_2^-	600-690
		Fe^{3+}	743
		Nd^{3+}	880-900
Diopside	$CaMgSi_2O_6$	Mn^{2+}	585 690
		$[TiO_6]$	415-450
		Cr^{3+}	685-700 785
		V^{2+}	700
		Fe^{3+}	690 760
		Nd^{3+}	870-920
Apatite	$Ca_5(PO_4)_3(F,Cl,O,OH)$	Mn^{2+}	560-580
		Mn^{5+}	1170
		Eu^{2+}	451
		Eu^{3+}	570-650 695 700
		Ce^{3+}	360-430
		Dy^{3+}	480-570 663 750
		Gd^{3+}	312
		Er^{3+}	403 545 1540
		Pr^{3+}	485 600 650
		Sm^{3+}	560-650 734
		Tb^{3+}	415 480-550
		Tm^{3+}	360-450 700
		$(UO_2)^{2+}$	460-550
		Nd^{3+}	870-890 909 1070 1340
Wollastonite	$CaSiO_3$	Mn^{2+}	550-620
		Fe^{3+}	700
		Cr^{3+}	840
		Nd^{3+}	850-950
Calcite	$CaCO_3$	Mn^{2+}	605-630
		Ce^{3+}	340-380 545 700
		Dy^{3+}	485-580 680 760
		Sm^{3+}	600-650
		Eu^{3+}	575 618
		Pb^{2+}	312
Feldspars	$(K,Na)AlSi_3O_8$	Mn^{2+}	560-570
		Fe^{3+}	700-750
		Pb^{+}	850-860
		Pb^{2+}	296
		Cr^{3+}	785
		Eu^{2+}	400-410 614-624
		Ce^{3+}	325-335
		Gd^{3+}	316
		Dy^{3+}	485-575
		Er^{3+}	500-530
		Nd^{3+}	895

Table 3.2. Luminescence activators and related bands at room temperature for most common mineral phases present in lapis lazuli rocks. Data from [MacRae and Wilson 2008] and [Gaft et al. 2015].

3.2. Diopside: crystal structure and chemistry

Diopside is a monoclinic mineral belonging to the pyroxene family; more specifically, it is an inosilicate with a single calcium and magnesium chain, whose general chemical formula is $CaMgSi_2O_6$. Diopside's was the first pyroxene structure ever determined [Warren and Bragg 1928] and since then a lot of information about this mineral have been collected, hence a good description of its characteristics can be found in the literature [Deer et al. 1977]. It was named in 1806 by Rene Just Haüy, from the Greek διζ- for "double" and οψτζ-, "appearance", in allusion to two possible orientations of the prism zone.
Diopside forms a complete solid solution with hedenbergite ($CaFeSi_2O_6$). To evaluate the composition of a pyroxene from the chemical analysis of the mineral, a quadrilateral plot such as the one shown in figure 3.5 can be used. In the corners there are the pure terms (100% composition of the indicated mineral), whereas inside the trapezoid area the names of the minerals with intermediate composition are reported; it should be noted that wollastonite ($Ca_2Si_2O_6$) is actually a pyroxenoid and does not fall into this representation. The colour of diopside ranges between white, pale green and dark green; moving towards hedenbergite, the mineral can show a more yellow/brownish green shade. In thin section it appears colourless and it does not present pleochroism.

In terms of paragenesis, diopside is a common constituent of igneous basic and ultra-basic rocks; the crystals more rich in iron are present in various metamorphic rocks, in particular limestone or carbonates, but can also be formed in conditions of pressure and temperature typical of regional metamorphism. Relatively pure diopsides occur in some thermally metamorphosed impure dolostone and in skarns [Deer et al. 1977]. As pyroxenes are solid solutions, in metamorphic rocks part of diopside can be substituted by the jadeite ($NaAlSi_2O_6$) component, an end-member stable at high P-T conditions in metamorphosed granitoid according to the reaction Jadeite + Quartz = Albite [Holland 1980]. This substitution is directly proportional to the pressure conditions of recrystallisation [Holland 1983], and in particular Ca and Mg are replaced by Na and Al, respectively, to maintain the balance of the charges following the equivalence Na + Al = Ca + Si.

The essential feature of all pyroxene structures is the linkage of SiO_4 tetrahedra by sharing two out of four corners to form continuous chains of composition $(SiO_3)_n$.
The general chemical formula of a pyroxene is $M2M1T_2O_6$, where:

- M2 refers to cations in a distorted octahedral coordination, that lie principally between the bases of SiO_3 chains (Ca, Na);

- M1 represents cations in a regular octahedral coordination, that lie principally between the apices of SiO_3 chains (Mg, Fe);
- T stands for tetrahedral coordination.

The structure can also be regarded as made up of layers of tetrahedra alternating with layers of polyhedra with six-fold or higher coordination (Figure 3.6) [Deer et al. 1977].

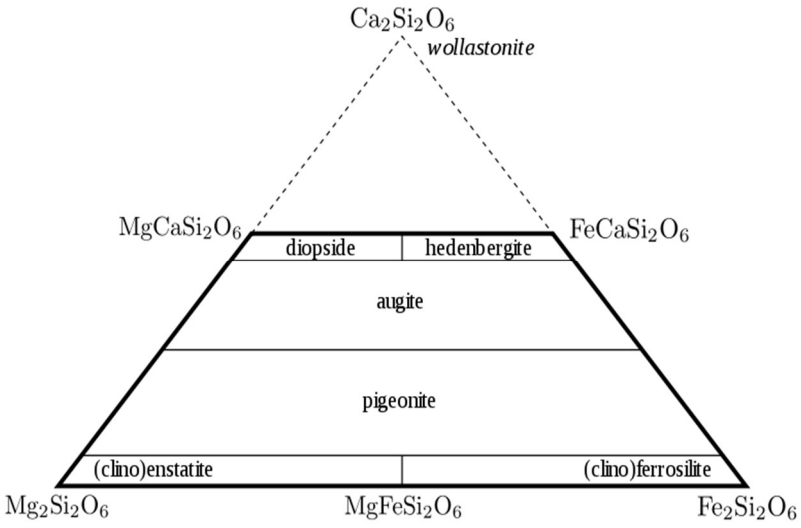

Figure 3.5. Composition ranges of the Ca-Mg-Fe clinopyroxenes in the quadrilateral nomenclature, modified after [Morimoto 1988]. The ideal location of wollastonite, a pyroxenoid, is also indicated.

Si can be replaced by small amounts of Al, usually without exceeding a 10% substitution, and the content of Al_2O_3 can vary between 1 and 3 wt%. Si substitution can involve also other small cations such as Fe^{3+}. The M1 site, generally occupied by Mg, can be also occupied by vicariant elements, such as Al^{3+}, Fe^{3+}, Ti^{4+}, Cr^{3+}, V^{3+}, Zr^{4+}, Zn^{2+}, Fe^{2+}, and Mn^{2+}, given in an ideal site-occupancy order. The M2 site, occupied by Ca, can be similarly occupied by minor quantities of vicariant elements as Mg^{2+}, Fe^{2+}, Mn^{2+}, Sr^{2+} [Morimoto 1988]. Generally, an average TiO_2 content of 0.54 wt% can be present. The MnO content of the Mn-rich terms of the series is generally low, but the amount increases in the more iron-rich terms, going from an average of 0.13 wt% for diopside to one of 3.60 wt% for hedenbergites. For Cr-diopside the content of Cr_2O_3 can exceed 1 wt% [Deer et al. 1977]. The example composition of a Cr-diopside reported in table 3.3 reflects these average values.

A study by Vinokurov [Vinokurov 1966] of the Mn^{2+} electron paramagnetic resonance spectra in a number of diopsides has shown that Mn^{2+} may replace Ca, as well as Mg ions; Zn also may substitute for Mg. The replacement of Mg by Fe^{2+} is generally accompanied by an increase in the refractive indices [Deer et al. 1977].

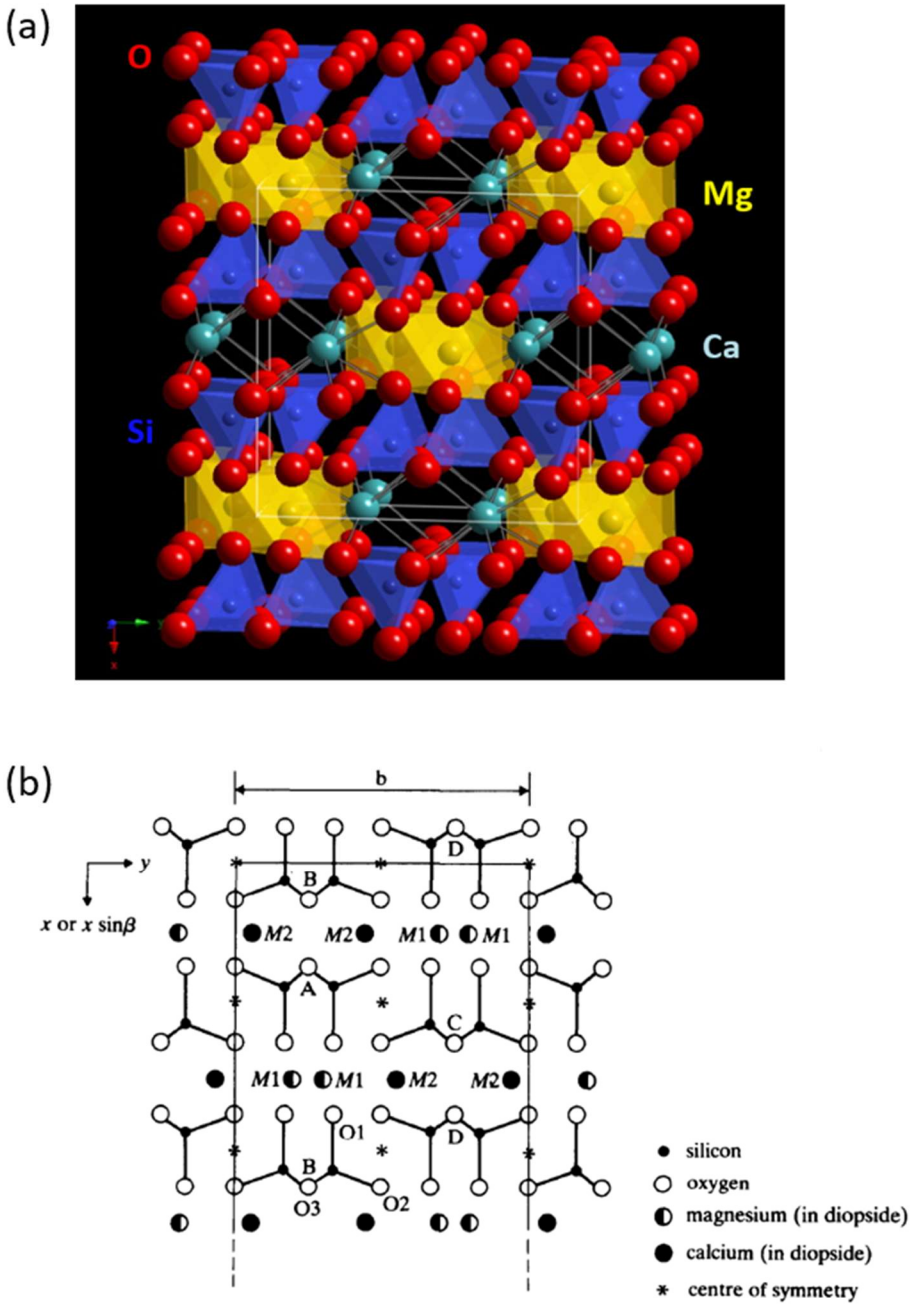

Figure 3.6. (a) 3D rendering for the structure of diopside, highlighting the sequence of tetrahedra and polyhedra alternate layers; (b) Projection along *z* axis of an idealized pyroxene structure, showing the (SiO_4) chains and two distinct cation sites M1 and M2 (from [Deer et al. 1977]).

Table 3.3 Main features for diopside. [1] The chemically analysed sample is specifically a Cr-diopside, as the Cr_2O_3 content reveals. Data from [Anthony et al. 2001].

Diopside					
Formula		$CaMgSi_2O_6$	**Optical Properties**	Color	Transparent to opaque
Mineral Group		Pyroxenes			Colorless, white, yellow, pale to dark green, black
Main occurrences		In metamorphic impure marble and carbonate-silicate metamorphic rocks (previously defined also as calciphyre)			colorless in thin section
Association		Calcite, forsterite, chondrodite, monticellite, clinohumite, scapolite, wollastonite, grossular, vesuvianite, tremolite, quartz		Streak	White, gray, gray-green
				Luster	Vitreous or dull
				Optical Class	Biaxial (+)
Crystal Data	System	Monoclinic	**Chemistry**	sample provenance	Dutoitspan mine, South Africa[1]
	Class	2/m		composition (wt%)	SiO_2: 54.09 TiO_2: 0.28 Al_2O_3: 1.57 Fe_2O_3: 0.74 Cr_2O_3: 2.03 FeO: 1.47 MnO: 0.09 MgO: 16.96 CaO: 21.10 Na_2O: 1.37 K_2O: 0.15 H_2O^+: 0.22 H_2O^-: 0.08 rem: 0.49 total: 100.64
	Twinning	Simple or multiple twins on {100} or {010}, common.			
Cell Data	Space Group	C2/c			
	a (Å)	9.746			
	b (Å)	8.899			
	c (Å)	5.251			
	β	105.63°			
	Z	4			
Physical Properties	Fracture	Uneven to conchoidal			
	Tenacity	Brittle			
	Hardness	5.5÷6.5			
	Density measured (g/cm^3)	3.22÷3.38			
	Density calculated (g/cm^3)	3.278			

3.3. Diopside: activators and quenchers

Despite the structure of diopside has been known and investigated since the beginning of XX century, studies on the determination of its activators, and much less its quenchers, are not so widespread in the literature. In 1996, for example, Modreski and Aumente-Modreski in their review on fluorescent minerals [Modreski and Aumente-Modreski 1996] reported unknown activators for this mineral, despite an evident blue-white colour of fluorescence.

In a more recent luminescence database [MacRae and Wilson 2008] it is stated that diopside at room temperature shows two luminescent bands centred at 585 nm and 670 nm respectively, activated by Mn ions, whereas a band at 415 nm is due to Ti ions; the oxidation state for the ions is not reported. The cited reference leads to a work carried out back in the 1940s, involving the synthesis of new silicate phosphors for television screens production [Smith 1949]. According to the author, synthetic Ti-doped diopside ($CaO{\cdot}MgO{\cdot}2SiO_2$:Ti) shows a broad luminescence band at about 400 nm (figure 3.7a). On the other hand,

$CaO{\cdot}MgO{\cdot}2SiO_2$:Mn exhibits two bands, one at 585 nm and the other at 670 nm (figure 3.7b). Activation by Ce introduced during the synthesis is also verified, inducing a broad band centred around 370 nm (not reported).

These features are mostly confirmed also in latest studies on natural diopside. The 450 nm band has been ascribed to the TiO_6 complex; intense bands at 585 and 690 nm can be related to Mn^{2+} ions in M2 (Ca^{2+}) and M1 (Mg^{2+}) sites respectively [Gaft et al. 2015]. It is reported in synthesis studies that the intensities of these two bands are most affected by variations of the firing conditions, with the red band increasing at the expense of the orange one as the firing time is increased. The most plausible explanation is attributed to a diffusion process, in which Mn^{2+} diffuses from the Ca lattice sites to those of Mg, with a corresponding decrease in the orange emission and an increase in the red [Smith 1949]. Moreover, narrow lines found near 684 nm belong to Cr^{3+} activation and the band peaking at 690 nm has been also ascribed to Fe^{3+} [Gorobets and Rogojin 2002].
Time-resolved spectroscopy identified for the broad band peaking occurring at approximately 785 nm a connection to Cr^{3+} centre in weak crystal field [Gaft et al. 2015]. Excitation by continuous-wave laser (532 nm and 780 nm) revealed also luminescence lines in the IR region which may be ascribed to Nd^{3+} and a broad structured band, peaking at approximately 700 nm, ascribable to Cr^{3+} in average crystal field or to V^{2+}(Figure 3.8) [Gaft et al. 2015].

Generally there is no mention to the action of specific sensitizers. However, it has also to be stressed out that in silicates the $(SiO_4)^{4-}$ groups themselves can absorb UV radiation and transfer this energy to Mn^{2+} (or other activators). Hence the silicate framework of the mineral acts as a sensitizer [Rakovan and Waychunas 1996]. The same lack of information is found for quenchers: Fe^{3+} can be assumed as the most probable, as it is the most widespread and strong quencher for rare earths and transition metals activation [Marfunin 1979]. Other efficient quenching ions are Fe^{2+}, Co^{2+} and Ni^{2+}, even if to a lesser extent than Fe^{3+}.
It follows then that a study of diopside crystals inside lapis lazuli rocks in terms of correlations between trace elements detected and characteristic luminescence might complement these previous works from the literature. Moreover, the use of multivariate analysis techniques (chapter 7) on the acquired data could reveal co-activation effects, as they comprehensively consider the whole system under investigation.

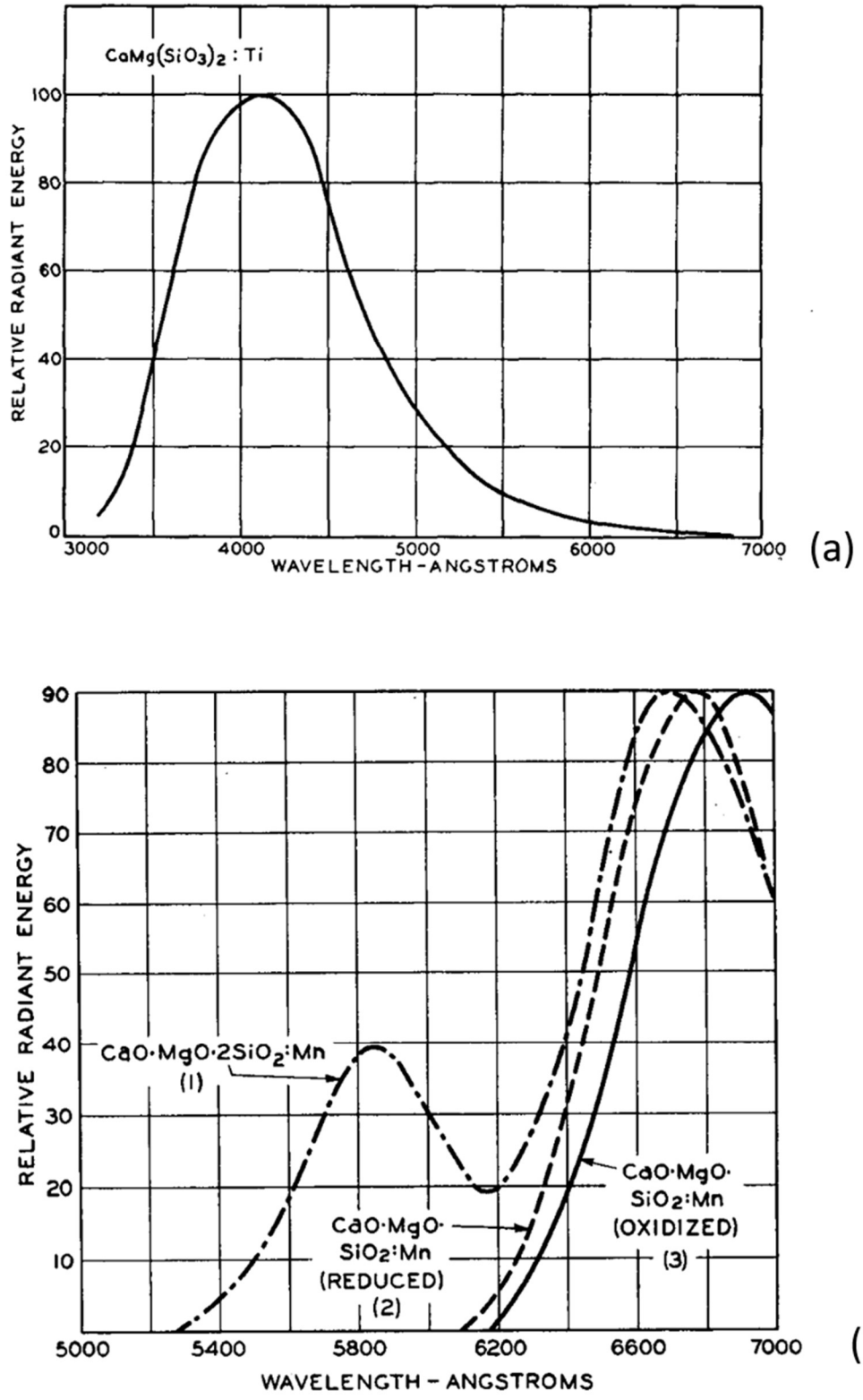

Figure 3.7. (a) luminescence spectrum of synthetic $CaO{\cdot}MgO{\cdot}2SiO_2$:Ti, showing a broad band centred at about 400 nm; (b) luminescence spectrum of synthetic $CaO{\cdot}MgO{\cdot}2SiO_2$:Mn (1) where the two bands at 585 nm and 670 nm are evident. From [Smith 1949].

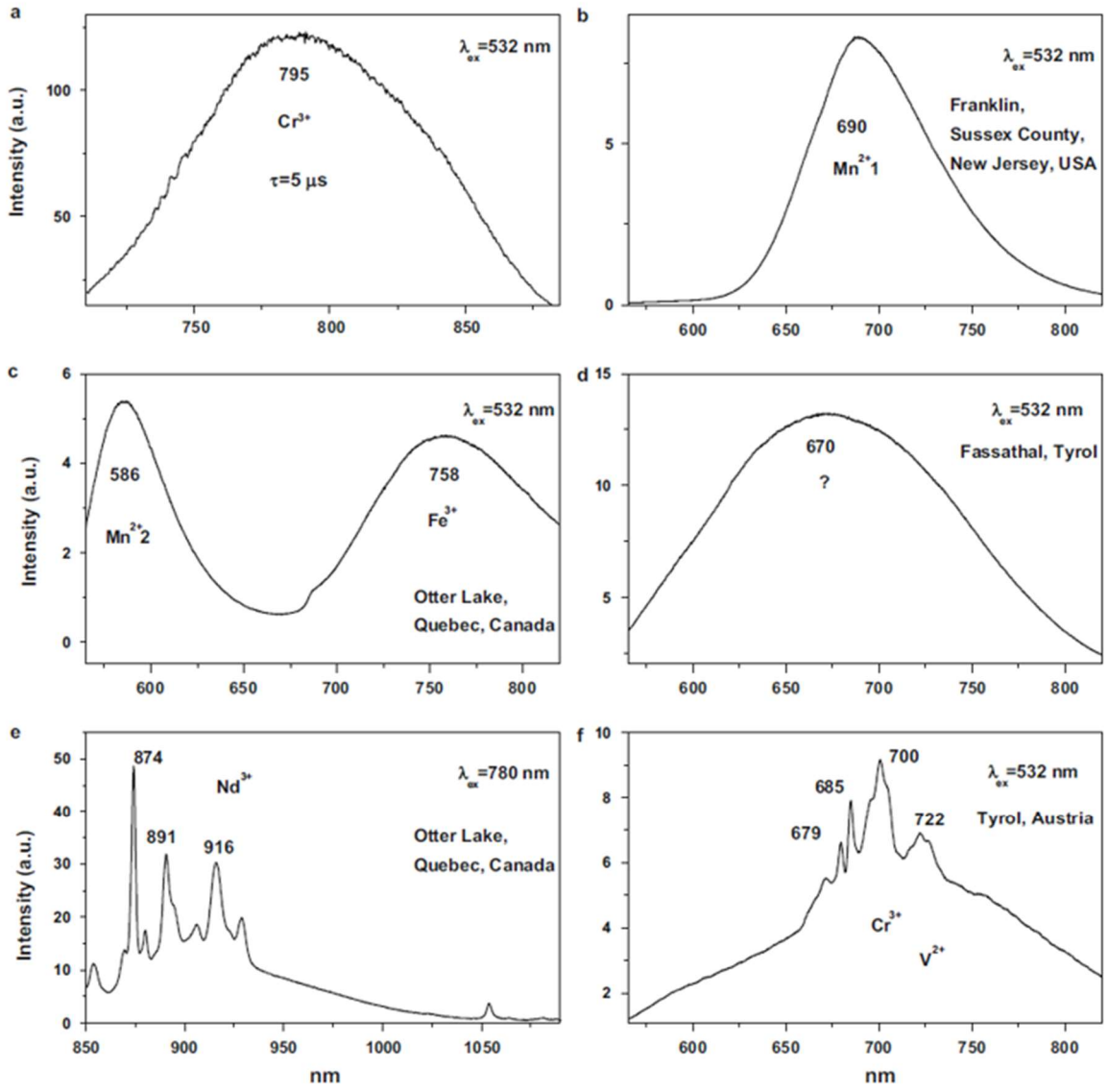

Figure 3.8. Laser-induced time-resolved spectrum of diopside demonstrating Cr^{3+}centres (a); CW luminescence spectra of diopside demonstrating evidently Cr^{3+}, Fe^{3+}, Mn^{2+}, Nd^{3+} and possibly V^{2+} centres (b-f). Excitation wavelengths and origins of crystals are reported. (from [Gaft et al. 2015])

4. Samples

An overview of the various kinds of lapis lazuli samples subjected to analyses in this thesis work is presented. They range from raw lapis lazuli material, collected directly from quarries, stored in museums collections or acquired by intermediaries, to precious archaeological artefacts found in strategical sites of the mid-East during different archaeological campaigns. Their dissimilar origin makes them play different roles in the present study, that are outlined in each of the following sections.

4.1. Reference geological samples

A collection of 56 raw lapis lazuli rocks has been put together during the decade-long study performed by the Physics for Cultural Heritage group at University of Torino. The available samples are divided in 5 provenances, summarized in table 4.1. Afghan (21) and Chilean (9) samples were purchased at mineral Expos from reliable international traders; their origin was certified from Badakhshan and Coquimbo areas respectively. Other samples were purchased directly in the Country of origin, such as for Myanmar provenance. Rocks from Siberia have been instead collected from quarries still accessible by geologists sent to a dedicated recovery mission and they belong to the Mineralogy and Lithology section of the Museum of Natural History from the University of Florence. For these samples, as well as for those from Tajikistan, we have the exact georeferenced coordinates. Tajik lapis lazuli (4 samples) come from Pamir Mountains, specifically from Lyadzhuar Dara deposit at 4,800 m above sea level and approximately 76 km south of Khorugh in Gorno-Badakhshan. It is noteworthy to observe that the Lyadzhuar Dara deposit is only at about 200 km northeast of Sar-e-Sang mines in Badakhshan region. Siberian samples came from Sludyanka River (7 samples) and Malaya Bistraya River (4 samples) valleys, about ten kilometres apart from each other and approximately at 100 km SSE of Irkutsk, that is located on Lake Baikal's shore. Moreover a non-georeferenced sample (Cat. Numb. 390) from an unknown place in the Irkutsk area and belonging to the historical collection of the abovementioned museum was included. Lapis lazuli from Myanmar (10 samples) were the latest addition to the set of reference geological samples and were retrieved by collaborators from the Mogok area.

This collection of rocks was employed as reference set for the creation of the provenance protocol (section 2.3.1), published so far with the inclusion of Afghan, Tajik, Siberian and Chilean provenance; Myanmar origin is currently under analysis and has also been investigated during this PhD. From most of the samples, thick petrographic sections (ca. 100 μm thickness) have been prepared (Figure 4.1). The sections,

after the preliminary characterisation described in section 2.3.1, have been at first analysed by means of Ion Beam Analysis at INFN – Legnaro National Laboratories (Padua, Italy): measurements in vacuum at the microbeam line require the coating of the samples with a thin layer of graphite to avoid the charging of the material. Subsequently, within the framework of my PhD, a selection of the sections has been measured also at the external microbeam line of AGLAE accelerator, in the C2RMF laboratories under the Louvre museum in Paris (see table 4.2).

Table 4.1 Provenance and area of origin for reference geological lapis lazuli samples.

Provenance (current nation)	**Area**	**Number of samples**	**Acquisition**	**Years of acquisition**
Afghanistan	Badakhshan	21	Bought from reliable international traders	2010-2014
Tajikistan	Lyadzhuar Dara, Pamir Mtn (georeferenced)	4	Bought from Global Mining LLC	2007
Russia (Siberia, near Lake Baikal)	Sludyanka River (georeferenced)	7	Expedition	2012
	Malaya Bistraya River (georeferenced)	4	Expedition	2012
	Near Irkutsk	1	Bought from reliable international trader	1985
Myanmar	Mogok	10	Expedition	2014-2015
Chile	Coquimbo	9	Bought from reliable international traders	2010-2014

Table 4.2. Summary of analyses in LNL and AGLAE for thick petrographic sections.

Provenance	Sample	INFN-LNL	AGLAE
Afghanistan	Afg 47860	✓	
Afghanistan	Afg 12397	✓	✓
Afghanistan	Afg 388	✓	
Afghanistan	TME_AFG1	✓	✓
Afghanistan	TME_AFG2	✓	
Afghanistan	TME_AFG3	✓	✓
Afghanistan	TME_AFG4	✓	✓
Afghanistan	TME_AFG6	✓	
Tajikistan	Pamir 1	✓	
Tajikistan	Pamir 2 bis	✓	✓
Tajikistan	Pamir 3	✓	✓
Tajikistan	Pamir 4	✓	
Siberia	M15920	✓	
Siberia	390	✓	✓
Siberia	BK1-SR	✓	
Siberia	BK2-SR	✓	
Siberia	BK3-SR	✓	✓
Siberia	BK4-SR	✓	
Siberia	BK6-SR	✓	✓
Siberia	BK7-SR	✓	✓
Siberia	BK8-MBR	✓	
Siberia	BK9-MBR	✓	✓
Siberia	BK10-MBR	✓	✓
Siberia	BK11-MBR	✓	
Chile	Chile 1	✓	
Chile	Chile 2	✓	
Chile	Chile 3	✓	
Chile	Chile 4	✓	
Chile	Chile 5	✓	
Chile	Chile 16980	✓	
Chile	Chile 12403	✓	
Chile	Chile 12405	✓	
Myanmar	MYA 02	✓	
Myanmar	MYA 03	✓	✓
Myanmar	MYA 04	✓	✓
Myanmar	MYA 06	✓	✓
Myanmar	MYA 07	✓	
Myanmar	MYA 08	✓	
Myanmar	MYA 09	✓	✓
Myanmar	MYA 10	✓	✓
Myanmar	MYA 11	✓	✓
Myanmar	MYA 12	✓	✓

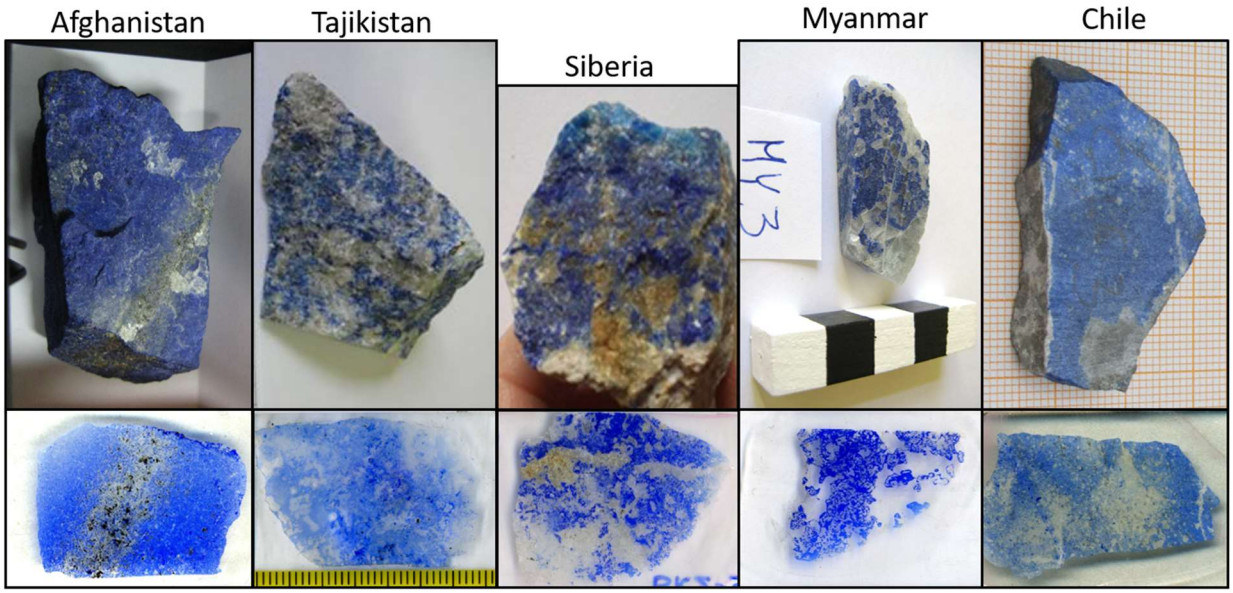

Figure 4.1. Examples of bulk rocks and thick petrographic sections from lapis lazuli rock reference set.

4.2. Archaeological samples from Shahr-i Sokhta site

In the early 1970s, archaeologists discovered and investigated lapis lazuli working areas in Shahr-i Sokhta. The site, located in eastern Iran and dated back to the III millennium BCE, was a consumer of high quality lapis lazuli beads, and, in part, a hub for the trade routes of this semi-precious blue stone. Caravans linked the city and other towns on the Iranian Plateau to a widespread network of long-distance exchanges towards the western markets. A large amount of production waste fragments or partially carved stones and finished or broken beads was retrieved during the archaeological excavation and the examinations have been focused so far on the study of the manufacturing processes [Vidale 2017; Tosi and Piperno 1973]. The majority of lapis lazuli wasters consists in flakes or blocks, followed by fragments with polished surfaces, furrows or pieces with a more regular shape and polished, but not drilled [Tosi and Piperno 1973].

A collaboration with archaeologists from the Universities of Padova and Bologna was started during this PhD, with the aim to deepen the knowledge on raw materials suppliers for Shahr-i Sokhta and to shed light on the incoming trading routes for the hub. First results were obtained applying the provenance protocol and will be disclosed in sections 8.1.2.1/2/3. The 19 lapis lazuli samples sent for analyses from Prof. Massimo Vidale are listed in table 4.3: most of them are fragments of manufacturing waste, but some carved manufacts are also present in the collection. The stone finds were collected from the surface (labelled as “S”) or in two adjacent excavated squares (EWK-EWP, see figure 4.2). Some examples of different shapes can be seen in figure 4.3, together with the most precious piece of the set, a completely cylinder carved seal found on site (sample CS10335/2a). A characteristic that groups together most of the samples is the presence of superficial pyrites very small in size, most of them strongly affected by sulphur loss, probably caused by oxidation reactions; such distinctive features resulted evident already during the preliminary screening with optical microscopy and SEM-EDX. These samples were mainly analysed in AGLAE, due to their archaeological value that required preferably non-invasive techniques and no carbon coating. However, 6 samples from the production waste subset had the approval for the creation of cross sections, so they were embedded in resin and cut to expose the internal part (figure 4.4). In the newly uncovered areas, some unaltered pyrite crystals could be found and were analysed in vacuum at INFN-LNL along with diopside.

.

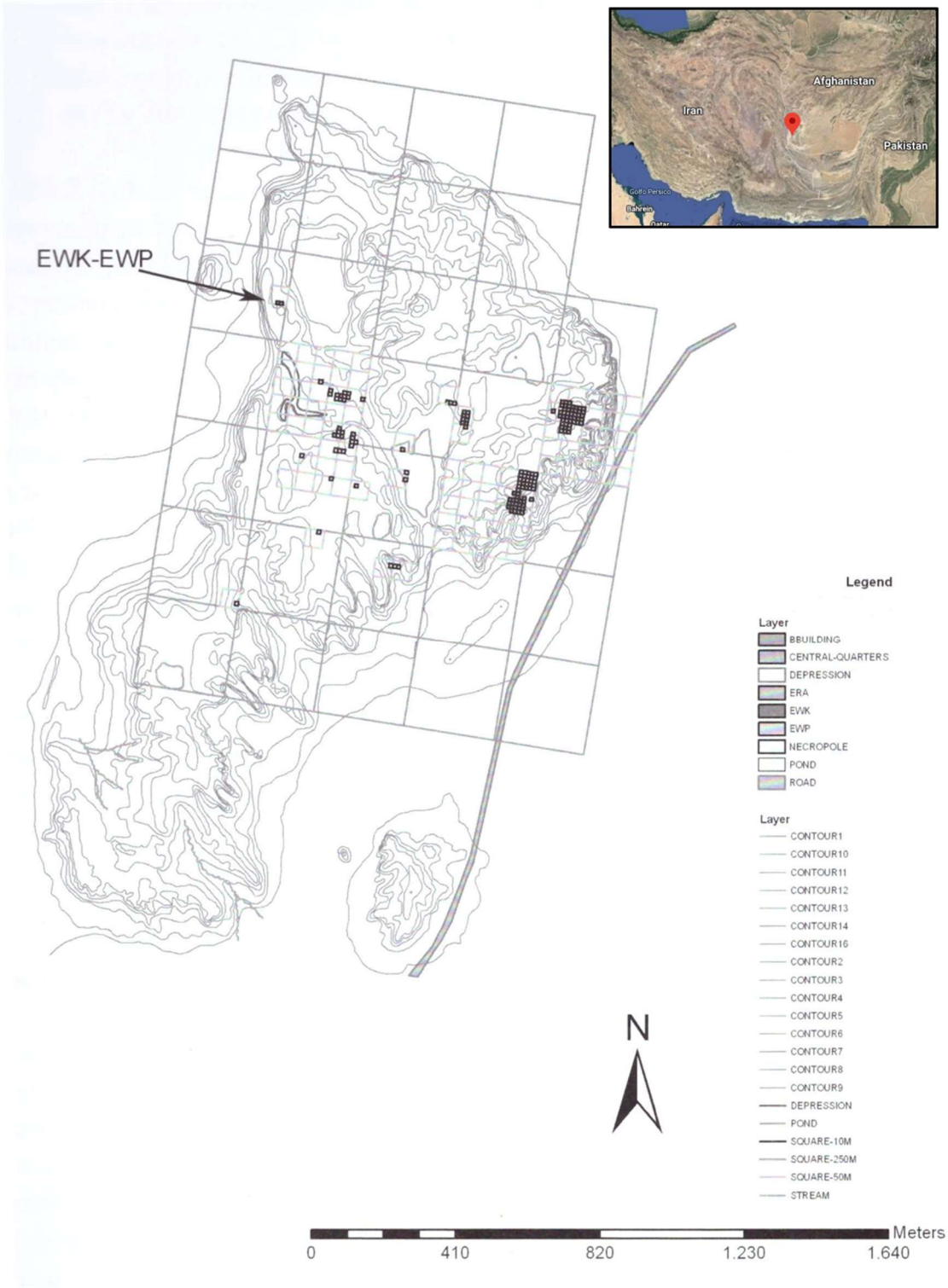

Figure 4.2 Topographic map of Shahr-i Sokhta site with the location of excavation squares EWK-EWP, where lapis lazuli working areas were excavated (from [Vidale 2017]). Location of the archaeological site is reported in the geographical map, top right (©Google).

Table 4.3. Samples from Shahr-i Sokhta analysed at AGLAE and LNL. Short names have been assigned to be used in data analysis.

Sample	Short name	Shape	Facility	Additional Notes
EWK-EWP-178	SiS-178	Rock fragment	AGLAE	
EWK-EWP-180	SiS-180	Rock fragment	AGLAE	
EWK-EWP-181	SiS-181	Rock fragment	AGLAE	
EWK-EWP-186	SiS-186	Rock fragment	AGLAE	
EWK-EWP-187	SiS-187	Rock fragment	AGLAE	
EWK-EWP-205	SiS-205	Partially worked rock	AGLAE	Perfectly flat on one side, shell-like carved decoration on the opposite
AKQ-S-4	SiS-4	Rock fragment	AGLAE	Quite flat
EKQ-S-67	SiS-67	Rock fragment	AGLAE	
EWK-S-324	SiS-324	Rock fragment	AGLAE	
EWK-S-325	SiS-325	Rock fragment	AGLAE	
Raccolta74-331	SiS-331	Rock fragment	AGLAE	Green traces on the surface (Cu oxides?)
Raccolta74-333	SiS-333	Rectangular	AGLAE	Green traces on the surface (Cu oxides?)
CS10335/20a	Seal	Carved and perforated seal	AGLAE	
AKQ-S -28	SiS-28	Rock fragment	AGLAE/LNL	Cross section
RTT-SPP-336	SiS-336	Rock fragment	AGLAE/LNL	Cross section
RTT-SPP-337	SiS-337	Rock fragment	LNL	Cross section
AKQ-S -24	SiS-24	Rock fragment	LNL	Cross section
AKQ-S -44	SiS-44	Rock fragment	LNL	Cross section
AKQ-S -62	SiS-62	Rock fragment	LNL	Cross section

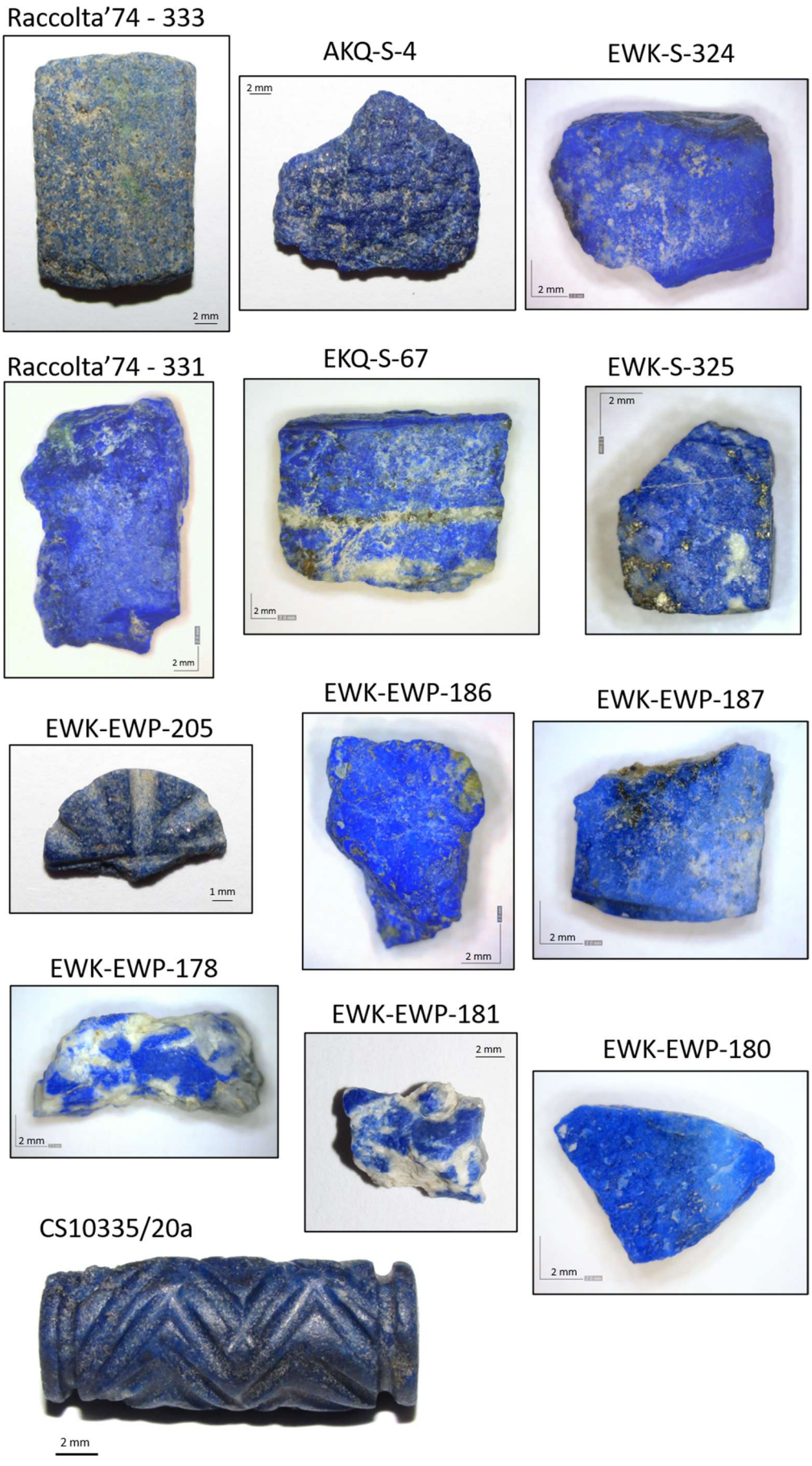

Figure 4.3. The Shahr-i Sokhta lapis lazuli samples analysed as such in AGLAE.

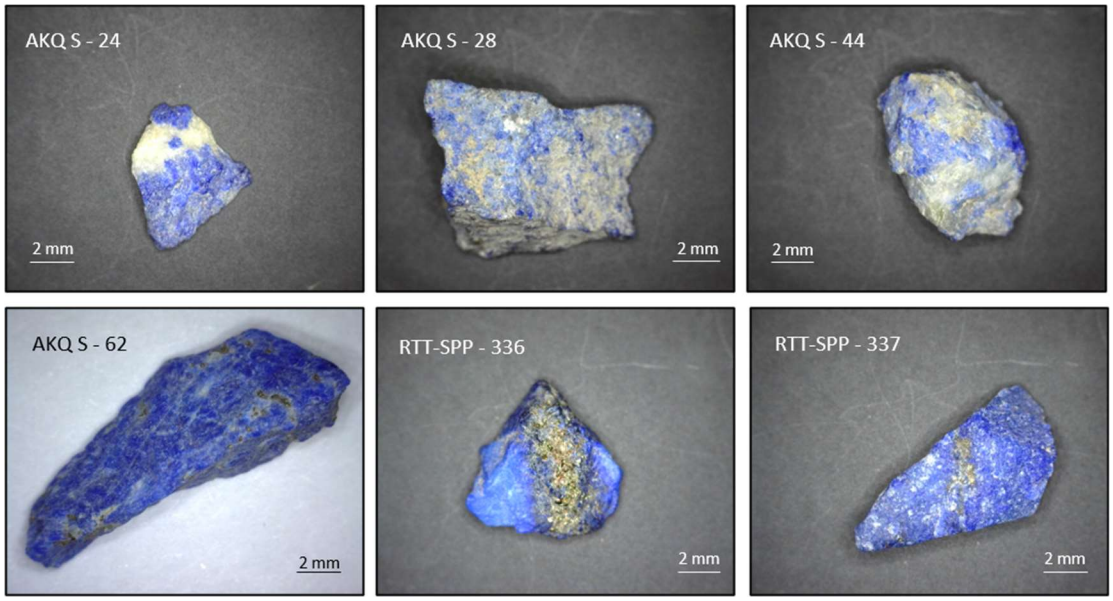

Figure 4.4. The 6 Shahr-i Sokhta lapis lazuli fragments later prepared as cross sections and analysed at INFN-LNL.

4.3. Archaeological samples from Indus Valley sites

The Indus Valley Civilisation (IVC) was a Bronze Age civilisation settled in the north-western regions of South Asia, lasting from 3300 BCE to 1300 BCE [Kenoyer 1997]. One of the three early civilisations of the Near East and South Asia, together with Ancient Egypt and Mesopotamia, it was the most widespread, as its sites span from northeast Afghanistan, through much of Pakistan, and into western and north-western India [Wright 2010]. Harappa and Mohenjo-Daro were the megapolis of the IVC, but other relevant sites developed along the local rivers (Rehman Dheri, Lakhanjo-Daro, Dholavira…) [Dyson 2018; Law 2014; Law 2008]. Within this civilisation, lapis lazuli was known and used together with other stones to manufacture beads as early as 3300 BCE, as proved by some findings in the archaeological sites of Harappa, Pakistan [Kenoyer 1997]. Additionally, Shortughaï is considered the northernmost IVC settlement, a trading post at just few hundreds kilometres from Badakhshan quarries [Kenoyer 1998]. On IVC areas is also located Mehrgarh, the Neolithic site that presented the first evidence of the use of lapis lazuli recorded so far: few small beads unearthed in burials [Jarrige 1991].

In figure 4.5 source sites for the Indus Valley samples analysed in the present work are indicated for an immediate overview. These samples, 5 rock fragments measured in air during the second run at AGLAE (September 2020), listed in table 4.4 and shown in figure 4.6, are part of a lapis lazuli set investigated via Sulphur Isotope Analysis in 2014 by Prof. Randall Law from Wisconsin-Madison University [Law 2014], who kindly provided them for further investigation.

Table 4.4. Summary of Indus Valley samples analysed at AGLAE.

Sample	Origin	Provider	Shape	Parts	Additional Notes
HR-83	Harappa, Pakistan	HARP	Rock fragment	2 (a/b)	
L-Mfrag	Loal Mari, Pakistan	Q. Mallah	Rock fragment	1	
L-Mbead	Loal Mari, Pakistan	Q. Mallah	Bead roughout	1	
L-D	Lakhanjo-daro, Pakistan	Q. Mallah	Rock fragment	1	
SHT-1	Shortughaï, Afghanistan	J-F. Jarrige	Rock fragment	2 (a/b)	Only part b was analysed

4.4. Geological samples from Chagai Hills

In addition to archaeological samples, 4 rock fragments attributed to the Chagai Hills area of western Balochistan Province (Pakistan) were sent for analysis from Dr. Randall Law. Since 1980s, Chagai Hills (precisely at the location called Bi Bi Dick, see figure 4.5) are rumoured to be another potential historical source of lapis lazuli [Law 2014], but no evidence of the existence of a quarry has been produced yet. Chagai Hills had already been the scene of mistaken mineral sources attribution: in 1989 Jean-François Jarrige and Usman Hassan reported the existence of old turquoise mining pits near Dalbandin. Unfortunately, an XRD analysis on a sample locally collected resulted instead as “agatized” chrysocolla, a hydrated copper silicate with a bright blue-green colour impregnated with silica [Law 2008]. The 4 geological samples under analysis in this work are genuine lapis lazuli, confirmed by the characterisation made by Law in 2014. The results of his Sulphur Isotope Analysis showed that it was impossible to discriminate with such technique between Chagai Hills and 7 rock samples from Badakhshan [Law 2014]. Moreover, as indicated in table 4.5, these samples have been provided by different scholars (who got such samples from others) or purchased locally, so the results obtained from Ion Beam Analysis performed in this work can be fundamental not only in discriminating Chagai Hills provenance from other areas, but also – and first of all – to confirm a similarity between these four samples. Results obtained on Chagai Hills samples are discussed in section 8.1.3.

Table 4.5. Summary of Chagai Hills samples analysed at AGLAE.

Sample	Origin	Provider	Shape	Parts	Additional Notes
CH-1	Chagai Hills, Pakistan (?)	Purchased in Quetta	Rock fragment	3	2 out of 3 fragments too small to be analysed by IBA
CH-2	Chagai Hills, Pakistan (?)	J-F. Jarrige *from U. Hassan*	Rock fragment	2 (a/b)	Only part a was analysed
CH-3	Chagai Hills, Pakistan (?)	M. Tosi *from E. Lizzioli*	Rock fragment	2 (a/b)	Only part a was analysed
CH-4	Chagai Hills, Pakistan (?)	M. Tosi *from E. Lizzioli*	Rock fragment	1	

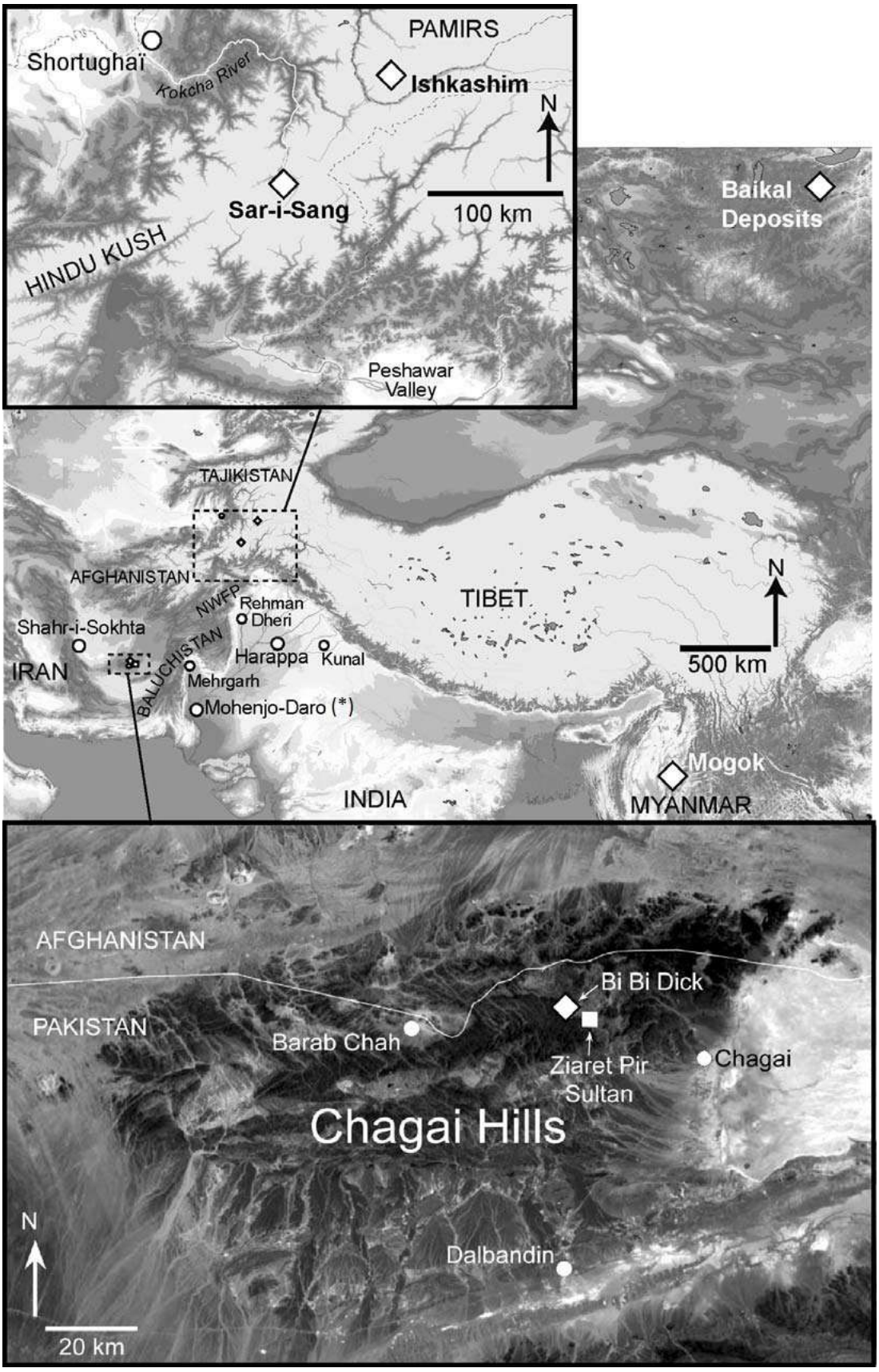

Figure 4.5. Map of Indus Valley archaeological sites and nearby lapis lazuli sources. (*) Loal Mari and Lakhanjo-daro sites are situated on the right bank of Indus river, within a 100 km radius from Mohenjo-daro. Shahr-i Sokhta site is also visible on the far left (modified from [Law 2008]).

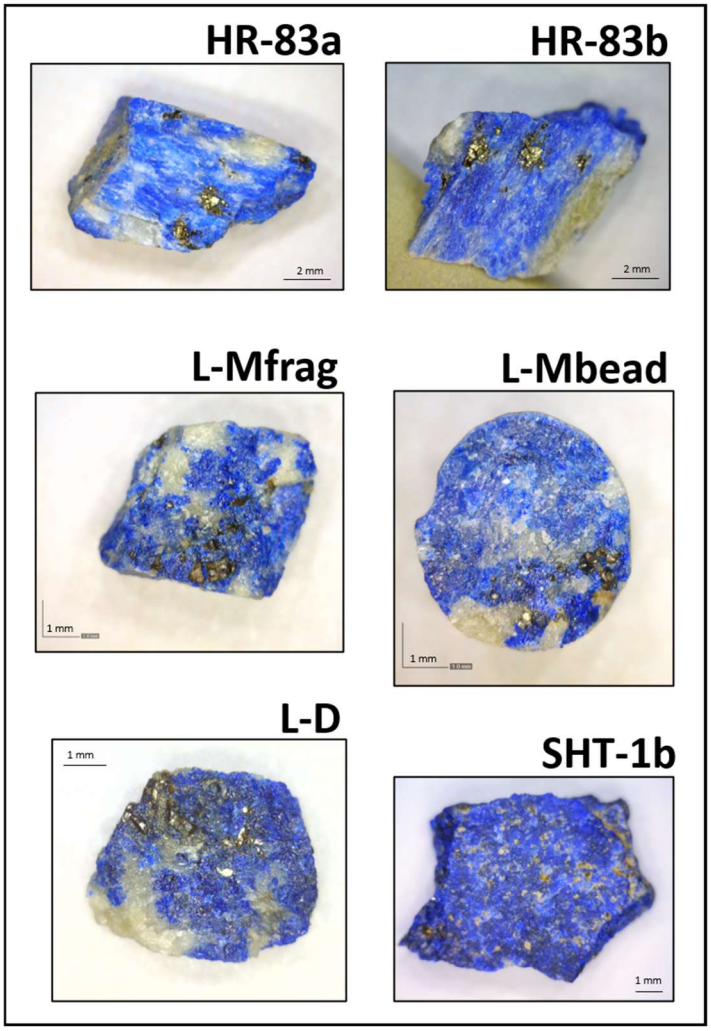

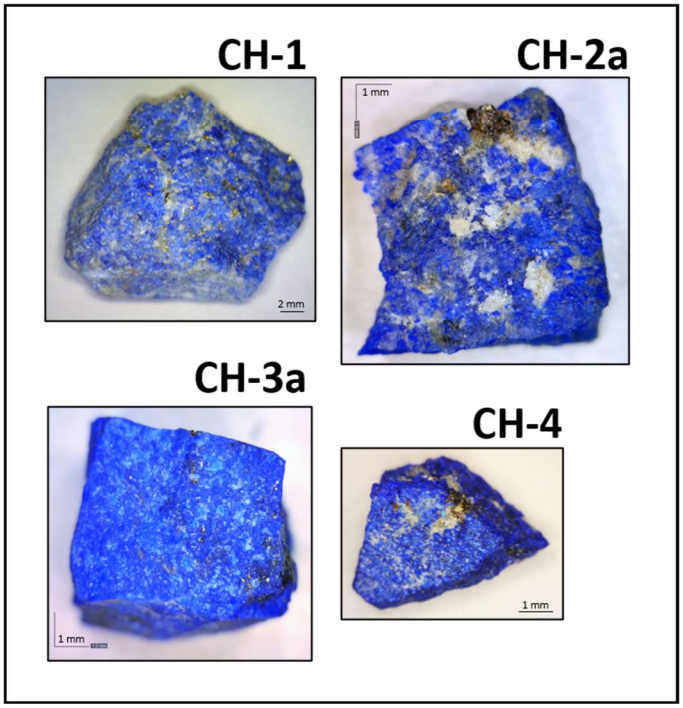

Figure 4.6. The IVC (above) and Chagai Hills (below) lapis lazuli samples analysed as such in AGLAE.

5. Techniques and experimental setup

A brief description of techniques, instrumentation and experimental conditions employed in this work is given in this chapter. Considering the multi-technique approach of the provenance studies on which the diopside luminescence characterization is implanted, a large number of complementary techniques (both bench-top type and large scale facilities) have been used to obtain the widest characterisation possible of lapis lazuli samples.

5.1. Optical microscopy

For preliminary observations of the mineralogical and textural features of the samples, as well as of the condition state of the surface layer for archaeological objects (e.g. presence of alterations), a Dino-lite Pro AM413ZTA optical microscope was used. This instrument works in reflective mode with self-provided LED illumination and a magnification of 220× can be reached. Moreover, the additional polarizer allows to control reflection and glare arising from polished surfaces or translucent minerals. The microscope can be used in direct contact with the surface or with the aid of a one-arm stand.

5.2. Cold-CL (cold cathodoluminescence)

Cathodoluminescence (CL) is the emission of photons in the UV-VIS-NIR range from a target hit by an electron beam. This technique finds frequent employment in the geological field, but can be as well used in the art market for the authentication of gems, such as yellow diamonds [Kitawaki et al. 2008], or in provenance studies for gems and stones [Wielgosz-Rondolino et al. 2020; Kuchařová et al. 2016]. Different minerals can show different CL colours, as the intrinsic luminescence is caused by their crystallographic structure (see chapter 3). Hence, with this technique the distribution of the different mineral phases in lapis lazuli can easily be observed, achieving the discrimination of minerals that under visible light appear similar (e.g. diopside and calcite) and need to be discerned for subsequent analyses.

A typical cold-CL apparatus consist of an electron source (the cold-cathode) and a microscope equipped with a CCD camera for image acquisition. The electron beam is defocused and shot on the sample from a lateral angle, generating an elliptical analysed area of about 1 cm^2.

The cold-CL setup used in this work, hosted at the Earth Science Department of the University of Torino, is shown in Figure 5.1. A “CITL Cold Cathode Luminescence 8200 mk3” instrument is equipped with a polarized optical microscope Olympus BH2 and a CCD camera Olympus E1 (5 Mpixel). The samples are placed in a vacuum chamber with a transparent window and the pressure is maintained at about 0.8 mbar.

Figure 5.1. The cold-CL apparatus in use at the Earth Science Department of the University of Torino.

At this stage sample coating is not necessary, because the working pressure is high enough to avoid charging effects. However, only petrographic thin sections or cross sections of lapis lazuli can be investigated with this setup, due to the geometry of the chamber and of the sample holder. Employed accelerating voltage and current were 15 kV and 500 µA respectively. Since most constitutive minerals of lapis lazuli show an intense luminescence in the visible wavelengths, the necessary acquisition time using standard camera conditions ranges from only 1 s to 20 s. The total magnification is 10×, due to the microscope objective (4×) and a removable lens (2.5×). The complete mapping of the whole section can be performed by moving the sample by means of two micro-translators on a X-Y plane.

5.3. SEM-EDX (Scanning Electron Microscope with Energy Dispersive X-ray Spectrometry)

As last step for mineral characterisation under a compositional point of view, all kinds of samples (thick sections, cross-sections and as such) were analysed by means of Scanning Electron Microscope combined with an Energy Dispersive X-ray spectrometer (SEM-EDX). The interaction of a focused keV electron beam with matter generates the emission of several types of signal. The most common events and mostly used for investigation are backscattered and secondary electrons, characteristic X-rays and luminescence. Images are produced by scanning the beam on the surface and choosing the appropriate detector mode: the microstructure of the rock samples can be revealed by backscattered electrons images, whereas the characteristic X-rays allows to confirm the nature of the mineral phases, carrying out as well quantitative elemental analyses. It is worth stressing that the detection limit for this technique in high vacuum conditions is about 0.1 wt%, mainly due to the continuous Brehmsstralhung background, hence lacking the sensitivity for trace element analysis [Angelici 2015].

SEM-EDX analyses on thick sections were carried out in previous works [Angelici 2015] using a Cambridge Stereoscan S-360, equipped with a SDD energy-dispersive spectrometer (INCA X-act, Oxford Instruments), installed at the Earth Science Department of the University of Torino. An accelerating voltage of 15 kV and a dwell time of 60 s were used as common experimental parameters for all the measurements. Natural silicates and oxides (SPI Mineral and Metal standards) were chosen as standards and a ZAF data reduction program was used (within INCA Microanalysis Suite Oxford software package) for determining the chemical composition of major elements. This SEM has been replaced in the last years with a JEOL JSM-IT300LV equipped with Tungsten filament cathode, maintaining the same EDX system and operative conditions. A cobalt standard is generally analysed for correction and calibration of EDX acquired spectra both in energy and in intensity. With this setup, Shahr-i Sokhta samples cut in cross section were analysed under high vacuum conditions.

In addition, archaeological samples from Shahr-i Sokhta, uncut and unpolished, have been analysed at variable pressure (50 Pa) with a Zeiss EVO 60 Scanning Electron Microscope equipped with a LaB_6 filament and a Bruker Quantax 200 EDX microprobe, setting a voltage of 20 kV. The instrument is hosted in the scientific laboratories of the Centro Conservazione e Restauro “La Venaria Reale” in Venaria Reale, Torino (Italy). It has to be highlighted that at low pressures quantitative analyses cannot be performed; investigations with the Zeiss instrument were then limited to the recognition of mineralogical phases based on main elements presence.

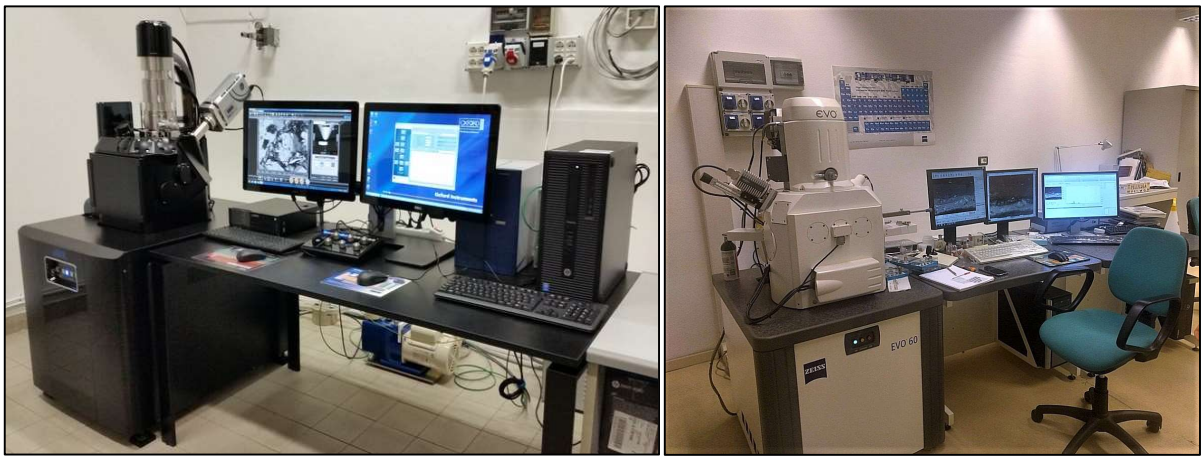

Figure 5.2. *Left*: The new JEOL JSM-IT300LV in use at the Earth Science Department of University of Torino. *Right*: the Zeiss EVO 60 hosted at the CCR "La Venaria Reale".

5.4. SEM-WDX (Scanning Electron Microscope with Wavelength Dispersive X-ray Spectrometry)

The sensitivity needed for trace element quantification can be reached in a SEM setup employing a different X-ray spectrometer. Wavelength-dispersive (WD) spectrometers are distinguished from the energy dispersive (ED) type by the fact that the X-rays are 'dispersed' according to their wavelength by means of Bragg diffraction, following the relation:

$$n\lambda = 2dsin\theta \qquad (5.1)$$

where *n* is a positive integer, λ is the wavelength of the incident radiation, *d* is the distance between two crystallographic planes and θ is the angle between the exciting radiation beam and the plane. Several analysing crystals of different spacings *d* are therefore needed in order to cover the whole range of wavelengths of interest; the most common are LiF, PET and TAP. There is a complementarity between WD and ED spectrometers, as the formers give high spectral resolution but generally lower intensity for a given beam current than the latters [Reed 2005]. However, with WD spectrometers there is more scope for increasing count-rates by increasing the beam current, as the limitation of maximum count-rate on the whole spectrum encountered with ED spectrometers is absent. Also, the typical values of peak-to-background ratio obtained with WD spectrometers range from a few hundred to over 1000 (for pure

elements) and are approximately a factor of ten higher than for ED spectrometers, resulting in lower elemental detection limits [Reed 2005].

Some tests on thick sections for trace elements identification were carried out in Japan with an electron probe micro-analyser equipped with four WD spectrometers (JEOL JXA-8230) and located at the Earth Sciences Department of Okayama University (figure 5.3). Specifically, two of the installed crystals are TAP type, one is PETJ and the fourth is LiF. Quantitative analyses were carried out with an accelerating voltage of 20 kV and a probe current of 200 nA. Probe diameter was 5 µm, allowing to select a single spot inside the chosen crystal. Standards used for calibration were natural or synthetic oxides and silicates and ZAF matrix correction was applied.

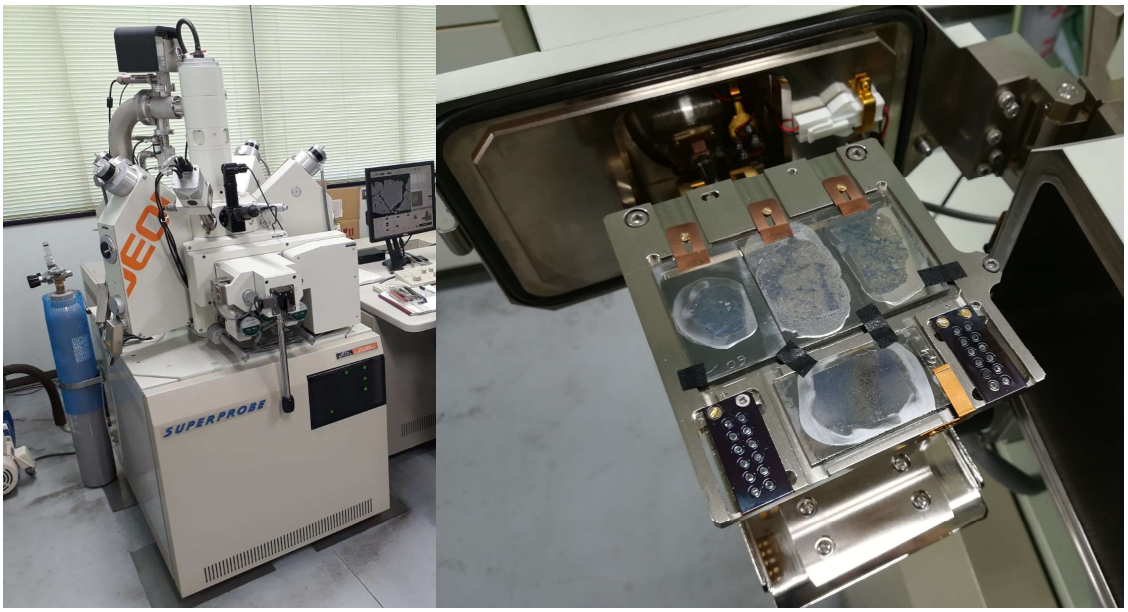

Figure 5.3. The JEOL JXA-8230 in use at the Earth Science Department of Okayama University. Sample holder on the right shows the analysed lapis lazuli thick sections together with the reference mineral standards.

5.5. Ion beam microprobe facilities

Trace elements analyses were primarily carried out by means of micro-Particle Induced X-ray Emission (µ-PIXE), the most common among Ion Beam Analyses (IBA), in accordance with the provenance protocol explained in section 2.3.1. This technique is based on the detection of emitted characteristic X-rays using as excitation source a beam of accelerated particles, most often protons. The output is then a spectrum in an energy range up to 20 keV, that can be properly fitted to retrieve quantitative information on specific

elements. Moreover, to study the luminescence features of the single minerals in a non-invasive way, micro-Ionoluminescence (μ-IL) analyses were performed simultaneously to μ-PIXE and exploiting the exact same probe. IL offers a higher detail in characterising the material than CL: the probe energy range is higher (MeV instead of keV), entailing a deeper region of analysis and a higher sensitivity [Corazza et al. 2001]. On the other hand, radiation damage effects on the sample can be more significant and have to be taken in consideration. μ-IL analyses have been performed in this study for the characterisation of one single mineral phase: diopside.

IBA were performed at different national and international facilities, depending on the assigned beamtime periods and on the particular needs of the work (analysis of rock samples rather than precious artefacts). In the next paragraphs a description for each facility is given and the experimental conditions are summarised and compared in table 5.1 at the end of the section.

5.5.1. INFN-LNL

Legnaro National Laboratories (LNL) is one of the big facilities of the Italian National Institute of Nuclear Physics (INFN), where four accelerating machines of different potentialities are currently in operation. The accelerator employed for IBA within this work was the AN2000, specifically dedicated to ion beam-based interdisciplinary research [Forneris et al. 2014; Lo Giudice et al. 2017; Battiato et al. 2016; Picollo et al. 2016]. The AN2000 consists in an electrostatic Van de Graaff accelerator with a single stage-belt charging system and a maximum working voltage of 2.5 MV. Obtainable accelerated ions are single-charged ^{1}H and ^{4}He. Among the five beam lines available, the 0° micro-beam line was used to perform μ-PIXE experiments; in the same analytical chamber the μ-IL setup can be installed (figure 5.4). The microprobe line is based on Oxford instrumentation and measurements are taken in vacuum (ca. 10^{-5} mbar). One optical microscope is available for sample positioning in the analytical chamber. The μ-beam is able to raster scan across the sample surface thanks to the Oxford Microbeam system, which is also controlling the μ-PIXE acquisition through OM-DAQ software.

A remote control allows to move the sample holder along three directions and also to rotate it, so the sample can be easily positioned and oriented with respect to the beam direction. Typical beam spot diameter is around 4-6 μm and the scanned area ranges from around 30×30 μm^2 to 2000×2000 μm^2. The PIXE detector installed is a hyper-pure Ge Ortec IGLET-X, positioned at 45° with respect to the ion beam. To simultaneously analyse light and heavy elements with the same detector, an Al funny filter is used [Gama et al. 2001]: this is a filter with a hole drilled at its centre and placed in front of the detector window. When a sample is in the chamber, the ion current is measured directly on the sample holder, integrating the charge deposited on the sample during the whole run. In the empty chamber, it is instead

possible to check the stability of the beam when it can reach directly the Faraday cup on the other side of the sample holder. Spectra analysis is carried out through the GUPIXWIN software (version 2.2.3) [Campbell et al. 2010] and to evaluate the H-value curve a set of reference mineral standards (SPI #02753-AB Mineral and Metal standards) was used. H is the calibration factor used to convert peak areas from the spectra to concentration values, and can be provided to the software as a constant or as energy-dependent.

The μ-IL apparatus set in the vacuum chamber of the microprobe facility was introduced in 2011 by our group. The photon emission induced by ion bombardment is collected through an Ocean Optics collimating lens that gathers the signal with an angle of 45° with respect to the beam direction. A system of optical fibres leads the light emitted from the sample to an Ocean Optics spectrometer. Two different spectrometers have been used for acquisition during this decade: an Ocean Optics USB4000 and an Ocean Optics QE Pro. The latter has a larger bandwidth (300-1000 nm) and is Peltier cooled, granting a better signal to noise ratio. With both detectors the spectra have been corrected in intensity in respect to the instrumental efficiency. The advantages of this setup is the possibility to acquire simultaneously PIXE and IL spectra on the same sample and in particular for the same point of analysis; therefore, the information obtainable is relative both to structure and elemental composition of the investigated material, and allows to move scrupulously onto activation and quenching studies.

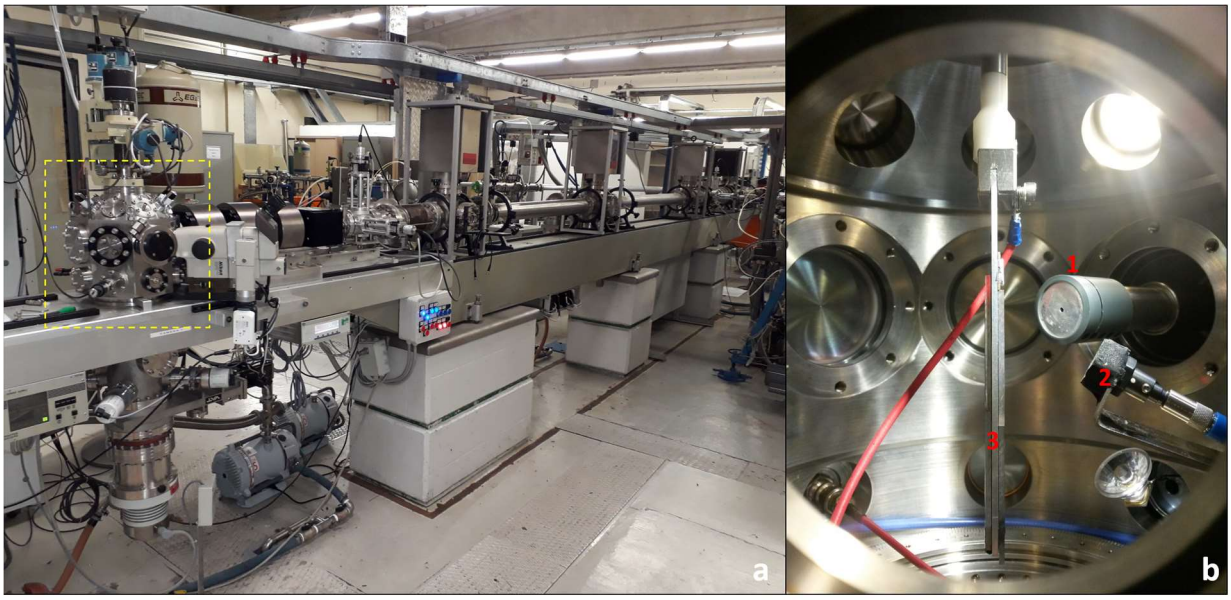

Figure 5.4. INFN-LNL facility. (a) The microbeam line: the analytical chamber is highlighted in yellow. (b) Inside the analytical chamber: (1) PIXE SDD detector with Al funny filter; (2) collimating lens for μ-IL signal; (3) sample holder. Charge on the samples is measured via the red wire.

5.5.2. NewAGLAE

Simultaneous IBA is performed also in other international facilities. During this PhD, I was granted, via European programmes IPERION CH and IPERION HS, two slots of beamtime (June 2019 and September 2020) at the ion accelerator NewAGLAE (New Accélerateur Grand Louvre d'Analyse Elémentaire, referred to simply as AGLAE in the following sections) for my personal project SIBILLA ("Simultaneous Ion Beam Investigations for Lapis Lazuli provenance Analysis"). The first version of AGLAE was installed in 1988 in the conservation and scientific laboratories of the C2RMF (Centre de Recherche et de Restauration des Musées de France) under the Louvre Museum, with the main purpose of applying of nuclear analytical techniques in the field of cultural heritage.

This facility consists in an extracted micro-beam line and measurements are performed in air instead of in vacuum. AGLAE is a 2MV Pelletron 6SDH-2 electrostatic tandem accelerator. It is equipped with two sources to produce the beam: available accelerated ions are single charged ^{1}H up to 4 MeV and ^{1}He, ^{2}He, ^{3}He and ^{4}He up to 6 MeV. The typical beam spot dimension is about 25-50 µm. The facility and particularly its external beam line underwent various improvements and upgrades during the last fifteen years and the new setup is well described in [Pichon et al. 2014]. As part of the Equipex NewAGLAE project, developed with the support of the city of Paris, the acquisition system of the extracted beam line has been profoundly modified from analogical signal processing to digital processing. This new system (Figure 5.5) allows the rapid acquisition of elemental and luminescence maps and is continuously optimised, in particular on the µ-IL setup.

The µ-PIXE setup relies now on a set of four SDD detectors: a detector called LE0, placed at 45° relative to the beam axis, is dedicated to the measurement of low energy X-rays (1-10 keV); the other three SDD detectors (HE1, HE2, HE3), screened with 100 µm mylar absorbers and positioned with a 50° relative angle to the beam axis, are dedicated to measure high energy X-rays (>3 keV), increasing the statistics on the detection of trace elements. Helium is fluxed in front of the LE0 detector to improve the detection efficiency of low energy X-rays, reducing their absorption from air components. The charge is monitored by recording silicon X-rays emitted by the Si_3N_4 100 nm thick exit window with a dedicated SDD detector. Using the mechanical scanning mode acquisition it is possible to combine a vertical magnetic scanning of the beam ("pen") with an horizontal target translation for the fast acquisition of elemental maps and corresponding spectra. The pen size is selectable from 50 µm to 1 mm: in this work it was used equal to 250 µm.

The IL setup consists in a 1 mm diameter optical fibre placed at 45° angle with respect to the beam direction, that collects the light and leads it to a research grade Ocean Optics QE65000 spectrometer[4] recording from 200 to 1000 nm with a resolution of 3 nm FWHM (with a 100 µm entrance slit) [Pichon et al. 2015a].

The great advantage of this system mainly consists in the simultaneous acquisition of PIXE and IL 2D information (both spectra and maps), that can be handled after acquisition with the homemade software AGLAEMap [Pichon et al. 2015b], extensively described in the following chapter. Also, the IL fixed setup should allow to overcome some issues in spectra intensity comparison, described in chapter 6. Particle Induced Gamma-ray Emission (PIGE) and Rutherford Backscattered Spectrometry (RBS) data are also collected, but have not been exploited for the purposes of this study. The quantitative elemental analysis is performed instead via TRAUPIXE [Pichon et al. 2015b], a custom-made software based on the aforementioned GUPIXWIN, that can combine low and high energy PIXE spectra using a single element as pivot. Classic standards used for calibration in this facility are Diorite (DrN, Service d'Analyse des Roches et des Minéraux), Granite (MA-N, Group International de Travail "Etalons Analytiques des Mineraux, Minerais et Roches") and Phlogopite (Mica-Mg, Centre de Recherche Petrographiques et Geochimiques) in powder, all of them rich in numerous different elements.

[4] A change of spectrometer occurred during the 2020 measuring session and its implications are discussed in chapter 6.

Table 5.1. Summary and comparison of the specifics for Ion Beam Analysis facilities used for lapis lazuli analysis in this work; (a) and (b) reflect the change in spectrometer equipment.
* Penetration ranges of the ion beam in analysed mineral phases, calculated with SRIM software [Ziegler 2010].

		FACILITIES	
		INFN-LNL	AGLAE
General features	Location	Legnaro (PD), Italy	Paris, France
	Measurement type	in vacuum	in air
	Beam energy	2 MeV	3 MeV
	Beam size	~ 5 µm	~ 25-30 µm
	Average beam current	200 pA	500 pA
	Max scanned area	2×2 mm^2	4×5 mm^2
µ-PIXE experimental conditions	Detector	1 HPGe	4 SDD (1 LE and 3 HE)
	Absorbers	Al funny filter	Mylar (100 µm)
	Acquisition software	OM-DAQ	AGLAEMap
	Standard(s)	SPI#02753-AB (various minerals)	DrN (diorite) MA-N (granite) Mica-Mg (phlogopite)
µ-IL experimental conditions	Collimating lens	74-UV (200-2000 nm)	-
	Optical fibre	1QP600-UV-VIS + P600-025-UV-VIS Ø=600 µm	QP1000-2-SR Ø=1 mm
	Spectrometer	[a]Ocean Optics USB2000 [b]Ocean Optics QE Pro	Ocean Optics QE65000
	Bandwidth	[a]350-900 nm [b]300-1000 nm	200-1000 nm
	Acquisition software	[a]OO Spectra Suite [b]OO OceanView	AGLAEMap
R values*	Diopside (density = 3.3 g/cm^3)	30 µm	60 µm
	Pyrite (density = 5 g/cm^3)	25 µm	48 µm

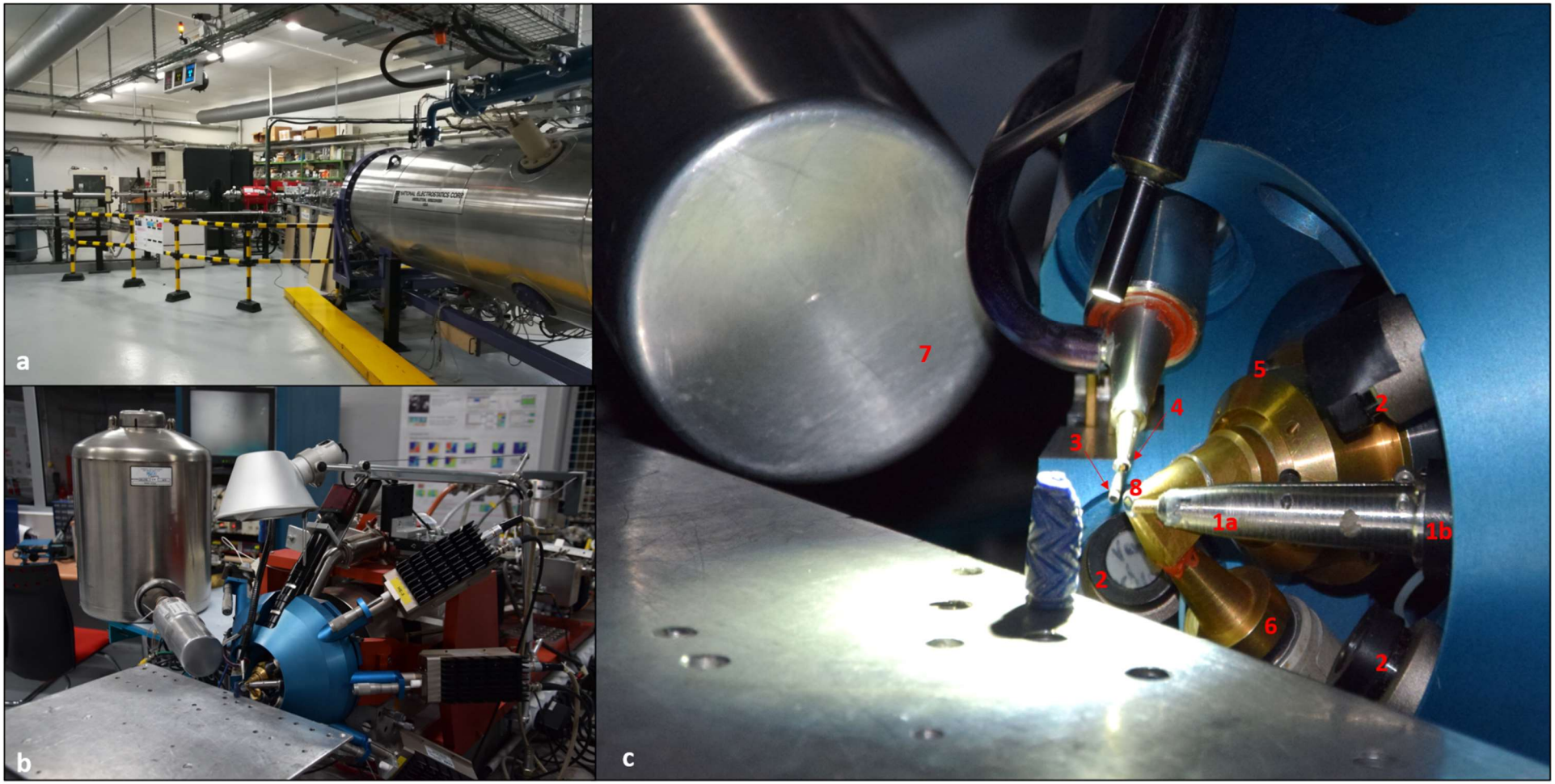

Figure 5.5. NewAGLAE facility. (a) The Pelletron accelerator and the microbeam line; (b) view of the NewAGLAE external beamline setup; (c) zoom on the setup during the measurements on one of our samples. Setup specifics: (1a) He flux magnetic nozzle connected to (1b) low energy SDD detector; (2) three high energy SDD detectors; (3) optical fibre; (4) external RBS detector; (5) annular RBS detector; (6) SDD dose detector; (7) HP-Ge Gamma-rays detector; (8) Si_3N_4 exit window.

6. IBA: methodology, data evaluation and issues

The analytical approach employed in the work for Ion Beam Analysis is here explained in detail, as it can be decisive in the critical evaluation of the results. Firstly, the adopted acquisition methodology for IBA in the different facilities is explained, together with the description of software used for performing a quantitative elemental analysis. The second aspect covered in this chapter is the initial evaluation that allows a screening for good data to be considered for provenance determination and luminescence features. Also, the fitting method for ionoluminescence spectra is briefly explained.
Last but not least, some instrumentation issues encountered during the data collection are presented, together with the strategies adopted to overcome them.

6.1. IBA acquisition methodology

After the preliminary characterisation described in section 2.3.1, the target crystals are analysed with an ion beam. Target crystals are generally chosen to be at least 100 μm in diameter, to ensure the presence of a homogeneous mineral phase also along *z* axis for the whole beam penetration range.
At INFN-LNL the crystals are found with the aim of an optical microscope installed in the analytical chamber and of large PIXE maps quickly acquired to have a general overview of the area. Shapes and composition of the various crystals help in the search for the target. Since the probe dimension can go down to about 5 μm, the final beam scan is generally limited to the core of the crystal of interest and the acquired area has a fixed dimension of 30 × 30 μm^2. Over this area the acquisition time is about 1 hour long, to have sufficient counting statistics for the identification of trace elements. During such a long irradiation on the same area, changes in the structural state of the crystal might occur, inducing a luminescence decay: for this reason, only the first acquired μ-IL spectra, the ones with higher intensity, are taken into account for each measurement. The PIXE spectra are then directly processed via GUPIXWIN software (version 2.2.3) [Campbell et al. 2010] for the quantification of major, minor and trace elements. Calibration for the quantification process is obtained by measuring reference mineral standards and finding in this way the H values (see section 5.5.1) for the energy range of interest. An example of energy dependent H-value curves for different target mineral phases is shown in figure 6.1. Reference standards are chosen on the basis of the elements to be quantified: natural minerals employed as standards for diopside and pyrite are listed in table 6.1. GUPIXWIN allows to insert all the acquisition parameters before the quantification, such as complete detector information, incident angle of the beam and respective

position of the detector, energy of the protons and all the filters interposed in front of the detector. Additionally, it can be specified the fixed or iterated matrix solution[5] mode, the elements chosen for quantification and the spectrum fitting parameters. In this work the elemental concentrations have always been normalised to a 100% total. GUPIXWIN output consists in concentration and limit of detection (LOD) in ppm (derived by peaks fitted areas) for each selected elements, the percentage of fit error and a decision label as to the presence of that element in the spectrum: "Y" if the element is present in amounts larger than one sigma above the quantization limit; "N" if it is more than one sigma below the LOD level; "?" if the reported value is somewhere between one sigma below the LOD value and one sigma above the quantization limit. It is up to the user to decide if accepting or rejecting the dubious detected value, depending on the specific case.

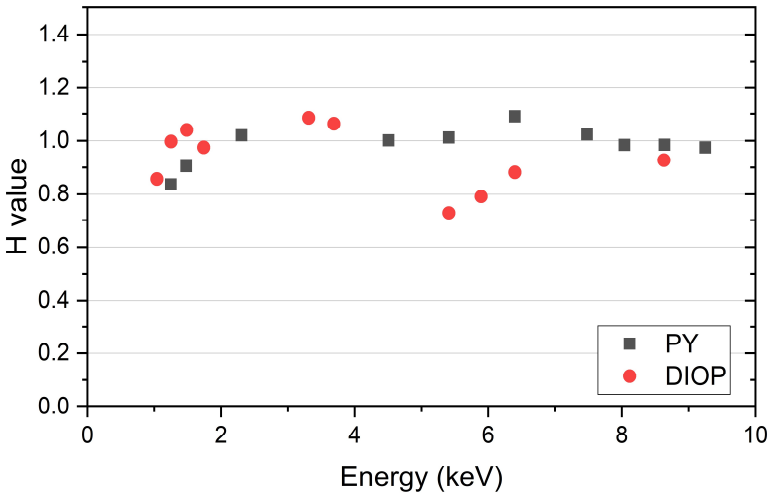

Figure 6.1. Energy dependent H values obtained from standards and used in GUPIXWIN for INFN-LNL pyrite and diopside data.

Table 6.1. All mineral standards used in GUPIXWIN calibration for diopside and pyrite analyses.

DIOPSIDE	PYRITE
Diopside	Marcasite
Cr-diopside	Galena
Sanidine	Rutile
Cobaltite	Haematite
Celestite	Magnetite
Apatite	Barite
Barite	Sphalerite
	Bismuth Selenide
	Gallium Arsenide
	Cubic Zirconia
	Nickel Silicide
	Chromite
	Cuprite
	Celestite

At AGLAE the only aid for target crystal recognition is a digital camera. The methodology adopted here is then the acquisition of a larger map that surrounds the whole crystal, and the inner part is then isolated afterwards with AGLAEMAP dedicated software [Pichon et al. 2015b]. The map is generally acquired on a 500 × 500 μm^2 area, with a pixel size of 25 µm (roughly the beam size): when larger maps are acquired instead, the dose is increased to maintain the same *dose per pixel* ratio. Data from all detectors is saved in an EDF file. A schematic explanation of AGLAEMAP interface is presented in figure 6.2. Elemental mapping is achieved by selecting a region of interest in the spectra and the corresponding picture can be saved. Also, a specific area can be drawn directly on the map or selected by

[5] Fixed matrix is the simplest case for trace elements calculation, as the composition of the target matrix is already known. If the major elements concentrations are not known *a priori*, these will be instead iterated by the program if provided with a list of element (both visible and invisible to the technique).

intensity range; counts are summed to create a total spectrum. This is used in our case to select only the target crystal information. Afterwards, spectra of selected pixels from all detectors can be saved in GUPIXWIN format. The same process can be applied for ionoluminescence information: in this case the normalisation is achieved by dividing each cumulative spectrum by the number of pixels in the selection. Standards used for μ-PIXE calibration at AGLAE are listed in section 5.5.2. Since at AGLAE different SDD detectors work together, the custom-made TRAUPIXE software [Pichon et al. 2015b] allows with a user-friendly interface to join the spectra acquired from low energy and high energy detectors using the pivot element procedure, and hence obtaining a univocal elemental composition for the selected area. The pivot is usually an element whose peak has strong intensity in both energy ranges. For the specific mineralogical phases studied in this work, diopside spectra requires Ca (Z=20) as pivot, whereas Fe (Z=26)

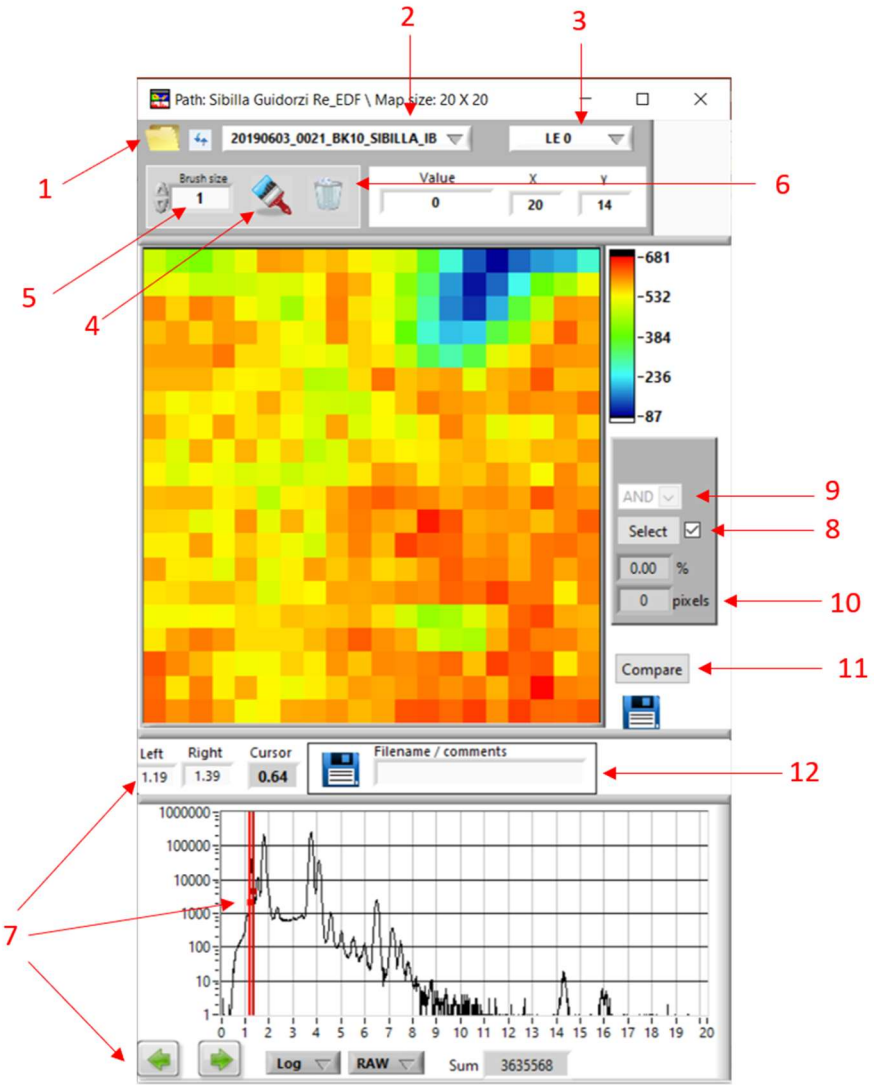

Figure 6.2. Overview of AGLAEMAP interface: (1) folder, (2) EDF file and (3) detector selection, (4) hand-selection tool for pixels with (5) variable size and (6) delete options, (7) tools for selecting the elemental peak of interest, (8)(9) tools for pixel selection based on intensity ranges, (10) number of pixels in the selection (if present), (11) compare images button, (12) spectra final extraction.

is used for pyrite. After this process, the output is exactly similar to the one obtained at INFN-LNL and it is possible to compare the results, as the concentration is in both cases normalised to 100%.

6.2. Preliminary data screening and treatment

The quantitative analysis on AGLAE μ-PIXE data performed via TRAUPIXE allows also an iterative refinement of the area selected in AGLAEMAP, on the basis of stoichiometry abidance for major elements and of the absence or limited presence of extrinsic elements not pertaining the mineralogical phase under investigation. For diopside, accepted ranges of concentration are reported in table 6.2. For pyrite, both the absolute concentration (50.2 ± 2.2 wt% for S and 45.6 ± 2.2 wt% for Fe) and the ratio of S and Fe (1.08 ± 0.10) are considered. Crystals that do not respect these constraints, that have most probably undergone an alteration or contamination process or were not big enough for IBA analysis, are hence discarded before further evaluation of the results.

Table 6.2. Accepted ranges of concentration for major and minor elements in diopside.

Element	*Conc. ranges (wt%)*
Mg	8.5 - 11.0
Si	25.0 - 27.0
Ca	13.5 - 17.0
Al	< 3.0
P, S, Cl, K	< 0.3

Moreover, μ-IL spectra for diopside crystals had to be deconvoluted and fitted for the study of luminescence activation and quenching from a quantitative point of view. Before proceeding with the multiple fit for this purpose, the wavelength (λ) has to be converted in energy (E) with the formula:

$$E(eV) = \frac{1239.8}{\lambda(nm)} \tag{6.1}$$

Then, as a first approximation, a sum of Gaussian curves is used to fit each spectrum: an example is shown in figure 6.3. The number of curves *n* may vary from 2 to 5, depending on spectrum features. A constant baseline is subtracted before fitting, considering the minimum *y* value. The formula used for the fit is then:

$$y = \sum_{i=1}^{n} \frac{A_i}{w_i\sqrt{\pi/2}}\ e^{-2\frac{(x-x_i)^2}{w_i^2}} \tag{6.2}$$

where x_i is the central position of the band, w_i its width and A_i its area. Luminescence features are represented quite well in this way and, despite some minor difference between original and cumulative fit spectra, the R^2 value for all the fits settled at 0.996 ± 0.002 and the fit error on the area quantification is generally below 0.05% .

6.3. Measuring issues

The first issue encountered when approaching the luminescence activation and quenching study derives from the fact that the amount of luminescent radiation recorded by an IL instrumentation strongly depends on the orientation of the collective system. This implicated the impossibility to compare intensities (i.e. peak areas) for spectra acquired during different measuring runs at INFN-LNL, considering that the μ-IL setup is installed and removed every time and the collective lens might have a slightly different angle. The SIBILLA project (section 5.5.2) was created precisely to overcome this problem, exploiting the fixed μ-IL setup of AGLAE facility to reanalyse reference geological samples and to be able to compare them even over different measuring runs. The project was granted two beamtime session during this PhD. However, due to technical problems and delays in the reparation, the usual spectrometer of the setup (Ocean Optics QE6500) had to be replaced during our second measuring run in 2020; this led to an issue on the calibration of spectra between measurement sessions. Calibration in wavelength between the two spectrometers was easily achieved using as reference the spectrum of He-rich air, measured without samples in front of the beam: numerous and thin peaks are in fact spread along the whole wavelength range (figure 6.4). As regards intensity, a calibration was attempted using as standard the light from a reference light source (Ocean Optics HL-2000-HP-FHSA) reflected on an absolute reflectance standard (Labsphere). However, when the calibration curve obtained in this way for the 2020 spectrometer (an Ocean Optics QEPro) was applied to the spectra, the resulting signal had lost most of the band information for wavelengths above 600 nm. Considering the importance of the band positions for provenance purposes, another approach was chosen, building instead a conversion curve with the comparison of spectra obtained during the two different runs from the same crystals in reference geological lapis lazuli samples. With this method, the information on band and peaks positioning was preserved. Nevertheless, due to the general heterogeneity of the measured crystals, it is possible that the area acquired in the two different session was not exactly the same: hence, it was preferred to exclude the spectra acquired in 2020 from the quantitative analysis for the activation/quenching study.

Lastly, some considerations on PIXE detectors have to be reported. The HPGe used at INFN-LNL in the last few years started presenting a real detector resolution slightly exceeding the nominal one (190-200 eV *vs* 160 eV). This resulted as a first effect in the increase of the LOD values. To avoid incurring in mistakes for the presence/absence decision of dubious assignations made by GUPIXWIN, such values are accepted only if by subtracting two sigmas to the concentration, the obtained value is still above LOD. Moreover, as the quantification problem caused by peak broadening seemed to be more relevant for lighter elements, in some cases the fixed matrix solution approach was used in GUPIXWIN, using the concentration for major elements retrieved by SEM-EDX.

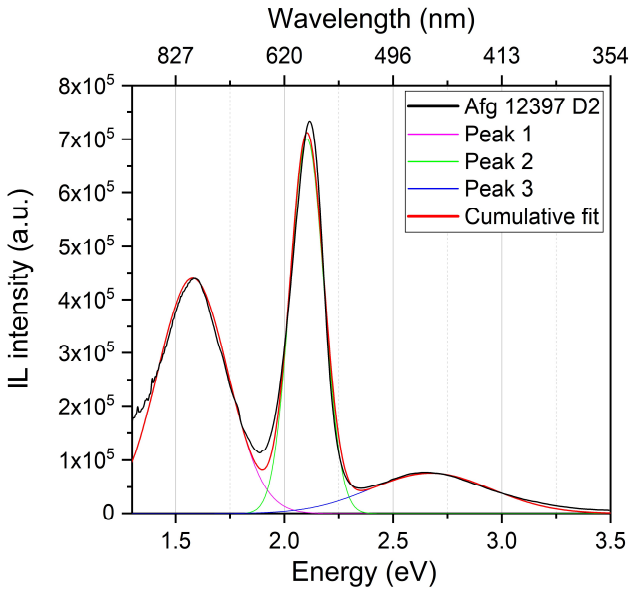

Figure 6.3. Fitting of µ-IL spectrum acquired from diopside D2 in sample Afg 12397.

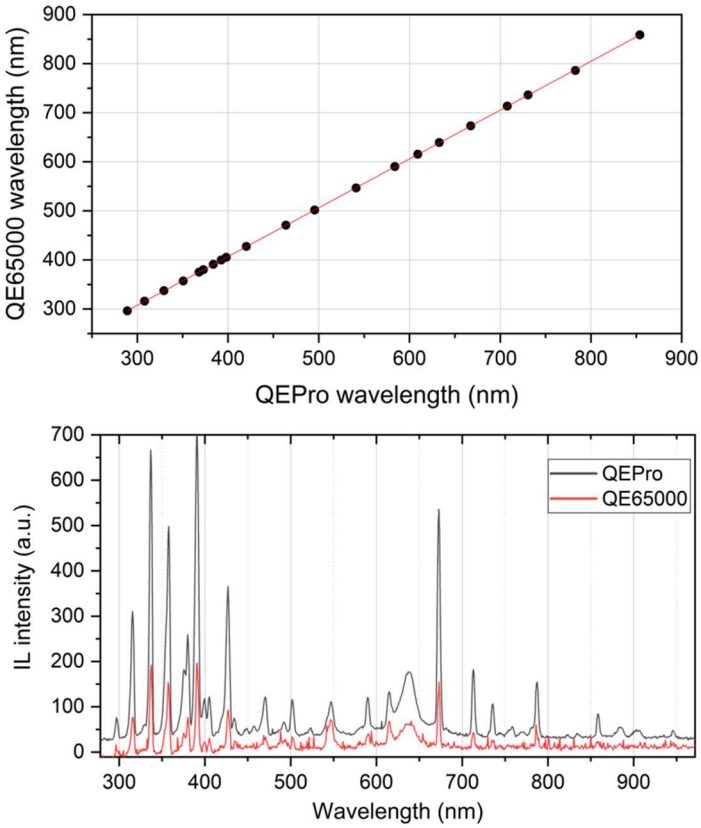

Figure 6.4. Calibration regression for wavelength of the two different used spectrometers (equation is y = 0.994x + 9.289) and He-rich air spectra comparison after the calibration.

AGLAE detectors suffered instead of a peak broadening only in the 2020 measuring run, due to some technical modifications of the setup carried out immediately before our run. This was noted especially for medium-high Z elements, that are particularly important in the identification of provenance markers for pyrite. For example, from figure 6.5 it can be seen that the Ni peak is covered by the broadening of Fe Kβ emission and that Ni and Cu contents for pyrites on the reference geological sample AFG1 are underestimated with respect to the acquisition at INFN-LNL. For this reason, data on pyrites acquired in 2020 have been discarded from the conclusions reported in chapter 8.

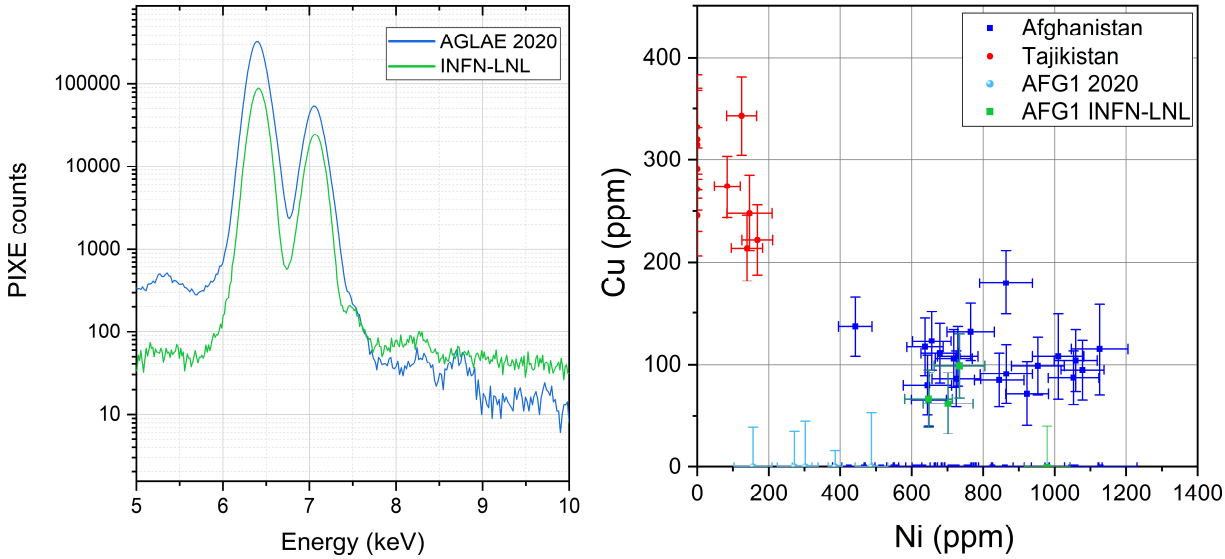

Figure 6.5. *Left:* comparison between μ-PIXE spectra on pyrites for sample AFG1 previously acquired at INFN-LNL and at AGLAE in 2020; the small Ni peak at 7.48 keV is just a shoulder in Fe Kβ peak for 2020 measurement. *Right*: results for provenance trace markers on pyrites for sample AFG1: all crystals analysed in 2020 have Cu < LOD and Ni lower than the minimum value measured at INFN-LNL.

7. Multivariate analysis

The amount of data produced by our long-term multi-technique study on lapis lazuli is significant. Moreover, the variables obtained from the different analytical methods are generally too many to identify the correlations between them merely by simple bivariate plots. For this reason, I tried to introduce in this research the use of multivariate analysis. The majority of my current knowledge on this topic is due to what I learned during the School of Chemometrics organized by the Department of Pharmacy of the University of Genova, together with personal study. *Chemometrics* is the term firstly assigned in 1974 by Svante Wold and Bruce Kowalski to a scientific sector that includes all mathematical techniques that aim at treating, elaborating and modelling chemical data. Today, chemometric methods overcame the strictly-chemical field and are used as a general methodology able to extract information from data of whichever nature [Todeschini 1998]. Chemometrics also includes the application of statistics to the design of experiments and simulations, topic that is not directly treated in this work.

Multivariate analysis (MVA) is the branch of statistical analysis which is concerned with the simultaneous investigation of two or more variable characteristics measured over a set of objects [Kachigan 1986]. Real data typically occur as a closely connected mix of primary and secondary information, noise and redundancy. This kind of analysis is employed for the exploration of such complex data, shading light to their structure, relations and correlations among them, relevance and adequacy [Todeschini 1998].
The goal is then to achieve a comprehensive overview of the system, considering all the measured variables, but extracting from them only the relevant information and discarding the noise. The three macro categories of the objectives of multivariate statistical analysis are [Kachigan 1986]:

1) Data reduction: with MVA it is possible to reduce large sets of data into sets with a smaller number of variables, that describe the original observations without sacrificing critical information.
2) Inference: MVA can provide procedures for stating the degree of confidence we have in the accuracy of the measurements and for making statements of our certainty that there are real (as opposed to chance) differences between sets of observations. The general aim here is to identify differences that can generalize our conclusions beyond the sample of observations upon which the conclusions were made.
3) Identification of existing relationships between and among sets of observations: associations unveiled by statistical analysis can be purely descriptive or experimental. In the first case, conclusions about the causal nature of the relationship should be drawn very carefully; for the second type, instead, we can be more confident, as the analysis is based on experiments where the variables are manipulated by researchers in order to look at the outcomes.

In addition, MVA methods that are most applicable to chemometrics can as well be divided into three main categories:

1) Exploratory Data Analysis or *data mining*, that is useful for gaining deeper insights into large, complex datasets, to find the hidden structure that results from the influence of all variables acting simultaneously; sample and variable relationships may be established and then used for further applications. Exploratory methods are also known as *unsupervised classification* methods (section 7.2).
2) Classification analysis: multivariate classification is also known as *supervised classification* and requires the definition of classification rules. These rules can be sub-models developed in the EDA phase of data collection, and the quality of such a classification scheme is determined on predictive ability of the model. Classification permits to assign an unknown sample to one of the classes defined by the rules in the model.
3) Regression analysis: these methods aim to develop a model that relates one set of variables, known as *independent variables*, to a set of responses, or *dependent variables*. The set of independent variables may itself be a compilation of variables from various types of sensors or may be generated by a single multichannel instrument, such as a spectrometer. With regression models it is then possible to predict new events and the quality of the model is once again determined by its predictive ability.

It must be remembered that chemometric models are not hard models applicable in a general way, but are empirical (or *soft*) models [Swarbrick and Westad 2016]. An empirical model is, by definition, an approximation made on the basis of a limited set of available data. As a direct consequence, data has to be representative of the situation to be modelled. A challenge in this regard when dealing with natural samples is their inherent heterogeneity, with cases where the same sample might show different characteristics depending on the measured area.

It is therefore common practice to select some samples suitable for a calibration development. In chemometrics there are two main strategies used to test the reliability of a model for future use on new samples:

1) Test set validation: this requires a rational sample selection method to separate the sample pool into a calibration (training) set and a validation (test) set.
2) Cross validation: typically, cross validation is used when there are not enough samples available in the pool to create a robust model and test it against a representative set.

In this work, both validation methods have been exploited.

Data are usually represented as $n \times p$ matrices, where n are the analysed objects and p are the measured variables. Variables can be discrete (e.g. trace element content quantified in ppm) or continuous, such as the complete wavelength range from a spectrum. They are called *predictors*, if independent, or *responses*, if dependent. Moreover, to objects can be associated one or more vectors containing the information on their belonging to predefined classes (figure 7.1). This kind of information can be used directly by the supervised method or can be added after the analysis for interpretation of the results in an unsupervised method [Nguyen and Holmes 2019].

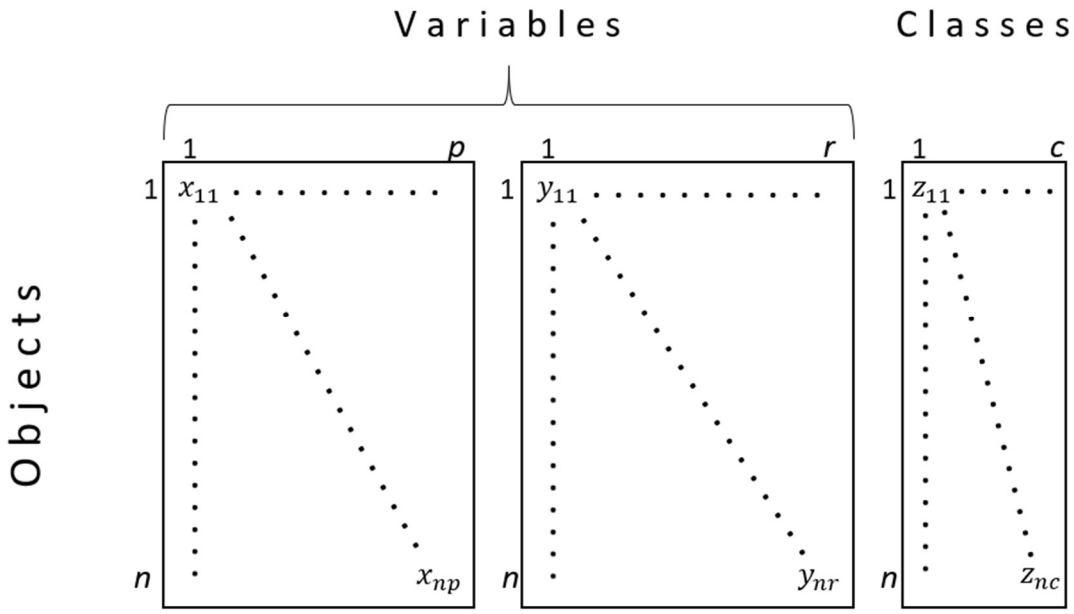

Figure 7.1. Dataset structure for MVA: $n \times p$ sub-matrix of discrete variables, $n \times r$ sub-matrix of continuous variables, $n \times c$ sub-matrix with additional information (e.g. classes).

The dispersion of the n observations can be characterised by the covariance matrix of the p variables. *Covariance* is a central theme in MVA and it describes the influence that one variable has on the others. Given two random variables X and Y, the theoretical covariance is defined by

$$\sigma_{XY} = \mathrm{Cov}(X , Y) = E(XY) - E(X)\,E(Y) \qquad (7.1)$$

where E is the expected value, that can be interpreted as the arithmetic mean of the variable. If X and Y are independent from each other, the covariance is necessarily equal to zero [Härdle and Simar 2015]. The *correlation* between the two variables X and Y is instead defined from the covariance as the following

$$\rho_{XY} = \frac{Cov\,(X,Y)}{\sigma_X\,\sigma_Y} \quad (7.2)$$

where σ_X is the standard deviation for variable X. The advantage of correlation with respect to covariance is that it is independent of the scale.
MVA can then identify variables that contribute the most to the overall variability in the data and helps to isolate those variables that are related (co-vary).

7.1. Data pre-treatment

A preliminary analysis is always necessary to check the data and prepare them for subsequent elaboration. Missing data should be labelled univocally (-999, NA…) and constant variables should be discarded, as they do not influence the variability of the system.
It is advisable to perform some transformations on variables that show non-normal or asymmetric statistical distributions. Also, almost in every case it is wise to perform a scaling of all the variables, to make them homogeneous and effectively comparable, without letting few variables shadowing the others for their high variance or their measurement scale. All the variables are simultaneously scaled with the same procedure, but independently from one another. However, these modifications of the variables should not be made lightly, as they reflect in great account to the final results of MVA and might lead to erroneous models and conclusions. The possibilities are many, but reported here are only transformation and scaling methods employed in this work.

Transformations have been applied only on data from μ-IL spectra, to eliminate systematic differences among samples. Specifically, a Standard Normal Variate (SNV) row pre-processing was performed to resolve global intensity effects and baseline shifts. It consists basically in autoscaling performed on objects instead of variables.

Autoscaling, one of the most common pre-treatment in the application of chemometrics, is the technique used for data scaling of variables. This operation is actually the sum of two, mean centring and unit variance scaling.
Firstly, data is centred according to the mean value of each variable, $\bar{x}_p$, then the new value is divided by the standard deviation of the specific variable, σ_p

$$x'_{np} = \frac{x_{np} - \bar{x}_p}{\sigma_p} \quad (7.3)$$

The mean of the autoscaled variables is then equal to zero, and their variance is equal to 1.
All datasets in this work have been autoscaled, exception made for LDA datasets since the classification technique naturally embeds autoscaling and no additional data pre-processing was needed.
As the available dataset contained a fraction of non-detects, i.e. trace elements occurring at concentrations below the limit of detection (LOD), the simplest approach was employed, that is using as substitutional value in the dataset a fraction of the LOD itself; it was chosen to use values equal to LOD/2, since they were proven to provide better results than 0 or total LOD [Farnham et al. 2002].

7.2. Unsupervised methods

Unsupervised methods look for the natural patterns in the data without being guided by an external classification rule. Once these patterns are established, rules can be developed and used to classify new samples.
Exploratory Data Analysis (EDA), unsupervised in nature, is typically the first step in any data analysis problem. It allows an analyst to get an initial feed for a data set, particularly the distribution of the data for each of the variables. The multivariate method for EDA applied in this work is Principal Component Analysis, explained in the following section.

7.2.1. PCA (Principal Component Analysis)

Principal Component Analysis (PCA) is one of the most powerful EDA methods known, unrivalled with its ability to provide a highly graphical environment. Moreover, PCA is an intermediate step for several MV analyses [Todeschini 1998]. It is an unsupervised method that aims to take large data sets and break them down into smaller, yet more informative, components (PCs) or *latent variables,* that are a collection of the most important sources of system variability. Each PC is orthogonal to all the others and they can be conveniently plotted against each other on a Cartesian coordinate system. In fact, the data transformation operated by PCA is a rotation of the original coordinate system. The first Principal Component (PC1) is the direction in a variable space that best preserves the relative distances between the objects, a latent variable which has maximum variance of the *scores*, which are the data values projected on the latent variable itself [Varmuza and Filzmoser 2009]. PC1 is defined by the loading vector

$$\boldsymbol{p}_1 = (p_1, p_2, \ldots., p_m) \tag{7.4}$$

when considering *m* variables. Scores are then linear combinations of loadings and original variables: for an object *i*, defined by a vector $\boldsymbol{x}_i$, the score t_{i1} of PC1 is

$$t_{i1} = x_{i1}p_1 + x_{i2}p_2 + \ldots + x_{im}p_m = \boldsymbol{x}_i^T \cdot \boldsymbol{p}_1 \qquad (7.5)$$

The last part of Equation 7.5 expresses this orthogonal projection of the data on the latent variable (figure 7.2). For all *n* objects arranged as rows in the matrix **X,** the score vector $\boldsymbol{t}_1$ of PC1 is obtained by

$$\boldsymbol{t}_1 = \mathbf{X} \cdot \boldsymbol{p}_1 \qquad (7.6)$$

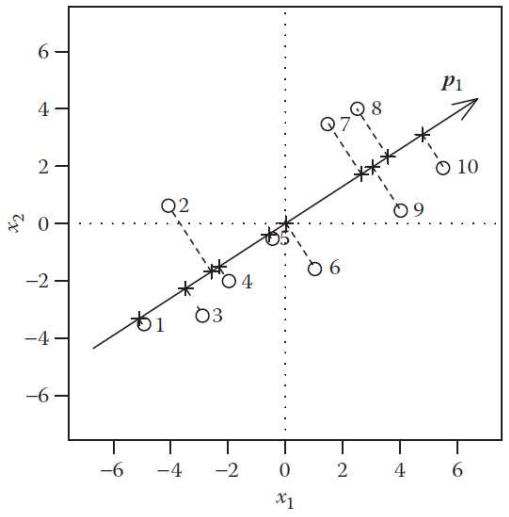

Figure 7.2. The first principal component (PC1) is defined by a loading vector p_1=[0.839, 0.544]. The scores are the orthogonal projections of the data on the loading vector. From [Varmuza and Filzmoser 2009].

The second Principal Component (PC2) is defined as an orthogonal direction to PC1 and again possessing the maximum possible variance of the scores. In general, further PCs can be computed up to the number of variables. Subsequent PCs are always orthogonal to all the previous ones, and their direction has to

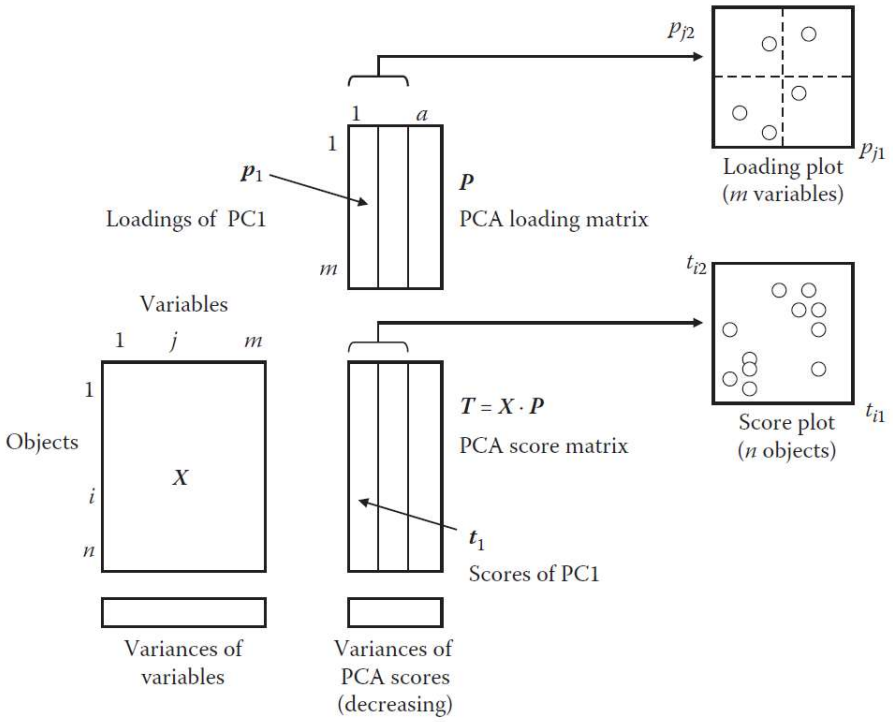

Figure 7.3. Matrix scheme for PCA. From [Varmuza and Filzmoser 2009].

cover the maximum possible variance of the data projected on such direction [Varmuza and Filzmoser 2009].

All loading vectors are collected as columns in the loading matrix, **P**, and all score vectors in the score matrix, **T** (see figure 7.3), providing the relation

$$\mathbf{T} = \mathbf{X} \cdot \mathbf{P} \tag{7.7}$$

with scores carrying sample information and loadings variable information [Swarbrick and Westad 2016].

Diagonalising the covariance matrix of the original data, the eigenvalues represent the explained variance of each PC, that decreases along the diagonal. The eigenvectors contain instead the weights to be applied for each sample to the original variables for obtaining the values of new components: they are then what were previously defined as loading vectors.

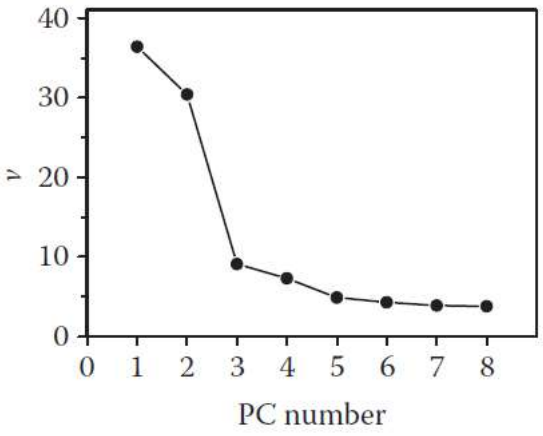

Figure 7.4. Scree plot for a dataset with eight variables. v is the explained variance, or percent of total variance, of PCA scores. In such a case, only the first two PCs can be selected, as they contain most of the system variability information. From [Varmuza and Filzmoser 2009].

Since the aim of PCA is dimension reduction and the variables are often highly correlated, a number of PCs lower than the number of variables is generally used. The selection of the number of significative PCs can be extracted from the so-called *scree plot*, where the explained variance is plotted *vs* the PC number. For many datasets, the plot shows a steep descent after a few components, since most of the variance is covered by the first PCs. The rule of the "broken stick" can be used, selecting all PCs up to the flat region (e.g. in figure 7.4 only the first two PCs are considered).

In this work, PCA plots are represented as *biplots*, a combination of a score plot and the corresponding loading plot for the selected PCs. Groups and clusters of data can be identified and their relationships with specific variables are immediately understandable: loadings of two variables pointing at the same direction in the PCs space mean that the variables are positively correlated; if they lay on the same line but are opposite in direction, the variables are negatively correlated; if instead the loadings are orthogonal, no correlation between variables is present.

7.2.1.1. Projection of an external dataset

When a new sample $\mathbf{x}_{1,m}$ comes in, it can be projected onto the PC model by the operation

$$\mathbf{t}_{1,N} = \mathbf{x}_{1,m} \cdot \mathbf{P}^{T}_{m,N} \quad (7.8)$$

that allows to compute its scores. This permits to see where the sample would fall in the PC space, without a re-elaboration of the model. This can be done also for small datasets, under the assumption that even if included in the original dataset, they would not modify significantly the PC model. Actually, this projection is generally used with a test dataset, to perform a sort of validation of the PCA model [Varmuza and Filzmoser 2009]. Anyway, this is not to be considered as a classification, as this would require a supervised method, but still as a kind of data exploration where outliers can be identified. In this perspective, this operation has been done in this work using the small datasets from archaeological samples of unknown provenance.

7.3. Supervised methods

The main goal of supervised methods is the prediction of qualitative and quantitative parameters finding specific relationships within the input data, in order to produce the correct output. The target attribute to be predicted can be of two types: categorical, leading to a classification of new samples, or numerical, if the created model produced a regression relationship. Categories, or classes, can be the groups observed during a previous unsupervised data exploration.

Models obtained via supervised methods require a validation before extending their use on unknown samples. The dataset is generally divided in a training set, used for the model building, and a test set, on which the model is tested. The model is also optimised during its creation with the *cross validation* process: the training set is subdivided in N blocks (where N is chosen by the user) that are used in N computations of the model as different preliminary test sets.

In this work, Linear Discriminant Analysis was used for lapis lazuli provenance classification, while Partial Least Squared Regression was introduced in the study of a regression method that could link luminescence intensity features and trace elements present as activators/quenchers in diopside.

7.3.1. LDA (Linear Discriminant Analysis)

Linear Discriminant Analysis is the simplest probabilistic method for classification purposes. The *a posteriori* probability for a class is given by the Bayes' theorem:

$$\mathrm{p}(c|\mathbf{x}) = \frac{\mathrm{p}(c) \cdot \mathrm{f}(\mathbf{x}|c)}{\sum_c \mathrm{p}(c) \cdot \mathrm{f}(\boldsymbol{x}|c)} \tag{7.9}$$

where:

- p(*c*) is the *a priori* probability of class *c*;
- f(**x**|*c*) is the *a posteriori* probability (density) of **x**, i.e. the probability that, under the condition that the class is *c*, X variable has the value **x**;
- p(*c*|**x**) is the *a posteriori* probability of the class, i.e. the probability that, when variable X has the specific value **x**, the object belongs to class *c*.

By definition, discriminant analysis aims to find discriminating features that separate samples into different data classes [Swarbrick and Westad 2016]. Class probability distributions are evaluated under two hypotheses:

1) normal (multivariate) distribution in each class;
2) same variance-covariance for all of the classes.

Hence, probability distributions are represented as Gaussian curves all with the same height and width. In the case of two categories, the value **x** for which $p(c_1|\mathbf{x}) = p(c_2|\mathbf{x})$ defines the *delimiter* between the two categories (figure 7.5b). In the case of more than two categories, a delimiter can be defined between each pair of them.

In LDA, delimiter – or discriminant – scores follow a linear trend, hence the separation between classes is defined by a line, a plane or a hyperplane (figure 7.5c). Since the mathematical function divides the whole space into as many classes as have been indicated, LDA will attempt to put a sample into the nearest class, independently of how far away the sample is from the class centroid. Therefore, a null class is not intended in this method.

LDA suffers from collinearity (i.e. some of the X variables are correlated) effects and requires more samples than variables being measured. Moreover, LDA is invariant to data autoscaling [Todeschini 1998].

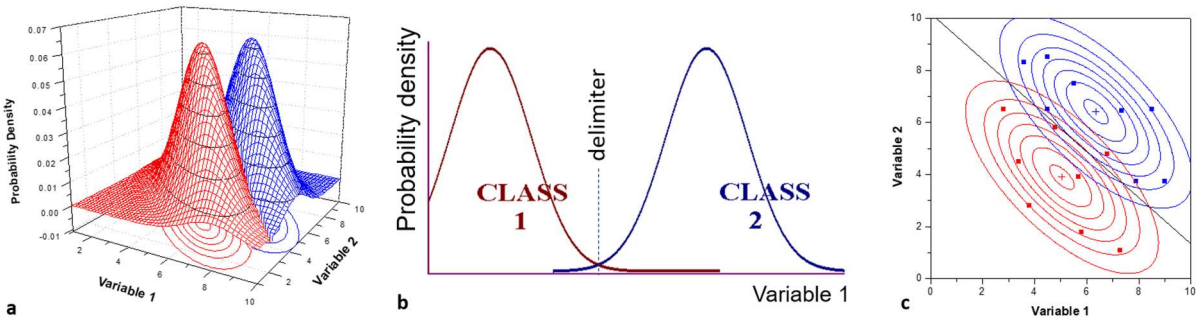

Figure 7.5. Probability density in the two-classes case: the delimiter defined as in (b) is expanded on the bivariate plane in (c) resulting in a line (modified from Prof. P. Oliveri, School of Chemometrics, 2020).

To evaluate the prediction ability of the model, the confusion matrix is built. This is a square matrix with on rows the real class memberships and on columns the classes assigned by the model. The ideal case with a 100% of prediction rate in cross validation is a diagonal matrix.

Moreover, the Mahalanobis distance (MD) can be analysed to evaluate the robustness of class assignations. MD, unitless and scale-invariant, is a measure of the distance between a point P and a distribution D in a multidimensional space and it is defined as follows

$$MD_{p,d} = \sqrt{(\boldsymbol{x}_p - \boldsymbol{x}_d)^T S^{-1} (\boldsymbol{x_p} - \boldsymbol{x_d})} \quad (7.10)$$

where x_d is the position of the distribution centroid and S is the covariance matrix. Hence, MD is equal to zero if P is at the mean of D.

7.3.2. PLSR (Partial Least Squared Regression)

In regression, the final aim is to model the relationship between one or more predictor variables (x) and one or more response variables (y). The general form of the multivariate linear regression model is

$$y_i = \beta_1 x_1 + \beta_2 x_2 + \ldots. + \beta_p x_p + \beta_0 + \varepsilon_i \quad (7.11)$$

or, in matrix form,

$$\mathbf{Y} = \mathbf{X}\beta + \varepsilon \quad (7.12)$$

where **X** is the matrix of the experimental variables or *predictor matrix*, β the column vector of the regression coefficients of the linear model and ε is the random experimental error in the determination of **Y**.

PLSR is a method for relating the two data matrices, **X** and **Y**, by a linear multivariate model, but goes beyond traditional regression in that it models also the structure of X and Y [Wold et al. 2001]. It derives its usefulness from its ability to analyse data with many, noisy, collinear, and even incomplete variables in both matrices.

PLSR is a biased method: it extracts components (known as PLS factors) in a similar way to PCA (and with a similar NIPALS algorithm), which compromise between explaining the variation in the X variables and predicting the responses in Y. The scores are estimated from X and the loading weights and are thus based on the covariance between X and Y. This means that PLS scores capture the part of the structure in X which is most predictive for Y [Swarbrick and Westad 2016]. On the other hand, a PLSR model is not of immediate interpretation, since it foresees a first phase in which the objects are projected on the latent variables and a second one in which from their scores it is possible to predict the responses. The closed form (eq. 7.11) of the regression can give information on the correlations of the model with the original variables.

After the validation of the model with a test set, just as in classification, some evaluation parameters can be analysed to define the fitting ability, such as the fraction of variance explained

$$R^2 = 1 - \frac{\sum_I (y_i - \hat{y}_i)^2}{\sum_I (y_i - \bar{y}_i)^2} \tag{7.13}$$

and the root mean squared error in calibration (RMSEC)

$$RMSEC = \sqrt{\frac{\sum_I (y_i - \hat{y}_i)^2}{I - A - 1}} \tag{7.14}$$

that can be calculated also for cross validation (RMSECV) and prediction (RMSEP) ability. These errors are not unitless and they depend from the scale of the response.

The number of latent variables to be considered in the model is the one that minimises the RMSECV (example in figure 7.6).

The choice of using PLSR on data from this work derived from its ability to treat multicollinear variables, as the ones involved in mechanisms of luminescence activation and quenching.

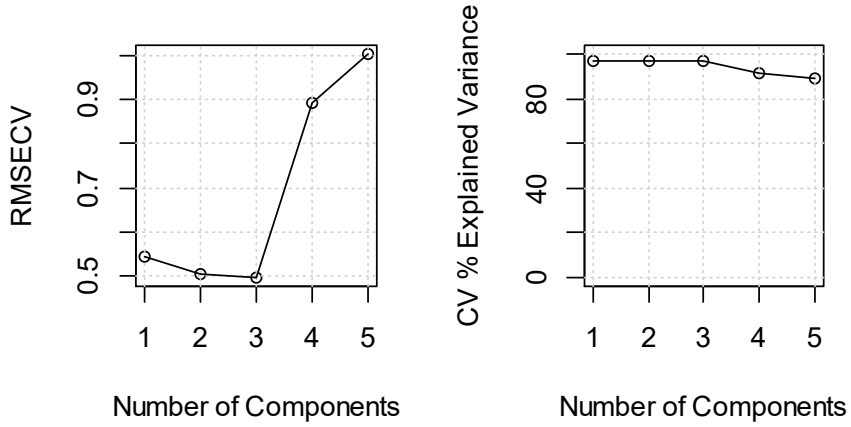

Figure 7.6. Evaluation plots of RMSECV and percentage of explained variance in cross validation for a PLS model. In this case 3 components should be chosen, that provide the minimum RMSECV value of 0.4928 and still cover more than 90% of explained variance.

7.4. Data fusion

Data fusion, largely applied in pharmaceutics and food science, can be very useful also in the case of simultaneous Ion Beam Analysis, where different signals and information are collected from the same sample.

Data fusion from different experimental results can be achieved with three levels of complexity: low-level, mid-level and high-level (figure 7.7). Low-level simply consists in joining the two or more datasets in one (the number of samples should be consistent between datasets) and then proceeding it to the required chemometric method. In mid-level data fusion, a selection of variables is performed before the joint: generally this is achieved with PCA, so that the majority of variance for the system is preserved. This can be fundamental when trying to apply LDA, as it requires for the number of variables to be equal or less to the number of samples. For the analytical purposes of this work, mid-level data fusion was chosen, considering that high-level (that entails strict data pre-treatment and a more subjective acceptance of the models) might be insidious for non-expert users and anyway often results to be less accurate when compared to low- and mid- level [Borras et al. 2015].

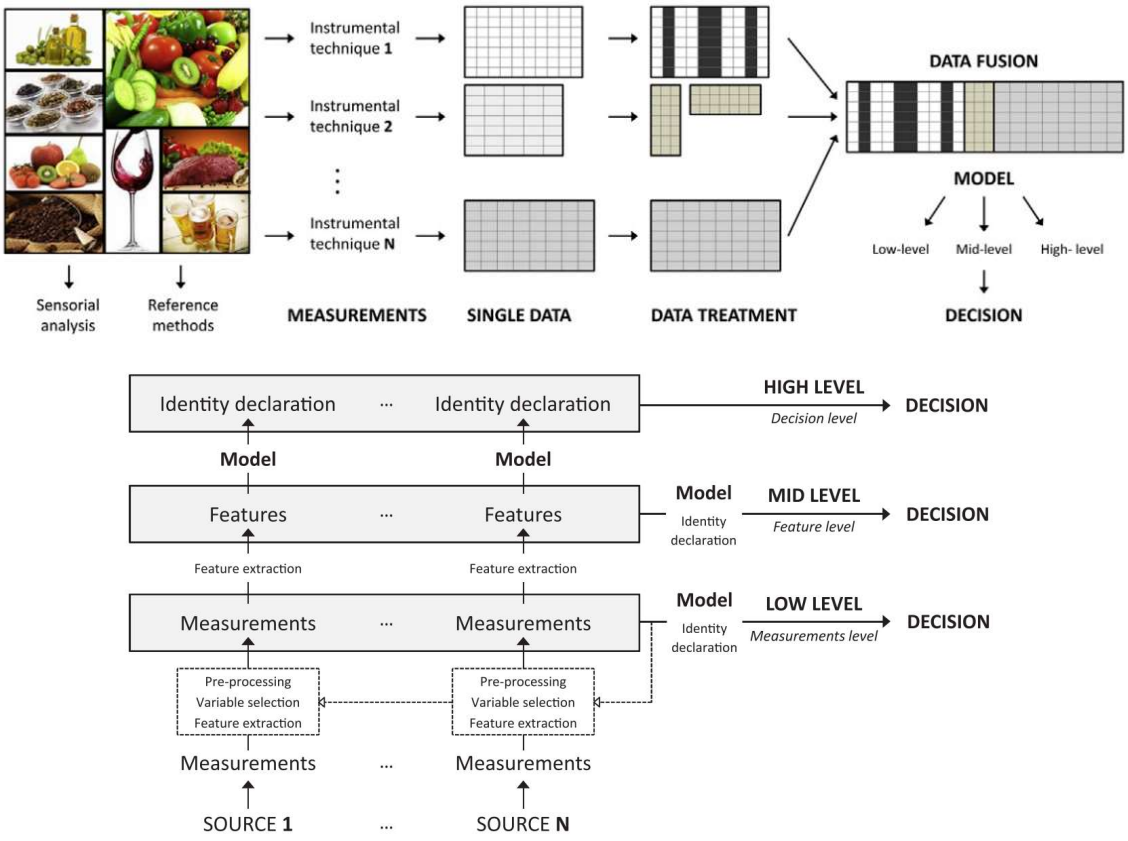

Figure 7.7. Data fusion: how it is reached (above) and a scheme of the three possible approaches. From [Borras et al. 2015].

7.5. Software

For MVA applied in this work, two kind of software were used: a custom-made Python script, built to adapt the PCA method to lapis lazuli provenance studies, and an interfaced R-based programme developed by the Chemometrics group at the Pharmacy Department of the University of Genova. Outputs obtainable from these software are briefly explained in the following sections.

7.5.1. Python script

The script was prepared using Spyder scientific environment in Python language. After loading the dataset in *csv* format, it is able to perform PCA and plot the *biplot* with overlapping scores and loadings for the selected PCs. Additional information on provenances (colour legend) is applied only in the plotting procedure and it does not influence the score values. Likewise, the polygons encircling scores from the same provenance are simply a guide for the eye and are not a class definition.

The script allows also to perform the projection of an external dataset described in section 7.2.1.1. To do so, the new data have to be scaled using the same mean and SD as the model, then their scores are calculated from equation 7.8 and plotted on the same space of the biplot.
Finally, it is also possible to label the new data to identify the outliers and the matching with existing groups.
The script to obtain the plot in figure 7.8 (a), with the description of each step, is reported in Appendix A.

7.5.2. CAT

The Chemometric Agile Tool (CAT) is an R-based software developed by the Chemometrics group at the Pharmacy Department of the University of Genova. It allows to quickly load files in different formats (e.g. .csv, .xlsx), to transform data and to apply both supervised and unsupervised multivariate methods. It was used first of all to verify the accuracy of the custom-made Python script, both in PCA model computation and in the projection of external datasets. In figures 7.8 (c), (d) and (f) the output for the same data used in figure 7.8 (a) is presented: the advantage of the Python script lies mainly on a higher plotting customisation, whereas CAT, thanks to its interface, has a quicker way for inserting parameters and the possibility to visualise diagnostic plots such as the scree plot (figure 7.8 (e)).
This tool was also used for SNV row pre-processing and for the application of the supervised methods (LDA and PLSR). Besides providing the results for the chosen method, it is possible to visualise as well some diagnostic plots such as Mahalanobis distances and RMSECV values *vs* component number.
It should be noted that PLS regression in CAT is only available as PLS1 algorithm, that can elaborate only a single response variable [Varmuza and Filzmoser 2009]: the implications of this limitation on the analysed data are discussed in section 8.2.3.

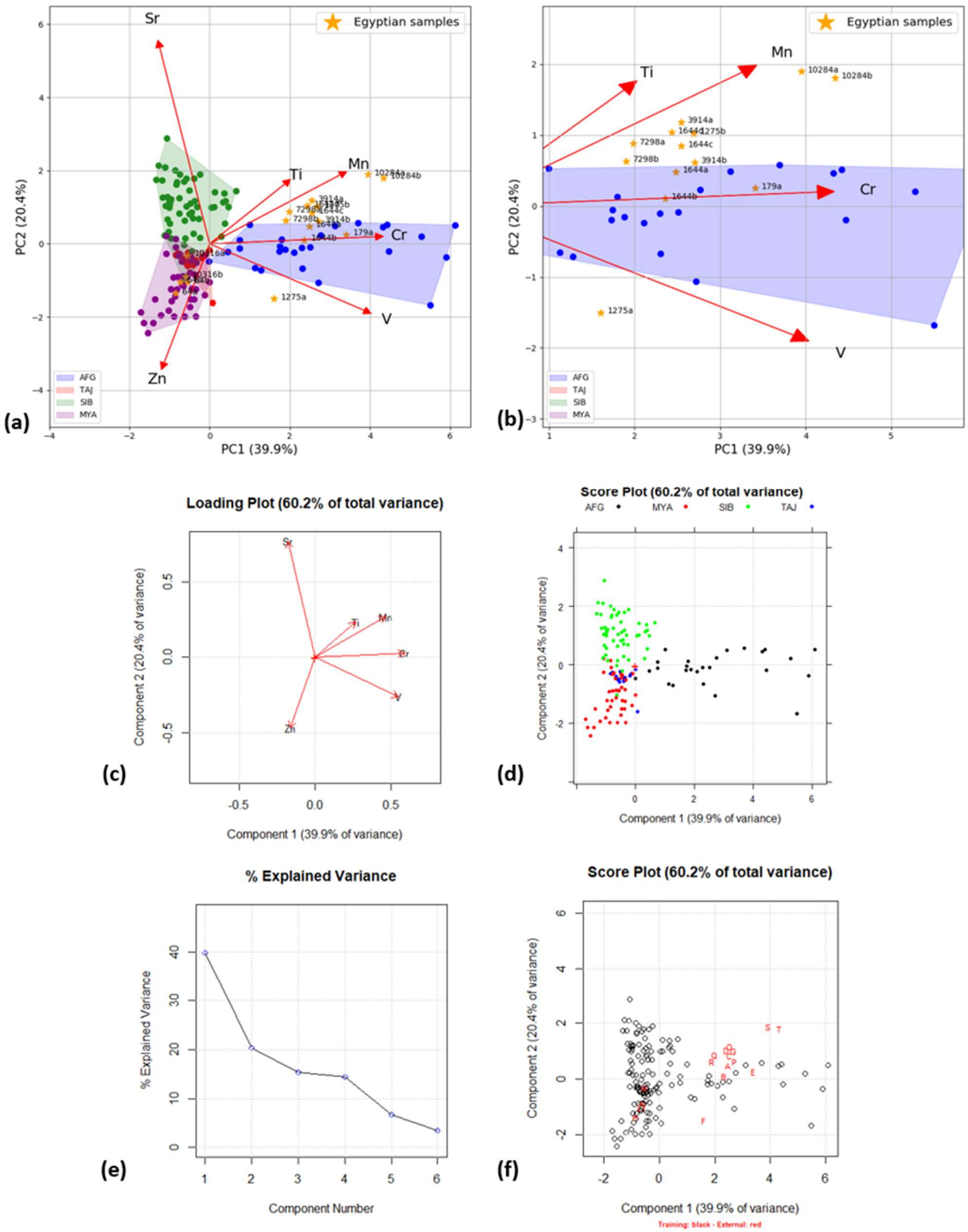

Figure 7.8. Software graphical outputs for PCA analysis: training dataset is from reference lapis lazuli rock samples, external dataset from Egyptian artefacts (data from [Lo Giudice et al. 2017]). Biplot with projections from Python script (a), with zoom (b) that allows a better readability of sample labels. Loading (c) and score (d) plots from CAT software, scree plot (e) and projection of the external dataset. It can be noted the limited ability for CAT in customisation of plots.

8. Results

In this chapter all the results obtained during the PhD from the previously described samples are reported. Prior characterisations of reference geological samples are taken as well in consideration in light of the new data.

The first part concerns studies on the lapis lazuli provenance issue. First of all, the summary for the new available Myanmar provenance is given, with a possible modification of the provenance protocol. A comparison of μ-PIXE results obtained at AGLAE from reference geological samples in respect to those collected at INFN-LNL is also provided, for a validation of the results subsequently shown. Moreover, the preliminary results of an alternative way to detect trace elements in diopside crystals with Wavelength Dispersive Spectrometry are presented. Then, archaeological samples are analysed; Shahr-i Sokhta manufacturing shards underwent a double IBA verification both in vacuum and with external beam. Archaeological samples from the Indus Valley Civilization sites and geological samples from Chagai Hills, analysed only in AGLAE, are addressed in sections 8.1.2.4 and 8.1.3 respectively. Multivariate methods employed for this research topic are Principal Component Analysis for data exploration and Linear Discriminant Analysis for classification.

The second part covers instead the investigation of activation and quenching processes that can be extrapolated by the simple observation of IL spectra and presence/absence of trace elements. An attempt of multivariate regression to define the direct effects of possible activators and quenchers on the IL intensity has also been made.

8.1. Provenance characterisation and determination

8.1.1. Reference geological samples

A comprehensive overview of the available reference geological samples was achieved during the PhD. Considering the dataset and the operative procedure for defining the geological origin of lapis lazuli previously published [Lo Giudice et al. 2017], the new IBA results on Myanmar rocks and data from all reference geological samples re-analysed at AGLAE, data exploration for diopside was performed using Principal Component Analysis. The outcome of the analysis is presented at the end of section 8.1.1.2 and is then taken into account for considerations on archaeological samples.

8.1.1.1. Myanmar samples

Following the procedure described in section 2.3.1, the 10 thick sections prepared from different samples have been firstly observed under optical microscope, cold-CL and SEM-EDX. These examinations have been mainly conducted by fellow researchers in the group: an example of the imaging outcome can be seen in figure 8.1. Crystals of interest among most of widespread mineral phases (diopside, lazurite, calcite) are up to some mm in grain size for these samples, characteristic that greatly facilitate the ultimate IBA analyses on specific minerals. From figure 8.1 (B) and (C) it can be seen how cold-CL is a great way to discern diopside (yellow emission) from calcite (red emission). Moreover, a comprehensive microprobe analysis [Vaggelli et al. 2019] allowed to separate the samples into three main groups on the basis of the identified phases: (1) the diopside-calcite group, with samples MYA07, MYA08, MYA09 and MYA12; (2) the nepheline-haüyne group, with samples MYA10 and MYA11; (3) the amphibole group, with samples MYA02, MYA 03, MYA 04 and MYA 06. All the identified mineral phases are reported in table 2.1. Subsequently, it was possible to exclude a correlation with Chilean provenance, as wollastonite was not found as main mineralogical phase in any sample. Also, the observed pyrite crystals, although smaller and in minor amounts compared to other provenance areas, are well preserved: this allows to confirm altered pyrites as a strong marker for the Siberian provenance.

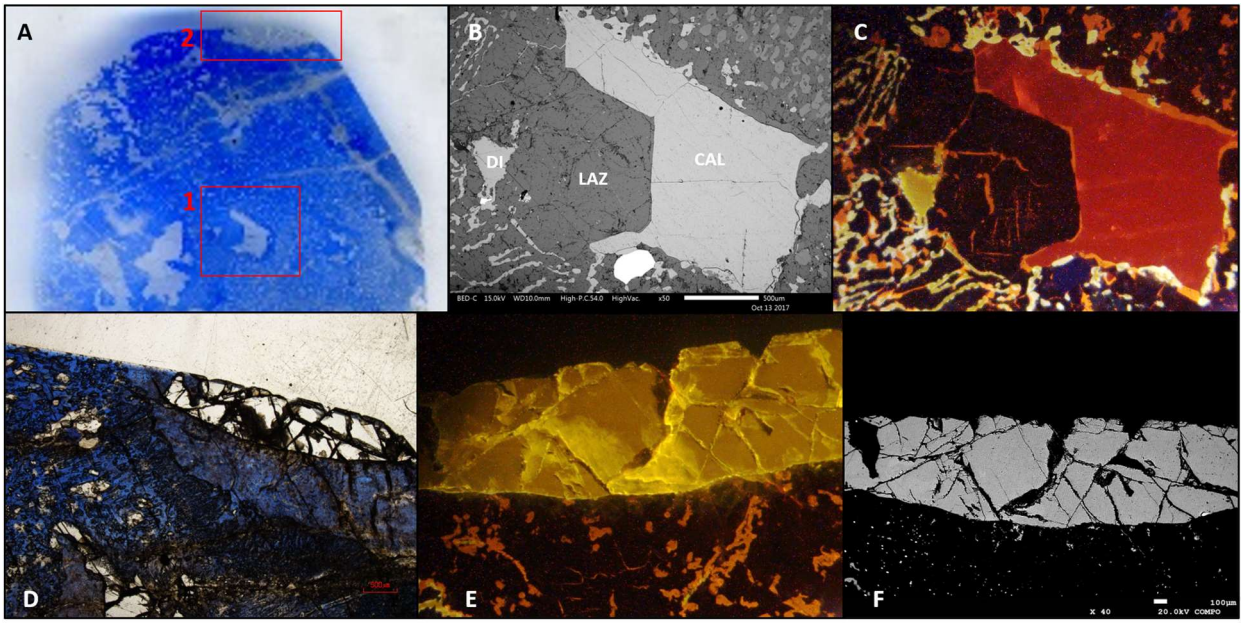

Figure 8.1. Preliminary microscopic characterisation for sample MYA09. Reflected light optical microscopy image (A): in red are highlighted areas investigated with different techniques. SEM-BSE images of area 1 (B) and area 2 (F), Cold-CL images of area 1 (C) and area 2 (E), photomicrograph in transmitted light of area 2 (D). Abbreviations: DI = diopside, LAZ = lazurite, CAL = calcite.

IBA were performed on 28 diopside crystals at INFN-LNL in vacuum with 2 MeV protons. For pyrite, due to the small dimensions, only 7 crystals were selected for IBA and specifically limited to samples MYA02, MYA06, MYA07, MYA10 and MYA12. The results from μ-PIXE measurements on diopside, compared to the reference dataset published in [Lo Giudice et al. 2017], are shown in figure 8.3. Although it was not found a strong marker for this new provenance, the low content of Sr - always below 150 ppm - in all the samples still allows to distinguish Myanmar from Siberia. Cr content resulted for all samples under the limit of detection, with an average LOD value of 50 ppm. These samples appear to be also poorer in Mn traces. Moreover, an element that was not previously included in the operative protocol, but seems to have relevance for Myanmar provenance is Zn: half of the samples show a content higher than 50 ppm that leads to an incompatibility with an Afghan provenance. Considering that this feature is not present in all samples, this can only be considered as a weaker marker. All the μ-IL spectra acquired for these diopside crystals (figure 8.2) present the main band at 585 nm and a much smaller band at 690 nm, similar to the one noticed in some Tajiki and Siberian samples [Re et al. 2015]. However, for sample MYA06 the latter band seems to spread wider on a range from 700 nm to 850 nm. Most of the samples also show the very broad band around 430 nm.

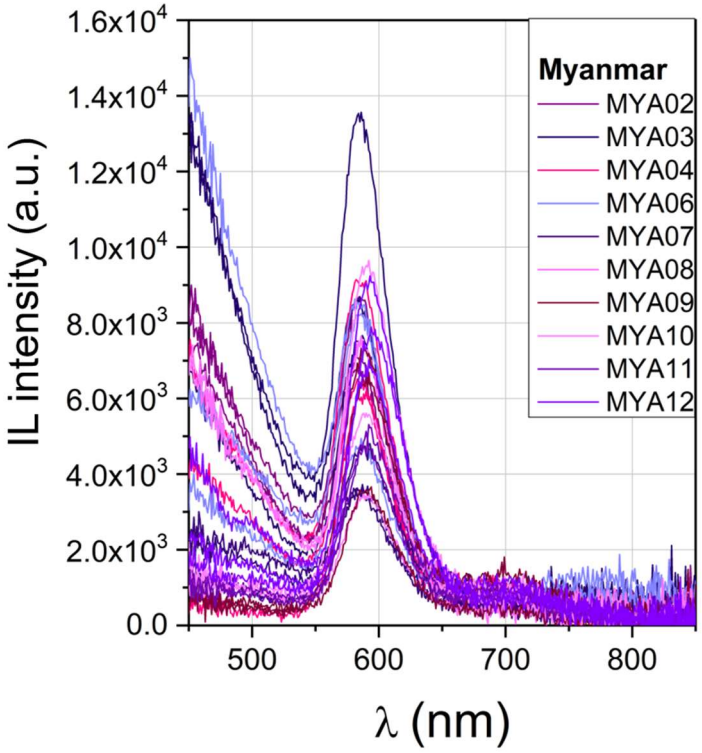

Figure 8.2. μ-IL spectra for diopside crystals measured in Myanmar samples.

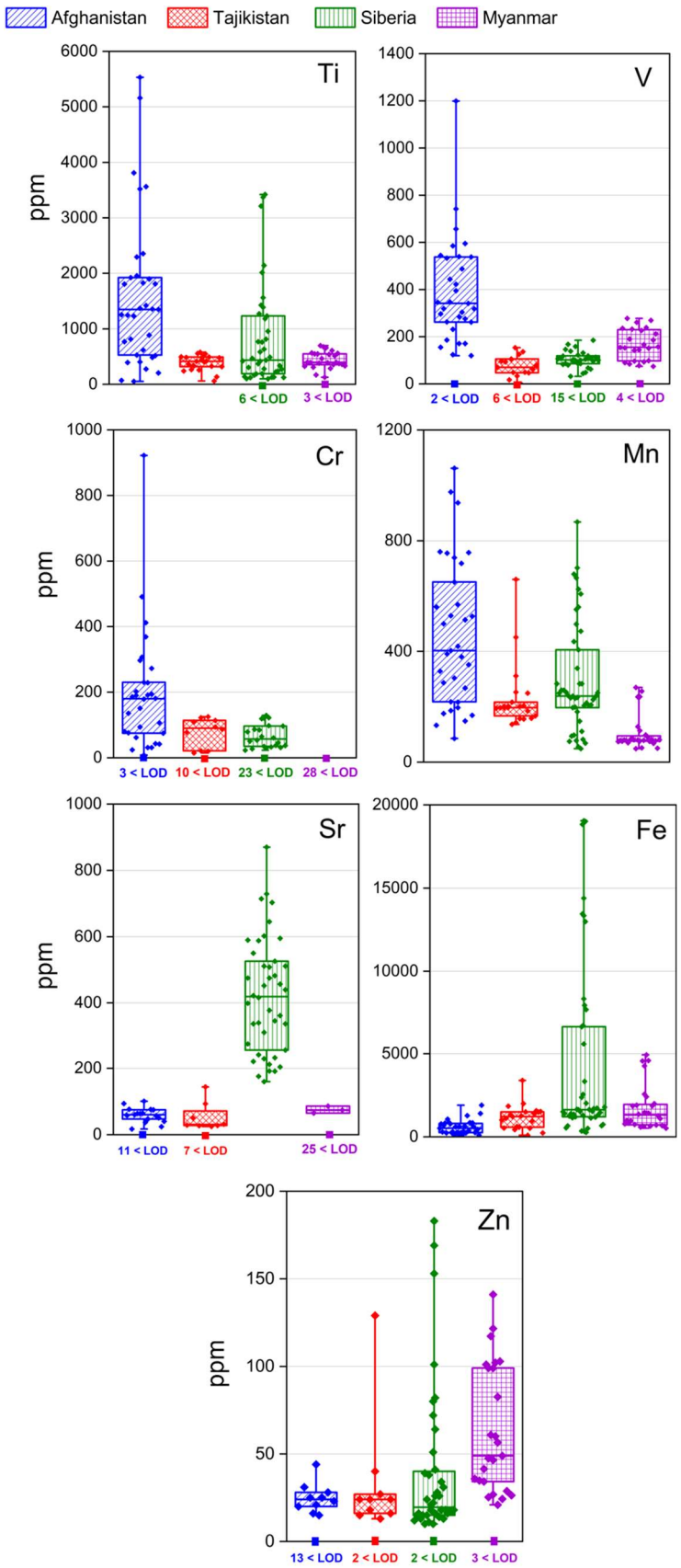

Figure 8.3. µ-PIXE results for trace elements in diopside, comparing Myanmar to the other reference geological samples [Lo Giudice et al. 2017], grouped by provenance area. The box plots represent the dispersion of the experimental points: the median line and the two percentile values 0.25 and 0.75. The squared symbols in correspondence to 0 value represent the number of measurements below the limit of detection (LOD).

With regards to pyrite crystals, no new trace element markers were found with µ-PIXE, even if in samples MYA02 and MYA12 Mo in concentrations around 100 ppm was found. In comparison to the strong markers identified for Afghanistan and Tajikistan (Cu and Ni), despite 7 points provide a still low statistics, some considerations can be made (figure 8.4). For all crystals, Ni content was found below 610 ppm (taking into account also the error), whereas Cu content raised up to 750 ppm. This certainly leads to an uncertainty in discrimination with Tajiki provenance and with a fraction of the measured Afghan samples. An arbitrary line can be drawn to maintain the ideal separation between Tajikistan and Afghanistan data, with equation Cu = 3/5 Ni (see figure 8.4). The protocol could then be modified as suggested in figure 8.5 where the discrimination between Tajiki and Myanmar samples remains unresolved, whereas the weaker markers help in the differentiation with Afghanistan. Nevertheless, it should be noted that pyrite results obtained with µ-PIXE for Myanmar samples seems to be consistent to those obtained with µ-XRF on the same samples (unpublished data), where found markers ranges are up to 1150 ppm for Cu and up to 400 ppm for Ni.

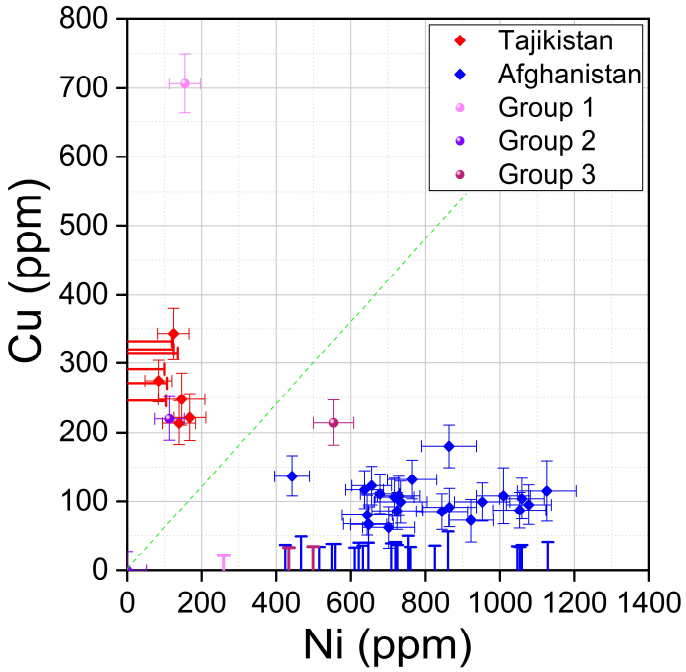

Figure 8.4. Trace element contents for markers in pyrite. Myanmar samples, in purple hue, are represented with a different colour for each group defined in [Vaggelli et al. 2019] and results are compared to data from the other reference geological samples [Lo Giudice et al. 2017]. The green dashed line is the ideal separation adopted in the new proposed protocol.

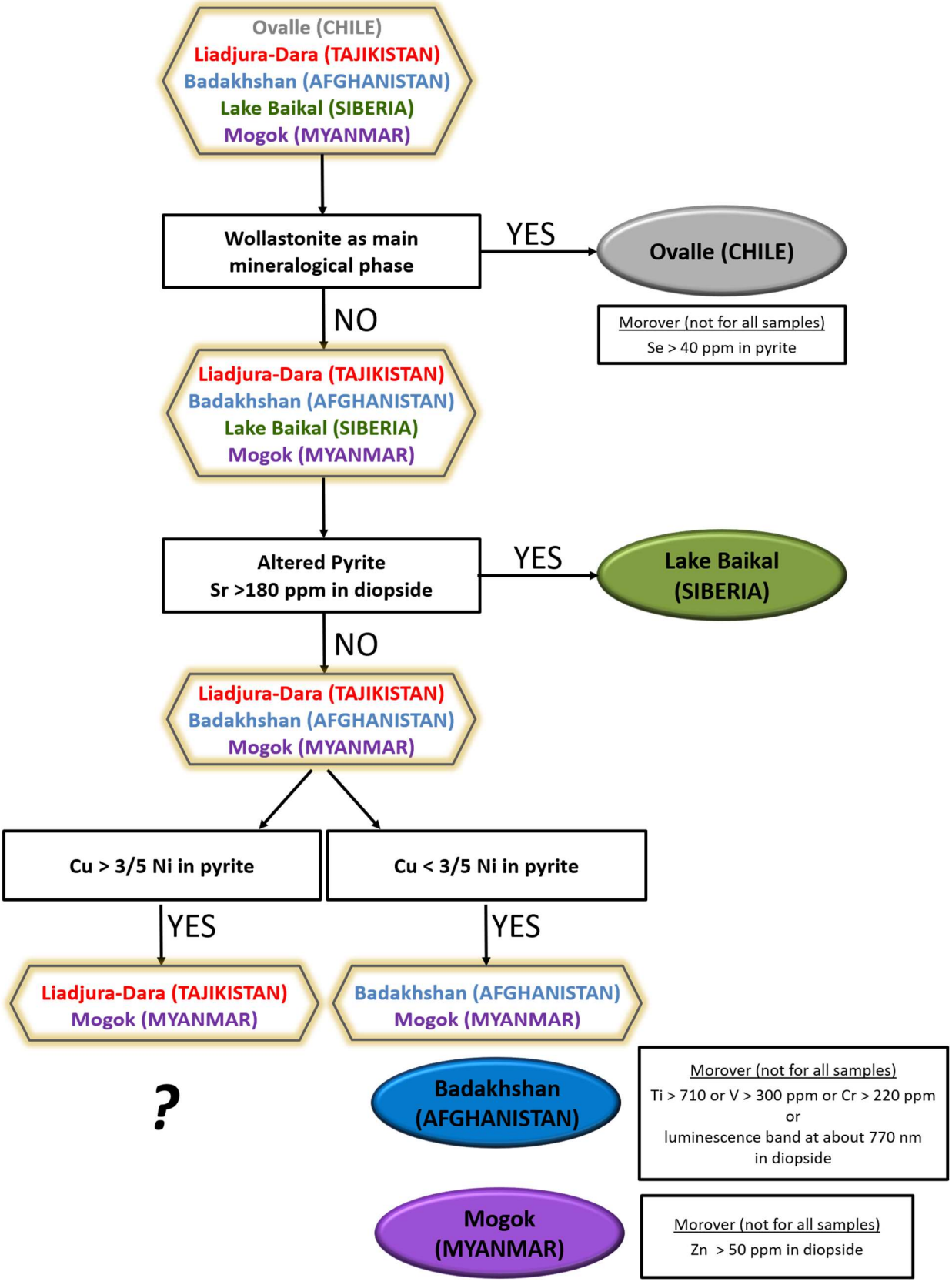

Figure 8.5. The new proposed flow chart of the operative protocol, revised considering also the Myanmar reference samples. Strong markers remain indicated along the main block chain, while weaker markers are reported next to each provenance balloon.

When separating the analysed diopside crystals according to the sample grouping previously mentioned, it can be seen an evident discrimination between group 2 and the others as regards the Mn and Fe contents (figure 8.6). For these two samples Mn is always detected above 200 ppm, whereas Fe is over 4000 ppm. Also, 2 out of 4 crystals from this group present a Sr content around 100 ppm: in all other samples Sr was not detected, with the exception of MYA12 (1 crystal). However, as it is thoroughly explained in [Vaggelli et al. 2019], this sample is a peculiar case for its paragenesis and its assignation to group 1 is tentative. This separation between Myanmar samples was further investigated by means of PCA, considering the first 3 PCs for a total explained variance of 80%: in figure 8.7, produced with the Python script described in chapter 6, it can be seen that group 2 separates from the others influenced by variables Mn, Fe and Sr, but also Ti shows a contribution. Moreover, the assignation of sample MYA12 to group 1 should still be considered dubious.

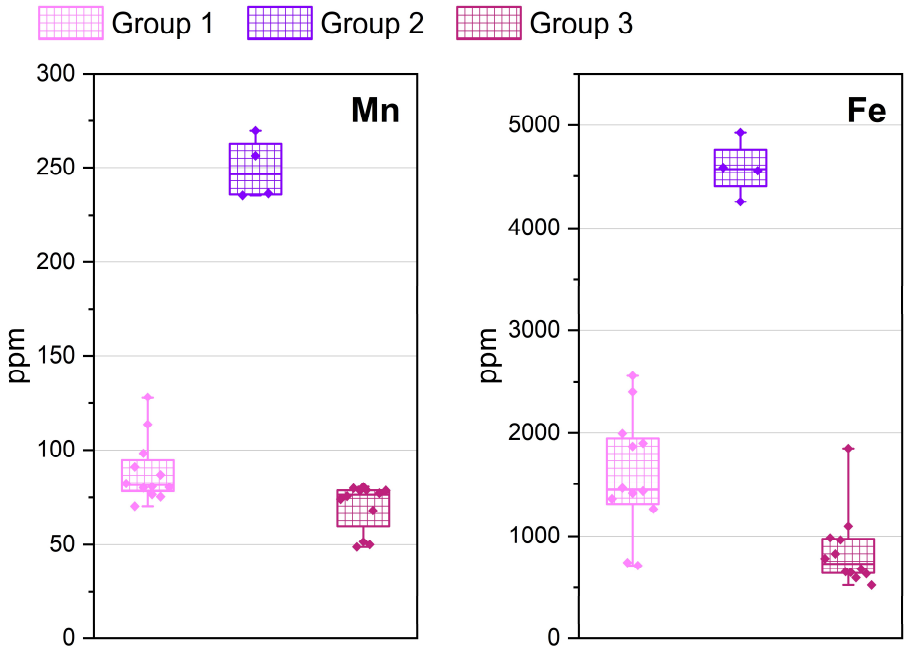

Figure 8.6. Content of Mn and Fe in diopside for the three different Myanmar groups. The box plots represent the dispersion of the experimental points: the median line and the two percentile values 0.25 and 0.75.

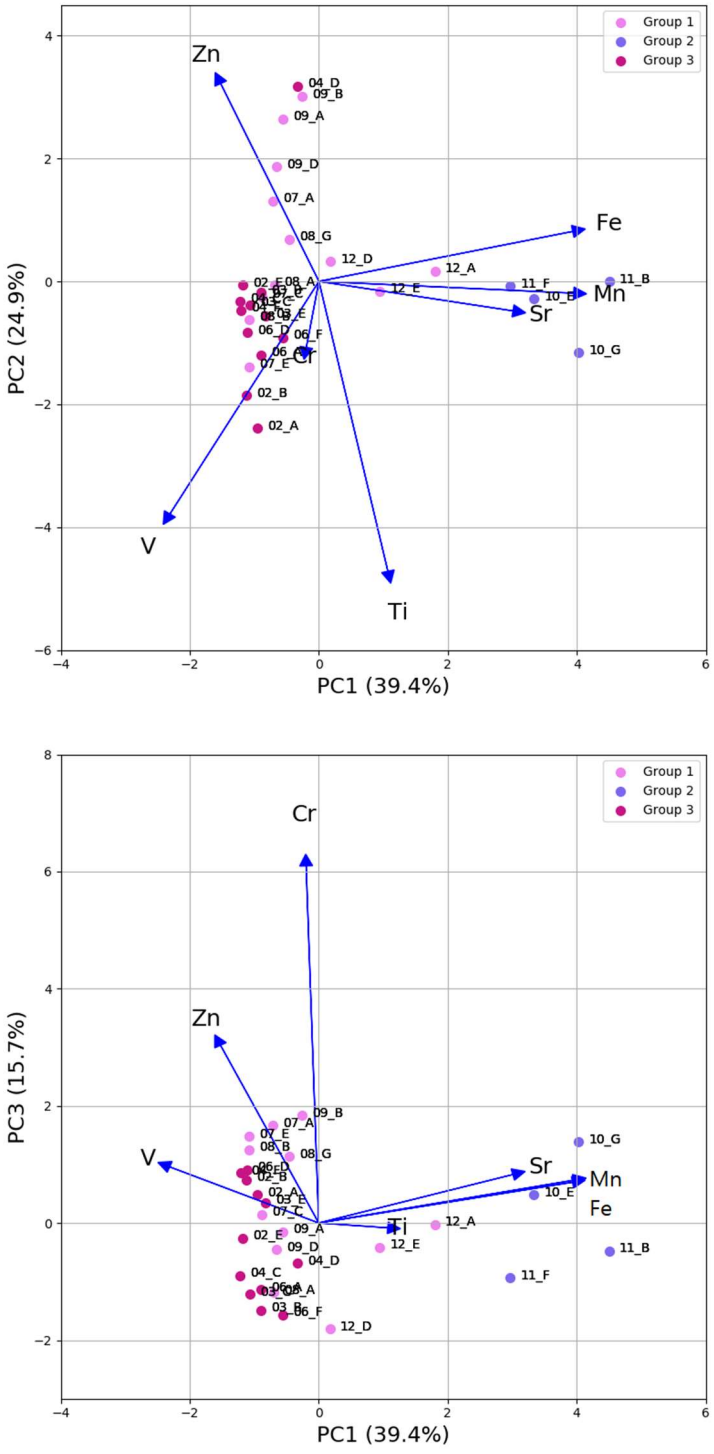

Figure 8.7. Biplots obtained from PCA analysis on µ-PIXE data for diopside in Myanmar samples, considering as variables the trace elements reported in figure 8.2. On the left PC1 *vs* PC2, on the right PC1 *vs* PC3; the percentage of explained variance for each PC is reported in brackets. It becomes evident a small contribution of Ti as well in the separation of group 2. Sample MYA12 results in both cases as tending towards group 2.

8.1.1.2. Reference geological samples analysed at AGLAE

As the principal aim of SIBILLA project (section 6.3) was to collect diopside data from different samples and provenances with a reproducible IL setup, a selection of reference geological samples that were previously investigated with the microbeam line of INFN-LNL during separated runs was measured again with AGLAE setup. This allows also to directly compare the results obtained with the two facilities, as concerns μ-PIXE technique. In this comparison study, some factors should be kept in consideration: first of all, the proton energy is different (2 MeV for INFN-LNL and 3 MeV for AGLAE), but in addition the beam operates in two different environments (high vacuum for INFN-LNL and in He-rich air for AGLAE). It can be seen from figures 8.8 and 8.9 that μ-PIXE quantifications in diopside crystals from measurements at AGLAE are generally in good agreement with the results obtained in vacuum at INFN-LNL, that have been considered so far in the compilation of the protocol, when evaluating the match with the total spread of INFN-LNL points (interval between minimum and maximum values). In some cases, concentrations for trace elements are slightly lower: this can be caused both by a minimal absorption of the signals by air components, but also by the heterogeneity of the target material and the different volumes investigated by the probe, due to the different proton energies employed. Such reduction in signals seems to be more relevant for high Z elements (e.g. Sr in diopside or Ni and Cu in pyrites) and it is definitely more significant for the second run in 2020. Nevertheless, the discriminant higher content of Sr in Siberian samples can be confirmed.

Considering all data acquired on diopside crystals from all provenances in both facilities, a PCA data exploration was performed. Results of PC1 *vs* PC2, selecting as final variables the μ-PIXE markers (stronger and weaker), can be seen in figure 8.10. Covering an explained variance of 60.3%, groups can be identified for Afghanistan, Siberia and Myanmar. Afghanistan is particularly discernible from others, influenced by Mn, Ti, V and Cr variables that show a positive correlation with each other; its complete separation from the Myanmar group could be regarded as an additional weaker marker for the provenance determination, although a similar PCA can be performed only if a considerable amount of samples are available to protocol users. For other provenances some overlap can be seen instead: Tajikistan is completely merged with Myanmar, reflecting the difficulty previously discussed in discriminating the two origins. Being PCA an unsupervised method, no additional information was provided to the algorithm, hence colours in figure 8.10 are added at a later time and the polygons encircling the data are simply a guide for the eye, but they do not define classes. Data from AGLAE was also added to PCA plots for Myanmar groups (figure 8.11), and the conclusions drawn from INFN-LNL data still stand.

μ-IL results on rock samples will be presented and discussed in section 8.2 on luminescence investigations.

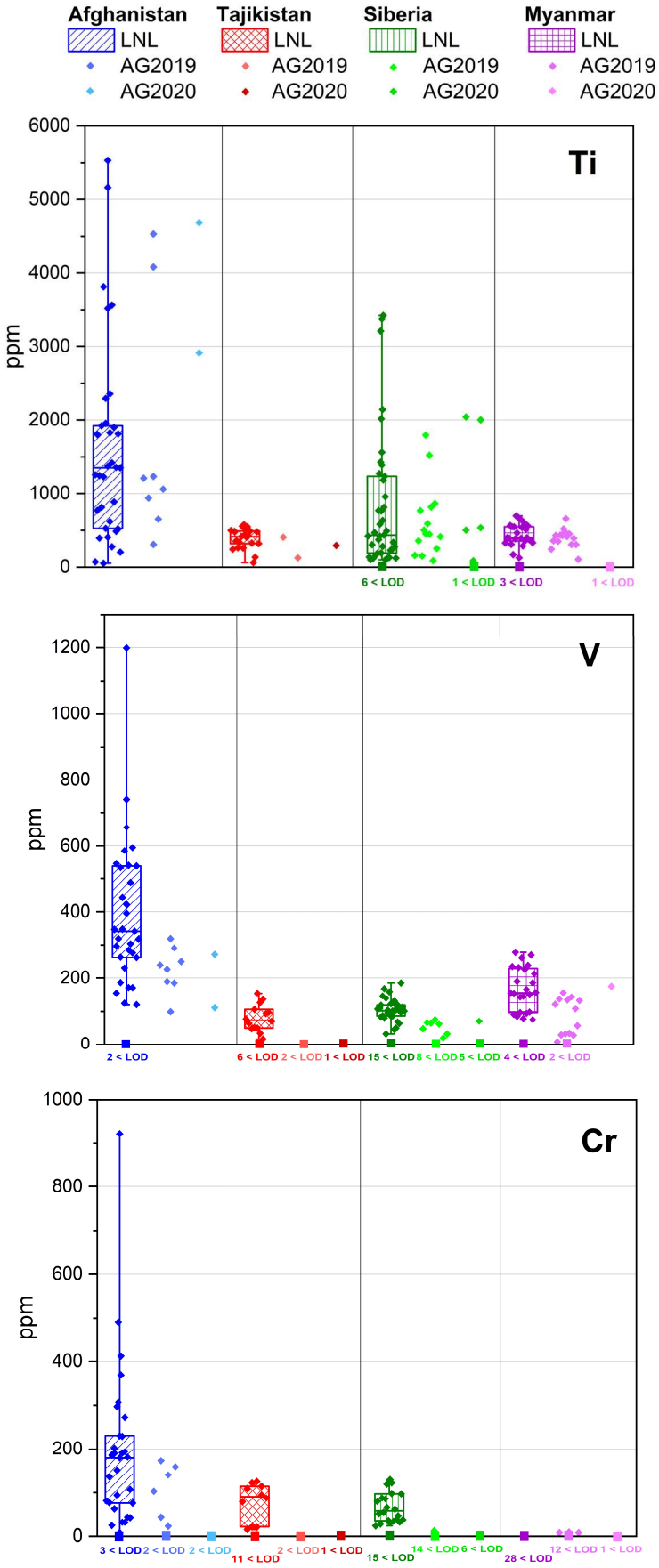

Figure 8.8. Comparison of μ-PIXE results for Ti, V and Cr in diopside, between reference geological samples acquired at INFN-LNL and at AGLAE in two different runs (2019 and 2020). The box plots represent the dispersion of the experimental points: the median line and the two percentile values 0.25 and 0.75. The squared symbols in correspondence to 0 value represent the number of measurements below the limit of detection (LOD).

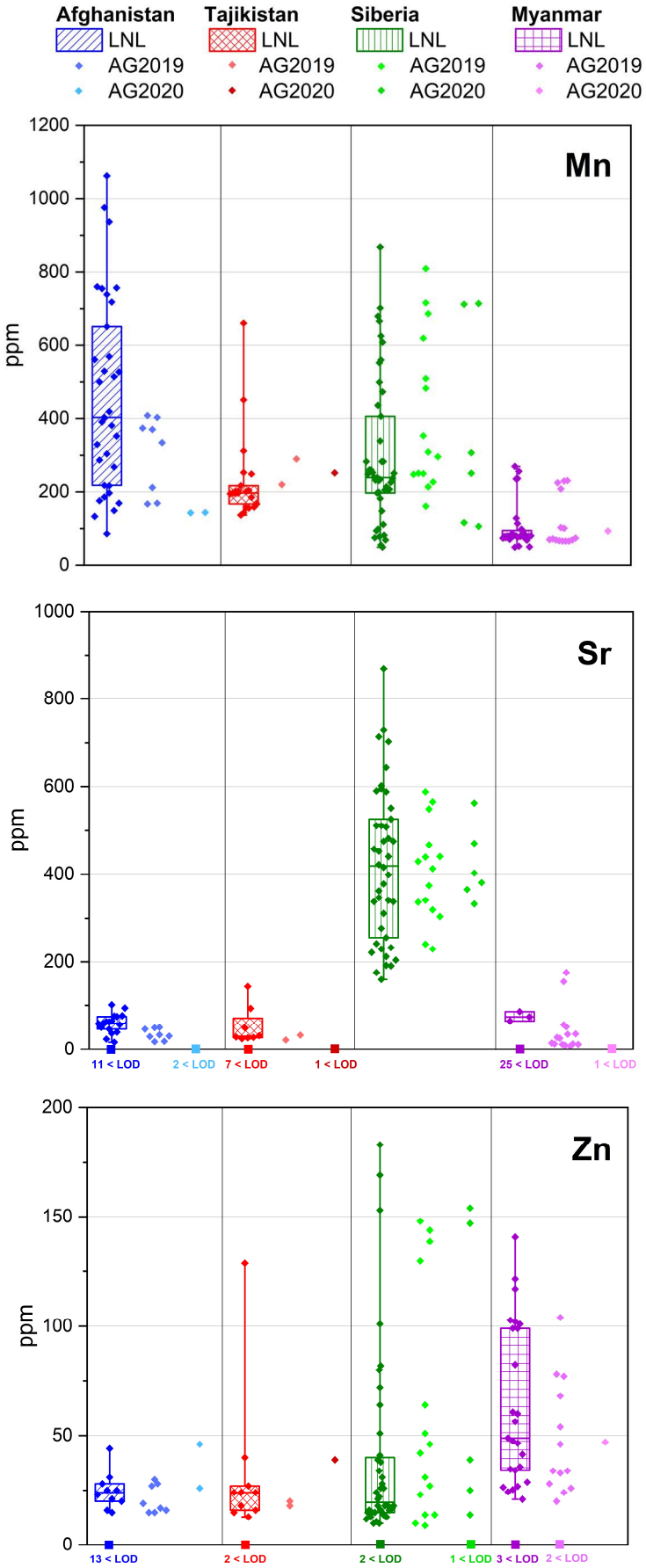

Figure 8.9. Comparison of µ-PIXE results for Mn, Sr and Zn in diopside, between reference geological samples acquired at INFN-LNL and at AGLAE in two different runs (2019 and 2020). The box plots represent the dispersion of the experimental points: the median line and the two percentile values 0.25 and 0.75. The squared symbols in correspondence to 0 value represent the number of measurements below the limit of detection (LOD).

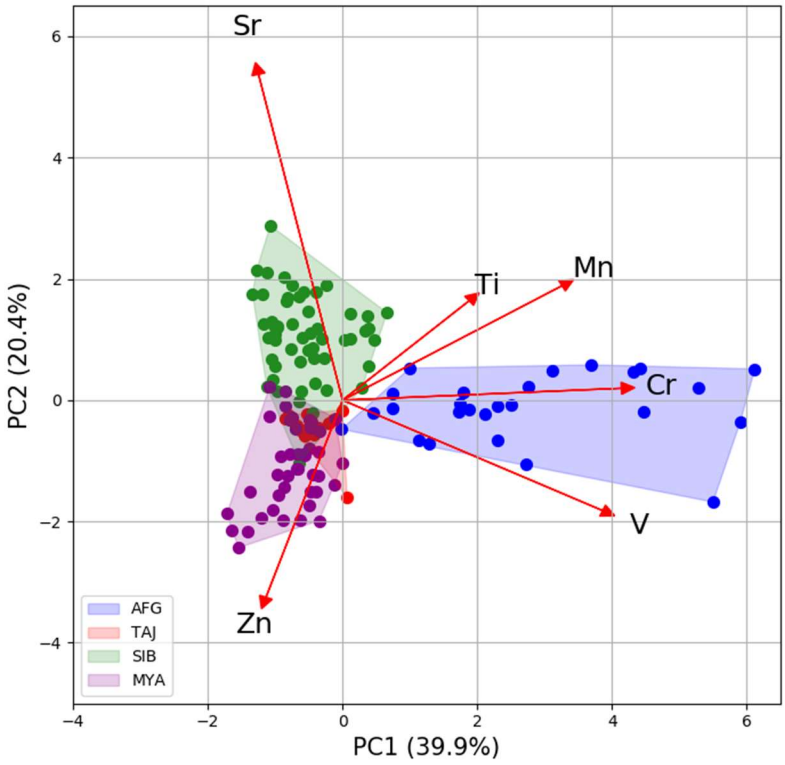

Figure 8.10. Biplot obtained from PCA analysis on all µ-PIXE data acquired on diopside crystals from all geological reference samples in both INFN-LNL and AGLAE facilities. Results of PC1 *vs* PC2, after selecting as final variables the µ-PIXE markers (stronger and weaker), are shown. The percentage of explained variance for each PC is reported in brackets. Colours and polygons encircling the data are simply a guide for the eye, but they do not define classes.

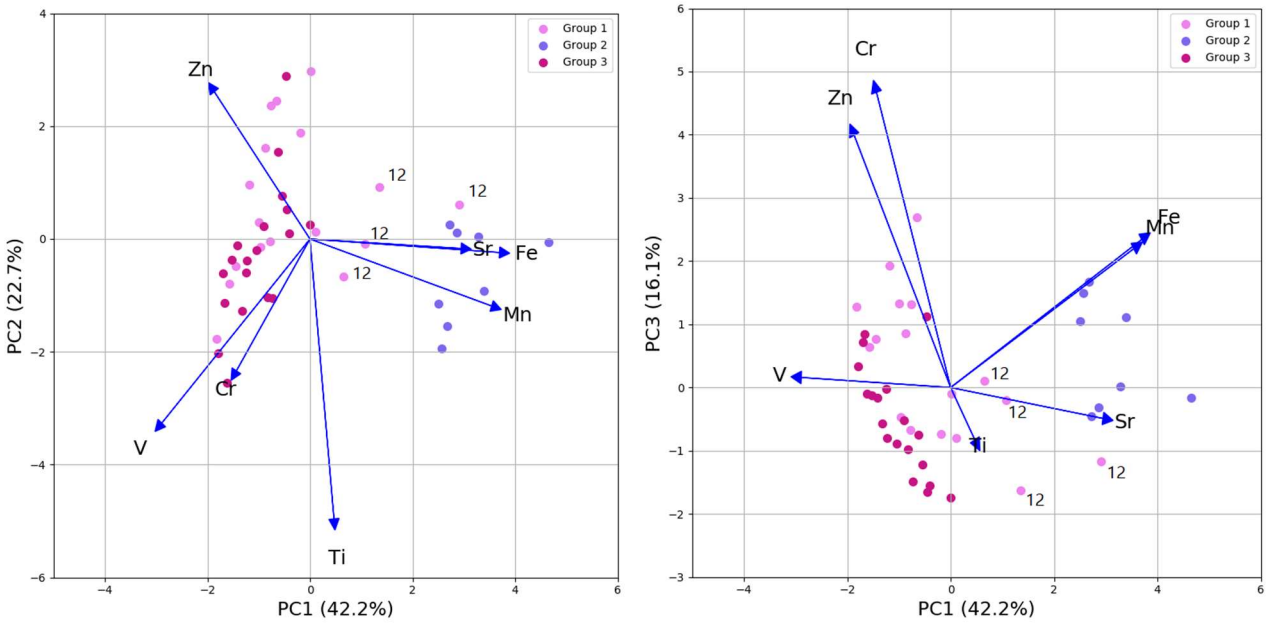

Figure 8.11. Biplots obtained from PCA analysis on µ-PIXE data for diopside in Myanmar samples, comprehensive of AGLAE results. On the left PC1 *vs* PC2, on the right PC1 *vs* PC3; the percentage of explained variance for each PC is reported in brackets. Sample labels are not reported for plot readability, but points belonging to sample MYA12 are indicated.

8.1.1.3. Trace elements quantification with SEM-WDX

PIXE has high performances in the quantification of trace elements, with very low LOD values that allows to detect parts per million concentrations, but it has a logistical limitation in the need of accessing accelerator facilities. During my participation to BE-ARCHAEO project in Okayama, Japan, I was able to employ a SEM-WDX. Wavelength Dispersive Spectrometry can reach LOD values comparable to PIXE, but working with an electron probe that can be found more easily in laboratories. Moreover, the analytical target can be effortlessly identified thanks to the clear SEM images, generally using backscattered electrons. On the other hand, working in high vacuum, samples need to be carbon coated: this prevents the application to archaeological items, but can still be very useful for collecting reference information from the database geological samples.

The calibration process with natural standards requires a good amount of time, as each emission line for elements of interest needs to be singularly evaluated for fitting and for a correct background subtraction. For this reason, and for my limited stay in Japan, a simple test was performed in this preliminary new approach, analysing with WDX 4 reference geological samples (one for each available provenance) that were previously investigated both at INFN-LNL and AGLAE. Using as reference optical and cold-CL images and μ-PIXE maps, it was easy to find the exact same target diopside crystals for samples MYA09 and BK7. Samples AFG1 and Pamir2 have a more complex texture, resulting in a more challenging selection of the target. SEM BSE images previously acquired with Turin instrumentation were a great support in finding the correct crystal in those cases.

The employed SEM-WDX performs a punctual analysis, whereas in our adopted analytical mode the PIXE proton beam scans an area. In order to uniform as much as possible the WDX acquisition method with the one used in the other two facilities, 4 points on the crystal area were measured (figure 8.12), then the quantitative results were averaged. ZAF matrix correction was applied. In plots from figure 8.13, mean and standard deviation are reported for each elemental concentration obtained from WDX. The comparison of the results for principal trace elements (Ti, Mn, Cr, Sr, Fe, Zn, Zr, Y) is shown. Considering 2-sigmas ranges, the agreement between data is quite good. The very small error bars for PIXE-AGLAE derive from the spectrum fit and are due to a higher statistics during acquisition, thanks to the three SDD detectors employed for high energy X-rays. Differences in concentration appear to be non-systematic: this is encouraging, as it has always to be taken into account the heterogeneity of the material and the different volumes investigated by the different probes. The Afghan sample seems to be subjected to a higher variability (e.g. for Ti, Fe, Y), but it was also the one for which the exact target identification was harder, as previously mentioned. A summary of measuring conditions for the three types of analysis is presented in table 8.1. In light of these preliminary results, SEM-WDX spectrometry seems to be a

promising alternative to μ-PIXE for the trace elements quantification in lapis lazuli mineral phases for reference geological samples. However, additional measurements are in need for a definitive conclusion.

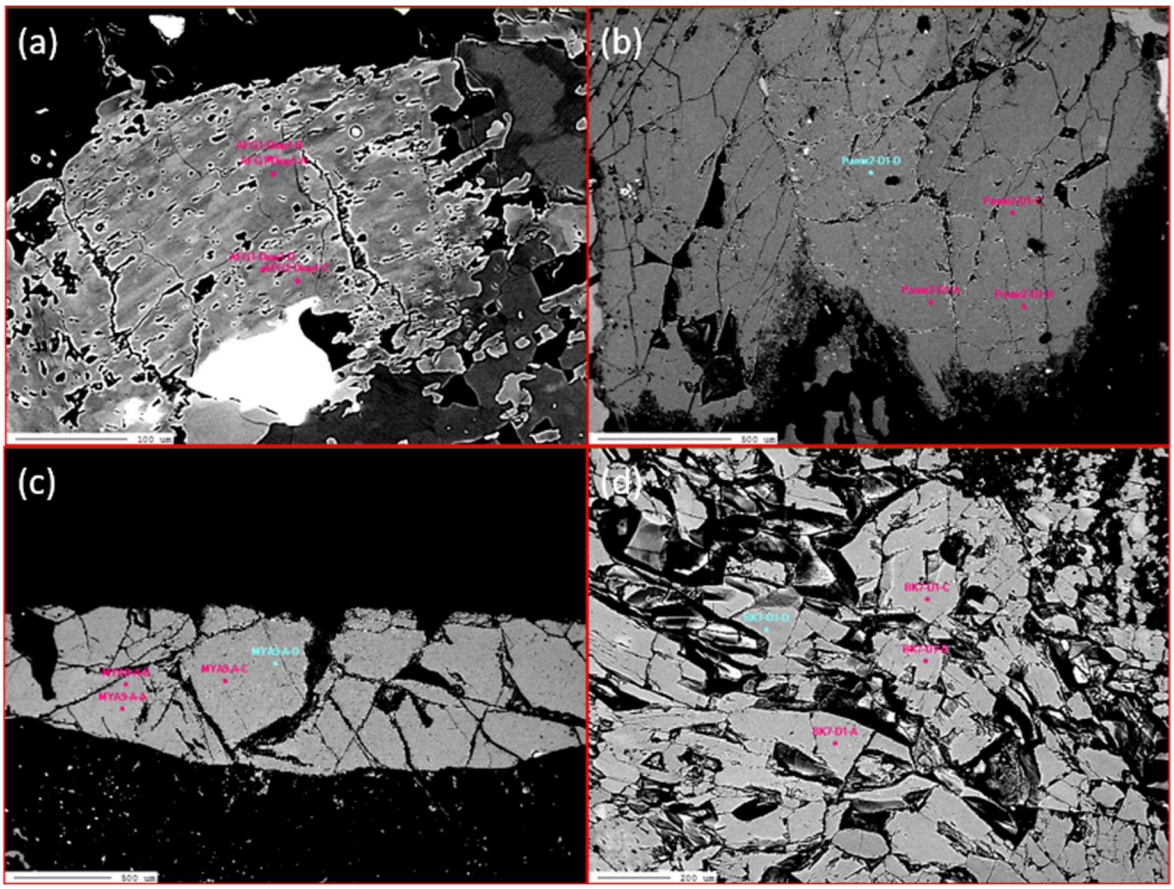

Figure 8.12. SEM-BSE images with indication of the points analysed by SEM-WDX for samples AFG1 (a), Pamir2 (b), MYA09 (c), BK7 (d).

Table 8.1. A comparison of measuring conditions and parameters for SEM-WDX, μ-PIXE at INFN-LNL and μ-PIXE at AGLAE.
* Penetration ranges in diopside (density = 3.3 g/cm^3), calculated with CASINO software [Drouin et al. 2007] for electron beam and with SRIM software [Ziegler 2010] for ion beams.

	WDX	μ-PIXE INFN-LNL	μ-PIXE AGLAE
Measurement type	in vacuum	in vacuum	in air
Probe	Electrons	Protons	Protons
Beam energy	20 keV	2 MeV	3 MeV
Beam size	~ 5 μm	~ 5 μm	~ 25-30 μm
Average beam current	200 nA	200 pA	500 pA
Acquisition mode	Punctual	Scanning	Scanning
R values*	2 μm	30 μm	60 μm

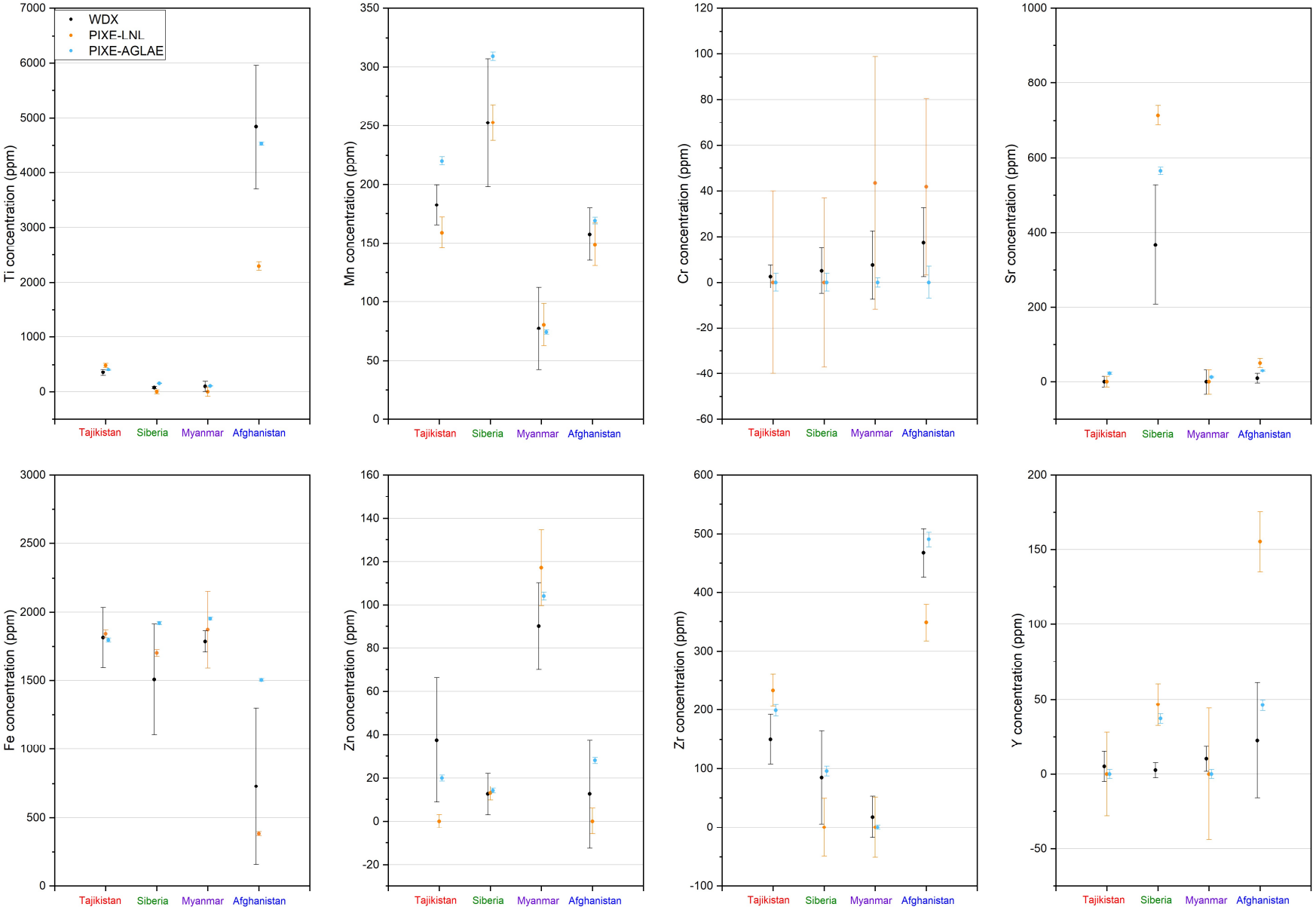

Figure 8.13. Intercomparison among trace elements concentration data obtained with SEM-WDX in Okayama, μ-PIXE at INFN-LNL and μ-PIXE at AGLAE.

8.1.2. Archaeological samples

In the following sections, the results obtained on archaeological samples are presented separately for each retrieval site and type of sample preparation.

8.1.2.1. Shahr-i Sokhta cross sections

The six cross sections obtained from Shahr-i Sokhta samples were firstly characterized with optical and CL microscopy and SEM-EDX, then they were analysed in vacuum at INFN-LNL. Wollastonite was not identified, so a correlation with Chilean provenance could be excluded. A synthesis of all mineral phases found in the different samples with SEM-EDX is compiled in table 8.2. Following further the provenance protocol to determine the geological origin of the raw material worked on site, 12 diopside and 9 pyrite crystals were measured. Samples SiS-28, SiS-44 and SiS-24 presented too small pyrite crystals on the cross section for a μ-IBA analysis. A quantitative elemental survey of pyrite crystals was also performed with SEM-EDX, to establish the composition of main elements (S and Fe) to be used in fixed matrix quantification via GUPIXWIN (see section 6.1). All pyrites showed no or little alteration, as no external rims can be seen in SEM-BSE images (clearly visible instead for Siberian reference geological samples [Angelici et al. 2015]) (figure 8.14).

Table 8.2. Mineral phases identified by means of SEM-EDX analysis in cross sectioned samples from Shahr-i Sokhta. X = detected but scarce.

SAMPLE	**44**	**24**	**28**	**62**	**336**	**337**
Lazurite	Yes	Yes	Yes	Yes	Yes	Yes
Diopside	Yes	Yes	Yes	Yes	Yes	Yes
Pyrite	X	X	Yes	Yes	Yes	Yes
Calcite	XX					
Dolomite	Yes	Yes				
K-feldspar	Yes	X	Yes	Yes		
Apatite	X	X	X	X	X	X
Iron Oxide (Fe, O)	X					
Galena? (Pb, S, Cu, Fe)	X					
Zircon		X	X		X	X
Titanite			X			
Phlogopite	X	Yes	Yes	X	Yes	Yes
Nepheline			Yes		Yes	
Spinel			X			
Celestina			X			
Uraninite			X	X		

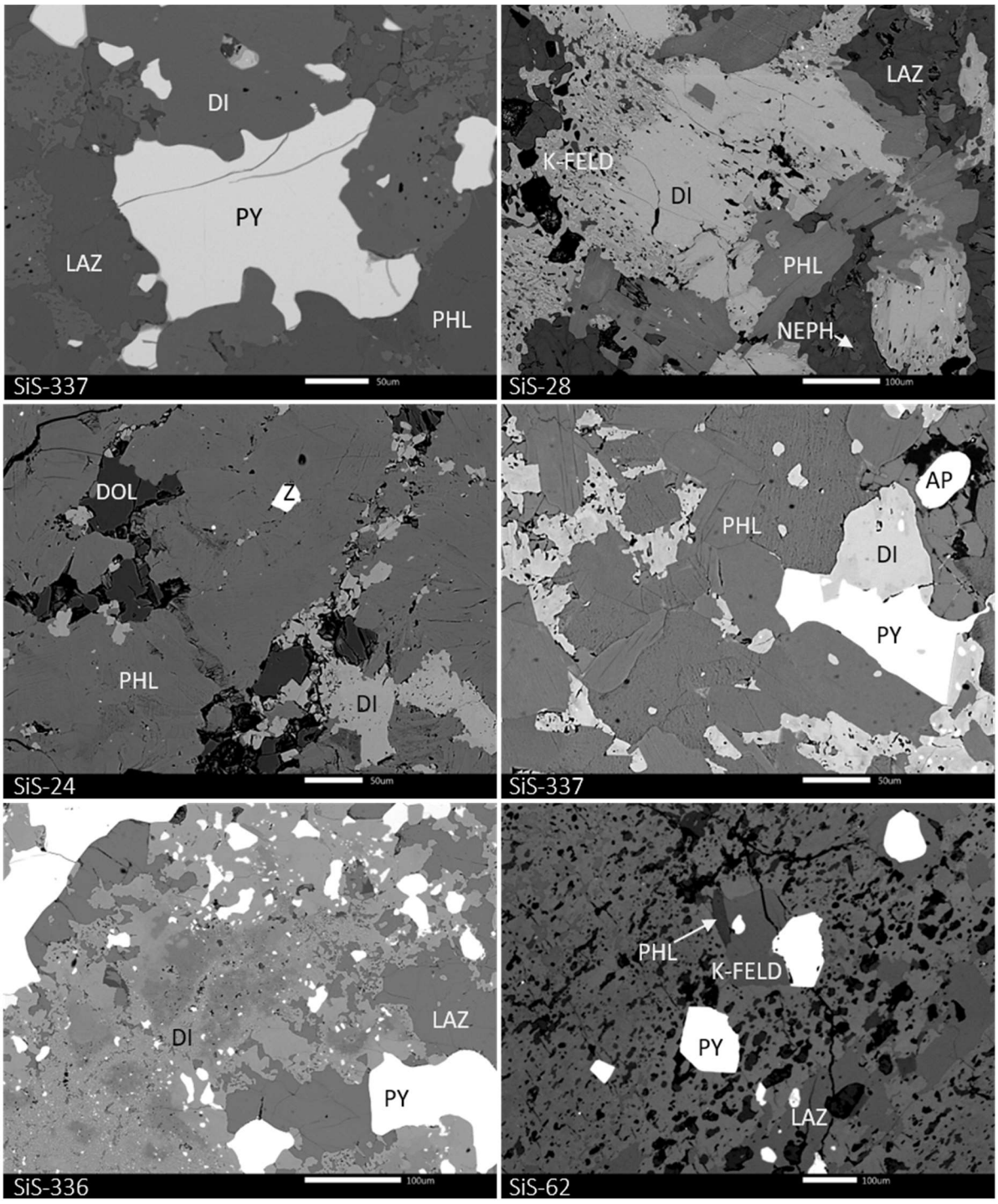

Figure 8.14. Examples of SEM BSE images for cross sections of Shahr-i Sokhta samples, with identification of mineral phases. DI = diopside, LAZ = lazurite, PY = pyrite, PHL = phlogopite, K-FELD = K-feldspar, NEPH = nepheline, DOL = dolomite, Z = zircon, AP = apatite.

Results for diopside markers obtained by μ-PIXE are shown in figure 8.15. Sr content remains below 100 ppm, excluding the Siberian provenance. Moreover, it emerges a higher Cr content, compatible only with reference Afghan samples from the 3rd quartile. Such a high concentration for Cr was detected even with

EDX microprobe, particularly in samples SiS-24, SiS-28, SiS-44 and SiS-337. V is also quite high and its median line is comparable to the Afghan one. Diopside is particularly low in Fe, and Zn (not reported in box plots) is below the LOD in almost all crystals except for one, with a content of 17 ppm only. All the μ-IL spectra (figure 8.16) show the main band at 585 nm, as well as a 770 nm band, weaker marker for the Afghan provenance. Moreover, only in spectra from sample SiS-336, two additional small peaks can be seen at 600 nm and 650 nm, while several others are located around 900 nm (figure 8.17). Such peaks were previously noted only in one Afghan sample of the database, AFG1. This was the Afghan sample bearing the higher Y content, in the hundreds of ppm: the same characteristic can be found in sample SiS-336, where the detected Y is equal to 200 ppm and 500 ppm for two crystals respectively.

Finally, sampled pyrites show a Ni content above 350 ppm and a Cu content below 200 ppm (figure 8.18), allowing to classify these Shahr-i Sokhta samples with quite good confidence as Afghan.

A test in projecting Shahr-i Sokhta diopside μ-PIXE data as an external dataset (see section 7.2.1.1) onto the space created by PCs seen in figure 8.10 provided the result in figure 8.19. The orange star markers corresponding to Shahr-i Sokhta cross section samples fall precisely at the centre of the Afghan group, as deduced by following the provenance protocol.

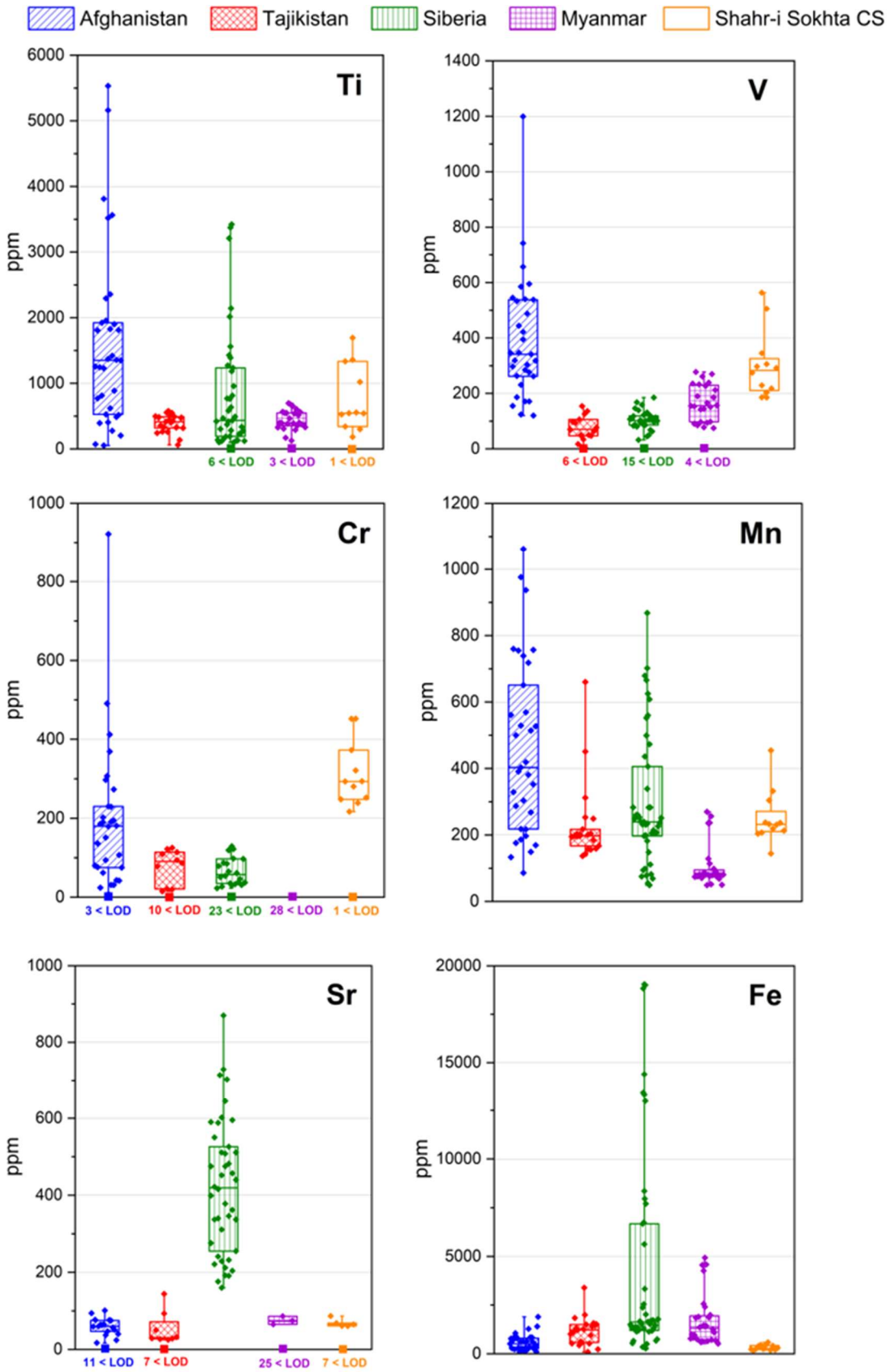

Figure 8.15. µ-PIXE results of trace elements in diopside for Shahr-i Sokhta cross section samples, compared to reference geological samples grouped by provenance area. The box plots represent the dispersion of the experimental points: the median line and the two percentile values 0.25 and 0.75. The squared symbols in correspondence to 0 value represent the number of measurements below the limit of detection (LOD).

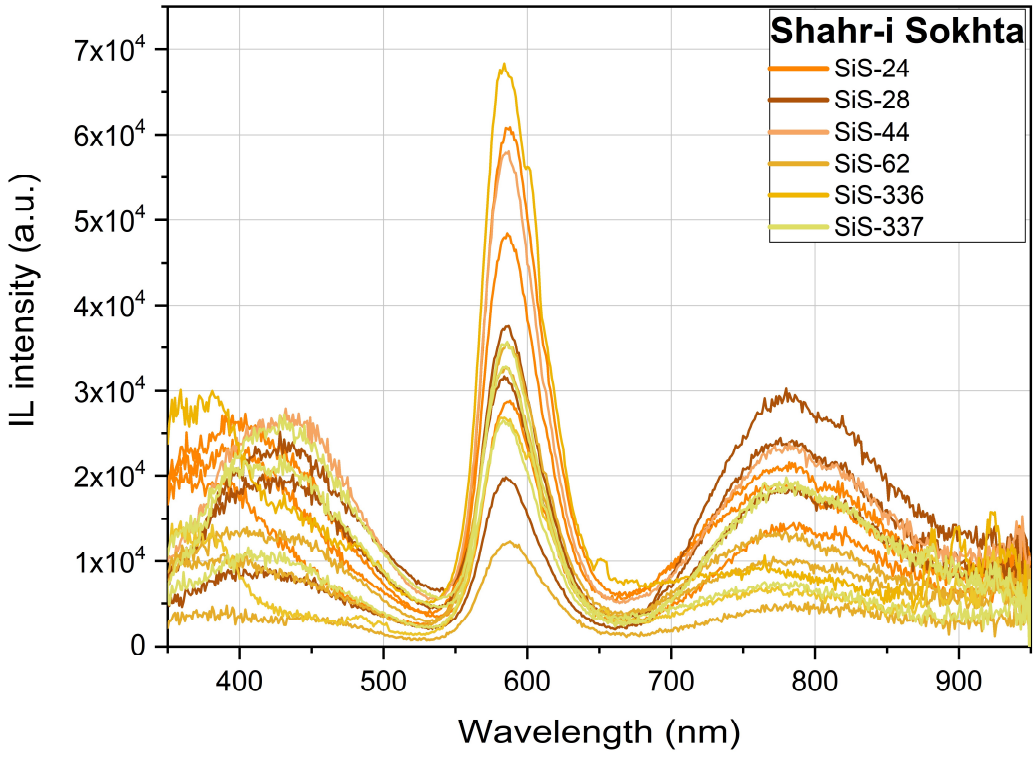

Figure 8.16. µ-IL spectra of diopside crystals analysed on Shahr-i Sokhta cross sections.

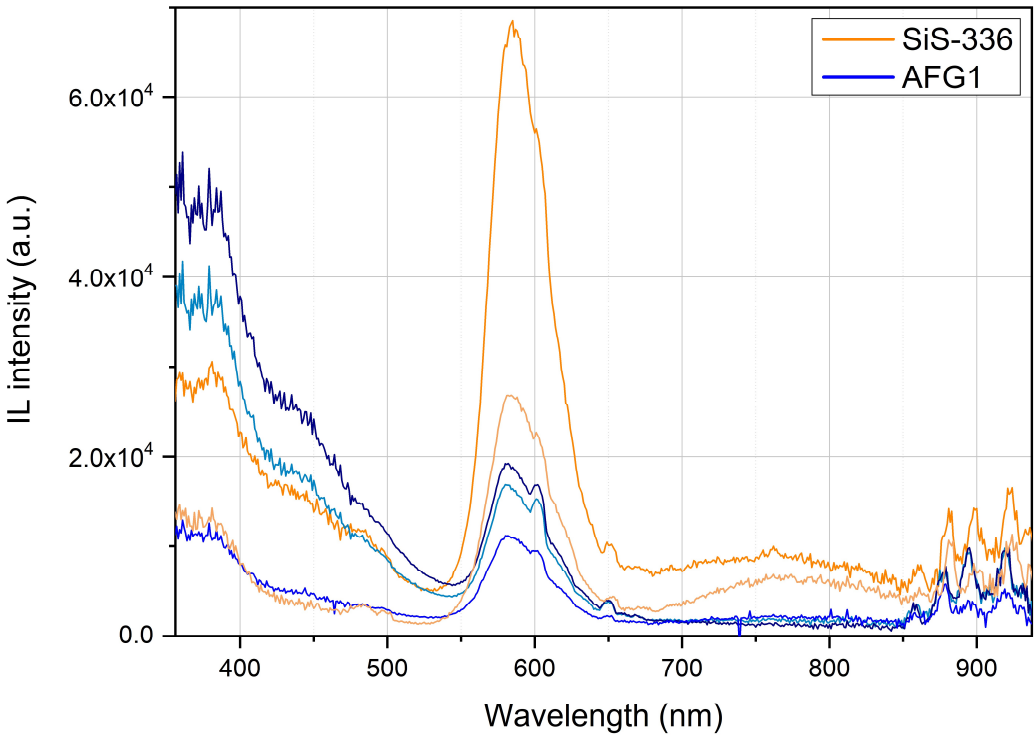

Figure 8.17. Comparison of µ-IL spectra acquired at INFN-LNL for samples SiS-336 (orange hues) and AFG1 (blue hues). Small peaks at 600 nm, 650 nm and around 900 nm are visible for both samples.

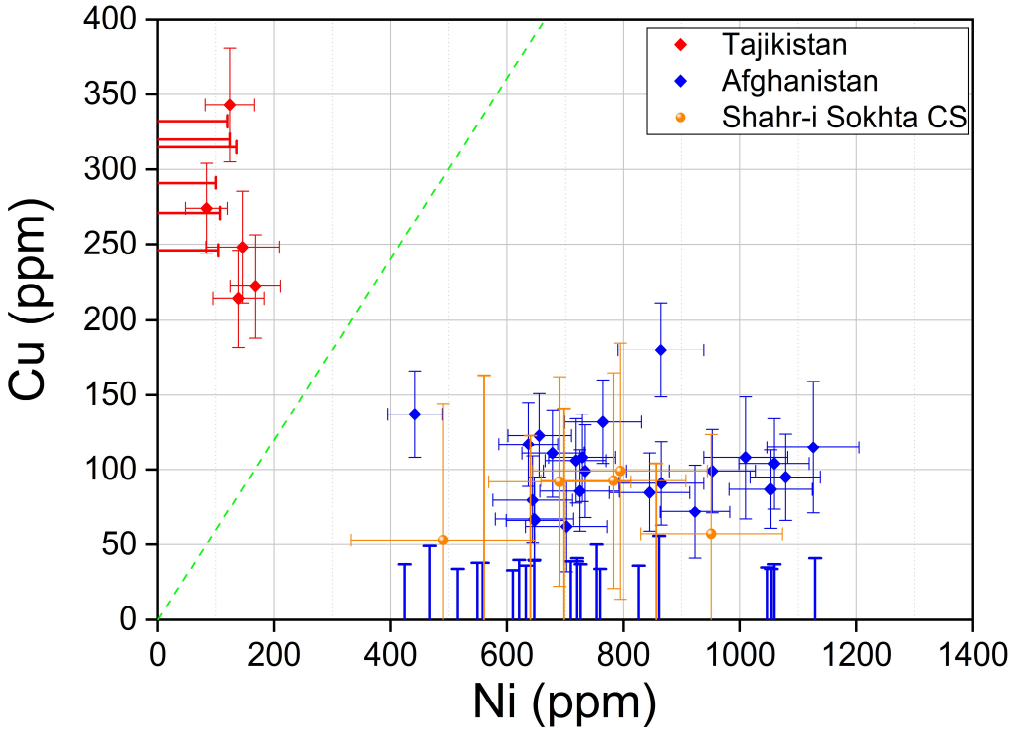

Figure 8.18. Results for strong markers in pyrite crystals from Shahr-i Sokhta cross sections. The green dashed line indicates the separation proposed in the new protocol.

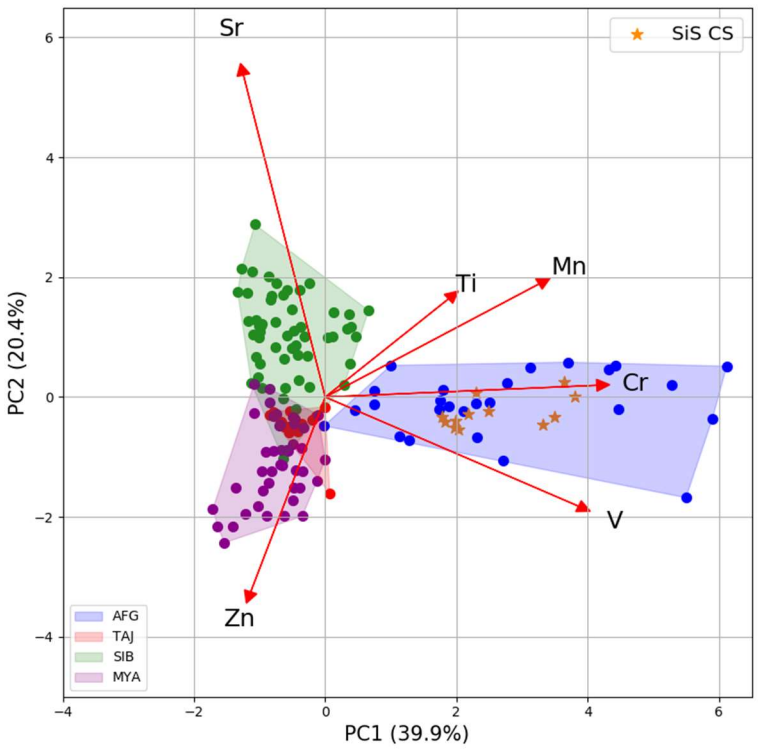

Figure 8.19. Projection of µ-PIXE data for trace elements in diopside from Shahr-i Sokhta cross sections (orange stars) on the PCs space obtained by means of PCA performed on reference samples. The percentage of explained variance for each PC is reported in brackets.

8.1.2.2. Shahr-i Sokhta samples at AGLAE

The additional 12 fragments from Shahr-i Sokhta were measured as such at AGLAE, just like provided by the archaeologists and without any pre-treatment. Due to geometrical constraints for their dimensions, samples were pre-characterised with optical microscopy in reflective light, but not with cold-CL. Additionally, on the basis of optical images acquired in OM, a survey of the surfaces was done by means of SEM-EDX at variable pressure (50 Pa, 20 kV) to select target diopside and pyrite crystals for the following IBA investigations. It was commonly found that superficial pyrites are very small for most of the samples and partially altered with loss of S on the rims (examples can be seen in figure 8.20), even if not completely transformed in iron oxide-hydroxides as seen in Siberian samples. EDX results excluded as well the presence of wollastonite. In total, μ-PIXE and μ-IL maps around 41 diopside and 16 pyrite crystals were acquired in AGLAE during both runs in 2019 and 2020. A selection of those crystals was discarded after data analysis, following the procedure described in section 6.2.

Box plots for diopside trace markers are shown in figure 8.21. Ranges for Ti and V reflects those previously seen for cross section samples. Mn and Fe seems to be slightly higher, but this might also be due to post-depositional alterations on the raw surfaces. The highest value for Mn is on both runs for sample SiS-67, that also shows high Sr content (162 ppm). Sample SiS-186 present a Sr concentration (270 - 370 ppm) in the Siberian ranges, being an outlier in respect to the others: however, this higher Sr content is found only in 2 out of 3 analysed diopsides, that at a closer look reveal some irregularities possibly filled with soil dirt. A confirmation to this hypothesis is that SiS-186 is one of the only two samples having Zn concentration higher than 100 ppm in diopsides, for both measuring runs. The other one is SiS-331, that presents on its surfaces some greenish areas that can be considered contaminations from external environment. Further examination of this green material is presented later in this section.

Interesting is instead the case of Cr, significantly lower in respect to the samples measured in vacuum at INFN-LNL (where was generally above 200 ppm). The SiS-336 cross section was also analysed with AGLAE extracted beam, to investigate further the possible activators for the small peaks. The Cr content measured on two crystals of this sample at AGLAE resulted in both cases under the limit of detection; Cr values for the same crystals at INFN-LNL were respectively the only point under LOD and the lowest detected one (see figure 8.15).

This seems to confirm the general tendency of lower detected PIXE concentrations at AGLAE, as seen for reference geological samples. In the next measuring runs, a comparison on at least one of the cross section samples with higher Cr concentration (e.g. SiS-337) will be performed, to check if this this trend is confirmed and if the different Cr ranges for cross sections are actually related to the specific samples.

μ-IL spectra for diopsides are presented in figure 8.22a. Due to the substitution of the spectrometer mentioned in section 6.3, in the plot 2019 and 2020 spectra are differentiated with solid or dashed lines.

The 585 nm band is present for all samples, and most of them also show the 770 nm band. However, samples SiS-178, SiS-181 and SiS-186 present instead a band more centred around 700 nm. These samples are also the ones presenting higher Mn content. The two spectra from sample SiS-336 show as expected the small peaks at 600 nm, 650 nm and around 900 nm, with a Y content of 199 and 220 ppm respectively (figure 8.22b). In addition, sample SiS-325 also show small evidences of such peaks, even with a Y content of just 15 ppm.

Trace elements concentrations of 13 pyrite crystals were obtained. A distinction between the two runs has been made clear in figure 8.23, where the issue mentioned in section 6.3 becomes evident: in 2020 the enlargement of the PIXE peaks due to instrumental changes results in the significant reduction of detected concentrations for elements with a high Z, such as Ni and Cu. The point at 700 ppm of Cu can be taken as example: this sample (SiS-333) presented the same peculiar contamination with greenish stripes on the surfaces as SiS-331, that could be traced back to Cu oxides and can explain the extremely high content for Cu. Comparable quantities of Cu were found also analysing diopside crystals on the same sample. However, the pyrite from the same sample but analysed in 2020 (yellow point near Tajiki group in figure 8.23) shows concentration significantly lower for both Cu and Ni. After this consideration, it was

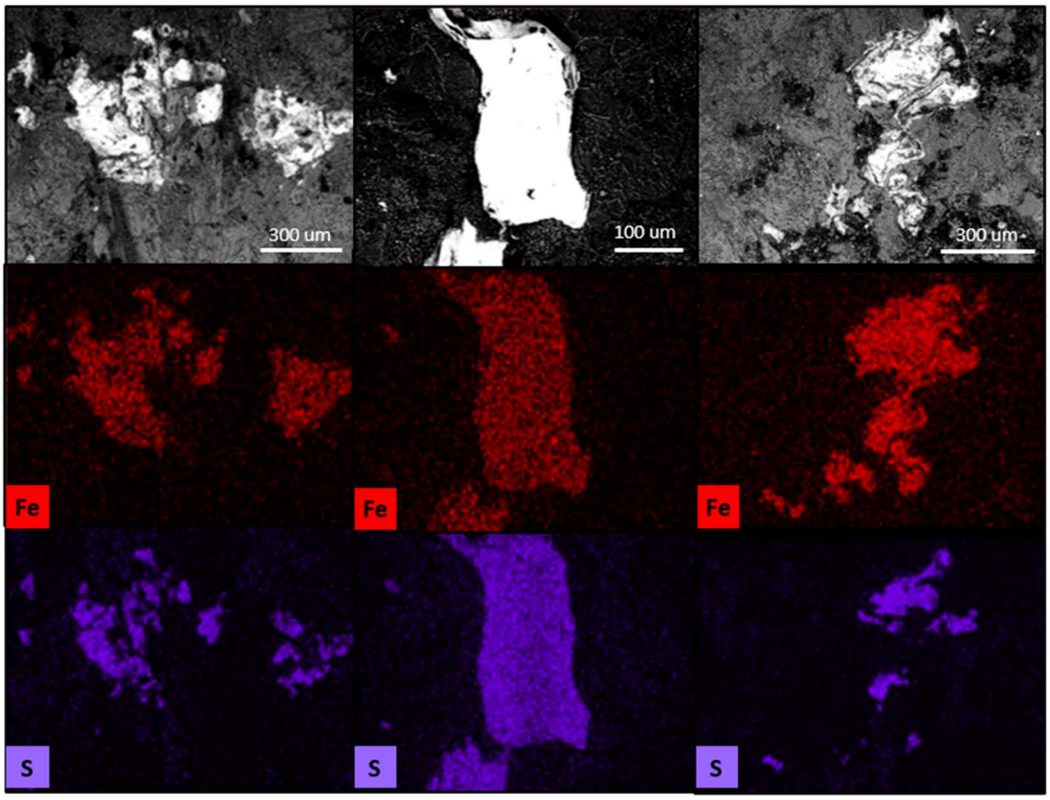

Figure 8.20. Examples of pyrite crystals analysed on surfaces of Shahr-i Sokhta samples. SEM BSE images (top), Fe (middle) and S (bottom) EDX maps for samples SiS-187, SiS-4, SiS-331 (from left to right).

chosen to discard all results for pyrites collected in the 2020 measuring session, especially for the Chagai Hills and Indus Valley samples that were analysed on that run only. Points will be re-acquired in the upcoming run.

Cu on sample SiS-333 was high enough to be detected via SEM-EDX (figure 8.24), that revealed in those green areas also high Zn and Cl content. Same contamination was found in sample SiS-331, as previously anticipated by μ-PIXE results, that for its Zn content is projected in the PCs space away from the Afghan group and beyond Myanmar (figure 8.25).

Results obtained at AGLAE on these samples, especially if compared to the cross sectioned ones, highlighted all the issues that can arise in the analysis of archaeological materials with troubled conservation history, that at the same time should be disturbed the least possible for their historical or artistic importance. Such results should then be always evaluated carefully. In this case, it might be worth to repeat the analyses after a cleansing of surfaces, especially on those samples showing lower Cr content and an absence of the 770 nm band, as they could confirm the result obtained by Casanova and Delmas [Casanova 1992; Delmas and Casanova 1990] where the analysed Shahr-i Sokhta samples had higher compatibility with a Tajik provenance than with an Afghan one.

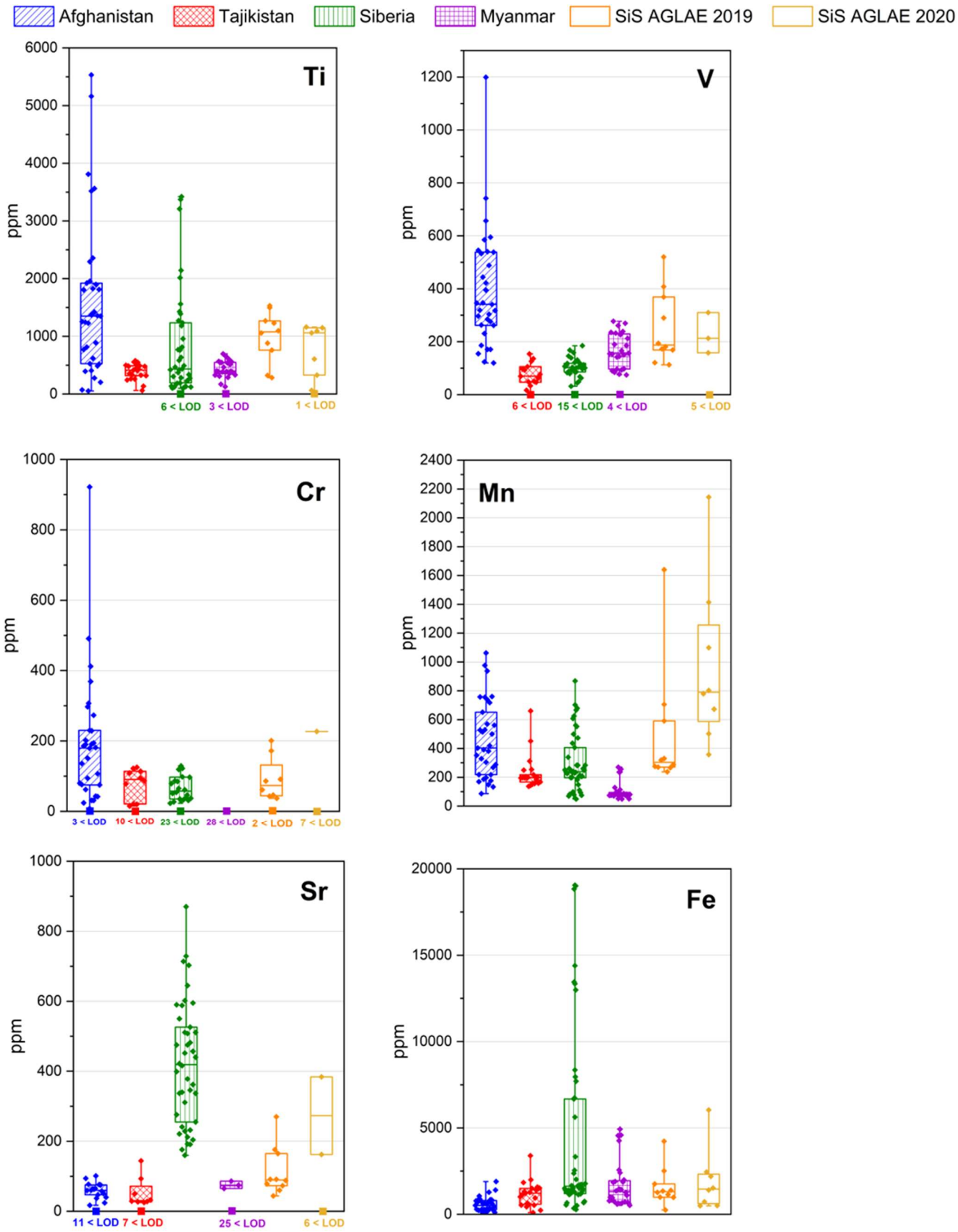

Figure 8.21. µ-PIXE results of trace elements in diopside for Shahr-i Sokhta samples analysed as such at AGLAE, compared to reference geological samples grouped by provenance area. Measuring sessions of 2019 and 2020 are considered separately. The box plots represent the dispersion of the experimental points: the median line and the two percentile values 0.25 and 0.75. The squared symbols in correspondence to 0 value represent the number of measurements below the limit of detection (LOD).

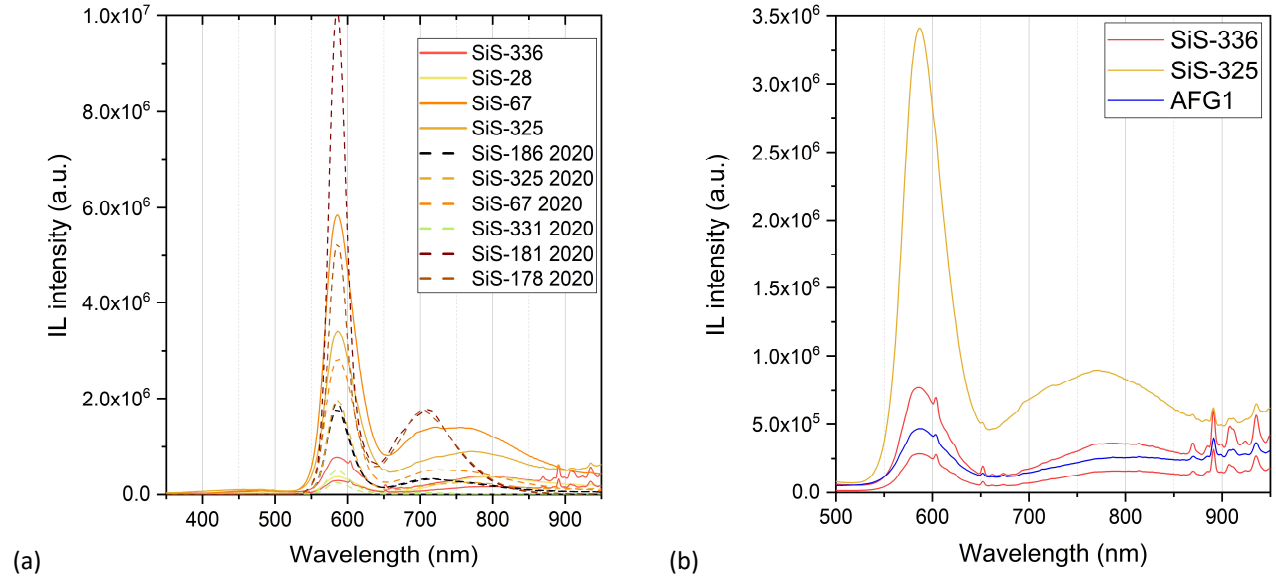

Figure 8.22. (a) µ-IL spectra of diopside crystals analysed on Shahr-i Sokhta samples at AGLAE. 2020 measurements are reported with dashed lines. The 2020 spectra were divided by a factor of 10 for better visualisation and comparison. (b) Comparison of µ-IL spectra acquired at AGLAE for samples SiS-336, SiS-325 and AFG1. Small peaks at 600 nm, 650 nm and around 900 nm are visible for all samples.

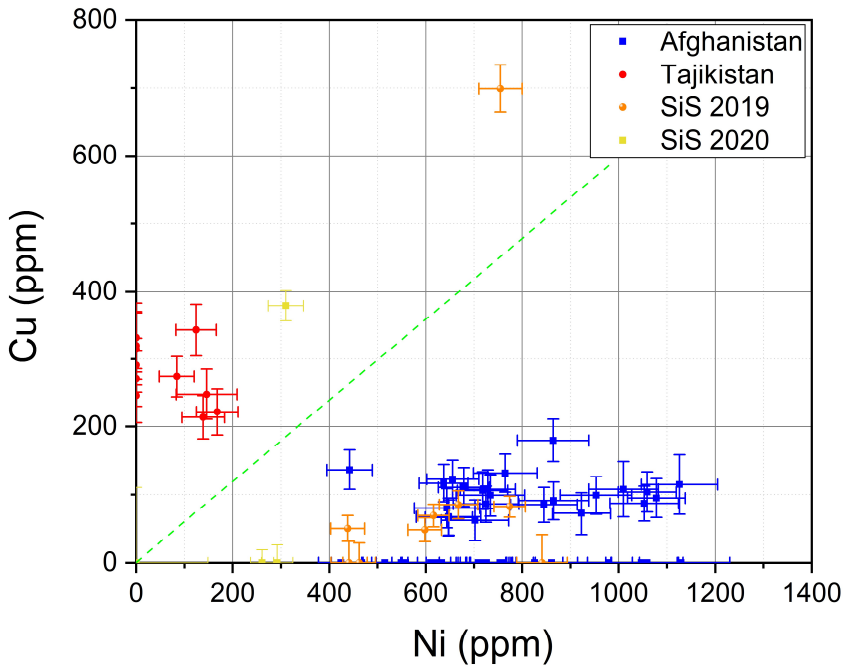

Figure 8.23. Results for strong markers in pyrite crystals from Shahr-i Sokhta samples analysed as such at AGLAE. Measuring sessions of 2019 and 2020 are considered separately. The green dashed line indicates the separation proposed in the new protocol.

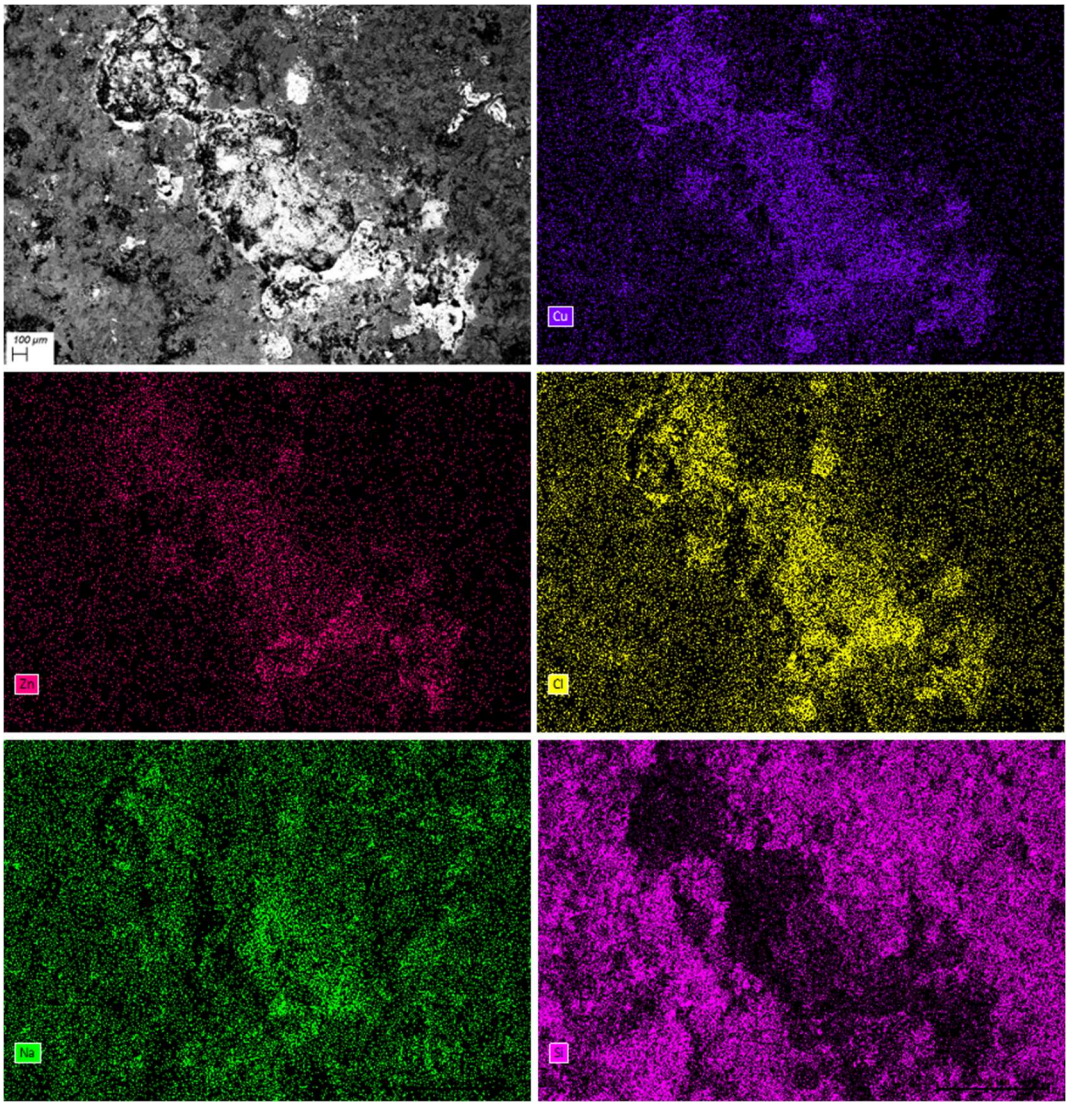

Figure 8.24. SEM-BSE image and EDX maps for one of the greenish areas on sample SiS-333. The high concentration of Cu, Zn and Cl is appreciable, together with absence of Si and some Na present in the central area.

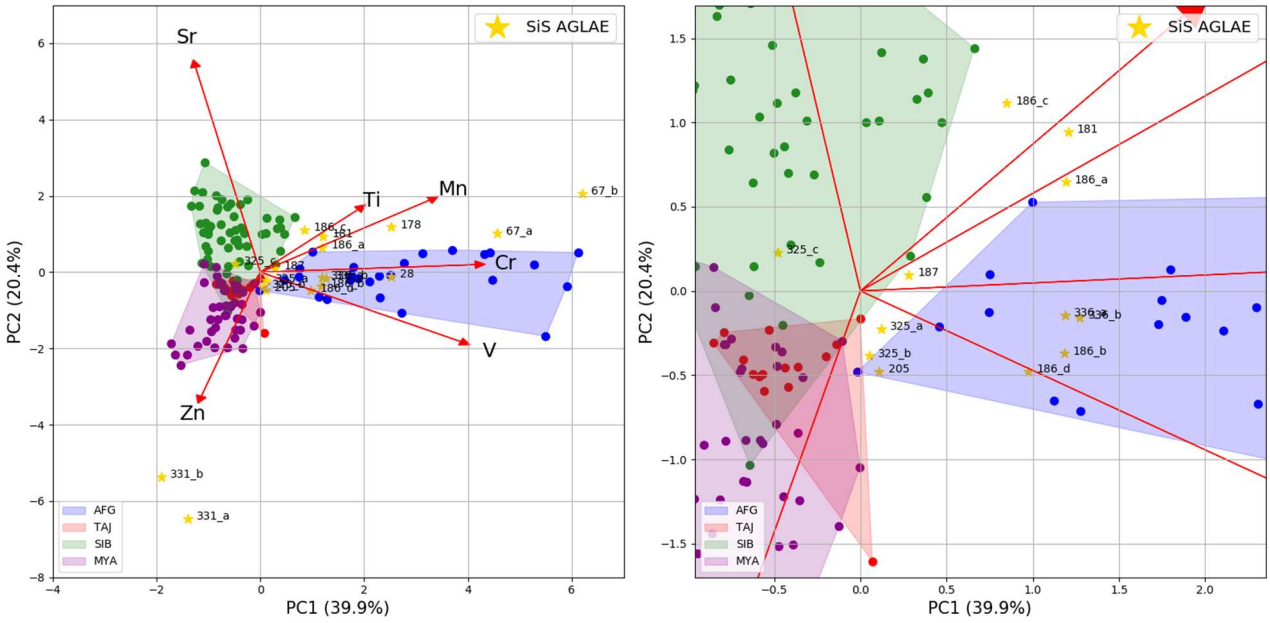

Figure 8.25. Projection of µ-PIXE data for trace elements in diopside from Shahr-i Sokhta samples as such (yellow stars) on the PCs space obtained by means of PCA performed on reference samples. The percentage of explained variance for each PC is reported in brackets. Labels of archaeological samples are reported to recognise the outliers. On the right, a zoom of the area around the origin of axes.

8.1.2.3. Seal

The marvellous lapis lazuli seal found at Shahr-i Sokhta (sample CS10335/20a) is here presented separately not only for the complete manufacturing that differentiate it from the other samples, but also in light of its results. It should be stressed out that even if it was found on the premises, this does not guarantee that it was actually produced locally. The carved decoration represents a challenge in the acquisition of large maps with probes such as electrons or protons, as the radiative signals emitted from the dips can be reabsorbed by the material without reaching the detector and then leaving the map incomplete in some parts or inducing analytical artifacts. After a preliminary characterisation with SEM-EDX at variable pressure (50 Pa, 20kV) that excluded the presence of wollastonite, on this sample only one large µ-PIXE map was acquired at AGLAE on the lateral side (figure 8.26), making sure to extract spectra during data analysis only from the prominent parts. Moreover, specific crystals were selected for IBA analysis throughout the sample, also from the flat parts of the end sides, where another large map was acquired, reaching a total of 11 diopside and 3 pyrite spectra extracted and quantified.

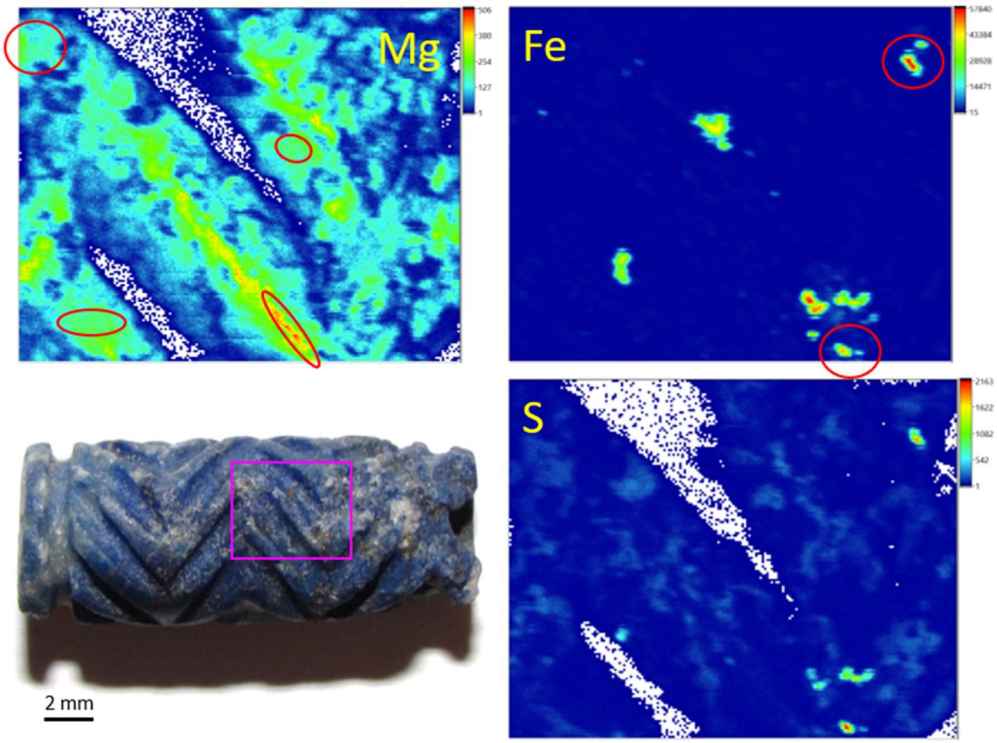

Figure 8.26. µ-PIXE bidimensional maps acquired on the seal, dimension 5 × 4 mm. Colour scale goes from blue (minimum value) to red (maximum value). Selected area on sample is denoted by the purple square. Mg, Fe and S maps are reported and points selected for spectra extraction are shown with red circles. It is visible the lack of signal from the dips, especially for low Z elements.

V content is on average lower that what was found in other Shahr-i Sokhta samples, remaining for all diopside crystals below 200 ppm (figure 8.27). Sr is generally well below the 180 ppm limit of Siberian provenance, exception made for two areas extracted from the same crystal, bearing a Sr content of 300 ppm. This area was investigated *a posteriori* with SEM-EDX, but nothing unusual was found from a compositional point of view. However, the crystal was not among the largest in dimensions and it has an irregular surface, and it is possible that the proton microbeam sampled a volume in a deeper region in respect to what can be reached by an electron microprobe, so this two points should be considered carefully. Furthermore, Cr was once again the most interesting trace element as it remained below the detection limit for all analysed crystals, both during 2019 and 2020 measuring runs. Adding to such results the absence of a 770 nm band in IL spectra (figure 8.28) and a Cu content in pyrites higher than 3/5 of Ni content (figure 8.29), it can be suggested that the seal was not made with Afghan lapis lazuli, but most probably Tajik. The possibility of an exploitation of Tajik quarries is supported also by the proximity of Pamir Mountains to the Afghan lapis lazuli sources, as can be seen in figure 4.5. Indeed, in light of the new proposed protocol, from a mere analytical point of view it cannot be excluded the possibility of Myanmar provenance, especially considering that detected Zn content varied between 44 and 108 ppm. This is evident also by the projection of the μ-PIXE diopside dataset on the PCs plot (figure 8.30). Such an outcome, carefully evaluated together with archaeologists, could have a major impact on the knowledge of trading routes passing by Shahr-i Sokhta.

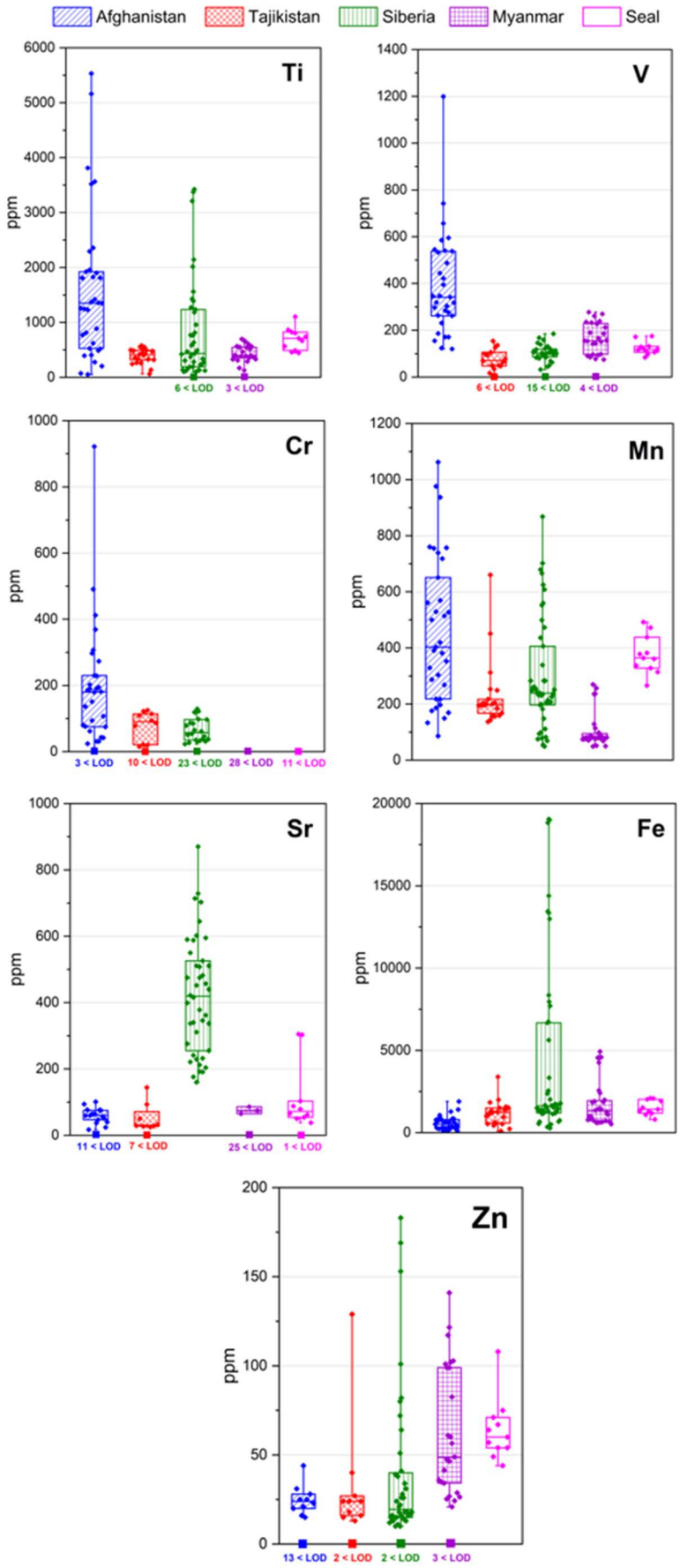

Figure 8.27. µ-PIXE results of trace elements in diopside for seal, compared to reference geological samples grouped by provenance area. The box plots represent the dispersion of the experimental points: the median line and the two percentile values 0.25 and 0.75. The squared symbols in correspondence to 0 value represent the number of measurements below the limit of detection (LOD).

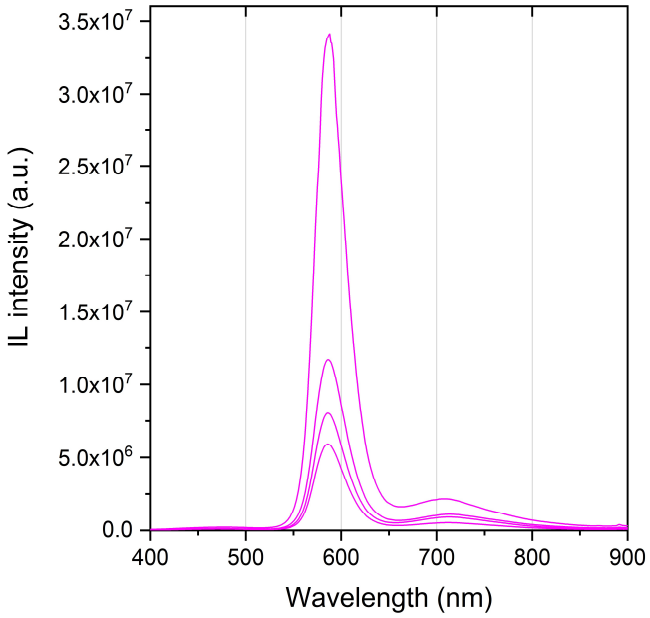

Figure 8.28. µ-IL spectra of four different diopside crystals analysed on the seal.

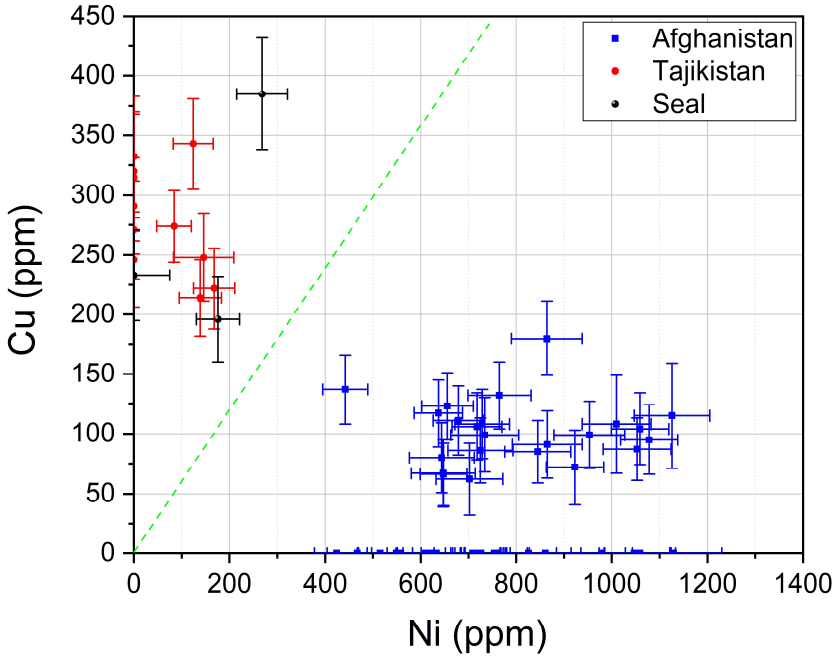

Figure 8.29. Results for strong markers in pyrite crystals from the seal. The green dashed line indicates the separation proposed in the new protocol. The point with Ni < LOD is the only one acquired in 2020.

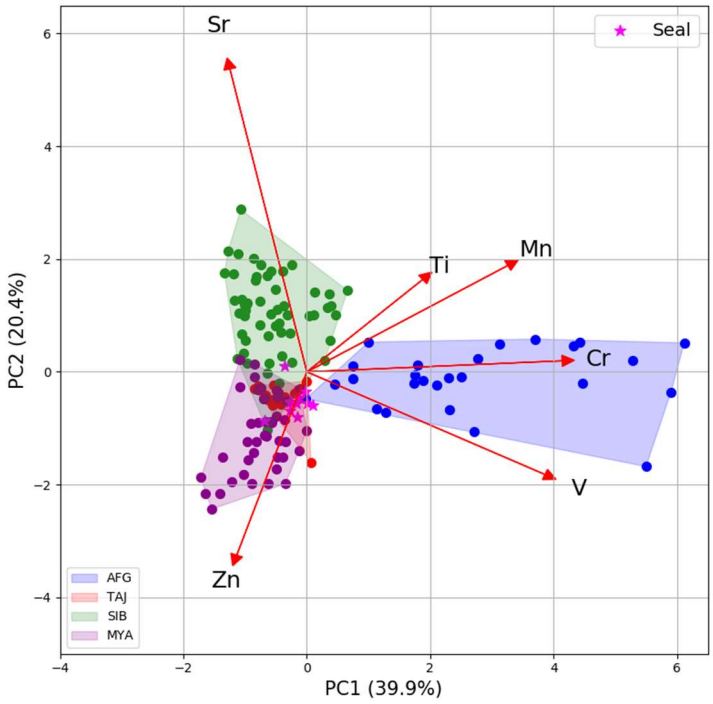

Figure 8.30. Projection of µ-PIXE data for trace elements in diopside from the seal (magenta stars) on the PCs space obtained by means of PCA performed on reference samples. The percentage of explained variance for each PC is reported in brackets.

8.1.2.4. Indus Valley samples

The 6 samples have been characterised under OM and SEM-EDX before performing µ-IBA on selected target crystals. All of them, with the exception for SHT-1, presented the lazurite phase intercalated by very big crystals or veins of white- and grey-coloured mineral phases. SHT-1 has instead a much finer texture with a preponderance of dark blue lazurite and small and homogeneously distributed pyrites, visible in particular on the cross section (figure 8.31). Harappan samples show very big and well preserved pyrites, as well as a seemingly preferred crystal orientation. Samples from Loal Mari and Lakhanjo-Daro present also localized alterations or contaminations of a reddish patina, that in SEM-EDX analysis revealed predominantly a very high Fe content.

At AGLAE, a total of 12 diopside crystals were chosen for PIXE elemental quantification and IL spectra collection. From box plots of µ-PIXE data in figure 8.32, it can be seen how concentration values are quite homogeneous among the samples, exception made for sample SHT-1 - retrieved on Shortughaï site - that is circled in yellow for each element. This sample has in particular a much higher content of Mn, Ti, V and Cr, most of them weaker markers for an Afghan origin. The three points with Sr content near 180 ppm belong instead to samples L-Mfrag and HR-83a, but there evidently is a variability within the samples,

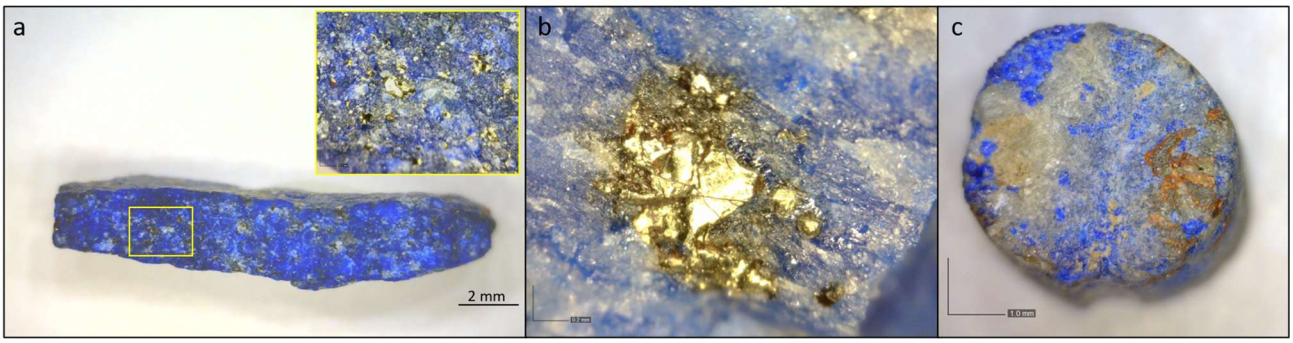

Figure 8.31. Optical microscopy images of (a) section of sample SHT-1, with the magnified area in the yellow rectangle; (b) pyrite crystal on sample HR-83a; (c) reddish patina on sample L-Mbead.

since other crystals in the same fragments have lower or even <LOD Sr concentrations. Zn was always detected below 40 ppm.

All samples show the IL band at 585 nm (figure 8.33). The band centred at 770 nm is visible for most samples, whereas for sample HR-83b the band is shifted towards 700 nm: this is one of the samples with Cr <LOD.

As previously explained, data from pyrites are not reported here and the analyses will be repeated in the next measuring session at AGLAE.

The outcome of the projection of diopside markers on PCA space highlights the difference of the Shortughaï sample in respect to the others (figure 8.34). This result seems to lead towards an Afghan provenance for this sample, compatible with the very close proximity of the site to the Sar-e-Sang quarries. With definitive results on pyrite crystals it will be possible to draw a more accurate conclusion.

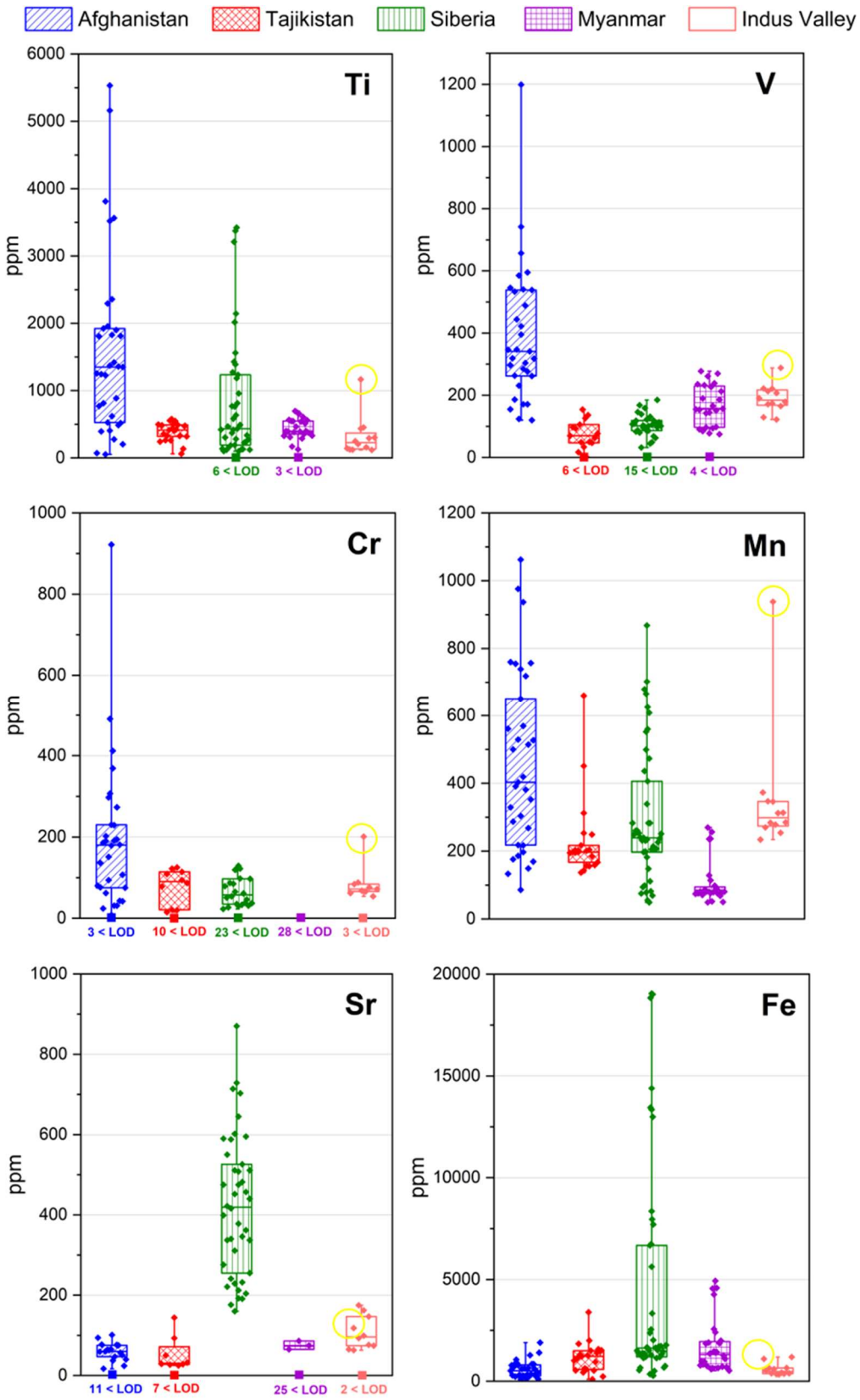

Figure 8.32. µ-PIXE results of trace elements in diopside for Indus Valley samples, compared to reference geological samples grouped by provenance area. The box plots represent the dispersion of the experimental points: the median line and the two percentile values 0.25 and 0.75. The squared symbols in correspondence to 0 value represent the number of measurements below the limit of detection (LOD). Sample SHT-1 (Shortughaï site) is circled in yellow.

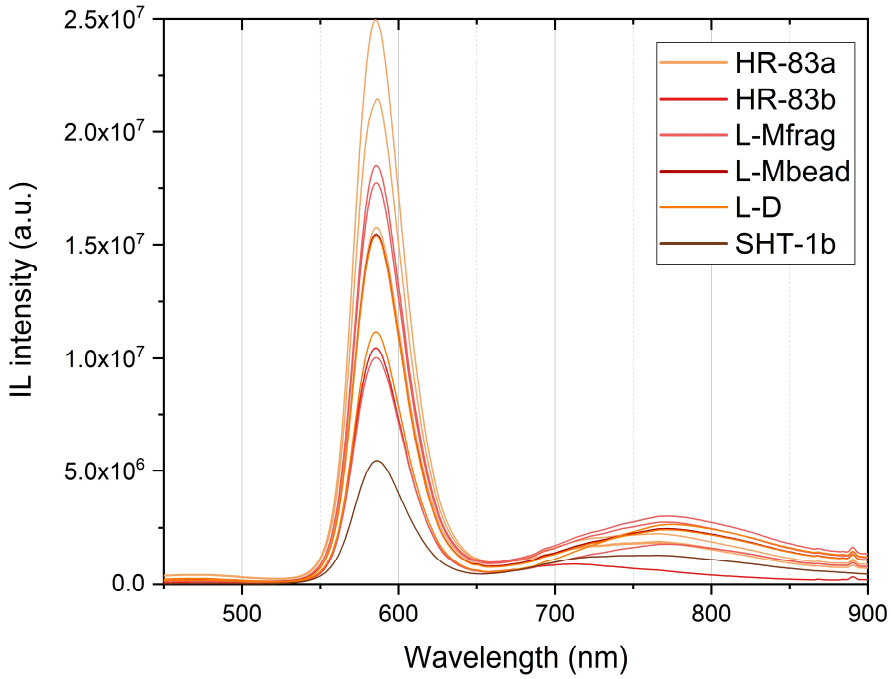

Figure 8.33. µ-IL spectra of diopside crystals analysed on Indus Valley samples at AGLAE.

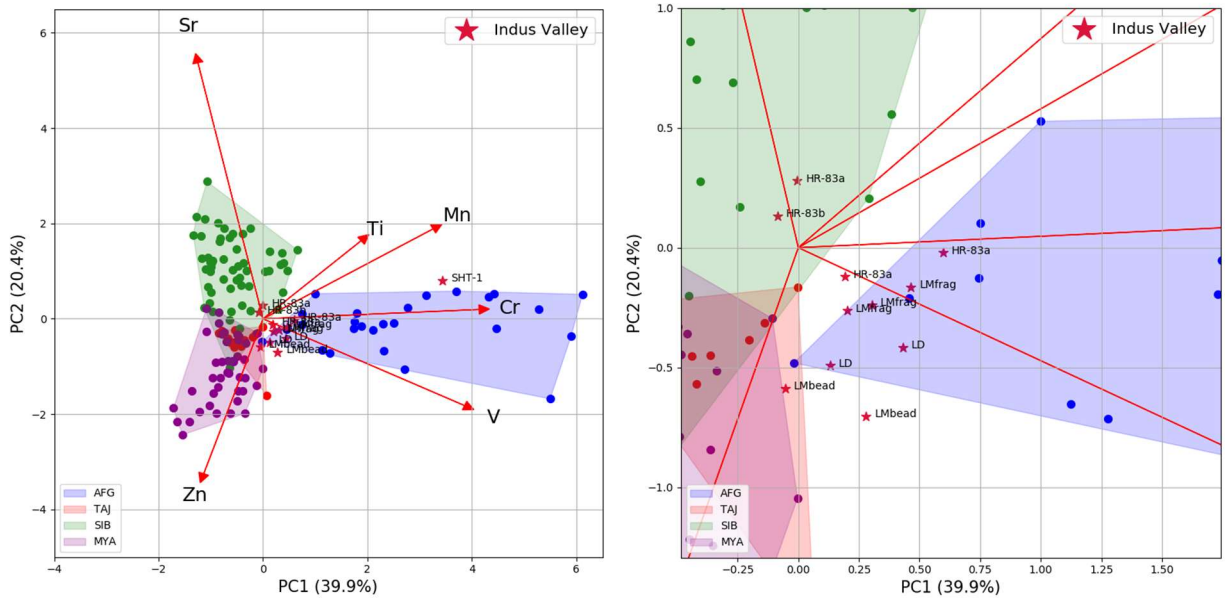

Figure 8.34. Projection of µ-PIXE data for trace elements in diopside from Indus Valley samples (red stars) on the PCs space obtained by means of PCA performed on reference samples. The percentage of explained variance for each PC is reported in brackets. Labels of archaeological samples are reported. On the right, a zooming of the area around the origin of axes.

8.1.3. Chagai Hills geological samples

The 4 lapis lazuli rock samples supposedly coming from Chagai Hills quarries were considered in the first instance as rocks of unknown provenance, and the protocol was applied to identify possible differences with the provenances already known.

These samples presented in optical images similar textures, with bright blue lazurite intertwined with smaller or larger crystals of white minerals, occasionally present in veins. Pyrites are diffused, sometimes in very large crystal occurrences: however, the analysis with SEM-EDX in variable pressure revealed for all of them a partial alteration with loss of S. Comparing optical and EDX maps for the largest pyrite crystal found in sample CH-2a (figure 8.35), it seems that the alteration could be present only at a very superficial level, as a homogeneous S distribution can be seen where the pyrite appears to be chipped. Most of large white crystals in sample CH-2a were identified as calcite, whereas diopside occurs in smaller crystals mixed with lazurite and other mineral phases. A very high Cl content was found with EDX in diopside crystals for sample CH-3a: all crystals selected from this sample were actually discarded after μ-PIXE quantitative analysis, since the concentrations of "contaminant" elements were found to be too high (3.6 wt% Na, 7.2 wt% Al, 1.2 wt% S, 0.4 wt% Cl, 2.6 wt% K on average). Hence, results for a total of 7 diopside crystals are reported in the box plots (figure 8.36), considering at least two crystals per sample CH-1, CH-2a and CH-4. At a general glance, V and Mn are present in medium-high ranges: the highest values belong all to sample CH-2a. The only two points above LOD for Sr are respectively one from CH-1 (176 ppm) and one from CH-4 (38 ppm). The same samples own the 2 points under LOD for Cr, whereas sample CH-2a has 2 out of three points with Cr above 100 ppm. Points below 50 ppm for Zn concentration belong instead to samples CH-1 and CH-4. Moreover, no other evident new marker was identified in diopside for any sample. By projecting the diopside dataset on PCs plot (figure 8.37), each sample falls in different areas

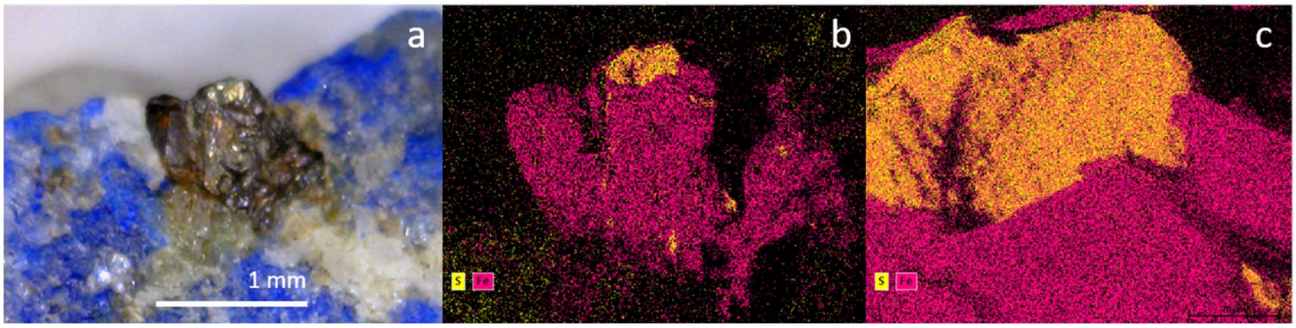

Figure 8.35. One of the pyrite crystals on sample CH-2a. (a) optical microscopy image; (b) combined S and Fe SEM-EDX maps; (c) zoom on the chipped part of the crystal.

of the PCs space. Sample CH-2a, the most alike to Afghan provenance features, overlaps only partially to the reference samples cloud. This is most probably due to its high Zn content, that may nonetheless derive from surface contaminants: analyses on a fresh cut of the samples might be decisive to confirm or exclude this possibility. We have a partial confirmation of the results obtained by Law with Sulphur Isotope Analysis [Law 2014], despite him having a lower number of reference geological samples (e.g. just 2 for Myanmar) and no Tajik provenance available: in his study, all Chagai Hills samples were only compatible with Afghan rocks. It arises therefore the need to increase our database on Afghan reference samples, to verify an exact compatibility for these hypothetical Chagai Hills rocks.

As regards μ-IL spectra (figure 8.38), all samples show the characteristic 585 nm band for diopside, and samples CH-2a and CH-4 present a band at long wavelengths clearly centred around 770 nm; for sample CH-1 the band spreads on a larger λ range, in a behaviour similar to what was observed for sample MYA06. Only in sample CH-4 Y was detected above LOD, with a content of 83 ppm, and in μ-IL spectra evidences for 600 nm and 650 nm peaks are present.

In addition, for sample CH-4 alone it was detected a widespread distribution of Cu throughout the whole rock, both in analysed diopsides and pyrites, but no green alteration were observed on the surfaces. As for Indus Valley samples, data from pyrites are not reported here and the analyses will be repeated in the next measuring session at AGLAE.

In conclusion, the investigated rock samples from Chagai Hills seem so far quite different from one another, hence their belonging to a common provenance is questionable. Moreover, the absence of specific new PIXE markers or IL features makes it currently impossible to identify any one of them as coming from a different provenance.

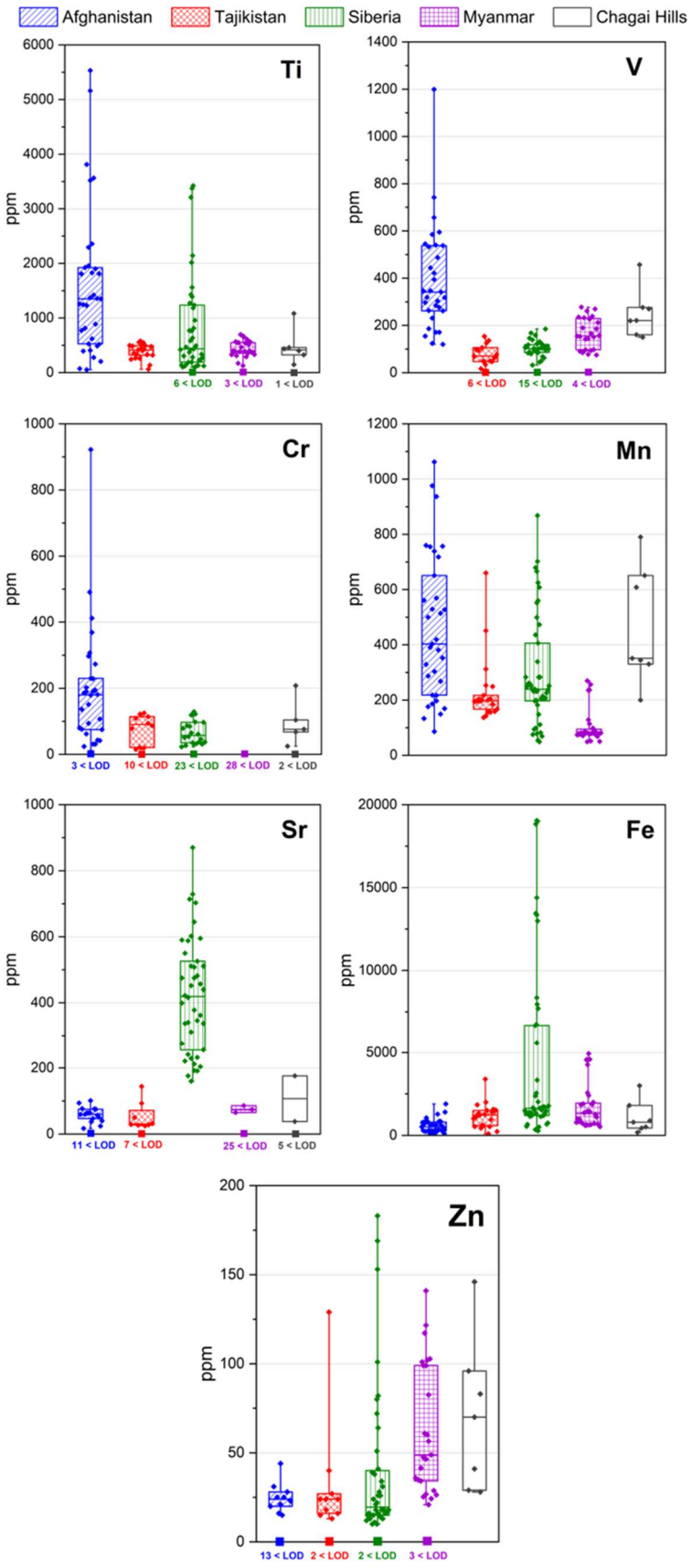

Figure 8.36. µ-PIXE results of trace elements in diopside for Chagai Hills samples, compared to reference geological samples grouped by provenance area. The box plots represent the dispersion of the experimental points: the median line and the two percentile values 0.25 and 0.75. The squared symbols in correspondence to 0 value represent the number of measurements below the limit of detection (LOD).

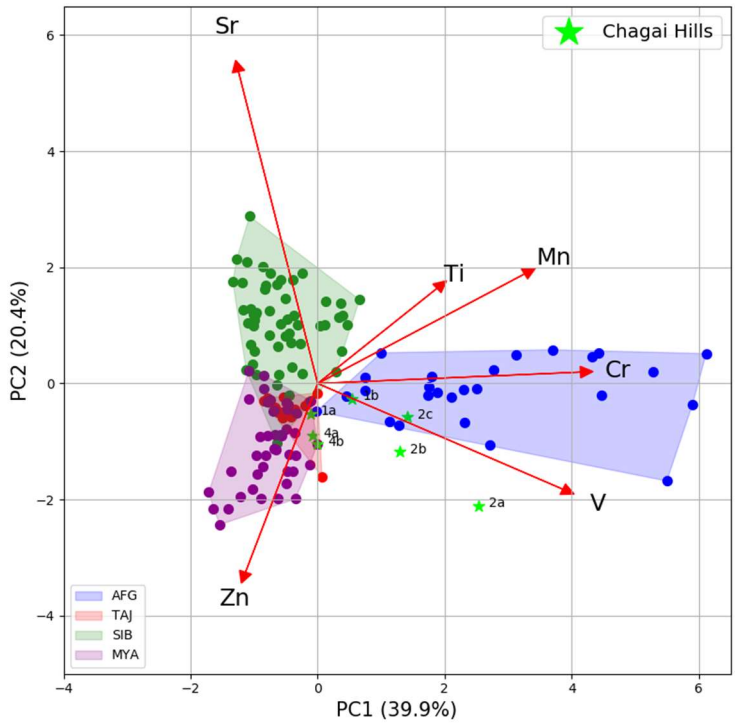

Figure 8.37. Projection of µ-PIXE data for trace elements in diopside from Chagai Hills samples (green stars) on the PCs space obtained by means of PCA performed on reference samples. The percentage of explained variance for each PC is reported in brackets. Short labels of archaeological samples are reported.

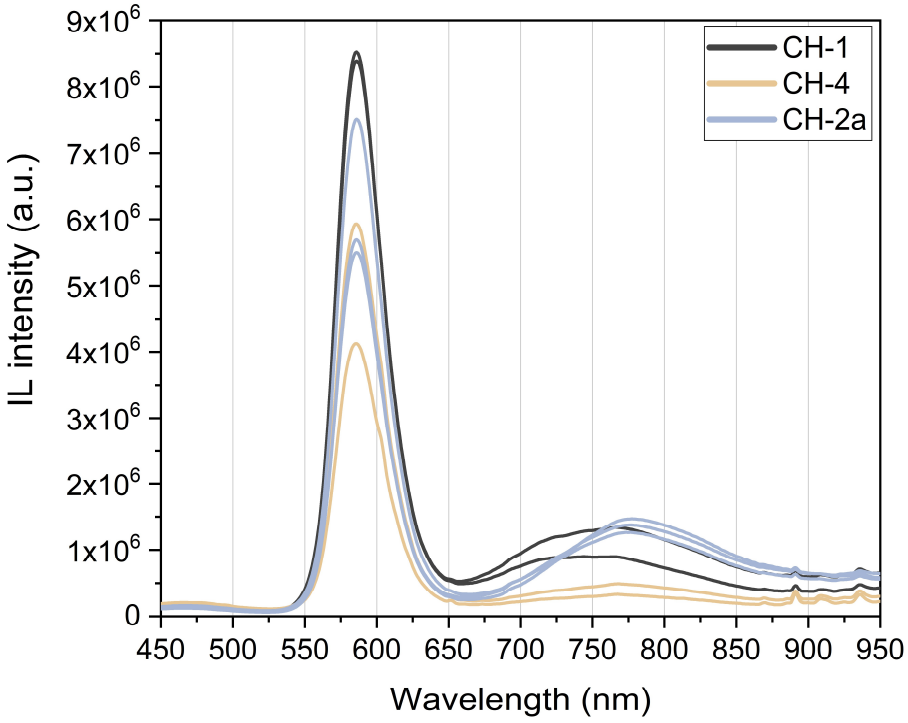

Figure 8.38. µ-IL spectra of diopside crystals analysed on Chagai Hills samples at AGLAE.

8.1.4. Multivariate analysis: classification

On the basis of μ-PIXE diopside data from reference geological samples, already explored with PCA, a supervised classification was also performed using LDA method. The considered variables are once again markers Ti, V, Cr, Mn, Zn and Sr contents. For the training set 131 analysed crystals were selected from the database; the 27 remaining formed the test set. The four classes defined *a priori* and fed to the algorithm were Afghanistan (AFG), Tajikistan (TAJ), Siberia (SIB) and Myanmar (MYA). The internal cross validation of the model using 5 different blocks provided a good result, with 81.3% of correct assignation to classes; wrong assignations occurred mainly for samples MYA10, MYA11 and MYA12 (the "outliers" in Myanmar rocks), AFG4 and the Siberian M15920. The test set included reference samples Siberia390 and AFG1, that had shown different characteristics in respect to other samples from their known provenance. Siberia390 was correctly assigned for 7 out of 8 crystals; AFG1 was instead mistakenly assigned for each one of its crystals (analyses both from INFN-LNL and AGLAE facilities). Removing AFG1 from the test set, the total percentage of correct predictions on that set in cross validation increased from 83.1% to 97.7%. This outcome suggests, as previously mentioned, that it is necessary an expansion of the analytical dataset on our Afghan samples.

Using the built model, classification predictions on archaeological samples data (table 8.3) showed results very similar to what was seen with the projection of datasets on the PCA space. The main difference in this approach is that the LDA classification method "forces" the membership of a sample to one of the classes defined *a priori*, so there are no unclassified objects. The Mahalanobis Distance (MD) of the point from the centroid of the assigned class can be an indicator of the classification robustness for the specific sample. An example is given in figure 8.39 for all points measured on the archaeological seal: with a such high MD from its category, doubts should arise on the assignation of crystal 076_D3b to SIB class. Moreover, the MD of a specific object from all class centroids can be investigated. In figure 8.39 it is evident that the difference in MD between MYA and TAJ classes for crystals 103_D1 and 103_D3 in the seal is minimal and the assignation to MYA class should be considered uncertain. Similar cases for which the decisive MD is so close to one of another class were found for samples SiS-205 (D2), L-Mfrag (D5) (TAJ and MYA uncertainty) and SiS-186 (D2) (TAJ and AFG uncertainty). It can be observed that the highest variability in assignation refers to samples analysed "as such", that can present, as described in the previous sections, superficial alterations or contaminations.

In addition, a test of mid-level data fusion was performed on μ-PIXE and μ-IL diopside data for the creation of a new model. Due to the issues in comparing IL intensities of spectra acquired in different measuring sessions (section 6.3), only data from AGLAE run in 2019 were considered. Unfortunately, Tajik

provenance had to be excluded in this case, since only two crystals were acquired and the number was too low to define a class.

Since the sum of 6 quantitative PIXE variables (the provenance markers also considered for unsupervised analysis) and 556 IL variables (all wavelengths in the range of interest 300-855 nm) exceeded the limit imposed by LDA for 30 samples[6], data fusion was achieved after performing variable reduction on the separate datasets with PCA. The choice of considering the first 3 PCs for PIXE and the first 3 PCs for IL was made upon the results of separate scree plots. 6 crystals (2 for each provenance) were chosen for the test set. The results of this model provided a total percentage of correct predictions in cross validation of 87.5% for training set and 100% for test set. Indeed, the statistics on objects is much lower in this case, so considerations should be made carefully. It seems however that the information contained in IL spectra could slightly contribute to an increase in the total prediction power of a classification model for lapis lazuli provenance.

Of course, not all the provenances available in the world are currently included in our dataset: the next step in supervised data analysis for this topic might then be the employment of a different classification method, one that allows the attribution of a sample to a "null" class: a good possibility might be Soft Independent Modelling of Class Analogy (SIMCA) [Swarbrick and Westad 2016].

[6] As explained in section 7.3.1, LDA method requires a number of variables equal to or less than the number of samples.

Table 8.3. Results of LDA classification for all the archaeological samples analysed in this work, obtained using only μ-PIXE data from diopside crystals. A classification for each analysed crystal is performed and reported in the table.

	Object	Class
Shahr-i Sokhta cross sections	SiS-337 D1	AFG
	SiS-337 D2	AFG
	SiS-337 D3	AFG
	SiS-336 D1	AFG
	SiS-336 D1	AFG
	SiS-62 D1	AFG
	SiS-62 D2	AFG
	SiS-62 D3	AFG
	SiS-44 D1	AFG
	SiS-24 D1	AFG
	SiS-24 D2	AFG
	SiS-24 D3	AFG
Seal	095_D1	TAJ
	095_D2	TAJ
	095_D4	TAJ
	076_D3	SIB
	076_D3b	SIB
	096_D4	TAJ
	097_D5	TAJ
	103_D1	MYA
	103_D3	MYA
	103_D4	TAJ
	103_D5	TAJ
Indus Valley	HR-83a D2	TAJ
	HR-83a D3	TAJ
	HR-83a D1	TAJ
	HR-83b D1	TAJ
	L-Mfrag D3	TAJ
	L-Mfrag D1	TAJ
	L-Mfrag D2	TAJ
	L-Mbead D1	TAJ
	L-Mbead D2	TAJ
	L-D D1	TAJ
	L-D D2	TAJ
	SHT-1b D1	AFG

	Object	Class
Shahr-i Sokhta AGLAE	SiS-336 D1	AFG
	SiS-28 D1	AFG
	SiS-336 D2	AFG
	SiS-67 D1	AFG
	SiS-325 D1	TAJ
	SiS-325 D2	TAJ
	SiS-187 D1	TAJ
	SiS-186 D1	SIB
	SiS-186 D2	TAJ
	SiS-205 D2	TAJ
	SiS-186 D1 2020	SIB
	SiS-186 D2 2020	TAJ
	SiS-325 D2 2020	TAJ
	SiS-67 D3	AFG
	SiS-331 D1	MYA
	SiS-331 D1BIS	MYA
	SiS-178 D2	AFG
	SiS-181 D4	AFG
Chagai Hills	CH-1 D1	TAJ
	CH-1 D3	TAJ
	CH-4 D1	MYA
	CH-4 D2	MYA
	CH-2a D1	AFG
	CH-2a D2	AFG
	CH-2a D3	AFG

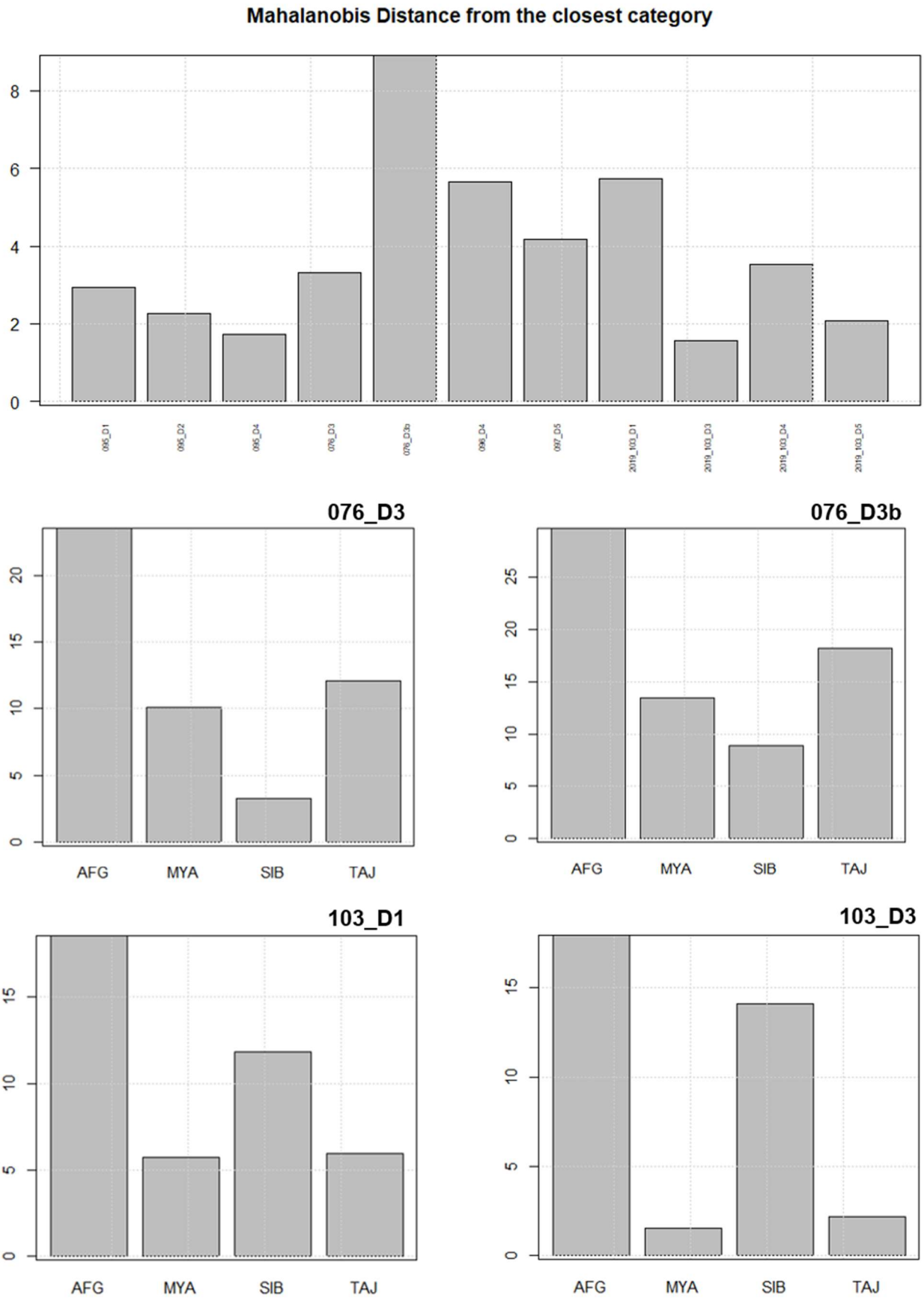

Figure 8.39. Mahalanobis Distance for all the points analysed on the archaeological seal from the centroid of their assigned class (top) and MD from all class centroids for specific points 076_D3, 076_D3b, 103_D1 and 103_D3.

8.2. Luminescence in diopside

From all the data collected on diopside during the provenance investigations, some consideration on luminescence mechanisms can be put forward. First of all, direct qualitative correlations between the trace elements detected with μ-PIXE and the μ-IL bands presence and intensities can be made, starting from literature information (section 3.3). Moreover, the bidimensional maps acquired at AGLAE are a great support for the understanding of cases where crystals present area-specific luminescence. Quantitative correlations can be made only on measurements acquired in the same conditions with the same reproducible setup: hence, in order to avoid the introduction of any instrumental error, only data from the 2019 measuring session at AGLAE were considered in bivariate and multivariate analysis for the regression of fitted IL bands (see section 6.3 for the discussion regarding this issue).

8.2.1. Activators

All the analysed diopside crystals showed in their μ-IL spectra the 585 nm band, that is commonly activated by Mn^{2+} ions in M2 sites. Mn has been always detected well above the limit of detection as trace element in all crystals, and its distribution in diopside crystals is generally appreciable also from AGLAE maps. In diopside crystals from Myanmar reference samples, Mn happens to be found in lower concentrations, with a median line at 80 ppm that for other provenances varies instead on a range between 200 and 400 ppm; a similar trend is found for 2019 AGLAE data. As probable direct consequence, the band for Myanmar samples has on average a lower intensity than other provenances: for spectra acquired at INFN-LNL (figure 8.3), the highest Myanmar bands are comparable to the lowest ones from Afghan samples [Re et al. 2015]. For μ-IL spectra acquired at AGLAE (figure 8.40) a similar comparison in intensity can be done without doubts at least for 2019 measuring run, but keeping in mind that only a subset of all the database samples was investigated. Here the intensity for Myanmar is similar to Siberian samples, but still lower than Afghan ones. The activation role of Mn^{2+} can involve as well the 690 nm band, seen in some samples from Tajikistan, Siberia and Myanmar, if the ion is located in M1 sites. This is what happens most probably in sample Pamir3, where for crystal D1, bearing a high Mn content of 660 ppm, the intensity of 585 nm band is modest and is overcome by the 690 nm band (figure 8.41). Figure 8.42 shows the relations in bivariate analysis between band areas (fitting process is described in section 6.2) and content of trace elements for known activators (section 3.3). It is evident from figures 8.42 (a), (b) and (e) that a simple linear correlation with Mn could not be found, also considering simultaneously both luminescence bands. Overall, no trends could be identified, not even among samples of the same provenance. The extremely low luminescence for most Siberian samples, despite a considerable amount

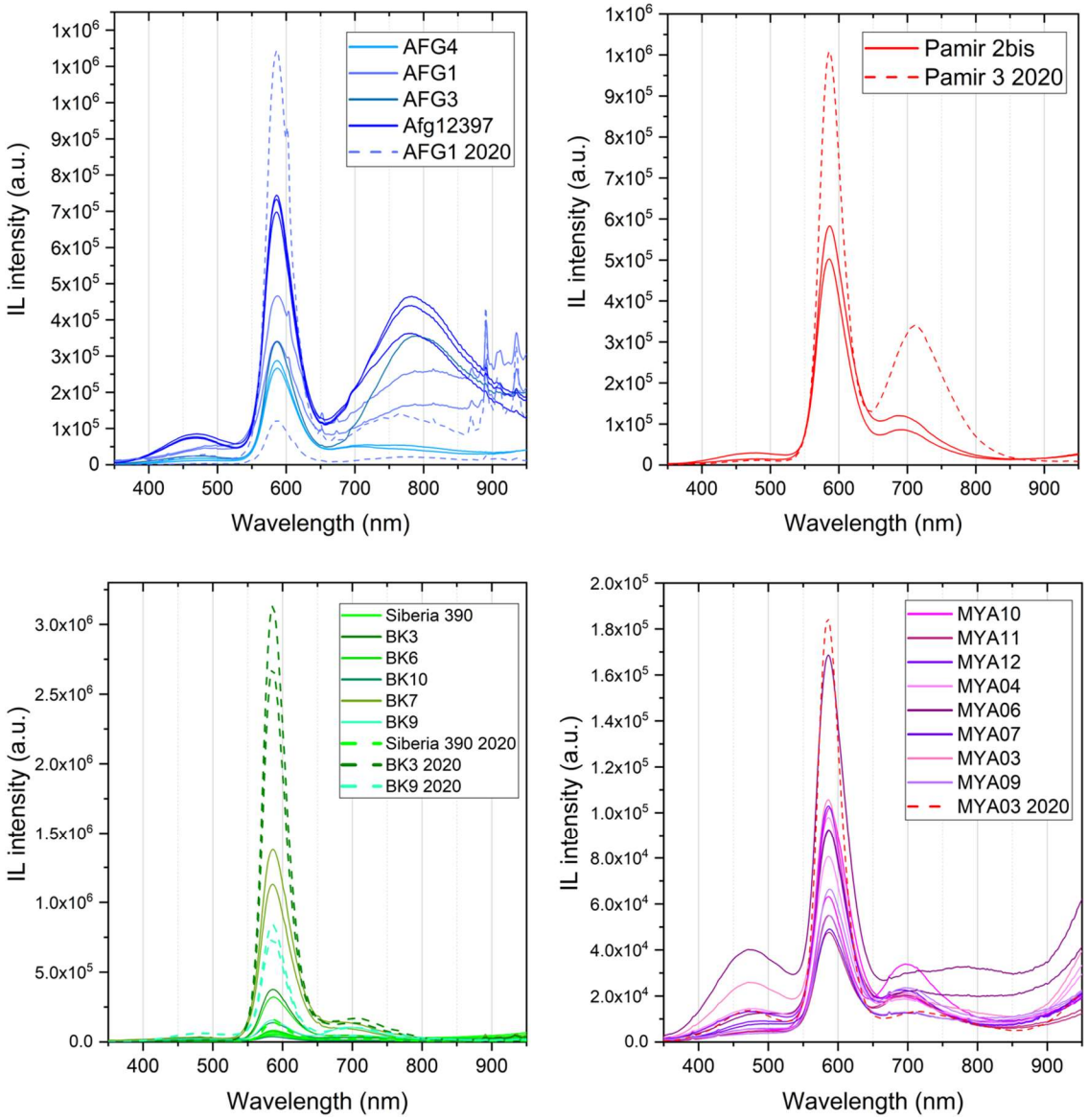

Figure 8.40. µ-IL spectra of diopside crystals from rock reference samples analysed at AGLAE: Afghanistan (blue), Tajikistan (red), Siberia (green) and Myanmar (purple). 2020 measuring run is distinguished by dashed lines. The only 2020 spectra for Myanmar was divided by a factor of 10 for better visualisation and comparison.

of Mn present (up to 800 ppm), suggested the possible co-operation of a quencher. This further investigation is covered in the following section.

V was also considered as activator of the 690 nm band. In figure 8.42 (c) and (d) only spectra on which the 690 nm band was detectable are taken into account, hence limiting the analysis to samples from Tajikistan, Siberia and Myanmar. Despite the weak trend that can be noticed for Myanmar samples in figure 8.42 (c), it still could not be defined a precise correlation and a regression equation for this band, even when considering both activators together (figure 8.42 (d)).

For the band centred at 770 nm, solely observed in Afghan reference samples and in most archaeological samples classified as Afghan, Cr^{3+} is the most probable activator candidate. A trend of the band area as a function of Cr content for Afghan samples can be appreciated in figure 8.42 (f). The behaviour for Shahr-i Sokhta samples is more erratic, but it should be kept in consideration that these samples were not clean and smooth thick sections: they are plotted for comprehensiveness of data, but they are not the best reference for luminescence regression purposes. In the plot is reported also sample MYA06, that showed the peculiar broad band from 700 nm to 850 nm, and is the only Myanmar sample where Cr was detected above LOD. It is however a very low content (about 10 ppm) and it is reflected as expected in a very low band area. A confirmation for Afghan samples arises also from AGLAE maps, as can be seen in the example of sample Afg 12397 (figure 8.43): in a homogeneous diopside crystal, identified by Mg distribution, luminescence of 770 nm band is more intense on the area where higher Cr concentration is localised. This variability found within the same crystal might also be one of the causes for the difficulty in retrieving a defined correlation trend among samples from the same provenance.

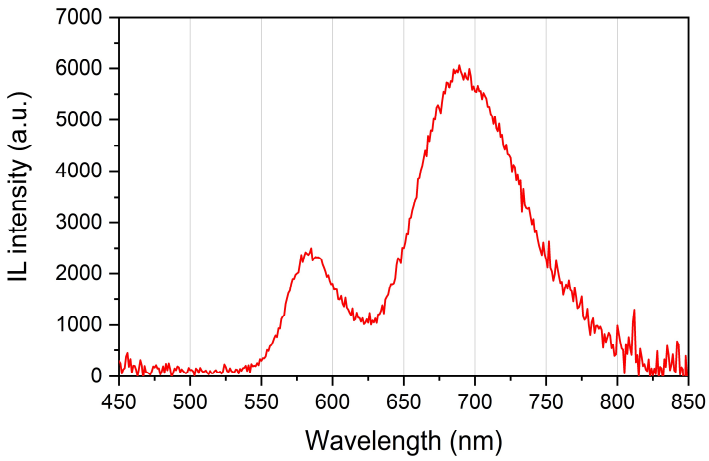

Figure 8.41. µ-IL spectra of diopside D1 from reference sample Pamir3, analysed at INFN-LNL.

The band centred around 450 nm, although detected in some spectra, is not investigated from an activation point of view, since the employed spectrometer is not optimised in intensity for that wavelength range.

All the above mentioned IL signals consist in broad bands that suggest a strong interaction of the activators with the local crystal field, as one would expect for ions such as Mn^{2+}, V^{2+}, Cr^{3+} and Ti^{4+}. During data acquisition, it was also noticed the interesting concurrence of small peaks at 600 nm and 650 nm, found both in reference geological samples and archaeological samples, and the presence of Y as trace element. As in some cases only a vague evidence of these peaks is present, it was not possible to achieve their fitting. From figure 8.44 it is however appreciable that evidences become more evident as Y concentration increases.

Finally, peaks around 900 nm are very much similar in positions and relative intensities to the result of a Nd^{3+} activation (see figure 3.8 (e)); in the case of REEs, very few ppm can be enough to produce such peaks. However, the sensitivity of the employed µ-PIXE setup did not allow to detect extremely low

concentrations of Nd, also considering that its L emission lines (5.23-5.72-6.60 keV) fall on the energy range covered by Cr, Mn and Fe K lines; Cr is particularly low for crystals showing 900 nm peaks (often below LOD), but Mn and Fe varies on ranges 170-300 ppm and 1000-1500 ppm respectively.

In general, these considerations on ionoluminescence activations have highlighted the complexity of the mechanisms involved, due to co-activation processes and to the heterogeneity of the natural mineral. Simple bivariate analysis seems unable to explain such processes. The opposing action of quenchers still has to be taken into account and is discussed in the next section.

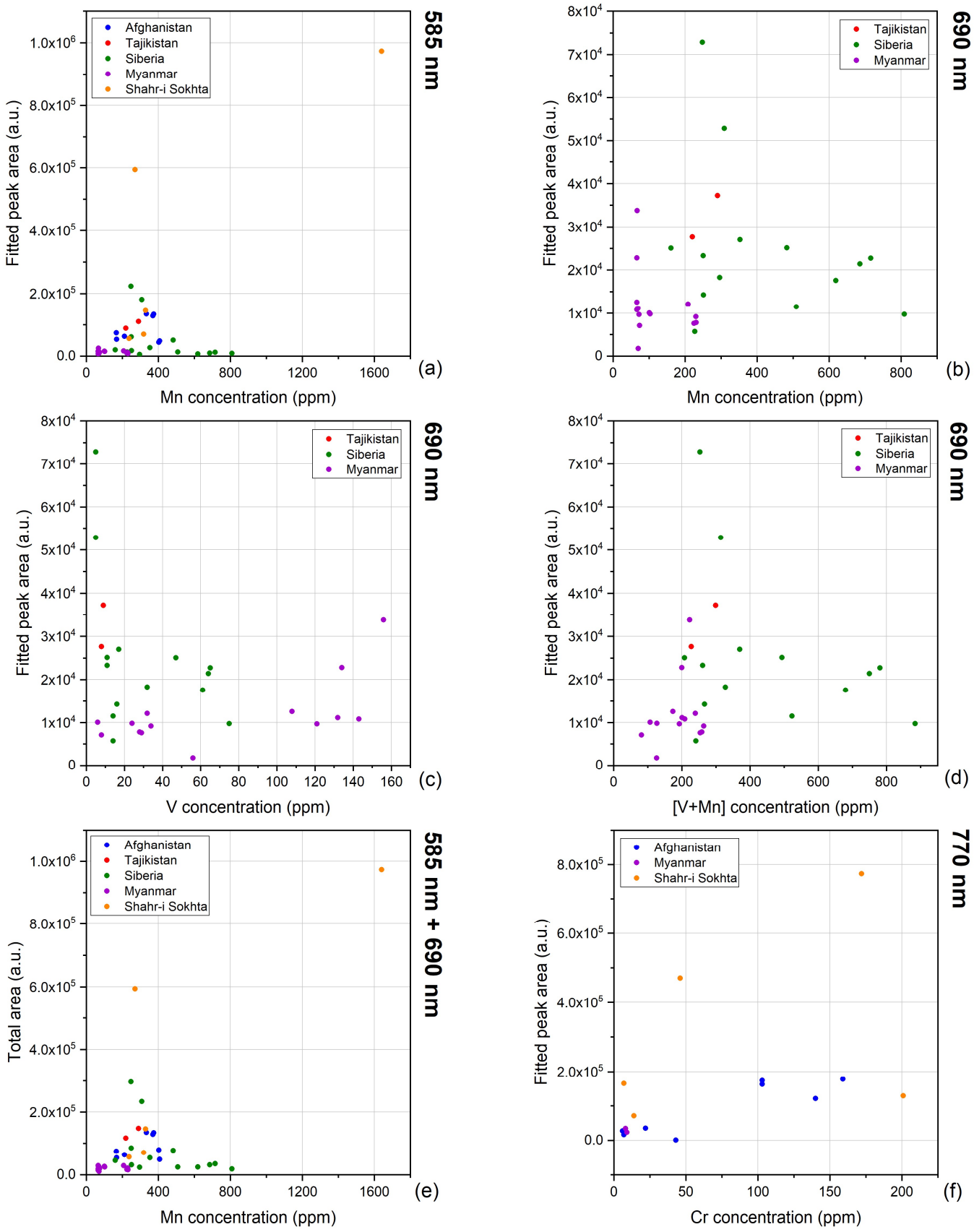

Figure 8.42. Bivariate analysis for ionoluminescence bands (fitted as Gaussian peaks) and concentrations of known activators. (a) 585 nm band *vs* Mn content, (b) 690 nm band *vs* Mn content, (c) 690 nm band *vs* V content, (d) 690 nm band *vs* (Mn+V) content, (e) sum of 585 nm and 690 nm band areas *vs* Mn content, (f) 770 nm band *vs* Cr content.

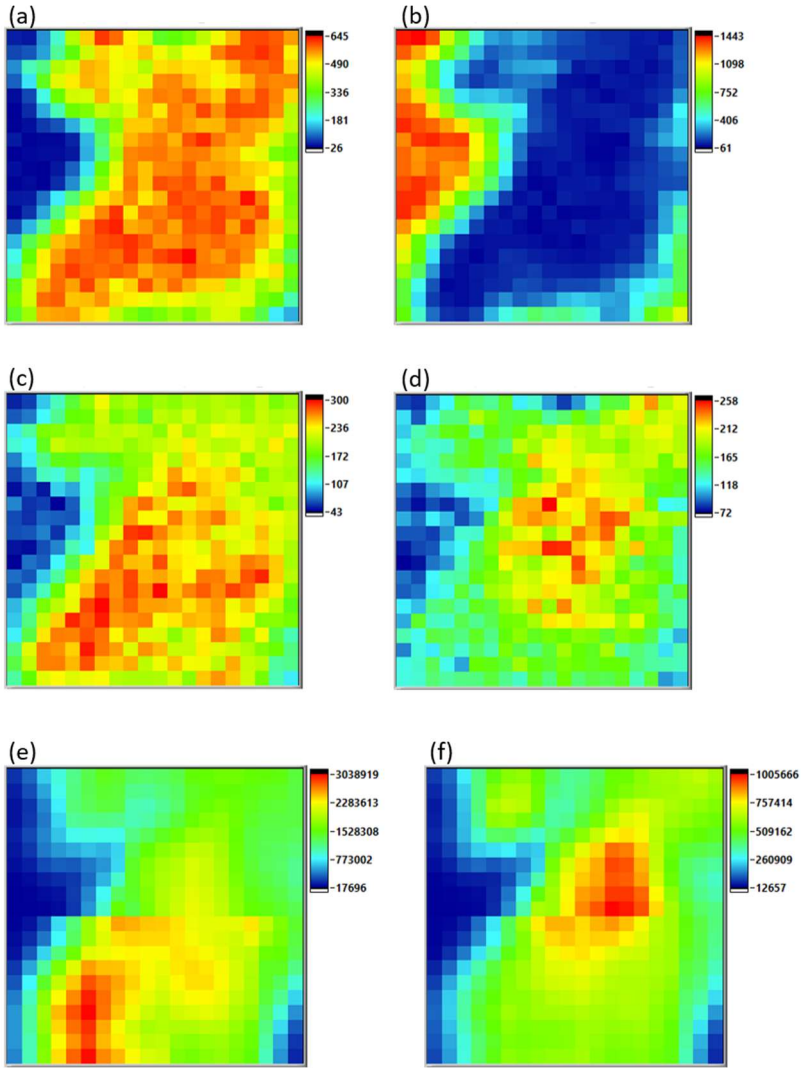

Figure 8.43. AGLAEMap images for sample Afg12397. Map is 500×500 µm^2. Spatial distribution of: Mg (a) and Al (b) content; Mn (c) and Cr (d) content; 585 nm band (e) and 770 nm band (f) intensity. The effect of Mn and Cr as activators for the two bands respectively is appreciable.

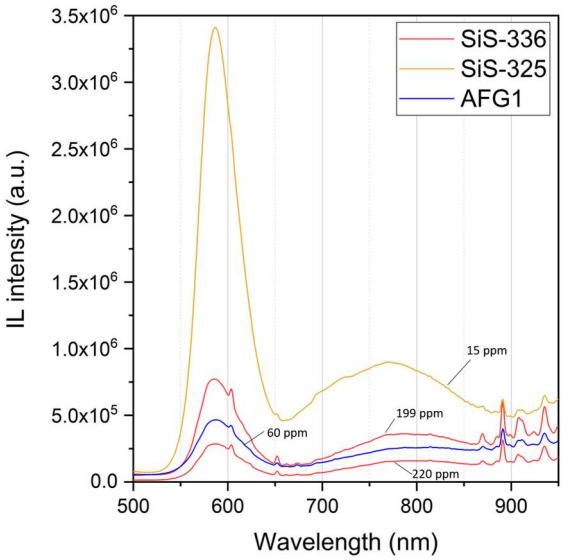

Figure 8.44. Comparison of µ-IL diopside spectra acquired at AGLAE in 2019 and showing the small peaks at 600 nm and 650 nm. Peaks around 900 nm are also visible. Y concentration for each crystal is reported with labels.

8.2.2. Quenchers

The quenching effects of specific trace elements were investigated mainly by means of AGLAE maps, taking advantage of their capability of correlating pixel by pixel the wavelength-selective region of the IL spectra with the content of a specific element from PIXE analysis. First of all, Fe was considered, as the only quencher reported in the literature for diopside. Its quenching power was verified in several samples, specifically in Pamir2bis, Siberia390, BK10, BK6, MYA07, MYA11, SiS-336, SiS-331 and SiS-180. An example can be seen in figure 8.45, where the luminescence of diopside D1 in sample BK10 is suppressed only on areas with high Fe content. The very high content of Fe in many Siberian samples (figure 8.46, presented with separated results from different measuring runs) also explains their low luminescence reported in the previous section. Normalising the Mn content on Fe content for the plot in figure 8.42 (a), these samples are all shifted towards the origin of the axes (figure 8.47 (a)). However, even applying this corrections to the plot, a univocal relation between band areas and trace element concentrations is still not found. Figure 8.47 (c) sums up the contributes for both 585 nm and 690 nm bands given by activators Mn and V and quencher Fe: besides the previously seen almost-linear trend for Afghan samples, other direct correlations cannot be retrieved with this kind of analysis.

In the study of bidimensional maps, another contribute emerged in the quenching of luminescence signal, the presence of Ti. Ti is generally always present above the limit of detection in analysed crystals, but it seems to be a quenching agent only at high concentrations: it is then a case of *concentration quenching*. An example of the effect can be seen in figure 8.48 for sample BK6: the area that bears about 700 ppm of Ti suffers from a strong luminescence quenching, whereas the adjacent one with less than 400 ppm shows the typical emission for 585 nm band. Cases of concentration quenching for Ti can be found in the literature, such as in Myanmar rubies, where the effect on cathodoluminescence emission is noticed already at concentrations of few hundreds of ppm [Garnier et al. 2002]. Quenching effect of Ti was found also in samples AFG1, AFG4, BK10, MYA09, SiS-336, and SiS-180 with a Ti content reaching values around 1700 ppm. This phenomenon makes it even more difficult to define the rules regulating luminescence induced by Ti (e.g. the band around 450 nm), since at some threshold concentration value the effect becomes competitive. More targeted experiments should be done to understand this process and define the threshold, but, as previously discussed, the natural origin of the material introduces a lot of uncertainties. With a view to continue the study using only non-invasive techniques, a survey with EXAFS/XANES using synchrotron radiation could provide as a starting point more information on the oxidation state of activators and quenchers present, as well as their crystallographic environment such as coordination number and interatomic distances.

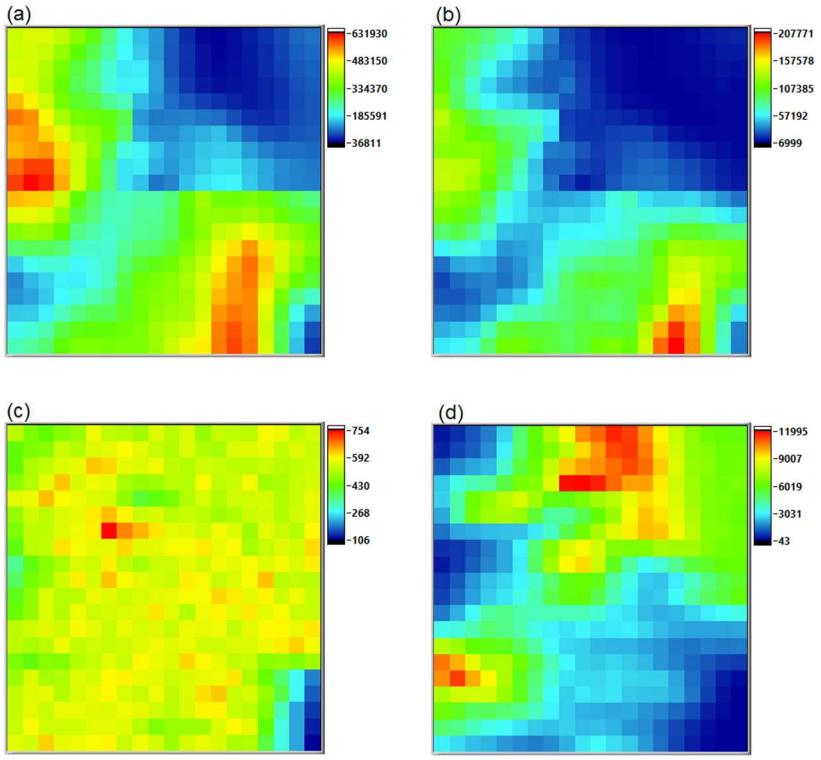

Figure 8.45. AGLAEMap images for sample BK10. Map is 500×500 μm^2. Spatial distribution of: 585 nm band (a) and 690 nm band (b) intensity; Mg (c) and Fe (d) content. Mg is the indicator of the diopside crystal: where Fe is present, luminescence in (a) and (b) is suppressed.

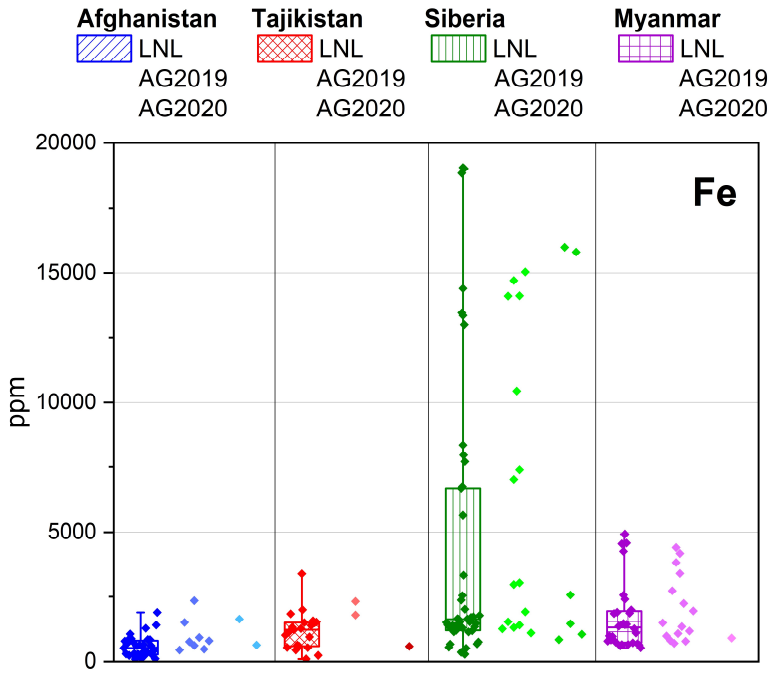

Figure 8.46. Comparison of μ-PIXE results for Fe in diopside, between reference geological samples acquired at INFN-LNL and at AGLAE in two different runs (2019 and 2020). The box plots represent the dispersion of the experimental points: the median line and the two percentile values 0.25 and 0.75.

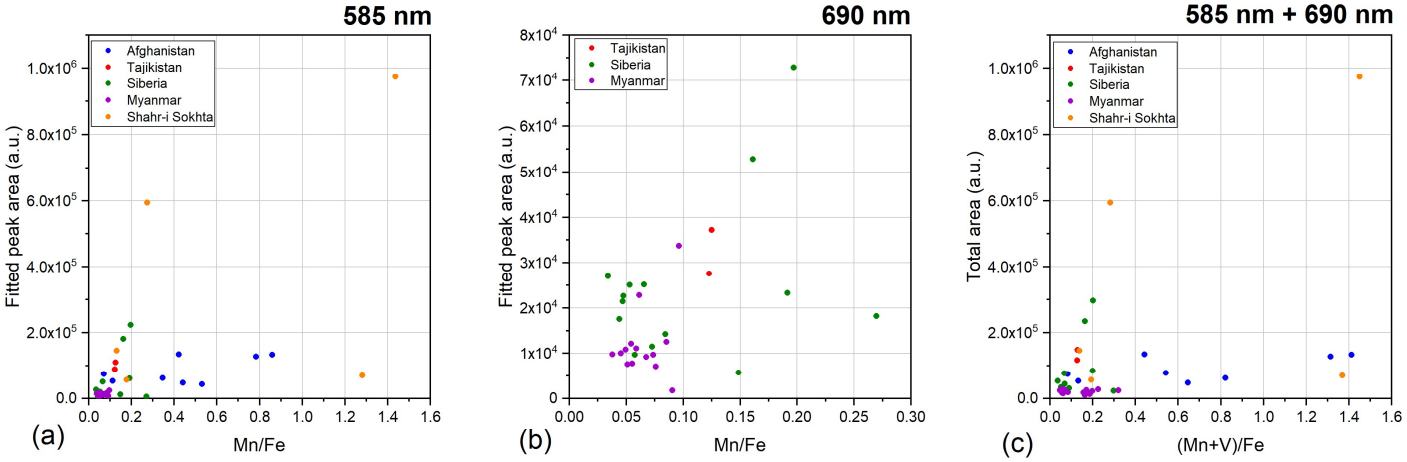

Figure 8.47. Bivariate analysis for ionoluminescence bands (fitted as Gaussian peaks) and concentrations of known activators and quencher Fe. (a) 585 nm band *vs* Mn/Fe content, (b) 690 nm band *vs* Mn/Fe content, (c) sum of 585 nm and 690 nm band areas *vs* (Mn + V)/Fe content.

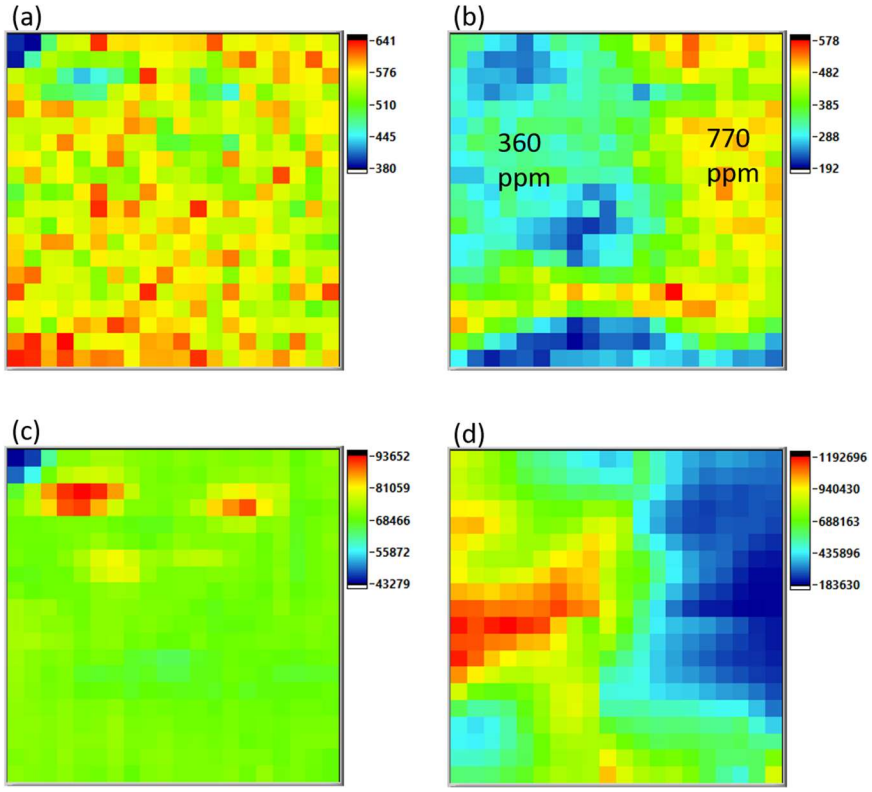

Figure 8.48. AGLAEMap images for sample BK6. Map is 500×500 µm^2. Spatial distribution of: Mg (a) and Ti (b) content; Ca content (c) that identifies two small calcite crystals within the diopside; 585 nm band intensity (d). Where Ti content is above about 700 ppm, luminescence is suppressed.

8.2.3. Multivariate analysis: regression

Since from aforementioned observations it resulted clear that μ-IL band intensities depend on the simultaneous effect of multiple agents (activators, quenchers, site occupancy), an approach to the subject with multivariate regression was attempted. Partial Least Squared regression was chosen as method for its capability in treating multicollinear variables. The employed software, CAT, is so far implemented only with PLS1 algorithm, that permits to build a model for the regression of only one response variable from multiple predictors. Tests were performed approaching the issue from two points of view: firstly considering the fitted band area of interest as response and the trace elements as predictors, then aiming at a numerical regression of the single activator content from the spectral range covered by the interested bands. In the second case, SNV row pre-processing was applied to spectra before the regression. However, as indeed one could expect, this first attempt provided quite high errors in cross validation of the model, especially when the involved responses are band areas: some examples can be seen in table 8.4. An encouraging result turns out when considering the percentage of explained variance in CV for the models predicting trace element contents, which varies between 60 and 90%. CV is performed with 5 blocks and a randomisation of rows is applied before model computation, to exclude a bias due to similarities within provenance classes.

The next step in finding the correct approach will be the employment of PLS2 algorithm [Varmuza and Filzmoser 2009], that allows to compute a model for multiple responses (in this case intensities for each wavelength value on a range of interest) from multiple predictors.

Table 8.4. Results of PLS regression for various combinations of response and predictor variables. Absolute RMSECV is in arbitrary units for band areas and in ppm for trace elements. RMSECV% is calculated as RMSECV/ averaged value of each parameter. LV = latent variables, neg = negative.

Response	Predictors	LV for min RMSECV	RMSECV	RMSECV (%)	Explained Variance in CV (%)
585 nm band area	Ti, V, Cr, Mn, Fe	4	48164	109	15.37
770 nm band area	Ti, V, Cr, Mn, Fe	1	62362	64	19.04
690 nm band area	Ti, V, Mn, Fe	1	15789	84	neg
Mn	λ, 550-800 nm	10	98	36	73.82
V	λ, 550-800 nm	5	54	64	63.74
Fe	λ, 550-800 nm	10	1516	42	87.36

9. Conclusion

The complexity of lapis lazuli paragenesis offers to archaeometrists a wide range of analyses that can be carried out to discover its secrets. In this work only a part of them have been addressed, providing interesting results for different points of view, from historical implications to material characterisation. The amount of data collected on both reference geological samples and archaeological items made in lapis lazuli allows to draw further hypotheses for the provenance study at the basis of the work.

In particular, thanks to the analysis of the new Myanmar geological samples, it was possible to add a new provenance to the operative protocol already published. The discrimination from Chilean and Siberian samples is still achievable by strong markers such as absence of wollastonite or altered pyrites and low Sr content. Evidence was found of the difficulty in discriminating the new provenance from the Tajik one, whereas weaker differences with Afghan provenance can be found in Zn content and in an IL band at 770 nm. A tentative new protocol diagram was then proposed on the basis of these outcomes. Moreover, μ-PIXE results on diopside substantiate the separation of Myanmar samples in the same three groups previously identified via SEM-EDX compositional observations.

The IBA results obtained on diopside at INFN-LNL facility have been confirmed by the analysis carried out at AGLAE, and an additional comparison was performed for trace elements quantification via SEM-WDX. Such comparison provided encouraging results for the use of Wavelength Dispersive Spectrometry as an alternative to μ-PIXE, albeit limited to reference geological samples that can be carbon coated. Principal component analysis applied to all μ-PIXE data on diopside, available from both facilities, confirmed the Ti, V, Cr, Mn, Zn and Sr concentrations as the most relevant variables for a separation in groups according to sample provenance. The grouping seems to be particularly effective for the Afghan provenance, influenced by Ti, V, Cr and Mn contents. Siberia and Myanmar sample grouping relies mostly on their Sr and Zn content, respectively; Tajik samples are completely overlapped to Myanmar, confirming the discrimination difficulty observed in the compilation of the protocol. In general, PCA was proved to be a good tool to have a quicker overview of the dataset while being in great agreement with the protocol; in the near future, PCA will be applied also to μ-IL data, as soon as a statistically significant amount of spectra comparable in intensity will be available.

The provenance protocol was then applied to archaeological samples, that underwent a complete characterization starting from observations in optical microscopy, SEM-EDX at variable pressure and cold-CL (when applicable). Among Shahr-i Sokhta samples, cross sections analysed at INFN-LNL resulted to be most compatible with an Afghan provenance. A more complex outcome turned out from the fragments measured as such at AGLAE, with a dubious assignation of several samples. This kind of analysis, with an extracted ion beam on archaeological samples that did not underwent any pre-treatment, underlined the

issues that can arise in such cases: a particular relevance emerged from superficial alteration (e.g. loss of S in pyrites) or contaminations with soil dirt or other mineral phases such as Fe or Cu oxides. A solution for upcoming measuring sessions could be the definition of a cleaning procedure for the samples, developed under archaeologists directions to avoid the loss of information on archaeological context. Another issue on measuring artistic objects arose from the analysis of the lapis lazuli seal found at Shahr-i Sokhta: the dips constituting the wonderful decoration can cause problems of self-absorbance of the emitted X- or visible radiation. Enough crystals could nonetheless be measured, and the application of the protocol produced a very interesting result, as this sample seems to be non-compatible with an Afghan provenance. This conclusion could represent an interesting point of discussion for the trading routes topic among archaeologists. Samples from Indus Valley presented as well an internal variability, as only the Shortughaï fragment seems to be in good agreement with an Afghan provenance, and distinguishes itself for its higher contents of Mn, Ti, V and Cr. Lastly, geological samples coming from the hypothetical source in Chagai Hills have been considered as of unknown origin and the protocol was applied. In addition to presenting different characteristics in diopside trace composition from one another, no common marker was found so far for the four samples. It can be excluded then that they might all belong to the same quarry, but not that at least one of them could indeed come from a Chagai Hills source.

All datasets of diopside crystals trace markers coming from archaeological and Chagai Hills samples were also projected as external dataset on the PCA model built with reference geological samples, providing in most cases a compatibility with the provenance group identified by means of the protocol, and in some cases some additional insights. For instance, it allowed to immediately identify outliers among Shahr-i Sokhta samples analysed as such, or differences among Chagai Hills samples, that supposedly came from the same source.

The application of a classification method such as LDA to the diopside μ-PIXE data, building the model with reference geological samples and predicting a class membership for archaeological samples, provided very interesting outputs, with a prediction rate for the model (81.3%) that can be regarded as quite high considering the heterogeneity of the natural samples. Moreover, LDA, always with a particular attention to Mahalanobis distances, allows to assign a provenance class to samples that with the simple protocol rules resulted dubious. As of course the reference geological samples available do not cover all possible provenances in the world, it might be useful in the future a comparison using a classification method that can assign samples also to a null class, such as SIMCA.

The study of μ-IL spectra from an activation and quenching point of view allowed to confirm qualitatively the role of Mn and Cr as activators for the 585 nm - 690 nm and 770 nm bands respectively. Moreover the effect of Fe as quencher was verified in 9 samples, together with the presence of Ti acting as concentration quencher. Small peaks at 600 nm and 650 nm, never reported before for diopside, seems to have a correlation with Y content. Generally present alongside those signals, the set of peaks around

900 nm can be assimilated to the ones reported in the literature for a Nd^{3+} activation.

Issues in the instrumentation setup limited the number of samples that could be compared from a quantitative point of view, but attempts were made on a dataset from 43 diopside crystals all measured in the same session at AGLAE. Bivariate correlations, considering areas of the 585 nm, 690 nm and 770 nm bands versus trace element contents of activators and quenchers, were studied, but a simple regression was not found, apart from a weak trend among Afghan samples. This suggests that activators and quenchers might act simultaneously in the production of several bands and that a more complex model is needed to describe the mechanisms involved. For this reason an approach with multivariate regression was attempted. However, the first step in using a Partial Least Squared Regression method with one response (area of a specific band or single activator/quencher content) and multiple predictors provided too high errors in cross validation and too low explained variance for the building of a robust model. The next step will be the employment of PLS2 algorithm, that allows to compute a model for multiple responses from multiple predictors. Luminescence mechanisms are undeniably a complex field to investigate, but one of the aim of this work was to collect new insights and data that can be in the near future employed in the provenance study. It is anyway undoubtful the contribution that multivariate analysis can provide in the treatment of the huge amount of data that comes out from such a widespread investigation.

Bibliography

AITKEN, M.J. 1985. *Thermoluminescence dating*. Academic Press, London.

AJÒ, D., CASELLATO, U., FIORIN, E., AND VIGATO, P.A. 2004. Ciro Ferri's frescoes: A study of painting materials and technique by SEM-EDS microscopy, X-ray diffraction, micro FT-IR and photoluminescence spectroscopy. *Journal of Cultural Heritage 5*, 4, 333–348.

ALEKSANDROV, S.M. AND SENIN, V.G. 2006. Genesis and composition of lazurite in magnesian skarns. *Geochemistry International 44*, 10, 976–988.

ANGELICI, D. 2015. Petrographic and minero-chemical characterisation of lapis lazuli: a provenance study of rocks and artefacts from Cultural Heritage. PhD thesis, Earth Sciences, Università degli Studi di Torino.

ANGELICI, D., BORGHI, A., CHIARELLI, F., ET AL. 2015. μ-XRF Analysis of Trace Elements in Lapis Lazuli-Forming Minerals for a Provenance Study. *Microscopy and Microanalysis 21*, 2, 526–533.

ANTHONY, J.W., BIDEAUX, R.A., BLADH, K.W., AND NICHOLS, M.C. 2001. Handbook of Mineralogy. Mineral Data Publishing.

BACCI, M., CUCCI, C., DEL FEDERICO, E., ET AL. 2009. An integrated spectroscopic approach for the identification of what distinguishes Afghan lapis lazuli from others. *Vibrational Spectroscopy 49*, 1, 80–83.

BALLIRANO, P. AND MARAS, A. 2006. Mineralogical characterization of the blue pigment of Michelangelo's fresco "The Last Judgment." *American Mineralogist 91*, 7, 997–1005.

BATTIATO, A., LORUSSO, M., BERNARDI, E., ET AL. 2016. Softening the ultra-stiff: Controlled variation of Young's modulus in single-crystal diamond by ion implantation. *Acta Materialia 116*, 95–103.

BAUER, M. 1904. *Precious stones: a popular account of their characters, occurrence and applications*. Charles Griffin & Co., London.

BORELLI, A., CIPRIANI, C., INNOCENTI, C., AND TROSTI, R. 1986. Caratterizzazione del lapislazzuli. *La Gemmologia 11*, 24–27.

BORRAS, E., FERRÉ, J., BOQUÉ, R., MESTRES, M., ACENA, L., AND BUSTO, O. 2015. Data fusion methodologies for food and beverage authentication and quality assessment - A review. *Analytica Chimica Acta 891*, 1–14.

BRÖGGER, W.C. AND BACKSTROM, H. 1891. Die Mineralien der Granatgruppe. *Zeitschrift fur Krystallographie und Mineralogie 18*, 209–276.

BULGARELLI, G.M. AND TOSI, M. 1977. La lavorazione ed il commercio delle pietre semipreziose nelle città dell'Iran protostorico (3200-1800 a.C.). In: *Geo-Archeologia*. Japadre Editore, L'Aquila, 37–50.

CALLIGARO, T., COQUINOT, Y., PICHON, L., ET AL. 2014. Characterization of the lapis lazuli from the Egyptian treasure of Tôd and its alteration using external μ-PIXE and μ-IBIL. *Nuclear Instruments and Methods in Physics Research, Section B: Beam Interactions with Materials and Atoms 318*, PART A, 139–144.

CALLIGARO, T., COQUINOT, Y., PICHON, L., AND MOIGNARD, B. 2011. Advances in elemental imaging of rocks using the AGLAE external microbeam. *Nuclear Instruments and Methods in Physics Research, Section B: Beam Interactions with Materials and Atoms 269*, 20, 2364–2372.

CALUSI, S., COLOMBO, E., GIUNTINI, L., ET AL. 2008. The ionoluminescence apparatus at the LABEC external microbeam facility. *Nuclear Instruments and Methods in Physics Research, Section B: Beam Interactions with Materials and Atoms 266*, 10, 2306–2310.

CAMPBELL, J.L., BOYD, N.I., GRASSI, N., BONNICK, P., AND MAXWELL, J.A. 2010. The Guelph PIXE software package IV. *Nuclear Instruments and Methods in Physics Research, Section B: Beam Interactions with Materials and Atoms 268*, 20, 3356–3363.

CASANOVA, M. 1992. The Sources of the Lapis Lazuli found in Iran. *South Asian Archaeology, Monographs in World Archaeology*, Prehistory Press, 49–56.

CASANOVA, M. 2001. Les lapis lazuli, la pierre precieuse de l'Orient ancien. *Dialogue d'Histoire Ancienne 27*, 2, 149–170.

CASANOVA, M. 2013. *Le Lapis-Lazuli dans l'Orient Ancien*. Editions du CTHS, Paris.

CIPRIANI, C., INNOCENTI, C., AND TROSTI-FERRONI, R. 1988. Le collezioni del museo di mineralogia di Firenze: (VI) Lapislazzuli. *Museologia Scientifica 5*, 1–2, 17–30.

COENRAADS, R.R. AND CANUT DE BON, C. 2000. Lapis lazuli from the Coquimbo Region, Chile. *Gems and Gemology 36*, 1, 28–41.

CORAZZA, M., PRATESI, G., CIPRIANI, C., ET AL. 2001. Ionoluminescence and cathodoluminescence in marbles of historic and architectural interest. *Archaeometry 43*, 4, 439–446.

CROWFOOT PAYNE, J. 1968. Lapis Lazuli in Early Egypt. *Iraq 30*, 1, 58–61.

CUITINO, G.L. 1986. Mineralogia y genesis del yacimiento de lapislazuli Flor de los Andes, Coquimbo, Norte de Chile. *Revista Geologica de Chile 27*, 57–67.

CZELUSNIAK, C., PALLA, L., MASSI, M., ET AL. 2016. Preliminary results on time-resolved ion beam induced luminescence applied to the provenance study of lapis lazuli. *Nuclear Instruments and Methods in Physics Research, Section B: Beam Interactions with Materials and Atoms 371*, 336–339.

D'AMATO, S. 2000. Il lapislazzuli dell'Egitto Predinastico e Protodinastico: Saggio sugli Indicatori di Scambio nelle Fasi Formative dell'Antico Regno. Masters' Thesis, Anthropology, Università degli Studi di Bologna.

DEACHA, N., ELOSUA, C., MATIAS, I., AND ARREGUI, F.J. 2017. Luminescence-based optical sensors fabricated by means of the layer-by-layer nano-assembly technique. *Sensors (Switzerland) 17*.

DEER, W.A., HOWIE, R.A., AND ZUSSMAN, J. 1977. *Rock-Forming Minerals - Single-Chain Silicates*. The Geological Society.

DELMAS, A.B. AND CASANOVA, M. 1990. The Lapis Lazuli sources in the ancient east. *South Asian Archaeology*, Istituto Italiano per il Medio ed Estremo Oriente.

DERAKHSHANI, J. 1999. Kupfer und Lapislazuli. In: *Text und Archäologie. Ein Beitrag für die Publikation "Türkis und Azur, Kieselkeramik im Orient und Okzident"*. Staatliche Museen Kassel, Kassel.

DERRICK, M. 1990. *Infrared Spectroscopy in Conservation Science*. The Getty Conservation Institute, Los Angeles.

DITALIA TCHERNIJ, S., HERZIG, T., FORNERIS, J., ET AL. 2017. Single-Photon-Emitting Optical Centers in Diamond Fabricated upon Sn Implantation. *ACS Photonics 4*, 10, 2580–2586.

DROUIN, D., COUTURE, A.R., JOLY, D., TASTET, X., AIMEZ, V., AND GAUVIN, R. 2007. CASINO V2.42—A Fast and Easy-to-use Modeling Tool for Scanning Electron Microscopy and Microanalysis Users. *Scanning 29*, 3, 92–101.

DYSON, T. 2018. *A Population History of India: from the First Modern People to the Present Day*. Oxford University Press.

ESQUIVELA, R.C. AND BENAVIDES MUÑOZ, M.E. 2005. Mineralogía y origen del yacimiento de lapislázuli Flor de los Andes, Chile. *Boletín de Mineralogía 16*, 57–65.

FARNHAM, I.M., SINGH, A.K., STETZENBACH, K.J., AND JOHANNESSON, K.H. 2002. Treatment of nondetects in multivariate analysis of groundwater geochemistry data. *Chemometrics and Intelligent Laboratory Systems 60*, 1–2, 265–281.

FAVARO, M., GUASTONI, A., MARINI, F., BIANCHIN, S., AND GAMBIRASI, A. 2012. Characterization of lapis lazuli and corresponding purified pigments for a provenance study of ultramarine pigments used in works of art. *Analytical and Bioanalytical Chemistry 402*, 6, 2195–2208.

FORNERIS, J., LO GIUDICE, A., OLIVERO, P., ET AL. 2014. A 3-dimensional interdigitated electrode geometry for the enhancement of charge collection efficiency in diamond detectors. *Europhysics Letters 108*, 1.

FREUND, K.P. 2013. An assessment of the current applications and future directions of obsidian sourcing studies in archaeological research. *Archaeometry 55*, 5, 779–793.

GAFT, M., REISFELD, R., AND PANCZER, G. 2015. *Modern Luminescence Spectroscopy of Minerals and Materials*. Springer Mineralogy.

GAMA, S., VOLFINGER, M., RAMBOZ, C., AND ROUER, O. 2001. Accuracy of PIXE analyses using a funny filter. *Nuclear Inst. and Methods in Physics Research, B 181*, 150–156.

GAMBARDELLA, A.A., COTTE, M., DE NOLF, W., ET AL. 2020. Sulfur K-edge micro- and full-field XANES identify marker for preparation method of ultramarine pigment from lapis lazuli in historical paints. *Science Advances 6*, 18, 1–10.

GAMBARDELLA, A.A., SCHMIDT PATTERSON, C.M., WEBB, S.M., AND WALTON, M.S. 2016. Sulfur K-edge XANES of lazurite: Toward determining the provenance of lapis lazuli. *Microchemical Journal 125*, 299–307.

GANIO, M., POUYET, E.S., WEBB, S.M., SCHMIDT PATTERSON, C.M., AND WALTON, M.S. 2018. From lapis lazuli to ultramarine blue: Investigating Cennino Cennini's recipe using sulfur K-edge XANES. *Pure and Applied Chemistry 90*, 3, 463–475.

GARNIER, V., OHNENSTETTER, D., GIULIANI, G., BLANC, P., AND SCHWARZ, D. 2002. Trace-element contents and cathodoluminescence of "trapiche" rubies from Mong Hsu, Myanmar (Burma): Geological significance. *Mineralogy and Petrology 76*, 3–4, 179–193.

GERSTEN, J.I. AND SMITH, F.W. 2001. *The Physics and Chemistry of Materials*. Wiley.

GOROBETS, B.S. AND ROGOJIN, A.A. 2002. *Luminescent spectra of minerals*. All-Russia Institute of Mineral Resources, Moscow.

GÖTZE, J. 2002. Potential of cathodoluminescence (cl) microscopy and spectroscopy for the analysis of minerals and materials. *Analytical and Bioanalytical Chemistry 374*, 4, 703–708.

GUCSIK, A. 2009. *Cathodoluminescence and its Application in the Planetary Sciences*. Springer.

GUIDORZI, L., RE, A., PICOLLO, F., ET AL. 2020. Multi-technique study of He+ micro-irradiation effects on natural quartz crystals contained in archaeological pottery. *Nuclear Inst. and Methods in Physics Research, B 479*, June, 143–149.

HÄRDLE, W.K. AND SIMAR, L. 2015. *Applied Multivariate Statistical Analysis*. Springer-Verlag Berlin Heidelberg.

HARLEY, R.D. 1970. *Artists' Pigments c. 1600-1835*. Butterworths, London.

HENDERSON, B. AND IMBUSCH, G.F. 1989. *Optical Spectroscopy of Inorganic Solids*. Clarendon Press, Oxford.

HERRMANN, G. 1968. Lapis Lazuli : The Early Phases of Its Trade. *Iraq 30*, 1, 21–57.

HERRMANN, G. AND MOOREY, P.R.S. 1983. Lapis Lazuli. In: E. Ebeling, ed., *Reallexikon der Assyriologie und Vorderasiatischen Archäologie, vol. VI*. De Gruyter, Berlin, 489–492.

HOGARTH, D.D. AND GRIFFIN, W.L. 1976. New data on lazurite. *Lithos 9*, 39–54.

HOGARTH, D.D. AND GRIFFIN, W.L. 1978. Lapis lazuli from Baffin Island - a Precambrian meta-evaporite. *Lithos 11*, 37–60.

HOGARTH, D.D. AND GRIFFIN, W.L. 1980. Contact-metamorphic lapis lazuli: the Italian Mountain deposits, Colorado. *Canadian Mineralogist 18*, 59–70.

HOLLAND, T.J.B. 1980. The reaction albite= jadeite + quartz determined experimentally in the range 600-1200 °C. *American Mineralogist 65*, 129–134.

HOLLAND, T.J.B. 1983. The experimental determination of activities in disordered and short-range ordered jadeitic pyroxenes. *Contributions to Mineralogy and Petrology 82*, 214–220.

IVANOV, V.G. 1976. The geochemistry of formation of the rocks of the lazurite deposits of the southern Baikal Region. *Geokhimiya 1*, 47–54.

JARRIGE, J.-F. 1988. *Les Cites Oubliees De L'Indus: Archeologie Du Pakistan*. Musée Guimet, Association Française d'Action Artistique, Paris.

JARRIGE, J.-F. 1991. Mehrgarh: Its Place in the Development of Ancient Cultures in Pakistan. In: M. Jansen, M. Mulloy and G. Urban, eds., *Forgotten Cities on the Indus*. Verlag, Mainz am Rhein, 34–49.

KACHIGAN, S.K. 1986. *Statistical Analysis: An Interdisciplinary Introduction to Univariate and Multivariate Methods*. Radius Press, New York.

KAMMERLING, R.C., SCARRATT, K., BOSSHART, G., ET AL. 1994. Myanmar and its gems - An update. *Journal of Gemmology 24*, 3–40.

KEISCH, B. 1972. *Secrets of the past: Nuclear Energy Application in Art and Archaeology*. U.S. Atomic Energy Commission.

KENOYER, J.M. 1997. Trade and Technology of the Indus Valley: New Insights from Harappa, Pakistan. *World Archaeology 29*, 2, 262–280.

KENOYER, J.M. 1998. *Ancient Cities of the Indus Valley Civilization*. Oxford University Press.

KITAWAKI, H., ABDURIYIM, A., AND OKANO, M. 2008. Identification of melee-size synthetic yellow diamonds in jewelry. *Gems and Gemology 44*, 3, 202–213.

KUCHAŘOVÁ, A., GÖTZE, J., ŠACHLOVÁ, Š., PERTOLD, Z., AND PŘIKRYL, R. 2016. Microscopy and Cathodoluminescence Spectroscopy Characterization of Quartz Exhibiting Different Alkali–Silica Reaction Potential. *Microscopy and Microanalysis 22*, 01, 189–198.

LAW, R. 2014. Evaluating potential lapis lazuli sources for Ancient South Asia using Sulfur Isotope Analysis. In: *'My Life is like the Summer Rose' Maurizio Tosi e l'Archeologia come modo di vivere*. Archaeopress, Oxford.

LAW, R.W. 2008. Inter-Regional Interaction and Urbanism in the Ancient Indus Valley: A Geologic Provenance Study of Harappa's Rock and Mineral Assemblage. PhD Thesis, Anthropology. University of Wisconsin-Madison.

LINDON, J., TRANTER, G.E., AND KOPPENAAL, D., EDS. 2017. *Encyclopedia of Spectroscopy and Spectrometry*. Academic Press.

LO GIUDICE, A., ANGELICI, D., RE, A., ET AL. 2017. Protocol for lapis lazuli provenance determination: evidence for an Afghan origin of the stones used for ancient carved artefacts kept at the Egyptian Museum of Florence (Italy). *Archaeological and Anthropological Sciences 9*, 4, 637–651.

LO GIUDICE, A., RE, A., CALUSI, S., ET AL. 2009. Multitechnique characterization of lapis lazuli for provenance study. *Analytical and Bioanalytical Chemistry 395*, 7, 2211–2217.

MACRAE, C.M. AND WILSON, N.C. 2008. Luminescence database I - Minerals and materials. *Microscopy and Microanalysis 14*, 2, 184–204.

MARFUNIN, A.S. 1979. *Spectroscopy, luminescence and radiation centers in minerals*. Springer-Verlag.

MARK, S. 1997. *From Egypt to Mesopotamia. A Study of Predynastic Trade Routes*. College Station.

MARSHALL, D.J. 1988. *Cathodoluminescence of Geological Materials*. Unwin Hyman Ltd., London.

MCKEEVER, S.W.S. 1985. *Thermoluminescence of solids*. Cambridge University Press.

MITCHELL, A. 2018. *Geological Belts, Plate Boundaries, and Mineral Deposits in Myanmar*. Elsevier.

MODRESKI, P.J. AND AUMENTE-MODRESKI, R. 1996. Fluorescent Minerals. *Rocks & Minerals 71*, 1, 14–22.

MOORE, T.P. AND WOODSIDE, R.W.M. 2014. Sar-e-Sang. *The Mineralogical Record 45*.

MOOREY, P.R.S. 1994. *Ancient Mesopotamian Materials and Industries: the Archaeological Evidence*. Clarendon Press, Oxford.

MORIMOTO, N. 1988. Nomenclature of Pyroxenes. *Mineralogy and Petrology 39*, 1, 55–76.

NGUYEN, L.H. AND HOLMES, S. 2019. Ten quick tips for effective dimensionality reduction. *PLoS Computational Biology 15*, 6, 1–19.

PICHON, L., CALLIGARO, T., GONZALEZ, V., LEMASSON, Q., MOIGNARD, B., AND PACHECO, C. 2015a. Implementation of ionoluminescence in the AGLAE scanning external microprobe. *Nuclear Instruments and Methods in Physics Research B 348*, 68–72.

PICHON, L., CALLIGARO, T., LEMASSON, Q., MOIGNARD, B., AND PACHECO, C. 2015b. Programs for visualization, handling and quantification of PIXE maps at the AGLAE facility. *Nuclear Instruments and Methods in Physics Research Section B: Beam Interactions with Materials and Atoms 363*, 48–54.

PICHON, L., MOIGNARD, B., LEMASSON, Q., PACHECO, C., AND WALTER, P. 2014. Development of a multi-detector and a systematic imaging system on the AGLAE external beam. *Nuclear Instruments and Methods in Physics Research, Section B: Beam Interactions with Materials and Atoms 318*, PART A, 27–31.

PICOLLO, F., BATTIATO, A., BERNARDI, E., ET AL. 2016. All-carbon multi-electrode array for real-time in vitro measurements of oxidizable neurotransmitters. *Scientific Reports 6*, 1–8.

RAKOVAN, J. AND WAYCHUNAS, G. 1996. Luminescence in Minerals. *The Mineralogical Record 27*.

RE, A., ANGELICI, D., LO GIUDICE, A., ET AL. 2013. New markers to identify the provenance of lapis lazuli: Trace elements in pyrite by means of micro-PIXE. *Applied Physics A: Materials Science and Processing 111*, 1, 69–74.

RE, A., ANGELICI, D., LO GIUDICE, A., ET AL. 2015. Ion Beam Analysis for the provenance attribution of lapis lazuli used in glyptic art: The case of the “collezione Medicea.” *Nuclear Instruments and Methods in Physics Research, Section B: Beam Interactions with Materials and Atoms 348*, 278–284.

RE, A., LO GIUDICE, A., ANGELICI, D., ET AL. 2011. Lapis lazuli provenance study by means of micro-PIXE. *Nuclear Instruments and Methods in Physics Research, Section B: Beam Interactions with Materials and Atoms 269*, 20, 2373–2377.

RE, A., ZANGIROLAMI, M., ANGELICI, D., ET AL. 2018. Towards a portable X-ray luminescence instrument for applications in the Cultural Heritage field. *The European Physics Journal Plus 133*, 362.

REED, S.J.B. 2005. *Electron Microprobe Analysis and Scanning Electron Microscopy in Geology*. Cambridge University Press, New York.

RIVANO, S. 1975. El lapislazuli de Ovalle (Provincia de Coquimbo, Chile) [The lapis lazuli from Ovalle (Coquimbo Province, Chile)]. *6°Congreso Geologico Argentino*, 165–177.

ROBBINS, M. 1990. Activators in fluorescent minerals. *Rocks and Minerals 65*, 1, 35–41.

ROY, A., ED. 1986. *Artists' Pigments: a Handbook of Their History and Characteristics*. Archetype Publications, London.

SARIANIDI, V.I. AND KOWALSKI, L.H. 1971. The lapis lazuli route in the ancient East. *Archaeology 24*, 12–15.

SCHMIDT, C.M., WALTON, M.S., AND TRENTELMAN, K. 2009. Characterization of lapis lazuli pigments using a multitechnique analytical approach: Implications for identification and geological provenancing. *Analytical Chemistry 81*, 20, 8513–8518.

SMITH, A.L. 1949. Some New Complex Silicate Phosphors Containing Calcium, Magnesium, and Beryllium. *Journal of The Electrochemical Society 96*, 5, 287–296.

SMITH, G.D. AND KLINSHAW, R.J. 2009. The presence of trapped carbon dioxide in lapis lazuli and its potential use in geo-sourcing natural ultramarine pigment. *Journal of Cultural Heritage 10*, 3, 415–421.

SOFIANIDES, A.S. AND HARLOW, G.E. 1990. *Gems and Crystals from the American Museum of Natural History*. Simon and Schuster, New York.

SWARBRICK, B. AND WESTAD, F. 2016. An Overview of Chemometrics for the Engineering and Measurement Sciences. In: *Handbook of Measurement in Science and Engineering*. 2309–2407.

TODESCHINI, R. 1998. *Introduzione alla Chemiometria*. EdiSES, Naples.

TOSI, M. 1974. The Lapis Lazuli trade across the Iranian plateau in the 3rd millennium B.C. In: *Gururājamanjarikā, Studi in onore di G. Tucci*. Istituto Universitario Orientale, Napoli, 3–22.

TOSI, M. AND PIPERNO, M. 1973. Lithic Technology behind the Ancient Lapis Lazuli Trade. *Expedition Magazine 16*, 1, 15–23.

TOSI, M. AND VIDALE, M. 1990. 4th Millennium BC Lapis Lazuli Working at Mehrgarh, Pakistan. *Paléorient 16*, 2, 89–99.

TYKOT, R.H. 2004. Scientific methods and applications to archaeological provenance studies. *Physics Methods in Archaeometry*, IOS Press.

VAGGELLI, G., ES SEBAR, L., BORGHI, A., ET AL. 2019. Improvements to the analytical protocol of lapis lazuli provenance: First study on Myanmar rock samples. *European Physical Journal Plus 134*, 3.

VAN LOON, A., GAMBARDELLA, A.A., GONZALEZ, V., ET AL. 2020. Out of the blue: Vermeer's use of ultramarine in Girl with a Pearl Earring. *Heritage Science 8*, 1, 1–18.

VARMUZA, K. AND FILZMOSER, P. 2009. *Introduction to Multivariate Statistical Analysis in Chemometrics*. CRC Press.

VIDALE, M. 2017. *Lapis Lazuli Bead Making at Shahr-i Sokhta*. Antilia, Rome.

VINOKUROV, V.M. 1966. Electron Paramagnetic Resonance Data on Isomorphism of Manganese and Iron Ions in Certain Minerals. *Geochemistry International 3*, 996–1002.

VON ROSEN, L. 1988. *Lapis Lazuli in Geological Contexts and in Ancient Written Sources*. Astrom Editions, Partille, Sweden.

WARREN, B.E. AND BRAGG, W.L. 1928. The structure of diopside $CaMg(SiO_3)_2$. *Zeitschrift fur Krystallographie und Mineralogie 69*, 168–193.

WIELGOSZ-RONDOLINO, D., ANTONELLI, F., BOJANOWSKI, M.J., GŁADKI, M., GÖNCÜOĞLU, M.C., AND LAZZARINI, L. 2020. Improved methodology for identification of Göktepe white marble and the understanding of its use: A comparison with Carrara marble. *Journal of Archaeological Science 113*.

WINTER, I.J. 1999. The Aesthetic Value of Lapis Lazuli in Mesopotamia. In: A. Caubet, ed., *Cornaline et Pierres Précieuses: La Méditerranée de l'Antiquité à l'Islam*. Musée du Louvre, Paris, 43–58.

WOLD, S., SJÖSTRÖM, M., AND ERIKSSON, L. 2001. PLS-regression: A basic tool of chemometrics. *Chemometrics and Intelligent Laboratory Systems 58*, 2, 109–130.

WRIGHT, R.P. 2010. *The Ancient Indus: Urbanism, Economy, and Society*. Cambridge University Press, New York.

YACOBI, B.G. AND HOLT, D.B. 1990. *Cathodoluminescence Microscopy of Inorganic Solids*. Plenum Press, New York.

ZIEGLER, J.F., ZIEGLER, M.D., AND BIERSACK, J.P. 2010. SRIM – The stopping and range of ions in matter. *Nuclear Instruments and Methods in Physics Research, Section B: Beam Interactions with Materials and Atoms 268*, 1818–1823.

ZÖLDFÖLDI, J. 2011. Interdisziplinäre Studien zur Königsgruft von Qatna. In: P. Pfälzner, ed., *Qatna Studien Bd. 1.* Harrassowitz Verlag.

ZÖLDFÖLDI, J. AND KASZTOVSZKY, Z. 2003. Provenance study of Lapis lazuli by non-destructive Prompt Gamma Activation Analysis (PGAA). *BCH Supplement 51*, 677–691.

ZÖLDFÖLDI, J., RICHTER, S., KASZTOVSZKY, Z., AND MIHALY, J. 2006. Where does Lapis lazuli come from? Nondestructive provenance analysis by PGAA. *Proceeding of the 34th International Symposium on Archaeometry, Zaragoza - Spain, 2004*, 353–361.

Acknowledgements

First of all, thanks are due to my supervisors: Prof. Alessandro Lo Giudice, for introducing me to the wonderful world of lapis lazuli, supporting my ideas and providing the best advice from his wide expertise; Dr. Alessandro Re, for his patience in teaching me all the secrets of Ion Beam Analysis and beyond, sharing long beamtime runs and always finding the time to answer my long lists of questions.

A special thanks goes also to all the members of the Solid State Physics Group, that offered me the best working environment, both from a professional and personal point of view. A mention to a former member is essential: Dr. Debora Angelici, whose previous work on lapis lazuli was fundamental for the basis of this manuscript.

I would also like to acknowledge all the researchers that contributed in various ways to my work: from the Department of Earth Sciences at UniTo Prof. Alessandro Borghi, for his invaluable help with SEM-EDX measurements, Prof. Luca Martire and Dr. Roberto Cossio for the availability of the cold-CL apparatus and reference standards respectively; all the people from AN2000 at INFN-LNL, in particular Valentino Rigato, Leonardo La Torre and Davide Carlucci; the C2RMF people from NewAGLAE, especially Claire Pacheco, Quentin Lemasson, Laurent Pichon and Brice Moignard; Prof. Toshio Nozaka from Okayama University for his support with my WDX tests; all the teachers from the School of Chemometrics in Genova, that made me discover a whole new way of addressing data analysis.

From the archaeological field my thanks are for Prof. Massimo Vidale from University of Padova, Dr. Dennys Frenez from University of Bologna and Dr. Randall Law from University of Wisconsin-Madison for providing not only the samples, but also all the knowledge around them.

Part of this work could not have been achieved without the financial support of European H2020 Programmes IPERION CH (Grant Agreement n. 654028), IPERION HS (Grant Agreement n. 871034) and MSCA-RISE BE-ARCHAEO (Grant Agreement n. 823826).

And finally, the biggest thank you to Dani and Maçka, always by my side, and all my family and friends that supported me during this intense but stimulating experience.

Appendix A

Python script for PCA on μ-PIXE data from diopside in lapis lazuli

```
import pandas as pd
# loading main dataset
df=pd.read_csv(r'database_filepath.csv',\
            sep=';',names=['Ti','V','Cr','Mn','Zn','Sr','Provenance'])

from sklearn.preprocessing import StandardScaler
features = ['Ti','V','Cr','Mn','Zn','Sr']

# Separating out the target
x = df.loc[:, features].values
y = df.loc[:,['Provenance']].values
# Standardizing the features with autoscaling
scaler=StandardScaler()
x = scaler.fit_transform(x)

# defining mean and standard deviation obtained for variables in database dataset
mean=scaler.mean_
sc=scaler.scale_

from sklearn.decomposition import PCA
# creating a dataframe with the 6 PCs
pca = PCA(n_components=6)
principalComponents = pca.fit_transform(x)
principalDf = pd.DataFrame(data = principalComponents,\
                           columns = ['principal component 1', 'principal component 2',\
                                      'principal component 3', 'principal component 4',\
                                      'principal component 5', 'principal component 6'])
# additional information on provenance
finalDf = pd.concat([principalDf, df[['Provenance']]], axis = 1)

# explained variance (%)
var=pca.explained_variance_ratio_
P1=round(var[0]*100,1)
P2=round(var[1]*100,1)

# defining function "encircle" for the creation of polygons
import numpy as np

from scipy.spatial import ConvexHull
def encircle(x,y, ax=None, **kw):
    if not ax: ax=plt.gca()
    p = np.c_[x,y]
    hull = ConvexHull(p)
    poly = plt.Polygon(p[hull.vertices,:], **kw)
    ax.add_patch(poly)


# loading of external dataset with archaeological objects
newdata=pd.read_csv(r'external_filepath.csv',\
            sep=';',names=['names','ti','v','cr','mn','zn','sr'])

var = ['ti','v','cr','mn','zn','sr']

w = newdata.loc[:, var].values

# separating the labels
z = newdata.loc[:,'names'].values

# scaling the new dataset according to mean and SD values previously obtained from the model
newdata_SC = scaler.transform(w)
# transforming new scaled dataset according to equation 7.8
ND_PCA=pca.transform(newdata_SC)

# plotting scores
import matplotlib.pyplot as plt
fig = plt.figure(figsize = (8,8))
ax = fig.add_subplot(1,1,1)
ax.set_xlabel('PC1 (%2.1f'%P1+'%)',fontsize = 15)
ax.set_ylabel('PC2 (%2.1f'%P2+'%)', fontsize = 15)
```

```
targets = ['AFG','TAJ','SIB','MYA']
colors = ['b', 'r', 'forestgreen','darkmagenta']
for target, color in zip(targets,colors):
    indicesToKeep = finalDf['Provenance'] == target
    ax.scatter(finalDf.loc[indicesToKeep, 'principal component 1']
               , finalDf.loc[indicesToKeep, 'principal component 2']
               , c = color
               , s = 50)
    encircle(finalDf.loc[indicesToKeep, 'principal component 1']
               , finalDf.loc[indicesToKeep, 'principal component 2'],
               ec= color, fc= color, alpha=0.2, linewidth=1)
ARCH=ax.scatter(ND_PCA[:,0],ND_PCA[:,1], s=80,c='orange',marker='*',label='Egyptian samples')
# adding labels to archaeological objects
for i, txt in enumerate(z):
        ax.annotate(txt, (ND_PCA[i,0],ND_PCA[i,1]), textcoords='offset points',xytext=(8, -1) )


# adding two separate labels
first_legend=ax.legend(handles=[ARCH], markerscale=2.5, fontsize='x-large')
ax.add_artist(first_legend)
ax.legend(targets, loc=3)

ax.grid()
ax.set_ylim([-5,6.5])
ax.set_xlim([-4,6.5])

# plotting loadings
feature_vectors = pca.components_.T
arrow_size, text_pos = 7.0, 8.0,

for i, v in enumerate(feature_vectors):
    ax.arrow(0,  0,  arrow_size*v[0],  arrow_size*v[1],  head_width=0.2,  head_length=0.2,  linewidth=1,
color='red')
    ax.text(v[0]*text_pos,   v[1]*text_pos,   features[i],   color='black',   ha='center',   va='center',
fontsize=18)
```

Appendix B

Report on PhD activities

Attended courses

- School of Chemometrics - Multivariate Analysis, University of Genova, Department of Pharmacy, Genova, Italy, 13-17 January 2020.
- Metaljet X-ray source service training, Instructor: Irene Cimatti - Excillum, University of Torino, September 2019.
- Introduction to Scientific Programming in Python, Instructor: Dr. Alessandro Erba, University of Torino, November – December 2018.
- VII School of IR and Raman Spectroscopy: the application for Cultural Heritage, Venaria Reale, Torino, Italy, 12-16 November 2018.
- 3rd IPERION CH Doctoral Summer School "Towards an European infrastructure on heritage science: advances in the characterization, diagnosis and treatment evaluation of heritage materials", Ravenna, Italy, 16-20 July 2018.
- Theoretical-practical course for using TEM-EDS, Instructor: Prof. Elena Belluso, University of Torino, June 2018.
- Micro-Raman practical course, Instructor: Prof. Piergiorgio Rossetti, University of Torino, May 2018.
- Bioinspired Materials, Instructor: Dr. Federico Bosia, University of Torino, March 2018.
- Introduction to Matlab programming language, Instructor: Dr. Gessica Umili, University of Torino, January 2018.

Attended conferences

- 17th International Conference on Nuclear Microprobe Technology and Applications – ICNMTA 2020, 14-15 September 2020, online.
- MetroArchaeo 2019 – Metrology for archaeology and cultural heritage, Firenze, Italy, 4-6 December 2019.
- Technart 2019, Bruges, Belgium, 7-10 May 2019.
- XVIII International Symposium on Luminescence Spectrometry, Brest, France, 19-22 June 2018.
- X Congresso Nazionale dell'Associazione Italiana di Archeometria , Torino, Italy, 14-16 February 2018.
- Art'17 – 12th International Conference on non-destructive investigations and microanalysis for the diagnostics and conservation of cultural and environmental heritage, Torino, Italy, 22-24 November 2017.

Presentations

- Oral presentation: "New ion micro-beam analysis results in provenance determination of archaeological lapis lazuli" - L. Guidorzi, A. Re, A. Lo Giudice, A. Borghi, L. Es Sebar, V. Rigato, L. La Torre, D. Carlucci, D. Frenez, M. Vidale - 17th International Conference on Nuclear Microprobe Technology and Applications – ICNMTA 2020, 14-15 September 2020, online.
- Oral presentation: "BE-ARCHAEO: BEyond ARCHAEOlogy - A powerful tool to develop Japan/Europe innovative and interdisciplinary research" – E. Diana, N. Matsumoto, L. Guidorzi – EURAXESS RISE seminars, 19 May 2020, online.
- Oral presentation: "Thermoluminescence dating laboratory improvements tested on an archaeological rescue site in Trino, Vercelli province, Italy" L. Guidorzi, F. Fantino, E. Durisi, M. Ferrero, A. Re, L. Vigorelli, L. Visca, M. Gulmini, G. Dughera, G. Giraudo D. Angelici, E. Panero and A. Lo Giudice – MetroArchaeo 2019, Firenze, Italy, 4-6 December 2019.
- Oral presentation: Internal Seminar on the research group activity and personal PhD project. IRAMAT-CRP2A laboratory – Université Bordeaux-Montaigne, Pessac, France, 11 September 2018.
- Oral communication: "Combined IonoLuminescence and PIXE micro-analyses of natural diopside for activators and quenchers identification" L. Guidorzi, A. Re, D. Angelici, S. Molinengo, F. Picollo, L. La Torre, V. Rigato, G. Pratesi, A. Lo Giudice – XVIII International Symposium on Luminescence Spectrometry, Brest, France, 19-22 June 2018.
- Poster: "Non invasive Macro X-ray Fluorescence Scanning analysis of laquered oriental and japanning artworks furniture from Piedmont Castles" C. Caliri, P. Croveri, G. Ferraris, V. Gucciardi, L. Guidorzi, A. Lo Giudice, P.

Luciani, A. Mazzinghi, M. Nervo, A. Re, F.P. Romano, C. Ruberto, F. Taccetti and S. Tagliante, MA-XRF scanning in Conservation, Art and Archaeology, Catania, Italy, 15-16 October 2019.

- Poster: "Improving the protocol for provenance determination of lapis lazuli with new analyses on Myanmar samples" L. Guidorzi, A. Re, D. Angelici, F. Fantino, A. Borghi, G. Vaggelli, V. Rigato, L. La Torre, D. Carlucci and A. Lo Giudice - Technart 2019, Bruges, Belgium, 7-10 May 2019.
- Poster: "A characterization of lapis lazuli rocks by means of p-XRF" L. Guidorzi, A. Lo Giudice, A. Re, M. Nervo, D. Angelici, A. Agostino, M. Gulmini, A. Borghi, C. Ruberto, L. Castelli, F. Taccetti and G. Pratesi - Technart 2019, Bruges, Belgium, 7-10 May 2019.
- Poster: "Developing of a combined XRF scanner and 2D/3D X-ray and visible imaging apparatus" A. Lo Giudice, A. Re, L. Guidorzi, M. Nervo, D. Angelici, R. Boano, R. Giustetto, L. Castelli, C. Czelusniak, L. Giuntini, C. Ruberto, F. Taccetti - Technart 2019, Bruges, Belgium, 7-10 May 2019.
- Poster: "Ceramic forgeries aged by radiation: towards a new method for their identification" L. Guidorzi, A. Re, F. Picollo, F. Fantino, L. Martire, E. Belluso, G. Artioli, L. Peruzzo, S. Boesso, V. Rigato, L. La Torre, D. Carlucci, A. Lo Giudice – Convegno tematico dell'Associazione Italiana di Archeometria, Reggio Calabria, Italy, 27-29 March 2019.
- Poster: "Instrumentation and technique developments at the thermoluminescence dating laboratory of the University of Turin" L. Guidorzi, A. Lo Giudice, F. Fantino, A. Re, D. Angelici, M. Gulmini - X Congresso Nazionale dell'Associazione Italiana di Archeometria, Torino, Italy, 14-16 February 2018.
- Poster: "Thermoluminescence for dating Myanmar monuments: a new local laboratory and first measurements" F. Fantino, L. Guidorzi, D.T. Myat, A. Lo Giudice, A. Re, P. Davit - X Congresso Nazionale dell'Associazione Italiana di Archeometria, Torino, Italy, 14-16 February 2018.

Projects

- "SIBILLA: Simultaneous Ion Beam Investigations for Lapis Lazuli provenance Analysis", IPERION CH/IPERION HS FIXLAB project at AGLAE (Accélérateur Grand Louvre d'Analyses Elémentaires), C2RMF. Palais du Louvre, Paris, France (2019-2020).
  Role: Project leader
- "BE-ARCHAEO: BEyond-ARCHAEOlogy – an advanced approach linking East to West through science, field archaeology, interactive museum experiences", Horizon 2020 MSCA-RISE-2018 grant n. 823826 (2019-2023).
  Role: Early Stage Researcher
- "ALCHIMIA: AnaLysis of Cultural Heritage Items with Micro Ion beAms ", Istituto Nazionale di Fisica Nucleare – Laboratori Nazionali di Legnaro (INFN-LNL) experimental project (2017-2021).
  Role: Participant

Periods in external facilities/institutions

- Visiting student at IRAMAT-CRP2A laboratory – Université Bordeaux-Montaigne, Pessac, France (3 days, 2018).
- ESR in BE-ARCHAEO Project, Okayama University, Okayama, Japan (2 months, 2019).
- NewAGLAE beamtime runs, C2RMF, Palais du Louvre, Paris, France (10 days, 2019-2020).
- INFN-LNL beamtime runs, Legnaro (PD), Italy (18 days, 2018-2020).

Teaching activities

- "Progetto Lauree Scientifiche", University of Torino, Bachelor Degree course in Material Science. Laboratory assistant. January-February 2020. Total hours: 20.
- Course: Diagnostic physics with laboratory. Teacher: Prof. Alessandro Lo Giudice, Dr. Alessandro Re. University of Torino, Bachelor's Degree course in Material Science. Laboratory assistant. April-May 2018. Total hours: 12.
- Course: Dating methods. Teacher: Prof. Alessandro Lo Giudice. University of Torino, Master's Degree course in Physics. Laboratory assistant. December 2017 - February 2018. Total hours: 32.

Supervision of graduate students

- Co-Supervisor of 1 Bachelor's thesis in Material Science and Technology (April 2019).
- Co-Supervisor of 2 Master's theses in Physics (ongoing).

Other research activities (not reported in PhD thesis)

- Multi-technique study of He^+ micro-irradiation effects on natural quartz crystals contained in archaeological pottery, for authentication purposes (see paper #2 and #8).
- MA-XRF applied on paintings and furniture (see paper #1 and #4).
- μ-PIXE analysis on red-figured pottery shards for the discrimination of different workshops in Southern Italy (see paper #6).
- μ-PIXE analysis on polychrome Egyptian statuette.
- H2020 MSCA-RISE BE-ARCHAEO project related activities: optical microscopy, FORS and μ-XRF analyses on Japanese archaeological glass beads and pottery fragments; contribution to the development of an interactive archaeometrical database.

Third Mission

IAPS School Day - 11 November 2019
Notte dei Ricercatori 2019 – 23 November 2019

Appendix C

Published Papers

1) L. Sottili, L. Guidorzi, A. Mazzinghi, C. Ruberto, L. Castelli, C. Czelusniak, L. Giuntini, M. Massi, F. Taccetti, M. Nervo, S. De Blasi, R. Torres, F. Arneodo, A. Re, A. Lo Giudice "The Importance of Being Versatile: INFN-CHNet MA-XRF Scanner on Furniture at the CCR "La Venaria Reale"" *Applied Sciences* (2021) 11, 1197.

2) L. Guidorzi, A. Re, F. Picollo, P. Aprà, F. Fantino, L. Martire, G. Artioli, L. Peruzzo, S. Boesso, V. Rigato, L. La Torre, A. Lo Giudice "Multi-technique study of He^+ micro-irradiation effects on natural quartz crystals contained in archaeological pottery" *Nuclear Inst. and Methods in Physics Research Section B* (2020) 479, pp. 143-149.

3) L. Guidorzi, F. Fantino, E. Durisi, M. Ferrero, A. Re, L. Vigorelli, L. Visca, M. Gulmini, G. Dughera, G. Giraudo, D. Angelici, E. Panero, A. Lo Giudice "Age determination and authentication of ceramics: advancements in the thermoluminescence dating laboratory in Torino (Italy)" *Acta IMEKO* (*in journal editing*).

4) L. Sottili, L. Guidorzi, A. Mazzinghi, C. Ruberto, L. Castelli, C. Czelusniak, L. Giuntini, M. Massi, F. Taccetti, M. Nervo, A. Re, A. Lo Giudice "INFN-CHNet meets CCR La Venaria Reale: first results" *Proceedings of 2020 IMEKO TC4 International Conference on Metrology for Archaeology and Cultural Heritage – MetroArchaeo 2020* (2020) pp. 507-511, ISBN: 978-929900849-2.

5) L. Guidorzi, F. Fantino, E. Durisi, M. Ferrero, A. Re, L. Vigorelli, L. Visca, M. Gulmini, G. Dughera, G. Giraudo, D. Angelici, E. Panero, A. Lo Giudice "Thermoluminescence dating laboratory improvements tested on an archaeological rescue site in Trino, Vercelli province, Italy" *Proceedings of 2019 IMEKO TC4 International Conference on Metrology for Archaeology and Cultural Heritage - MetroArchaeo 2019* (2019) pp. 199-204, ISBN: 978-929900845-4.

6) L. Guidorzi, A. Re, M. Gulmini, P. Davit, V. Rigato, L. La Torre, D. Carlucci, A. Lo Giudice "Towards the quantification of trace metals in pottery shards for discriminating different workshops in Southern Italy" *Laboratori Nazionali di Legnaro Annual Report 2019* (2020) 259, pp. 131-132, ISSN: 1828-8561.

7) G. Peroni, L. Pacher, V. De Nadal, M. Campostrini, P. Aprà, A. Re, A. Lo Giudice, L. Guidorzi, P. Olivero, R. Cherubini, N. Cartiglia, V. Rigato, F. Picollo "Fabrication and characterization of DIACELL diamond-based detectors for in vitro cellular radiobiology" *Laboratori Nazionali di Legnaro Annual Report 2019* (2020) 259, pp. 126-127, ISSN: 1828-8561.

8) L. Guidorzi, A. Re, F. Picollo, F. Fantino, L. Martire, G. Artioli, L. Peruzzo, S. Boesso, V. Rigato, L. La Torre, D. Carlucci, A. Lo Giudice "He^+ irradiation of quartz for the identification of ceramic forgeries aged by radiation", *Laboratori Nazionali di Legnaro Annual Report 2018* (2019) 258, pp. 161-162, ISSN: 1828-8561.

9) A. Re, A. Lo Giudice, L. Guidorzi, L. Es Sebar, L. La Torre, D.Carlucci, V. Rigato, G. Pratesi "Luminescence Properties of Lapis Lazuli Investigated by means of a Proton Micro-Beam", *Laboratori Nazionali di Legnaro Annual Report 2017* (2018) 25, pp. 132-133, ISSN: 1828-8561.

Appendix D

Quantitative Raw Data

In the following pages, tables reporting all the quantitative results shown in the plots of this thesis are listed.

Major elements concentrations expected for the specific mineral phases are generally reported in wt% values, minor and trace elements are instead expressed in ppm.

Elements resulting under limit of detection (LOD) are indicated with a 0 ± 0 value.

Sample	Area	Mg			Al			Si			S			Cl			K			Ca			Ti			V		
		conc	err	LOD	conc	err	LOD	conc	err	LOD	conc	err	LOD	conc	err	LOD	conc	err	LOD	conc	err	LOD	conc	err	LOD	conc	err	LOD
		wt%	*wt%*	*wt%*	*wt%*	*wt%*	*wt%*	*wt%*	*wt%*	*wt%*	*ppm*	*ppm*	*ppm*	*ppm*	*ppm*	*ppm*	*ppm*	*ppm*	*ppm*	*wt%*	*wt%*	*wt%*	*ppm*	*ppm*	*ppm*	*ppm*	*ppm*	*ppm*
MYA_07	A	8.08	1.21	0.10	*	*	*	26.42	3.96	0.02	0	0	127	0	0	108	0	0	180	20.15	3.02	0.002	128	43	61	145	31	50
MYA_07	C	8.51	1.28	0.09				26.55	3.98	0.01	0	0	127	0	0	106	0	0	176	19.34	2.90	0.002	465	70	55	227	34	51
MYA_07	E	8.32	1.25	0.09				26.59	3.99	0.01	0	0	120	0	0	102	0	0	171	19.40	2.91	0.002	657	99	51	261	39	50
MYA_03	B	10.84	1.63	0.05				26.19	3.93	0.01	0	0	114	0	0	61	0	0	161	18.09	2.71	0.003	391	59	48	143	28	43
MYA_03	C	10.93	1.64	0.05				26.17	3.92	0.01	0	0	113	0	0	61	0	0	163	18.07	2.71	0.003	384	58	48	166	28	43
MYA_03	E	10.98	1.65	0.05				26.10	3.91	0.00	0	0	111	0	0	59	0	0	160	18.22	2.73	0.004	289	43	50	190	28	44
MYA_10	E	7.59	1.14	0.10				26.57	3.99	0.02	0	0	125	0	0	105	0	0	174	19.82	2.97	0.001	678	102	52	0	0	56
MYA_10	G	9.03	1.36	0.09				26.43	3.96	0.01	0	0	124	0	0	63	0	0	166	18.83	2.82	0.002	540	81	54	151	32	52
MYA_09	A	9.42	1.41	0.08				26.42	3.96	0.01	0	0	120	0	0	101	0	0	164	18.81	2.82	0.003	0	0	83	78	27	42
MYA_09	B	8.35	1.25	0.09				26.10	3.91	0.02	429	77	78	0	0	66	0	0	174	20.65	3.10	0.002	0	0	59	0	0	77
MYA_09	D	9.17	1.37	0.08				26.36	3.95	0.02	0	0	120	0	0	63	0	0	165	19.25	2.89	0.003	170	37	53	97	28	48
MYA_12	A	10.18	1.53	0.06				26.33	3.95	0.01	0	0	116	0	0	60	266	61	99	18.21	2.73	0.003	355	53	48	0	0	44
MYA_12	D	10.66	1.60	0.05				26.15	3.92	0.01	0	0	110	0	0	93	0	0	153	18.26	2.74	0.003	308	46	46	94	24	41
MYA_12	E	10.00	1.50	0.07				26.35	3.95	0.01	0	0	113	0	0	62	0	0	157	18.31	2.75	0.003	398	60	46	85	25	42
MYA_08	A	11.01	1.65	0.05				26.07	3.91	0.01	0	0	107	0	0	57	0	0	154	18.24	2.74	0.002	392	59	46	153	27	43
MYA_08	B	10.30	1.54	0.06				24.24	3.64	0.01	137	78	81	0	0	69	0	0	125	23.88	3.58	0.004	377	57	68	186	38	60
MYA_08	G	8.36	1.25	0.09				26.52	3.98	0.02	0	0	124	0	0	105	0	0	171	19.62	2.94	0.001	402	60	54	98	30	49
MYA_04	D	9.74	1.46	0.07				26.46	3.97	0.01	0	0	116	0	0	60	0	0	160	18.38	2.76	0.003	0	0	46	0	0	65
MYA_04	C	11.01	1.65	0.05				26.18	3.93	0.01	0	0	111	0	0	94	0	0	155	17.89	2.68	0.004	361	54	46	239	36	41
MYA_04	F	10.08	1.51	0.06				26.28	3.94	0.01	0	0	110	0	0	58	0	0	157	18.58	2.79	0.001	327	49	47	233	35	42
MYA_02	A	10.27	1.54	0.05				26.27	3.94	0.01	0	0	113	0	0	59	0	0	162	18.40	2.76	0.003	696	104	48	270	40	48
MYA_02	B	10.67	1.60	0.06				26.17	3.93	0.01	0	0	114	0	0	62	0	0	161	18.25	2.74	0.003	608	91	47	277	42	48
MYA_02	E	10.62	1.59	0.06				26.25	3.94	0.01	0	0	114	0	0	96	0	0	102	18.15	2.72	0.004	331	50	45	155	27	42
MYA_11	F	8.61	1.29	0.08				26.65	4.00	0.01	0	0	121	0	0	62	0	0	169	18.62	2.79	0.001	548	82	47	90	28	47
MYA_11	B	10.31	1.55	0.06				26.32	3.95	0.01	0	0	110	0	0	58	0	0	159	17.84	2.68	0.003	513	77	47	75	26	46
MYA_06	D	9.57	1.44	0.07				26.30	3.94	0.01	0	0	120	0	0	102	0	0	171	19.01	2.85	0.002	549	82	48	213	32	48
MYA_06	F	11.08	1.66	0.05				26.17	3.93	0.01	0	0	112	0	0	95	0	0	159	17.89	2.68	0.002	561	84	47	157	28	45
MYA_06	A	10.49	1.57	0.06				26.18	3.93	0.01	0	0	112	0	0	98	0	0	162	18.42	2.76	0.002	566	85	47	235	35	45

Sample	Area	Cr			Mn			Fe			Cu			Zn			As			Sr			Y			Zr		
		conc	err	LOD	conc	err	LOD	conc	err	LOD	conc	err	LOD	conc	err	LOD	conc	err	LOD	conc	err	LOD	conc	err	LOD	conc	err	LOD
		ppm	*ppm*	*ppm*	*ppm*	*ppm*	*ppm*	*ppm*	*ppm*	*ppm*	*ppm*	*ppm*	*ppm*	*ppm*	*ppm*	*ppm*	*ppm*	*ppm*	*ppm*	*ppm*	*ppm*	*ppm*	*ppm*	*ppm*	*ppm*	*ppm*	*ppm*	*ppm*
MYA_07	A	0	0	69	114	17	12	1413	212	10	0	0	12	102	15	7	0	0	13	0	0	27	0	0	48	0	0	44
MYA_07	C	0	0	45	76	14	15	1463	219	11	0	0	11	99	15	6	0	0	18	0	0	40	0	0	41	97	33	39
MYA_07	E	0	0	64	80	13	12	1434	215	11	0	0	11	99	15	5	0	0	15	0	0	25	0	0	45	93	30	38
MYA_03	B	0	0	36	52	13	13	645	97	11	0	0	11	27	5	5	0	0	13	0	0	27	0	0	32	76	28	30
MYA_03	C	0	0	40	49	12	13	651	98	11	0	0	5	25	6	7	0	0	12	0	0	23	0	0	33	0	0	37
MYA_03	E	0	0	63	79	12	12	593	89	8	0	0	9	21	5	6	0	0	6	0	0	40	0	0	33	0	0	27
MYA_10	E	0	0	58	237	36	16	4927	739	14	0	0	7	34	6	6	0	0	13	0	0	30	0	0	55	179	39	49
MYA_10	G	0	0	65	236	35	13	4259	639	14	0	0	13	24	6	6	0	0	14	86	21	22	0	0	46	218	38	49
MYA_09	A	0	0	39	81	15	15	1869	280	9	0	0	11	117	18	4	0	0	15	0	0	33	0	0	44	0	0	51
MYA_09	B	0	0	66	98	15	14	2406	361	10	0	0	11	141	21	7	0	0	15	0	0	26	0	0	39	0	0	58
MYA_09	D	0	0	39	87	14	13	1360	204	10	0	0	13	103	15	6	0	0	14	0	0	28	0	0	45	0	0	61
MYA_12	A	0	0	58	91	14	14	1994	299	11	0	0	10	0	0	4	0	0	12	65	18	26	0	0	40	113	31	48
MYA_12	D	0	0	33	80	13	12	1899	285	13	0	0	9	0	0	10	0	0	12	0	0	27	0	0	31	111	30	40
MYA_12	E	0	0	55	128	19	12	2562	384	14	0	0	9	0	0	5	0	0	14	0	0	22	0	0	47	121	32	36
MYA_08	A	0	0	36	75	12	13	712	107	7	0	0	5	46	7	6	0	0	9	0	0	37	0	0	37	99	28	28
MYA_08	B	0	0	72	70	13	18	740	111	15	0	0	7	47	7	6	0	0	10	0	0	26	0	0	47	0	0	43
MYA_08	G	0	0	63	82	14	14	1264	190	8	0	0	10	101	15	7	0	0	14	0	0	41	0	0	41	0	0	43
MYA_04	D	0	0	32	78	14	15	1849	277	10	0	0	12	122	18	6	0	0	15	0	0	41	0	0	36	0	0	43
MYA_04	C	0	0	36	68	12	15	1096	164	10	0	0	6	60	9	5	0	0	7	0	0	22	0	0	43	84	26	32
MYA_04	F	0	0	63	80	12	12	963	144	10	0	0	6	61	9	5	0	0	11	0	0	24	0	0	31	126	29	35
MYA_02	A	0	0	60	77	12	13	678	102	10	0	0	10	35	6	4	0	0	5	0	0	34	0	0	46	122	33	37
MYA_02	B	0	0	60	76	12	11	825	124	9	0	0	6	56	8	3	0	0	13	0	0	35	0	0	43	96	32	35
MYA_02	E	0	0	53	50	11	13	632	95	7	0	0	6	41	6	7	0	0	12	0	0	22	0	0	32	72	29	34
MYA_11	F	0	0	36	256	38	13	4584	688	14	0	0	11	29	6	6	0	0	14	0	0	23	0	0	51	117	32	42
MYA_11	B	0	0	35	270	40	15	4553	683	13	0	0	7	36	6	5	0	0	6	74	18	24	0	0	46	88	28	45
MYA_06	D	0	0	60	79	13	12	983	147	9	0	0	12	83	12	6	0	0	10	0	0	21	0	0	35	93	31	28
MYA_06	F	0	0	34	80	12	11	522	78	9	0	0	6	26	6	6	0	0	12	0	0	31	0	0	43	75	28	31
MYA_06	A	0	0	34	74	13	11	779	117	10	0	0	6	49	7	5	0	0	13	0	0	37	0	0	34	101	28	37

Table D.1. Quantitative results for μ-PIXE analysis on diopside crystals in reference geological samples from Myanmar. IBA measurements performed in INFN-LNL. * Al concentration is excluded from quantification due to effects depending on poor detector spectral resolution. All absolute errors are considered as at least 15% of elemental concentration.

Sample	Area	Mg			Al			Si			S			Cl			K			Ca			Ti			V		
		conc	err	LOD	conc	err	LOD	conc	err	LOD	conc	err	LOD	conc	err	LOD	conc	err	LOD	conc	err	LOD	conc	err	LOD	conc	err	LOD
		wt%	*wt%*	*wt%*	*wt%*	*wt%*	*wt%*	*wt%*	*wt%*	*wt%*	*ppm*	*ppm*	*ppm*	*ppm*	*ppm*	*ppm*	*ppm*	*ppm*	*ppm*	*wt%*	*wt%*	*wt%*	*ppm*	*ppm*	*ppm*	*ppm*	*ppm*	*ppm*
SiS-337	D1	11.13	0.15	0.02	0.00	0.00	0.09	26.10	0.20	0.01	298	63	68	209	47	53	0	0	84	17.82	0.12	0.004	1358	63	58	203	50	79
SiS-337	D2	11.34	0.15	0.02	0.00	0.00	0.10	26.15	0.20	0.01	0	0	109	138	44	53	0	0	84	17.70	0.13	0.005	0	0	59	185	44	64
SiS-337	D3	11.19	0.15	0.01	0.00	0.00	0.10	26.17	0.20	0.01	0	0	67	312	49	53	0	0	82	17.54	0.13	0.003	1335	61	57	306	48	75
SiS-336	D1	10.99	0.15	0.02	0.00	0.00	0.09	26.21	0.20	0.01	792	68	65	293	47	52	189	44	80	17.55	0.13	0.004	1021	61	59	505	58	74
SiS-336	D2	9.29	0.16	0.04	0.78	0.13	0.06	26.78	0.22	0.01	930	74	68	327	51	55	890	55	79	16.83	0.12	0.005	1693	71	55	563	58	82
SiS-62	D1	10.14	0.15	0.04	0.00	0.00	0.10	26.39	0.21	0.01	1420	82	68	1079	62	54	384	48	82	17.90	0.13	0.006	555	47	55	229	43	65
SiS-62	D2	9.37	0.17	0.04	1.10	0.13	0.06	26.68	0.22	0.01	715	74	70	2183	79	54	1331	63	80	16.64	0.12	0.005	546	49	60	186	45	69
SiS-62	D3	9.83	0.17	0.04	0.44	0.14	0.07	26.84	0.22	0.01	881	76	70	588	58	56	241	49	82	16.69	0.12	0.005	542	49	59	218	45	68
SiS-44	D1	11.39	0.17	0.01	0.00	0.00	0.10	26.01	0.21	0.01	0	0	68	0	0	54	0	0	140	17.98	0.13	0.003	526	50	59	345	48	68
SiS-24	D1	10.56	0.15	0.03	0.00	0.00	0.09	26.28	0.20	0.01	475	64	67	776	55	52	879	52	80	17.88	0.13	0.003	184	40	53	297	40	57
SiS-24	D2	11.01	0.15	0.02	0.00	0.00	0.08	26.13	0.21	0.01	0	0	106	161	41	50	332	43	80	17.95	0.13	0.004	341	41	50	291	40	56
SiS-24	D3	11.01	0.15	0.02	0.00	0.00	0.08	25.99	0.19	0.01	0	0	66	277	45	51	0	0	84	18.36	0.13	0.004	301	38	51	275	38	55

Sample	Area	Cr			Mn			Fe			Cu			Zn			As			Sr			Y			Zr		
		conc	err	LOD	conc	err	LOD	conc	err	LOD	conc	err	LOD	conc	err	LOD	conc	err	LOD	conc	err	LOD	conc	err	LOD	conc	err	LOD
		ppm	*ppm*	*ppm*	*ppm*	*ppm*	*ppm*	*ppm*	*ppm*	*ppm*	*ppm*	*ppm*	*ppm*	*ppm*	*ppm*	*ppm*	*ppm*	*ppm*	*ppm*	*ppm*	*ppm*	*ppm*	*ppm*	*ppm*	*ppm*	*ppm*	*ppm*	*ppm*
SiS-337	D1	452	43	62	219	22	28	435	18	13	0	0	6	0	0	7	0	0	14	61	17	21	0	0	32	187	36	41
SiS-337	D2	281	39	61	233	20	18	250	14	12	0	0	6	0	0	7	0	0	6	0	0	25	0	0	40	0	0	44
SiS-337	D3	452	41	61	144	20	28	588	20	11	0	0	7	0	0	6	0	0	15	68	18	23	0	0	28	290	44	43
SiS-336	D1	0	0	71	454	29	28	461	21	18	0	0	8	0	0	7	0	0	16	0	0	16	494	47	45	221	42	43
SiS-336	D2	217	42	71	231	23	28	187	14	11	30	6	5	0	0	7	0	0	9	0	0	25	203	34	30	478	56	60
SiS-62	D1	239	37	62	237	21	24	396	17	12	0	0	6	17	5	5	0	0	9	60	19	19	0	0	21	254	43	38
SiS-62	D2	321	40	59	237	22	23	414	18	13	0	0	8	0	0	5	0	0	16	87	21	22	0	0	29	158	40	50
SiS-62	D3	293	40	63	207	21	26	251	15	12	0	0	13	0	0	5	0	0	18	0	0	26	0	0	31	211	42	45
SiS-44	D1	373	41	65	332	23	24	202	13	13	0	0	12	0	0	7	0	0	15	0	0	21	0	0	24	133	33	40
SiS-24	D1	294	36	58	304	21	18	172	13	15	20	6	7	0	0	5	0	0	6	65	19	19	0	0	23	477	56	65
SiS-24	D2	248	34	56	213	19	20	306	15	10	0	0	12	0	0	6	0	0	13	0	0	8	0	0	30	671	62	38
SiS-24	D3	252	34	54	204	19	21	226	14	12	0	0	13	0	0	5	0	0	6	0	0	15	0	0	49	659	62	39

Table D.2. Quantitative results for μ-PIXE analysis on diopside crystals in archaeological cross sections from Shahr-i Sokhta site. IBA measurements performed in INFN-LNL.

	Sample	Area	Mg			Al			Si			S			Cl			K			Ca			Ti			V		
			conc	err	LOD	conc	err	LOD	conc	err	LOD	conc	err	LOD	conc	err	LOD	conc	err	LOD	conc	err	LOD	conc	err	LOD	conc	err	LOD
			wt%	*wt%*	*wt%*	*wt%*	*wt%*	*wt%*	*wt%*	*wt%*	*wt%*	*ppm*	*ppm*	*ppm*	*ppm*	*ppm*	*ppm*	*ppm*	*ppm*	*ppm*	*wt%*	*wt%*	*wt%*	*ppm*	*ppm*	*ppm*	*ppm*	*ppm*	*ppm*
AGLAE 2019	SiS-336	D1	9.66	0.07	0.02	1.38	0.02	0.01	25.72	0.12	0.01	2594	71	77	627	39	49	708	46	38	16.06	0.07	0.01	1495	15	6	408	9	14
	SiS-28	D1	10.39	0.13	0.03	0.87	0.04	0.03	26.16	0.17	0.01	0	0	316	0	0	135	273	99	109	16.44	0.10	0.02	1269	32	14	369	16	22
	SiS-336	D2	9.44	0.12	0.04	1.85	0.05	0.03	26.29	0.18	0.02	1021	135	200	808	93	118	738	102	103	15.33	0.10	0.02	1229	26	16	520	16	22
	SiS-67	D1	10.01	0.12	0.02	1.93	0.05	0.03	25.96	0.17	0.01	628	111	171	1056	95	119	2140	123	85	15.60	0.10	0.02	760	19	13	290	12	16
	SiS-325	D1	10.18	0.10	0.03	1.39	0.03	0.02	26.61	0.14	0.01	533	75	124	544	62	86	731	56	62	15.65	0.08	0.01	283	9	9	181	7	9
	SiS-325	D2	10.21	0.10	0.02	1.59	0.04	0.02	26.59	0.15	0.01	678	89	143	726	67	90	988	77	69	15.27	0.08	0.01	322	11	10	173	7	10
	SiS-187	D1	8.41	0.08	0.02	3.61	0.05	0.02	26.02	0.14	0.01	2041	90	105	938	61	72	2180	82	56	13.89	0.07	0.01	1529	15	7	113	8	16
	SiS-186	D1	9.63	0.11	0.03	1.42	0.04	0.03	25.83	0.16	0.01	1298	118	154	1354	98	102	1835	111	67	16.25	0.09	0.02	1058	22	15	194	12	19
	SiS-186	D2	9.39	0.14	0.02	1.18	0.05	0.03	25.93	0.19	0.02	1094	173	250	1636	136	145	1201	111	102	16.96	0.11	0.02	1097	31	24	169	16	27
	SiS-205	D2	9.00	0.19	0.07	2.36	0.10	0.03	25.13	0.25	0.04	3017	287	277	869	180	246	2264	220	146	16.44	0.15	0.02	881	32	24	121	16	27
AGLAE 2020	SiS-186	D1	9.31	0.24	0.07	1.50	0.10	0.06	25.50	0.32	0.04	1277	312	401	1029	243	316	1433	261	170	16.51	0.18	0.05	1091	60	59	213	32	60
	SiS-186	D2	9.73	0.28	0.09	1.03	0.10	0.08	25.70	0.30	0.07	1052	377	505	1078	276	256	943	290	276	17.07	0.20	0.08	1060	70	71	158	37	72
	SiS-325	D2	9.63	2.59	0.13	1.39	0.29	0.08	25.87	1.53	0.06	743	10	627	659	374	716	1025	505	181	16.58	1.13	0.04	327	163	84	0	0	49
	SiS-67	D3	9.24	0.20	0.07	1.91	0.12	0.04	25.79	0.27	0.05	911	289	318	716	206	255	2971	646	186	16.52	0.15	0.04	1147	111	42	310	31	35
	SiS-331	D1	9.38	0.19	0.02	1.28	0.04	0.05	25.77	0.32	0.05	671	96	354	1072	243	287	1143	19	396	16.93	0.30	0.07	1162	28	76	0	0	143
	SiS-331	D1bis	8.96	0.26	0.09	1.74	0.12	0.05	25.49	0.33	0.07	2038	392	441	1489	307	246	581	253	265	16.23	0.18	0.07	606	49	54	0	0	56
	SiS-178	D2	8.97	0.24	0.10	2.25	0.12	0.05	27.04	0.31	0.05	1112	295	337	2093	297	348	1897	289	217	13.72	0.15	0.06	0	0	101	0	0	40
	SiS-181	D4	10.16	0.22	0.04	1.36	0.05	0.05	26.74	0.25	0.03	192	32	279	1630	138	201	2171	193	163	15.40	0.13	0.04	63	8	44	0	0	33

	Sample	Area	Cr			Mn			Fe			Cu			Zn			As			Sr			Y			Zr		
			conc	err	LOD	conc	err	LOD	conc	err	LOD	conc	err	LOD	conc	err	LOD	conc	err	LOD	conc	err	LOD	conc	err	LOD	conc	err	LOD
			ppm	*ppm*	*ppm*	*ppm*	*ppm*	*ppm*	*ppm*	*ppm*	*ppm*	*ppm*	*ppm*	*ppm*	*ppm*	*ppm*	*ppm*	*ppm*	*ppm*	*ppm*	*ppm*	*ppm*	*ppm*	*ppm*	*ppm*	*ppm*	*ppm*	*ppm*	*ppm*
AGLAE 2019	SiS-336	D1	0	0	7	330	4	4	2511	16	3	148	3	4	17	2	2	13	2	6	91	4	2	199	8	5	309	11	9
	SiS-28	D1	201	10	12	319	10	9	249	8	7	11	3	6	0	0	5	0	0	5	44	9	8	0	0	10	259	30	28
	SiS-336	D2	0	0	14	238	8	8	1346	21	5	84	5	7	0	0	5	22	5	9	165	16	16	220	21	14	381	33	35
	SiS-67	D1	172	8	10	1640	23	6	1142	18	15	52	4	5	46	4	4	0	0	5	60	10	10	0	0	10	175	23	26
	SiS-325	D1	46	4	6	270	6	4	989	13	4	1	1	4	14	2	2	0	0	2	91	8	3	15	5	3	412	20	18
	SiS-325	D2	43	4	7	266	6	5	1387	17	5	5	2	4	22	2	3	0	0	3	73	9	7	0	0	7	373	23	21
	SiS-187	D1	37	4	5	275	5	4	4227	18	4	33	2	3	27	2	2	10	2	4	78	6	4	0	0	5	263	15	12
	SiS-186	D1	86	6	9	591	10	6	1267	16	8	27	3	5	45	3	4	0	0	4	270	17	15	0	0	7	134	23	35
	SiS-186	D2	91	8	12	705	17	8	981	21	12	27	4	8	106	6	4	0	0	5	176	22	17	0	0	17	136	29	43
	SiS-205	D2	61	10	15	288	13	9	1762	39	11	76	7	9	54	7	5	14	7	8	88	20	26	0	0	26	383	63	62
AGLAE 2020	SiS-186	D1	0	0	36	672	31	20	1404	38	25	0	0	13	45	11	13	0	0	40	384	80	99	0	0	52	0	0	214
	SiS-186	D2	0	0	46	779	43	21	726	40	36	0	0	16	89	19	15	0	0	41	0	0	111	0	0	74	0	0	326
	SiS-325	D2	0	0	80	357	45	84	1521	44	148	0	0	58	39	28	28	0	0	43	0	0	427	0	0	91	653	61	126
	SiS-67	D3	227	136	28	2143	116	14	2194	47	16	68	29	8	52	11	8	0	0	12	162	50	56	0	0	53	320	56	106
	SiS-331	D1	0	0	33	802	105	25	6041	173	18	704	50	15	508	18	15	0	0	35	0	0	55	0	0	88	0	0	157
	SiS-331	D1bis	0	0	29	502	33	25	2450	81	24	805	41	19	400	31	13	0	0	32	0	0	78	0	0	108	0	0	181
	SiS-178	D2	0	0	26	1414	43	14	494	28	42	0	0	24	23	9	11	0	0	36	0	0	98	0	0	67	0	0	93
	SiS-181	D4	0	0	34	1099	49	10	506	27	30	0	0	9	0	0	9	0	0	12	0	0	54	0	0	49	0	0	48

Table D.3. Quantitative results for μ-PIXE analysis on diopside crystals in archaeological bulk samples from Shahr-i Sokhta site. IBA measurements performed in AGLAE; the two different measurement runs are reported separately.

	Sample	Area	Mg			Al			Si			S			Cl			K			Ca			Ti			V		
			conc	err	LOD	conc	err	LOD	conc	err	LOD	conc	err	LOD	conc	err	LOD	conc	err	LOD	conc	err	LOD	conc	err	LOD	conc	err	LOD
			wt%	*wt%*	*wt%*	*wt%*	*wt%*	*wt%*	*wt%*	*wt%*	*wt%*	*ppm*	*ppm*	*ppm*	*ppm*	*ppm*	*ppm*	*ppm*	*ppm*	*ppm*	*wt%*	*wt%*	*wt%*	*ppm*	*ppm*	*ppm*	*ppm*	*ppm*	*ppm*
2020	CS10335/20a	95_D1	9.50	0.17	0.06	1.35	0.07	0.06	26.27	0.23	0.03	902	225	310	0	0	272	645	170	225	17.05	0.14	0.03	489	34	39	110	17	34
	CS10335/20a	95_D2	9.30	0.21	0.05	1.30	0.08	0.06	26.41	0.28	0.04	0	0	409	745	227	293	547	184	282	17.40	0.18	0.03	805	49	43	121	23	43
	CS10335/20a	95_D4	9.95	0.17	0.05	0.98	0.06	0.05	26.26	0.22	0.03	0	0	320	0	0	220	0	0	199	16.85	0.13	0.02	459	31	36	131	16	30
	CS10335/20a	76_D3	8.72	0.18	0.09	1.33	0.07	0.04	26.07	0.25	0.04	2661	275	282	1078	189	242	1490	237	199	16.34	0.14	0.04	823	40	38	129	22	42
	CS10335/20a	76_D3b	8.09	0.27	0.12	1.65	0.12	0.06	26.36	0.35	0.07	2148	494	573	1478	339	438	1858	426	348	17.37	0.19	0.06	709	53	59	175	32	58
	CS10335/20a	96_D4	9.21	0.14	0.05	1.41	0.06	0.03	26.22	0.19	0.02	1190	193	243	992	154	191	866	149	177	16.81	0.12	0.03	864	32	31	116	17	31
	CS10335/20a	97_D5	8.84	0.16	0.05	1.67	0.07	0.05	26.27	0.21	0.03	1468	220	264	632	152	211	1288	157	166	16.62	0.12	0.03	663	29	32	106	16	31
2019	CS10335/20a	103_D1	8.49	0.10	0.03	1.95	0.05	0.03	26.69	0.16	0.01	1962	124	148	1405	94	107	2653	137	110	15.68	0.09	0.02	1103	19	13	97	10	18
	CS10335/20a	103_D3	9.69	0.14	0.01	2.02	0.07	0.04	28.27	0.21	0.02	2019	184	197	1690	148	153	1955	163	131	12.41	0.09	0.02	445	20	18	84	11	18
	CS10335/20a	103_D4	9.04	0.14	0.03	1.40	0.06	0.04	26.64	0.20	0.01	1174	164	225	1353	133	153	1260	139	122	16.86	0.11	0.03	566	22	20	172	13	20
	CS10335/20a	103_D5	9.70	0.14	0.03	1.35	0.06	0.04	26.32	0.20	0.02	481	138	230	890	117	150	1213	142	127	15.90	0.11	0.03	741	23	18	118	12	20

	Sample	Area	Cr			Mn			Fe			Cu			Zn			As			Sr			Y			Zr		
			conc	err	LOD	conc	err	LOD	conc	err	LOD	conc	err	LOD	conc	err	LOD	conc	err	LOD	conc	err	LOD	conc	err	LOD	conc	err	LOD
			ppm	*ppm*	*ppm*	*ppm*	*ppm*	*ppm*	*ppm*	*ppm*	*ppm*	*ppm*	*ppm*	*ppm*	*ppm*	*ppm*	*ppm*	*ppm*	*ppm*	*ppm*	*ppm*	*ppm*	*ppm*	*ppm*	*ppm*	*ppm*	*ppm*	*ppm*	*ppm*
2020	CS10335/20a	95_D1	0	0	22	438	21	12	1183	39	15	36	9	8	54	8	6	0	0	18	79	30	42	0	0	40	0	0	79
	CS10335/20a	95_D2	0	0	26	382	23	19	1292	53	20	49	11	10	49	10	10	0	0	25	0	0	50	0	0	71	0	0	100
	CS10335/20a	95_D4	0	0	19	364	19	12	805	31	13	42	8	9	44	7	4	0	0	10	50	22	28	0	0	39	168	51	71
	CS10335/20a	76_D3	0	0	38	328	19	17	2096	56	15	89	11	6	67	10	6	0	0	22	303	47	47	0	0	39	0	0	94
	CS10335/20a	76_D3b	0	0	62	378	28	21	1085	37	30	141	19	15	108	18	17	0	0	35	305	84	121	0	0	64	0	0	271
	CS10335/20a	96_D4	0	0	18	492	17	12	1423	29	15	55	8	10	71	8	4	0	0	10	54	19	19	0	0	27	123	40	62
	CS10335/20a	97_D5	0	0	19	472	17	13	1524	25	14	56	9	10	57	8	8	0	0	16	88	25	34	0	0	31	142	46	68
2019	CS10335/20a	103_D1	0	0	8	361	7	5	2024	15	7	157	5	4	75	4	3	0	0	3	103	11	4	0	0	10	179	21	25
	CS10335/20a	103_D3	0	0	10	266	10	6	2078	25	7	56	5	7	64	6	3	0	0	9	62	15	20	0	0	17	98	30	30
	CS10335/20a	103_D4	0	0	13	337	10	8	1926	20	9	69	6	8	60	6	6	0	0	7	66	15	18	0	0	21	222	37	36
	CS10335/20a	103_D5	0	0	10	314	10	8	1316	26	8	91	6	7	54	5	5	0	0	9	38	11	12	0	0	18	174	29	36

Table D.4. Quantitative results for μ-PIXE analysis on diopside crystals for the cylinder seal sample from Shahr-i Sokhta site. IBA measurements performed in AGLAE; the two different measurement runs are reported separately.

Sample	Area	Mg			Al			Si			S			Cl			K			Ca			Ti			V		
		conc	err	LOD	conc	err	LOD	conc	err	LOD	conc	err	LOD	conc	err	LOD	conc	err	LOD	conc	err	LOD	conc	err	LOD	conc	err	LOD
		wt%	*wt%*	*wt%*	*wt%*	*wt%*	*wt%*	*wt%*	*wt%*	*wt%*	*ppm*	*ppm*	*ppm*	*ppm*	*ppm*	*ppm*	*ppm*	*ppm*	*ppm*	*wt%*	*wt%*	*wt%*	*ppm*	*ppm*	*ppm*	*ppm*	*ppm*	*ppm*
HR_83a	D2	9.85	0.18	0.06	1.12	0.06	0.05	25.79	0.24	0.03	700	182	248	313	146	221	1425	153	136	16.99	0.14	0.03	437	49	53	174	28	46
HR_83a	D3	10.73	0.17	0.04	0.41	0.04	0.04	26.33	0.22	0.02	1241	193	254	374	126	181	536	138	139	16.78	0.13	0.02	205	24	36	221	16	26
HR_83a	D1	9.84	0.22	0.06	1.55	0.09	0.06	26.54	0.29	0.05	1201	265	344	1419	213	182	1207	218	187	15.05	0.14	0.04	453	42	43	171	23	36
HR_83b	D1	10.23	0.16	0.06	0.69	0.05	0.04	26.72	0.22	0.02	1086	192	265	394	121	187	661	144	143	16.54	0.12	0.04	249	26	39	122	16	28
L-Mfrag	D3	10.35	0.12	0.04	0.97	0.04	0.03	26.51	0.17	0.01	335	114	195	0	0	132	609	94	98	16.32	0.09	0.02	159	17	26	213	12	18
L-Mfrag	D1	10.38	0.17	0.04	0.97	0.06	0.03	26.34	0.22	0.02	0	0	275	0	0	199	672	143	143	16.18	0.12	0.02	123	21	33	207	15	24
L-Mfrag	D2	10.05	0.22	0.07	1.11	0.08	0.06	26.42	0.27	0.01	0	0	333	0	0	266	504	189	183	16.67	0.16	0.04	294	30	35	129	19	35
L-Mbead	D1	10.56	0.09	0.02	1.26	0.03	0.02	26.30	0.14	0.01	408	69	114	0	0	81	496	59	65	15.82	0.07	0.02	125	10	14	165	7	11
L-Mbead	D2	10.53	0.13	0.04	1.05	0.04	0.03	26.46	0.18	0.01	545	113	182	0	0	133	397	74	104	15.64	0.10	0.02	118	16	25	190	12	18
L-D	D1	10.39	0.17	0.04	1.06	0.06	0.04	26.64	0.23	0.04	0	0	258	0	0	202	861	152	137	16.27	0.13	0.03	142	23	34	222	18	24
L-D	D2	9.73	0.15	0.02	1.36	0.06	0.04	26.58	0.20	0.03	775	145	219	390	115	181	1018	110	128	15.69	0.11	0.03	303	25	31	179	15	25
SHT-1b	D1	8.51	0.16	0.06	2.93	0.09	0.04	26.21	0.22	0.03	1731	205	226	1041	142	167	886	145	133	14.17	0.11	0.03	1167	43	31	288	22	36

Sample	Area	Cr			Mn			Fe			Cu			Zn			As			Sr			Y			Zr		
		conc	err	LOD	conc	err	LOD	conc	err	LOD	conc	err	LOD	conc	err	LOD	conc	err	LOD	conc	err	LOD	conc	err	LOD	conc	err	LOD
		ppm	*ppm*	*ppm*	*ppm*	*ppm*	*ppm*	*ppm*	*ppm*	*ppm*	*ppm*	*ppm*	*ppm*	*ppm*	*ppm*	*ppm*	*ppm*	*ppm*	*ppm*	*ppm*	*ppm*	*ppm*	*ppm*	*ppm*	*ppm*	*ppm*	*ppm*	*ppm*
HR_83a	D2	0	0	33	346	20	16	335	18	22	0	0	14	0	0	11	0	0	39	0	0	81	0	0	86	0	0	146
HR_83a	D3	66	11	21	347	14	10	344	13	13	0	0	9	0	0	6	0	0	14	99	26	29	0	0	41	0	0	66
HR_83a	D1	0	0	28	312	24	14	423	29	15	0	0	20	0	0	11	0	0	52	162	45	55	0	0	73	0	0	125
HR_83b	D1	0	0	20	373	15	10	594	16	13	23	9	10	0	0	8	0	0	24	93	27	30	0	0	48	0	0	80
L-Mfrag	D3	68	8	15	278	10	10	366	10	8	52	6	6	32	4	5	0	0	7	175	22	22	0	0	24	380	49	64
L-Mfrag	D1	76	11	19	284	13	14	391	14	11	30	8	7	24	5	6	0	0	8	147	28	38	0	0	41	467	70	85
L-Mfrag	D2	88	16	24	313	22	11	653	35	15	26	9	10	0	0	8	0	0	12	0	0	44	0	0	62	415	92	128
L-Mbead	D1	54	5	8	254	7	6	652	13	6	57	3	4	32	3	4	0	0	3	76	9	8	0	0	8	244	22	25
L-Mbead	D2	84	9	14	270	10	9	390	11	9	75	7	6	36	5	5	0	0	7	63	16	19	0	0	19	427	48	63
L-D	D1	72	12	21	285	17	12	531	25	11	18	8	9	17	6	8	0	0	14	74	25	40	0	0	40	374	69	70
L-D	D2	62	10	18	234	14	14	1190	37	11	37	7	8	24	5	3	0	0	7	65	20	26	0	0	31	378	64	84
SHT-1b	D1	201	15	21	938	30	15	1097	33	19	145	10	5	23	6	8	0	0	89	118	27	36	0	0	90	151	47	88

Table D.5. Quantitative results for μ-PIXE analysis on diopside crystals for the archaeological samples from Indus Valley sites. IBA measurements performed in AGLAE, 2020 measurement run.

Sample	Area	Mg			Al			Si			S			Cl			K			Ca			Ti			V		
		conc	err	LOD	conc	err	LOD	conc	err	LOD	conc	err	LOD	conc	err	LOD	conc	err	LOD	conc	err	LOD	conc	err	LOD	conc	err	LOD
		wt%	*wt%*	*wt%*	*wt%*	*wt%*	*wt%*	*wt%*	*wt%*	*wt%*	*ppm*	*ppm*	*ppm*	*ppm*	*ppm*	*ppm*	*ppm*	*ppm*	*ppm*	*wt%*	*wt%*	*wt%*	*ppm*	*ppm*	*ppm*	*ppm*	*ppm*	*ppm*
CH-1	D1	10.50	0.29	0.07	0.79	0.09	0.08	25.73	0.34	0.07	0	0	477	0	0	390	1120	276	243	17.17	0.20	0.07	146	43	65	150	27	47
CH-1	D3	9.60	0.30	0.07	1.20	0.12	0.11	23.98	0.34	0.05	1209	432	627	0	0	447	2167	334	200	19.96	0.23	0.07	0	0	75	276	31	48
CH-4	D1	10.28	0.14	0.04	0.73	0.04	0.03	26.28	0.19	0.01	929	143	206	508	102	132	759	113	110	16.85	0.10	0.02	459	25	26	221	15	22
CH-4	D2	9.15	0.25	0.08	0.92	0.08	0.07	25.60	0.31	0.06	1183	347	451	1114	261	257	965	260	213	19.09	0.18	0.03	1082	58	54	161	31	60
CH-2a	D1	10.03	0.32	0.17	1.40	0.12	0.05	25.09	0.38	0.09	5228	634	517	1752	392	442	1341	346	296	16.53	0.21	0.06	399	56	71	457	43	57
CH-2a	D2	10.07	0.37	0.12	0.89	0.13	0.09	24.62	0.42	0.08	3690	615	517	0	0	507	2126	450	269	18.06	0.26	0.08	434	66	80	270	42	64
CH-2a	D3	9.34	0.32	0.02	1.72	0.14	0.08	25.26	0.39	0.07	3779	574	623	991	354	377	3838	501	334	16.41	0.22	0.08	324	54	72	220	37	60

Sample	Area	Cr			Mn			Fe			Cu			Zn			As			Sr			Y			Zr		
		conc	err	LOD	conc	err	LOD	conc	err	LOD	conc	err	LOD	conc	err	LOD	conc	err	LOD	conc	err	LOD	conc	err	LOD	conc	err	LOD
		ppm	*ppm*	*ppm*	*ppm*	*ppm*	*ppm*	*ppm*	*ppm*	*ppm*	*ppm*	*ppm*	*ppm*	*ppm*	*ppm*	*ppm*	*ppm*	*ppm*	*ppm*	*ppm*	*ppm*	*ppm*	*ppm*	*ppm*	*ppm*	*ppm*	*ppm*	*ppm*
CH-1	D1	0	0	36	344	26	25	441	25	22	0	0	15	28	11	15	14	24	27	0	0	83	0	0	167	0	0	190
CH-1	D3	68	22	38	351	25	17	181	20	29	0	0	37	29	10	15	0	0	33	176	74	98	0	0	68	796	184	278
CH-4	D1	25	9	16	200	11	11	507	19	7	150	9	5	41	6	5	6	6	8	38	13	16	81	22	30	317	47	56
CH-4	D2	0	0	36	330	26	26	791	33	22	3245	79	35	83	21	24	22	17	32	0	0	66	0	0	92	496	130	157
CH-2a	D1	208	35	44	651	46	34	2991	93	33	76	21	16	146	23	20	17	27	30	0	0	122	0	0	149	0	0	276
CH-2a	D2	104	29	45	608	48	26	882	58	38	244	34	25	96	19	26	29	31	38	0	0	110	0	0	169	0	0	284
CH-2a	D3	76	27	44	790	41	21	1804	56	41	71	19	20	70	17	15	0	0	44	0	0	82	0	0	89	478	192	268

Table D.6. Quantitative results for μ-PIXE analysis on diopside crystals for the geological samples from Chagai Hills. IBA measurements performed in AGLAE, 2020 measurement run.

	Sample	Area	Mg			Al			Si			S			Cl			K		
			conc	err	LOD	conc	err	LOD	conc	err	LOD	conc	err	LOD	conc	err	LOD	conc	err	LOD
			wt%	*wt%*	*wt%*	*wt%*	*wt%*	*wt%*	*wt%*	*wt%*	*wt%*	*ppm*	*ppm*	*ppm*	*ppm*	*ppm*	*ppm*	*ppm*	*ppm*	*ppm*
2019	Afg12397	D2	9.81	0.08	0.02	1.00	0.02	0.02	25.89	0.13	0.01	830	75	110	663	56	75	1140	66	52
	Afg12397	D2bis	9.72	0.08	0.02	1.10	0.03	0.02	25.86	0.14	0.01	951	84	123	710	62	82	1504	77	56
	Afg12397	D3bis	10.43	0.09	0.02	0.78	0.03	0.02	26.12	0.14	0.01	714	81	125	0	0	88	465	64	65
	AFG1	Diop1	8.88	0.06	0.01	2.54	0.03	0.01	26.37	0.12	0.01	1248	51	70	566	36	47	1202	40	37
	AFG1	Diop3	8.79	0.07	0.01	2.77	0.04	0.01	26.09	0.12	0.01	1413	63	79	385	37	53	1896	63	42
	AFG3	Diop1	9.95	0.06	0.01	0.80	0.02	0.01	26.01	0.10	0.00	1030	49	71	115	29	47	229	31	38
	AFG4	Diop1	10.88	0.08	0.02	0.72	0.02	0.01	27.10	0.12	0.01	559	59	93	156	38	62	123	40	48
	AFG4	Diop2	10.22	0.06	0.01	0.80	0.02	0.01	27.00	0.12	0.01	990	53	80	243	33	52	185	39	40
	Pamir2bis	D4	10.09	0.10	0.03	0.87	0.03	0.02	26.11	0.16	0.01	0	0	220	0	0	152	0	0	118
	Pamir2bis	D1	10.31	0.07	0.02	0.82	0.02	0.01	26.06	0.10	0.01	196	46	86	109	35	57	618	49	45
	Siberia390	D2	9.34	0.09	0.02	0.47	0.02	0.02	25.66	0.12	0.01	0	0	135	0	0	88	142	58	70
	Siberia390	D1	8.97	0.08	0.02	0.77	0.03	0.02	25.01	0.13	0.01	0	0	222	136	51	85	815	67	68
	Siberia390	D3	9.77	0.10	0.03	0.76	0.03	0.02	25.11	0.15	0.02	295	91	152	0	0	176	1544	100	77
	Siberia390	D4	9.33	0.14	0.05	0.84	0.04	0.03	25.04	0.18	0.02	0	0	370	0	0	144	1116	124	113
	BK3	D1	10.71	0.13	0.04	0.78	0.04	0.03	26.17	0.16	0.02	0	0	193	0	0	129	0	0	104
	BK6	D3	9.90	0.10	0.02	0.61	0.03	0.02	26.27	0.16	0.01	0	0	248	0	0	97	208	52	74
	BK6	D3bis	9.68	0.10	0.02	0.75	0.03	0.02	26.26	0.15	0.01	0	0	232	0	0	161	0	0	74
	BK6	D1	10.53	0.10	0.02	0.80	0.03	0.02	26.42	0.14	0.01	0	0	220	0	0	89	0	0	71
	BK7	D2	9.36	0.07	0.01	1.93	0.03	0.01	26.29	0.12	0.00	0	0	79	0	0	84	1369	46	40
	BK7	D1	10.13	0.06	0.01	0.66	0.01	0.01	26.23	0.11	0.01	0	0	70	0	0	73	0	0	37
	BK9	D2	9.40	0.09	0.03	1.33	0.04	0.02	24.65	0.14	0.01	0	0	146	0	0	92	436	74	77
	BK9	D1	9.89	0.12	0.03	0.93	0.04	0.03	26.16	0.18	0.01	206	112	189	0	0	210	1027	113	82
	BK9	D2bis	9.40	0.06	0.01	0.87	0.02	0.01	24.60	0.11	0.01	251	44	80	0	0	49	487	44	41
	BK10	D1	9.34	0.06	0.01	1.81	0.03	0.01	25.08	0.11	0.01	972	46	70	0	0	45	1098	47	36
	BK10	D2	9.62	0.08	0.02	1.22	0.03	0.02	25.06	0.13	0.01	228	60	108	0	0	115	143	49	55
	MYA_03	B	9.55	0.10	0.03	1.01	0.03	0.02	24.05	0.13	0.01	1174	107	151	236	63	98	0	0	80
	MYA_03	C	10.33	0.07	0.02	0.62	0.02	0.01	26.09	0.11	0.01	0	0	91	118	36	58	0	0	49
	MYA_04	F	9.90	0.06	0.01	1.36	0.02	0.01	25.84	0.12	0.01	0	0	75	0	0	49	215	39	39
	MYA_04	C	10.58	0.17	0.04	0.82	0.05	0.04	25.97	0.22	0.02	0	0	256	0	0	167	0	0	244
	MYA_06	D	9.72	0.06	0.01	1.74	0.02	0.01	26.08	0.11	0.01	0	0	111	0	0	69	0	0	34
	MYA_06	F	10.18	0.06	0.01	0.67	0.01	0.01	25.79	0.10	0.01	363	40	69	0	0	71	261	35	35
	MYA_07	E	9.35	0.06	0.01	2.48	0.03	0.01	25.45	0.11	0.01	0	0	68	0	0	44	0	0	36
	MYA_09	D	9.11	0.06	0.01	2.57	0.03	0.01	25.49	0.11	0.01	192	34	67	0	0	43	0	0	36
	MYA_09	A	9.27	0.06	0.01	2.34	0.03	0.01	25.99	0.11	0.01	0	0	67	0	0	70	0	0	35
	MYA_10	G	9.23	0.06	0.01	2.62	0.03	0.01	25.76	0.11	0.01	0	0	114	0	0	42	188	34	35
	MYA_10	F	8.95	0.13	0.03	3.25	0.07	0.02	25.59	0.17	0.01	0	0	178	0	0	206	1975	129	88
	MYA_11	F	8.59	0.10	0.03	3.15	0.06	0.02	25.91	0.16	0.01	0	0	151	0	0	104	1230	98	87
	MYA_11	B	9.01	0.14	0.03	2.64	0.07	0.03	25.80	0.19	0.01	0	0	363	0	0	143	808	118	110
	MYA_12	D	10.07	0.06	0.01	1.28	0.02	0.01	25.88	0.10	0.01	0	0	119	0	0	45	328	38	38
	MYA_12	E	9.41	0.20	0.02	2.83	0.11	0.05	25.34	0.24	0.02	2811	272	209	0	0	218	1208	195	167
2020	AFG1	D1	8.60	0.36	0.05	2.98	0.20	0.05	25.58	0.44	0.10	1653	515	703	812	329	400	1346	402	365
	AFG1	diopDX	8.68	0.19	0.05	2.51	0.10	0.05	25.85	0.24	0.03	3763	364	309	1927	225	148	706	177	203
	Pamir3	DZ	9.47	0.41	0.06	2.33	0.14	0.10	25.97	0.41	0.08	690	348	494	0	0	312	3425	275	418
	Siberia390	D1	9.37	0.20	0.07	0.71	0.05	0.06	24.83	0.26	0.03	0	0	364	181	26	213	521	61	159
	Siberia390	D1bis	9.59	0.21	0.07	0.78	0.07	0.06	24.84	0.28	0.04	384	618	376	0	0	262	1942	714	190
	BK3	D1a	10.56	0.62	0.13	0.75	0.03	0.07	26.71	0.47	0.11	0	0	703	0	0	537	0	0	253
	BK3	D1b	10.30	0.10	0.03	0.87	0.03	0.03	26.46	0.14	0.01	0	0	256	0	0	101	0	0	140
	BK9	D2a	9.33	0.15	0.06	2.33	0.09	0.05	25.25	0.21	0.03	1562	378	278	238	136	189	1058	64	174
	BK9	D2b	9.75	0.17	0.03	1.61	0.07	0.04	25.63	0.22	0.02	337	46	235	0	0	175	1012	165	179
	MYA_03	B	10.35	0.08	0.02	0.73	0.02	0.02	26.17	0.12	0.01	239	64	112	0	0	79	0	0	107

(follows)

Table D.7. Quantitative results for μ-PIXE analysis on diopside crystals in reference geological samples. IBA measurements performed in AGLAE; the two different measurement runs are reported separately.

	Sample	Area	Ca			Ti			V			Cr			Mn			Fe			Cu		
			conc	err	LOD	conc	err	LOD	conc	err	LOD	conc	err	LOD	conc	err	LOD	conc	err	LOD	conc	err	LOD
			wt%	*wt%*	*wt%*	*ppm*	*ppm*	*ppm*	*ppm*	*ppm*	*ppm*	*ppm*	*ppm*	*ppm*	*ppm*	*ppm*	*ppm*	*ppm*	*ppm*	*ppm*	*ppm*	*ppm*	*ppm*
2019	Afg12397	D2	17.11	0.16	0.002	1233	18	8	250	9	15	173	5	6	370	6	5	472	7	5	63	3	4
	Afg12397	D2bis	17.05	0.18	0.002	1209	19	10	240	10	15	159	5	7	374	7	5	435	7	5	77	3	4
	Afg12397	D3bis	16.43	0.08	0.02	1059	18	10	99	8	15	103	5	6	334	7	5	790	11	4	28	2	5
	AFG1	Diop1	13.83	0.06	0.01	4529	29	4	227	11	30	0	0	7	169	3	2	1503	10	2	20	1	3
	AFG1	Diop3	13.70	0.06	0.01	4081	28	5	319	12	28	0	0	6	167	3	3	2351	15	2	39	2	3
	AFG3	Diop1	17.79	0.05	0.001	307	6	5	291	5	6	140	3	5	212	3	3	612	4	2	28	1	3
	AFG4	Diop1	15.54	0.06	0.01	652	9	6	185	6	9	22	3	5	403	4	3	760	6	4	29	2	3
	AFG4	Diop2	15.66	0.04	0.002	939	9	5	189	6	10	43	3	4	408	4	2	925	6	4	55	2	2
	Pamir2bis	D4	17.99	0.15	0.003	126	8	10	0	0	9	0	0	9	290	6	4	2321	24	5	0	0	5
	Pamir2bis	D1	17.44	0.11	0.002	406	8	6	0	0	8	0	0	4	220	4	3	1795	14	3	0	0	4
	Siberia390	D2	18.48	0.06	0.003	446	12	11	75	7	11	0	0	6	809	9	4	14111	54	8	0	0	4
	Siberia390	D1	19.44	0.10	0.002	590	13	11	64	7	12	0	0	10	686	9	4	14701	78	8	0	0	4
	Siberia390	D3	17.90	0.10	0.01	502	14	13	61	8	13	0	0	11	716	10	5	15039	95	8	7	2	4
	Siberia390	D4	19.01	0.12	0.02	454	18	18	65	10	17	0	0	10	619	13	8	14096	76	14	0	0	6
	BK3	D1	17.00	0.10	0.01	88	11	13	0	0	11	0	0	12	250	7	6	1306	20	6	0	0	5
	BK6	D3	17.51	0.05	0.003	356	11	11	18	6	11	0	0	10	483	8	5	7384	33	7	10	2	4
	BK6	D3bis	17.15	0.11	0.003	767	14	10	0	0	14	0	0	10	509	8	5	7012	51	7	0	0	4
	BK6	D1	16.35	0.08	0.01	253	9	9	0	0	14	0	0	8	227	5	4	1527	18	4	0	0	4
	BK7	D2	16.20	0.10	0.001	160	5	6	0	0	5	0	0	5	248	3	2	1098	9	2	0	0	3
	BK7	D1	17.43	0.09	0.002	152	5	5	0	0	5	0	0	4	309	4	2	1917	12	3	0	0	3
	BK9	D2	19.74	0.17	0.003	864	17	14	0	0	16	0	0	10	251	6	5	1258	15	5	0	0	7
	BK9	D1	17.45	0.16	0.003	413	17	20	0	0	17	0	0	14	353	9	7	2974	35	8	0	0	8
	BK9	D2bis	20.29	0.12	0.002	816	10	9	20	5	10	0	0	3	214	3	3	1404	11	3	0	0	2
	BK10	D1	17.43	0.07	0.001	1795	13	6	32	6	15	0	0	3	296	4	2	10446	44	4	0	0	3
	BK10	D2	18.62	0.09	0.002	1519	16	8	47	8	16	12	3	5	161	4	4	3045	20	2	0	0	4
	MYA_03	B	20.25	0.08	0.003	431	13	12	137	8	12	0	0	8	69	4	6	804	9	2	0	0	8
	MYA_03	C	17.64	0.09	0.002	391	8	7	108	5	8	9	3	4	66	2	3	774	7	2	0	0	5
	MYA_04	F	17.33	0.05	0.002	357	7	6	121	4	6	0	0	4	72	2	2	977	6	2	0	0	4
	MYA_04	C	17.37	0.13	0.02	306	19	19	132	12	17	0	0	12	69	7	9	1174	17	7	0	0	16
	MYA_06	D	17.02	0.10	0.002	480	7	5	134	4	6	9	2	3	66	2	2	1076	8	1	0	0	2
	MYA_06	F	18.04	0.05	0.002	658	7	5	156	5	8	8	2	4	67	2	2	696	4	2	0	0	2
	MYA_07	E	16.77	0.06	0.002	518	7	5	143	4	7	8	2	4	66	2	2	1339	7	2	0	0	3
	MYA_09	D	17.44	0.10	0.002	244	5	5	56	3	5	0	0	3	70	2	2	1487	10	1	0	0	2
	MYA_09	A	16.65	0.09	0.002	106	4	5	0	0	4	0	0	2	74	2	2	1953	12	1	0	0	2
	MYA_10	G	16.40	0.07	0.002	415	6	5	32	3	6	0	0	4	208	3	2	3832	19	3	0	0	3
	MYA_10	F	14.68	0.09	0.02	428	15	13	34	8	14	0	0	8	230	7	6	3400	22	6	0	0	6
	MYA_11	F	15.64	0.12	0.002	452	13	11	29	7	12	0	0	10	225	6	5	4410	39	5	0	0	6
	MYA_11	B	15.98	0.10	0.02	435	17	16	28	9	16	0	0	14	231	8	8	4185	41	9	0	0	14
	MYA_12	D	17.17	0.09	0.001	349	6	5	0	0	6	0	0	3	101	2	2	2242	14	2	0	0	3
	MYA_12	E	14.83	0.13	0.03	305	23	29	0	0	24	0	0	22	103	9	10	2731	32	7	0	0	17
2020	AFG1	D1	13.02	0.20	0.07	4684	137	62	271	61	134	0	0	79	144	28	36	628	35	27	0	0	20
	AFG1	diopDX	14.18	0.13	0.03	2913	63	37	111	28	64	0	0	39	143	15	21	1637	30	14	112	12	14
	Pamir3	DZ	15.29	0.25	0.06	293	8	47	0	0	134	0	0	47	252	86	42	577	9	39	41	10	17
	Siberia390	D1	19.05	0.18	0.04	535	38	47	0	0	41	0	0	39	714	29	17	15806	194	31	0	0	16
	Siberia390	D1bis	18.26	0.17	0.06	502	24	30	70	13	27	0	0	26	712	20	14	15994	142	17	0	0	38
	BK3	D1a	16.38	0.31	0.08	0	0	70	0	0	51	0	0	36	251	46	24	1457	97	16	0	0	18
	BK3	D1b	16.68	0.09	0.01	87	10	12	0	0	15	0	0	10	307	8	5	2570	27	7	0	0	4
	BK9	D2a	16.93	0.13	0.02	2002	64	36	0	0	82	0	0	19	106	12	15	837	29	12	0	0	17
	BK9	D2b	17.61	0.14	0.03	2040	61	29	0	0	80	0	0	31	116	14	16	1049	26	13	0	0	10
	MYA_03	B	17.60	0.08	0.01	0	0	28	175	122	18	0	0	14	93	10	12	900	29	12	0	0	11

(follows)

	Sample	Area	Zn			As			Sr			Y			Zr		
			conc	err	LOD	conc	err	LOD	conc	err	LOD	conc	err	LOD	conc	err	LOD
			ppm	*ppm*	*ppm*	*ppm*	*ppm*	*ppm*	*ppm*	*ppm*	*ppm*	*ppm*	*ppm*	*ppm*	*ppm*	*ppm*	*ppm*
2019	Afg12397	D2	27	2	3	8	2	3	51	5	5	21	5	6	315	16	10
	Afg12397	D2bis	30	2	3	10	2	3	50	6	5	15	5	7	318	17	13
	Afg12397	D3bis	16	2	3	7	2	3	47	6	6	15	4	3	178	15	16
	AFG1	Diop1	28	1	2	15	1	2	30	3	2	46	4	3	490	13	6
	AFG1	Diop3	19	1	2	12	1	2	31	3	2	60	5	2	591	16	8
	AFG3	Diop1	15	1	2	0	0	2	34	3	2	11	2	2	401	11	6
	AFG4	Diop1	15	1	2	0	0	2	18	3	2	8	2	3	57	6	6
	AFG4	Diop2	17	1	1	0	0	2	19	2	2	4	2	1	34	4	5
	Pamir2bis	D4	18	2	3	0	0	4	33	6	5	0	0	5	71	12	13
	Pamir2bis	D1	20	1	2	9	1	2	22	3	1	0	0	3	199	10	7
	Siberia390	D2	139	4	2	11	3	5	413	14	6	0	0	6	219	19	32
	Siberia390	D1	130	4	3	9	3	5	319	12	6	0	0	9	115	16	28
	Siberia390	D3	144	4	3	0	0	5	374	16	8	0	0	5	154	21	36
	Siberia390	D4	148	6	4	0	0	8	229	22	16	17	9	13	0	0	38
	BK3	D1	9	3	3	0	0	4	439	22	15	23	8	10	86	24	47
	BK6	D3	46	3	3	0	0	12	304	15	5	0	0	9	153	19	32
	BK6	D3bis	51	3	3	0	0	8	336	14	6	0	0	6	91	17	30
	BK6	D1	10	2	3	0	0	3	240	12	7	14	5	6	0	0	23
	BK7	D2	14	1	2	0	0	2	588	11	3	33	4	3	82	9	24
	BK7	D1	14	1	1	0	0	2	564	10	3	37	3	3	96	8	21
	BK9	D2	31	3	3	0	0	4	440	17	6	0	0	8	0	0	35
	BK9	D1	64	4	3	0	0	7	429	25	12	0	0	16	0	0	51
	BK9	D2bis	27	1	1	0	0	2	467	9	3	0	0	2	66	7	18
	BK10	D1	42	1	2	0	0	4	548	10	2	0	0	2	317	12	21
	BK10	D2	23	2	2	0	0	3	340	11	5	0	0	4	266	14	22
	MYA_03	B	34	3	3	0	0	8	28	7	8	0	0	7	70	13	14
	MYA_03	C	34	2	2	0	0	4	13	3	3	0	0	4	47	6	6
	MYA_04	F	54	2	2	0	0	3	13	2	2	0	0	3	119	7	5
	MYA_04	C	46	5	4	0	0	6	0	0	13	0	0	10	0	0	32
	MYA_06	D	77	1	1	0	0	2	10	2	1	0	0	2	60	4	2
	MYA_06	F	33	1	1	0	0	1	12	2	1	0	0	2	72	5	3
	MYA_07	E	68	2	2	0	0	3	8	2	2	0	0	4	59	5	5
	MYA_09	D	78	2	1	0	0	3	15	2	2	0	0	2	8	3	4
	MYA_09	A	104	2	1	0	0	2	12	2	1	0	0	3	0	0	4
	MYA_10	G	20	1	1	0	0	4	35	3	2	6	2	2	140	6	5
	MYA_10	F	24	3	3	0	0	4	52	9	8	0	0	10	141	22	22
	MYA_11	F	28	3	3	0	0	9	57	8	10	0	0	12	91	15	18
	MYA_11	B	26	4	5	0	0	9	176	21	16	0	0	14	0	0	36
	MYA_12	D	6	1	1	0	0	2	26	3	2	0	0	2	89	6	6
	MYA_12	E	0	0	7	0	0	11	155	29	34	0	0	16	0	0	66
2020	AFG1	D1	46	16	18	0	0	65	0	0	134	0	0	196	460	217	288
	AFG1	diopDX	26	9	11	37	12	9	0	0	50	73	36	48	508	94	90
	Pamir3	DZ	39	18	15	0	0	202	0	0	138	0	0	158	0	0	324
	Siberia390	D1	154	13	6	0	0	24	381	65	70	0	0	32	0	0	200
	Siberia390	D1bis	147	9	4	0	0	87	470	41	22	0	0	21	184	49	79
	BK3	D1a	0	0	18	0	0	37	403	155	146	0	0	86	0	0	314
	BK3	D1b	14	2	3	0	0	7	365	17	10	50	8	9	0	0	32
	BK9	D2a	39	9	8	0	0	15	561	74	32	0	0	30	168	41	102
	BK9	D2b	25	8	8	0	0	14	332	53	41	0	0	44	198	74	101
	MYA_03	B	47	3	10	0	0	9	0	0	66	0	0	38	0	0	155

Sample	Area	S			Fe			Ni			Cu			Zn			Ga		
		conc	err	LOD	conc	err	LOD	conc	err	LOD	conc	err	LOD	conc	err	LOD	conc	err	LOD
		wt%	*wt%*	*wt%*	*wt%*	*wt%*	*wt%*	*ppm*	*ppm*	*ppm*	*ppm*	*ppm*	*ppm*	*ppm*	*ppm*	*ppm*	*ppm*	*ppm*	*ppm*
MYA_12	A	53.08	0.76	0.03	42.41	0.36	0.01	259	36	39	0	0	28	0	0	41	0	0	36
MYA_12	B	53.03	0.76	0.02	44.67	0.40	0.01	155	41	47	707	42	30	0	0	53	0	0	45
MYA_11	C	54.17	0.75	0.02	45.43	0.40	0.01	0	0	54	0	0	27	0	0	35	0	0	33
MYA_10	C	51.52	0.76	0.03	43.17	0.37	0.01	113	39	47	220	31	33	0	0	32	13	21	29
MYA_06	I	54.95	0.75	0.03	44.58	0.39	0.01	499	50	48	0	0	34	0	0	33	0	0	29
MYA_06	L	53.63	0.73	0.04	43.16	0.38	0.01	434	47	45	0	0	33	0	0	50	0	0	44
MYA_02	I	53.84	0.74	0.02	43.86	0.38	0.01	554	54	52	214	33	35	267	31	34	0	0	31

Sample	Area	As			Se			Mo			Pb			Al			Si			Ca		
		conc	err	LOD	conc	err	LOD	conc	err	LOD	conc	err	LOD	conc	err	LOD	conc	err	LOD	conc	err	LOD
		ppm	*ppm*	*ppm*	*ppm*	*ppm*	*ppm*	*ppm*	*ppm*	*ppm*	*ppm*	*ppm*	*ppm*	*ppm*	*ppm*	*ppm*	*ppm*	*ppm*	*ppm*	*ppm*	*ppm*	*ppm*
MYA_12	A	0	0	18	540	24	14	0	0	37	0	0	57	1845	631	830	0	0	446	3041	201	104
MYA_12	B	66	15	23	112	15	19	104	27	30	0	0	68	2880	613	742	1056	317	430	1443	151	146
MYA_11	C	65	16	22	52	13	13	0	0	44	0	0	75	2470	621	779	0	0	451	789	139	153
MYA_10	C	167	17	18	38	12	17	0	0	31	0	0	97	8417	802	765	7607	545	464	1780	167	147
MYA_06	I	0	0	36	0	0	17	0	0	56	0	0	52	2657	643	807	0	0	732	1447	161	159
MYA_06	L	0	0	21	0	0	18	0	0	51	0	0	61	1811	620	817	0	0	469	1339	157	127
MYA_02	I	506	24	27	42	14	20	102	33	37	0	0	164	1566	631	852	0	0	479	2980	205	137

Table D.8. Quantitative results for µ-PIXE analysis on pyrite crystals in reference geological samples from Myanmar. IBA measurements performed in INFN-LNL.

Sample	Area	S			Fe			Ni			Cu			Zn			Ga			As			Se		
		conc	err	LOD	conc	err	LOD	conc	err	LOD	conc	err	LOD	conc	err	LOD	conc	err	LOD	conc	err	LOD	conc	err	LOD
		wt%	*wt%*	*wt%*	*wt%*	*wt%*	*wt%*	*ppm*	*ppm*	*ppm*	*ppm*	*ppm*	*ppm*	*ppm*	*ppm*	*ppm*	*ppm*	*ppm*	*ppm*	*ppm*	*ppm*	*ppm*	*ppm*	*ppm*	*ppm*
SiS-337	P1	52.00	*		48.00	*		697	118	113	0	0	141	219	64	90	83	43	57	0	0	48	0	0	43
SiS-337	P2	52.00			48.00			641	106	105	0	0	123	246	60	82	54	38	55	0	0	40	0	0	33
SiS-336	P1	52.00			48.00			491	159	175	53	91	128	166	90	132	69	59	89	0	0	70	0	0	64
SiS-336	P2	52.00			48.00			856	95	82	0	0	104	235	52	66	97	32	44	27	13	20	0	0	32
SiS-62	P1	52.00			48.00			794	150	150	99	86	122	132	84	125	117	55	75	73	27	28	0	0	59
SiS-62	P2	52.00			48.00			561	130	128	0	0	163	290	80	107	130	50	69	0	0	53	15	18	29
SiS-62	P3	52.00			48.00			783	124	121	93	72	98	298	70	93	154	47	58	21	19	21	0	0	45
SiS-337	P3	52.00			48.00			691	122	125	92	70	96	155	71	104	101	46	64	0	0	54	66	18	18
SiS-336	P3	52.00			48.00			951	122	113	57	66	91	186	64	91	97	41	58	23	17	25	0	0	41

Table D.9. Quantitative results for µ-PIXE analysis on pyrite crystals in archaeological cross sections from Shahr-i Sokhta site. IBA measurements performed in INFN-LNL. * Due to problems in the acquisition of low energy signals, fixed matrix solution was used, considering for the concentrations of S and Fe the average values obtained by SEM-EDX analysis, and only elements above Fe energy are taken into account. For this set of measurements only, dubious concentrations ("?" according to GUPIXWIN software) are all considered as present.

	Sample	Area	S			Fe			Ni			Cu			Zn		
			conc	err	LOD	conc	err	LOD	conc	err	LOD	conc	err	LOD	conc	err	LOD
			wt%	*wt%*	*wt%*	*wt%*	*wt%*	*wt%*	*ppm*	*ppm*	*ppm*	*ppm*	*ppm*	*ppm*	*ppm*	*ppm*	*ppm*
	CS10335/20a	P1	41.53	0.61	0.19	36.80	0.51	0.16	268	53	62	385	47	30	258	49	48
	CS10335/20a	P2	39.77	0.61	0.11	38.99	0.52	0.16	176	45	70	196	36	35	292	47	46
	CS10335/20a	P3	46.94	0.52	0.09	41.68	0.43	0.10	0	0	150	233	26	38	0	0	38
AGLAE 2019	SiS-333	P1	46.52	0.41	0.06	48.14	0.37	0.09	755	45	49	699	35	28	784	43	37
	SiS-4	P2	51.57	0.40	0.04	44.64	0.35	0.04	841	52	48	0	0	41	111	39	38
	SiS-67	P2	44.17	0.38	0.06	44.29	0.34	0.06	668	40	39	85	21	28	137	28	31
	SiS-325	P1	49.90	0.40	0.05	46.88	0.37	0.08	441	37	48	0	0	31	105	28	13
	SiS-4	P1	50.56	0.33	0.04	44.46	0.28	0.03	774	33	30	82	16	22	64	19	20
	SiS-67	P1	49.74	0.40	0.03	43.70	0.32	0.05	598	35	35	48	17	27	67	23	30
	SiS-187	P2	46.47	0.38	0.07	41.88	0.31	0.05	462	34	47	0	0	29	51	23	29
	SiS-325	P2	52.89	0.36	0.04	42.27	0.30	0.05	438	35	49	50	19	27	139	26	29
	SiS-187	P1	36.72	0.35	0.08	40.76	0.31	0.06	616	32	29	69	17	22	111	21	25
AGLAE 2020	SiS-187	P1	47.96	0.64	0.11	44.00	0.60	0.15	0	0	149	0	0	111	0	0	52
	SiS-325	P3	49.69	0.29	0.04	46.77	0.25	0.04	261	24	40	0	0	19	87	12	19
	SiS-67	P3	53.90	0.32	0.03	41.85	0.25	0.04	292	32	55	0	0	26	0	0	24
	SiS-333	P3	50.04	0.31	0.04	45.66	0.26	0.04	310	37	56	379	23	22	2580	52	29

	Sample	Area	Ga			As			Al			Si			Ca		
			conc	err	LOD	conc	err	LOD	conc	err	LOD	conc	err	LOD	conc	err	LOD
			ppm	*ppm*	*ppm*	*ppm*	*ppm*	*ppm*	*ppm*	*ppm*	*ppm*	*ppm*	*ppm*	*ppm*	*ppm*	*ppm*	*ppm*
	CS10335/20a	P1	0	0	72	0	0	105	18067	1935	1242	100630	2928	1474	52158	1799	602
	CS10335/20a	P2	0	0	55	0	0	76	12314	1776	1538	107790	3029	1579	42603	1551	792
	CS10335/20a	P3	0	0	19	0	0	33	16907	1270	999	59370	1686	557	4810	469	491
AGLAE 2019	SiS-333	P1	0	0	50	0	0	46	7607	733	763	18028	775	513	6241	362	344
	SiS-4	P2	0	0	61	0	0	79	5968	689	864	12578	687	620	4528	321	282
	SiS-67	P2	0	0	22	0	0	45	18959	1065	669	42678	1127	462	16803	565	310
	SiS-325	P1	0	0	48	0	0	34	5475	682	892	10592	634	466	3089	286	234
	SiS-4	P1	0	0	20	0	0	32	8734	574	583	12758	515	405	8524	311	256
	SiS-67	P1	0	0	22	0	0	32	11978	789	518	16292	691	501	9059	399	369
	SiS-187	P2	0	0	40	0	0	37	19089	981	683	44343	1051	474	10248	411	312
	SiS-325	P2	0	0	27	0	0	37	4818	567	678	13300	565	395	4885	279	249
	SiS-187	P1	0	0	20	207	57	53	26108	1191	678	86797	1450	336	44085	789	312
AGLAE 2020	SiS-187	P1	63	32	40	0	0	70	7695	1618	1370	27061	1605	1035	14357	978	1023
	SiS-325	P3	0	0	22	0	0	18	5374	408	435	9204	356	332	3640	173	142
	SiS-67	P3	0	0	30	56	38	18	5920	465	494	12092	438	378	4182	216	152
	SiS-333	P3	56	14	12	0	0	17	3878	427	535	8513	408	385	11638	326	176

Table D.10. Quantitative results for µ-PIXE analysis on pyrite crystals in archaeological samples from Shahr-i Sokhta site, measured as such (seal and fragments). IBA measurements performed in AGLAE, measurement runs are reported separately for fragments.

Sample	Point	Mg			Al			Si			K			Ca			Ti		
		Conc	Err	LOD	Conc	Err	LOD	Conc	Err	LOD	Conc	Err	LOD	Conc	Err	LOD	Conc	Err	LOD
		ppm	*ppm*	*ppm*	*ppm*	*ppm*	*ppm*	*ppm*	*ppm*	*ppm*	*ppm*	*ppm*	*ppm*	*ppm*	*ppm*	*ppm*	*ppm*	*ppm*	*ppm*
Pamir2-D1	A	91739	55	5	5764	13	5	256325	77	5	0	0	5	182897	73	6	300	8	9
Pamir2-D1	B	90842	55	5	7482	15	5	257917	77	5	10	4	5	181579	73	6	427	8	8
Pamir2-D1	C	91225	55	5	6360	14	5	258313	77	5	0	0	5	183571	73	6	312	8	9
Pamir2-D1	D	90615	54	5	7315	15	4	257588	77	5	10	4	5	181680	73	6	369	8	9
MEAN		91105	55	5	6730	14	5	257536	77	5	5	2	5	182432	73	6	352	8	9
BK7-D1	A	92117	55	5	5386	13	4	258347	78	5	0	0	5	181350	73	6	92	7	9
BK7-D1	B	91414	55	5	5749	13	4	257701	77	5	11	5	5	180470	72	6	69	7	9
BK7-D1	C	91154	55	5	5537	13	5	257746	77	5	0	0	5	180553	72	6	58	8	9
BK7-D1	D	91502	55	5	4798	12	5	258928	78	5	11	11	5	181614	73	6	69	8	9
MEAN		91547	55	5	5367	13	5	258180	77	5	5	4	5	180997	72	6	72	8	9
MYA9-A	A	85718	51	5	14828	19	4	257304	77	5	0	0	5	178298	71	6	184	8	9
MYA9-A	B	84491	51	5	18410	22	5	256750	77	5	11	5	5	176027	70	6	161	8	9
MYA9-A	C	83580	50	5	19660	24	5	256392	77	5	32	31	5	175689	70	6	35	9	9
MYA9-A	D	84286	51	5	19002	23	4	255850	77	5	0	0	5	175620	70	6	12	8	9
MEAN		84519	51	5	17975	22	5	256574	77	5	11	9	5	176409	71	6	98	8	9
AFG1-Diop1	A	76443	46	4	24594	25	4	260473	78	5	33	4	5	149573	75	6	6019	10	9
AFG1-Diop1	B	83126	50	5	15147	20	4	258798	78	5	0	0	5	163281	65	6	3311	9	9
AFG1-Diop1	C	77946	47	5	23222	26	4	260738	78	5	33	5	5	152460	76	6	5114	9	9
AFG1-Diop1	D	77485	46	5	23069	25	4	260907	78	5	33	5	5	151732	76	6	4887	9	9
MEAN		78750	47	5	21508	24	4	260229	78	5	25	4	5	154261	73	6	4833	9	9

Sample	Point	Cr			Mn			Fe			Zn			Sr			Y			Zr		
		Conc	Err	LOD	Conc	Err	LOD	Conc	Err	LOD	Conc	Err	LOD	Conc	Err	LOD	Conc	Err	LOD	Conc	Err	LOD
		ppm	*ppm*	*ppm*	*ppm*	*ppm*	*ppm*	*ppm*	*ppm*	*ppm*	*ppm*	*ppm*	*ppm*	*ppm*	*ppm*	*ppm*	*ppm*	*ppm*	*ppm*	*ppm*	*ppm*	*ppm*
Pamir2-D1	A	0	0	7	196	10	12	1634	20	13	22	14	19	0	0	28	0	0	26	131	26	20
Pamir2-D1	B	11	7	7	184	10	12	2131	21	13	56	16	19	0	0	28	0	0	27	197	25	20
Pamir2-D1	C	0	0	7	184	10	12	1789	20	13	0	0	19	0	0	27	14	25	26	115	27	20
Pamir2-D1	D	0	0	7	161	10	12	1689	20	13	56	15	19	0	0	28	0	0	27	181	26	20
MEAN		3	2	7	181	10	12	1811	20	13	33	11	19	0	0	28	4	6	27	156	26	20
BK7-D1	A	0	0	7	253	10	12	1744	21	14	22	16	19	425	24	28	0	0	27	99	26	20
BK7-D1	B	23	7	7	311	10	11	1579	20	13	22	15	19	457	23	28	0	0	26	0	0	20
BK7-D1	C	0	0	7	276	10	12	1777	20	13	11	27	19	467	23	28	0	0	28	66	26	19
BK7-D1	D	0	0	7	173	10	11	917	18	13	0	0	19	127	23	28	0	0	26	197	26	20
MEAN		6	2	7	253	10	12	1504	20	13	14	15	19	369	23	28	0	0	27	90	19	20
MYA9-A	A	0	0	7	92	10	12	1875	20	13	122	16	19	0	0	28	14	21	26	82	26	19
MYA9-A	B	0	0	7	46	11	12	1731	20	13	78	17	19	0	0	28	14	57	26	0	0	19
MYA9-A	C	0	0	7	127	11	11	1808	20	13	78	16	19	0	0	28	0	0	27	0	0	21
MYA9-A	D	23	6	7	58	10	12	1709	20	13	78	16	19	0	0	29	14	42	26	0	0	20
MEAN		6	1	7	81	10	12	1781	20	13	89	16	19	0	0	28	11	30	26	21	7	20
AFG1-Diop1	A	34	7	7	149	10	11	319	15	13	0	0	19	76	23	26	0	0	27	520	26	19
AFG1-Diop1	B	0	0	7	184	10	11	275	15	13	0	0	19	0	0	27	14	36	26	432	26	20
AFG1-Diop1	C	11	10	7	172	10	12	1495	19	13	44	15	19	11	23	27	73	28	26	485	26	19
AFG1-Diop1	D	34	7	7	126	10	11	825	17	13	0	0	19	0	0	28	0	0	27	436	25	19
MEAN		20	6	7	158	10	11	728	17	13	11	4	19	22	12	27	22	16	27	468	26	19

Table D.11. Quantitative results for SEM-WDX analysis on diopside crystals in reference geological samples. Mean values for each element are reported.

Sample	Diopside Area	585 nm (2.119 eV)		690 nm (1.797 eV)		770 nm (1.610 eV)		430-450 nm (2.755-2.883 eV)		R-square
		Area	err	Area	err	Area	err	Area	err	
Afg12397	D2	128430.31	0.05			177726.0	0.1	38041.8	0.2	0.99422
Afg12397	D2bis	133790.44	0.05			173573.1	0.1	41184.4	0.2	0.99422
Afg12397	D3bis	134370.57	0.06			163025.3	0.1	53842.7	0.2	0.99456
AFG1	Diop1	53278.08	0.07			16285.5	0.4			0.99745
AFG1	Diop3	74410.82	0.07			26998.0	0.5			0.99787
AFG3	Diop1	62756.55	0.05			120972.1	0.1	9258.5	0.1	0.99648
AFG4	Diop1	43829.01	0.11	34538.7	0.3			5590.7	0.2	0.99702
AFG4	Diop2	47981.13	0.10					10197.7	0.2	0.99683
Pamir2bis	D4	110161.78		37213.9				8366.1		nd
Pamir2bis	D1	89105.84		27617.5				20781.5		nd
Siberia390	D2	8597.05	0.21	9712.9	0.9			5518.2	2.4	0.99682
Siberia390	D1	9244.59	0.22	21401.5	16.4					0.99745
Siberia390	D3	12085.74	0.37	22683.4	8.4					0.99713
Siberia390	D4	6569.26	0.23	17549.9	12.5					0.99839
BK3	D1	61034.50	0.15	23306.4	0.2					0.99669
BK6	D3	51241.59	0.16	25123.0	0.2			3524.6	0.1	0.99652
BK6	D3bis	13000.76	0.10	11456.7	0.3			1227.9	0.1	0.99304
BK6	D1	12607.85	0.12	5722.8	0.2					0.99581
BK7	D2	223578.93	0.20	72861.4	0.3			13997.8	0.1	0.99692
BK7	D1	181409.45	0.21	52821.9	0.3			5935.7	0.1	0.99667
BK9	D2	17144.04	0.13	14257.9	0.3			9889.3	0.2	0.99652
BK9	D1	26465.49	0.06	27005.7	0.1			11314.8	0.2	0.99439
BK10	D1	5087.93	0.06	18228.9	1.7			3699.0	0.3	0.99612
BK10	D2	19640.96	0.11	25043.8	0.5			15277.4	0.4	0.99563
MYA_03	C	15623.23	0.11	12537.2	0.4			16066.2	0.3	0.99633
MYA_04	F	12203.11	0.13	9677.4	0.3			8772.3	0.2	0.99682
MYA_04	C	14865.18	0.13	11081.0	0.3			8486.9	0.2	0.99686
MYA_06	D	13726.63	0.11			22797.6	0.9	4628.0	0.4	0.99697
MYA_06	F	25006.27	0.09			33746.4	1.1	23879.9	0.5	0.9952
MYA_07	E	7197.02	0.12	10803.5	0.7			3206.8	0.5	0.99734
MYA_09	D	8251.14	0.18	1759.4	0.3					0.99681
MYA_09	A	12066.92	0.09	7093.7	0.2					0.99538
MYA_10	G	16407.97	0.15	12122.5	0.3			1612.4	0.2	0.99742
MYA_10	F	11419.41	0.11	9189.2	0.2			4270.1	0.3	0.99762
MYA_11	F	9168.23	0.11	7613.9	0.1			2940.3	0.2	0.99418
MYA_11	B	7788.46	0.11	7763.3	0.1			2958.1	0.3	0.99397
MYA_12	D	15876.81	0.12	10067.0	0.2			8556.0	0.2	0.99617
MYA_12	E	14519.70	0.13	9793.2	0.2			5560.6	0.2	0.99666
SiS-336	D1	145954.67	0.06			165021.5	0.2	32732.1	0.2	0.99122
SiS-28	D1	70053.17	0.05			128640.0	0.1	14612.5	0.1	0.99626
SiS-336	D2	56267.20	0.05			70902.1	0.2	4712.6	0.1	0.99214
SiS-67	D1	973475.43	0.06			773238.9	0.1	40872.5	0.1	0.99629
SiS-325	D1	593477.68	0.06			470172.9	0.2	52100.5	0.2	0.99598

Table D.12. Quantitative results from the fitting process of μ-IL spectra. Areas and related errors for different IL bands are reported in arbitrary units and the R-square values for the total fit is indicated. Fit for Tajik samples did not converge, but band areas were still calculated. All considered spectra are from 2019 IBA measurement run in AGLAE.